

**Stress-induced permeability evolution in coal:
Laboratory testing and numerical simulations**

To the Faculty of Geosciences, Geoengineering and Mining
of the Technischen Universität Bergakademie Freiberg
approved

THESIS

to attain the academic degree of
Doctor of Engineering
Dr.-Ing.
submitted

by Dipl.-Ing. Yufeng Zhao

born on June 20, 1989 in Nei Mongol, China

Reviewers: Prof. Dr.-Ing. habil. Heinz Konietzky, Freiberg, Germany
Prof. Dr. Chrysothemis Paraskevopoulou, Leeds, UK
Prof. Dr. Hongwei Zhou, Beijing, China

Date of the award: 15.07.2020

Acknowledgements

First and foremost, I am pleased that I have spent precious and fruitful years at TU Bergakademie Freiberg. This work is accomplished only with the help of my colleagues at the Geotechnical Institute. I would like to thank all people who helped and supported me during my stay.

My deepest gratitude goes to Professor Heinz Konietzky, Head of Geotechnical Institute at TU Bergakademie Freiberg. He is one of the best teachers that I have ever met and he showed me how to conduct proper scientific research. It is my honor to be guided by Professor Konietzky. His encouragement, understanding and continuous support during my doctoral study will always be remembered. I learnt a large amount from him in an efficient way.

During this long journey, I owe great gratitude to all my colleagues. It is my pleasure to work with everyone at the Geotechnical Institute. This is a family for me in Germany. I would like to thank Mrs. Angela Griebisch for her friendly help whenever needed. I want to give great thanks to the staff working in the rockmechanical laboratory at TU Bergakademie Freiberg. I own gratitude to Dr. Thomas Frühwirth for offering his helpful advices for lab testing and insights about result analysis, Mr. Tom Weichmann and Mrs. Beatrice Tauch for lab assistance, Dr. Christian Jakob and Mr. Vishal Vilas Yadav for good work environment. I also want to thank Dr. Martin Herbst for his kind support sharing experiences in different scientific fields.

Dating back to the origin of this PhD journey, I would like to thank the China Scholarship Council (CSC) for financially supporting my study in Germany. Especially, many thanks go to Professor Hongwei Zhou, for his support in my application for the scholarship, and for recommending me to Professor Konietzky. I am grateful to Dr. Jiangcheng Zhong and Dr. Dongjie Xue for collecting coal samples from China for my on-going research.

Finally, I would like to give special thanks to my Chinese friends, for helping me dealing with a lot of daily issues during my stay in Germany. I also give great thanks to my parents and family members for their unconditional love and support.

Abstract

Underground coal seams, especially in great depth, are formed by low permeability coal rock. Mining operations produce a multiscale network of fractures in the coal seams. Simulation of fracture and damage mechanical problems using DEM models become popular. Permeability evolution in rocks is important for coal bed methane (CBM) and shale gas exploitation as well as for greenhouse gas storage. Therefore, this work presents laboratory tests and a coupled model using PFC^{3D} and FLAC^{3D} to simulate the stress induced permeability evolution in coal samples. The main content of the thesis can be summarized as follows:

1. The use of X-ray CT technique is introduced to reconstruct coal samples. Basic mechanical properties are determined via lab testing. Numerical models are generated in PFC^{2D}, PFC^{3D} and FLAC^{3D}, respectively.

2. Laboratory tests are performed to investigate the permeability evolution. A newly developed experimental system is employed to perform 3-dimensional loading and to measure the flow rate simultaneously. The evolution process is described by five distinct phases in terms of permeability and deformation. Peak permeability appears after peak stress. Peak stress and peak permeability of the samples depend heavily on confining pressure.

3. A new approach to simulate triaxial compression test is established with significant improved handling of the confinement. The tests are simulated in PFC^{3D} using a flexible wall boundary. In this thesis, triaxial test model is verified by comparing stress-strain response and fracture pattern of coal samples tested in the laboratory. The composition of the samples (matrix and inclusions) influences the peak strength. Force chain development and crack distributions are also affected. Increasing confinement leads to a change of damage pattern.

4. Coupled numerical simulations are described. The special designed coupling between PFC^{3D} and FLAC^{3D} is effective in simulating the permeability of damaged coal samples. The permeability of damaged coal samples is closely associated with crack pattern in general and crack width in particular. Relations between hydraulic properties and fracture data are established. A theoretical approach for evaluating the permeability is proposed based on fracture distribution and single crack behavior. The coupled models simulate the gas flow process (experimentally verified) as a function of opening and closure of microcracks.

Permeability and volumetric strain show good nonlinear exponential relation after a newly introduced expansion point. Piecewise relations fit the whole process, the expansion point can be treated as critical point. The structural characteristics of the samples influence this relation before and after the expansion point significantly.

Key words

Coal sample, X-ray CT, sample reconstruction, 3-axial compression test, permeability evolution, DEM, FDM, flow path, deformation pattern, damage pattern, coupled numerical simulation, volumetric strain, cracks, fractures.

Table of content

Acknowledgements	I
Abstract	III
Table of content.....	V
List of tables	VII
List of figures	IX
List of variables.....	XIII
1 General introduction.....	1
1.1 Research background	1
1.2 Significance.....	3
1.3 Research status / State of the art.....	4
1.4 Research content	7
1.5 Research strategy.....	9
2 CT reconstruction.....	11
2.1 Introduction	11
2.2 Sampling and Methodology	13
2.3 Sample reconstruction and numerical model set-up	18
2.4 Application.....	20
2.4.1 Coal sample reconstruction.....	20
2.4.2 Numerical simulation of coal samples under pure mechanical loading.....	25
2.5 Conclusions	32
3 Permeability evolution under triaxial compression.....	35
3.1 Introduction	35
3.2 Experimental setup.....	37
3.3 Test procedure	40
3.4 Results and discussion.....	41
3.5 Conclusions	54

4	Numerical simulation of triaxial tests	57
4.1	Introduction	57
4.2	Modelling	59
4.3	Calibration and verification.....	64
4.4	Sample reconstruction for modeling	75
4.5	Discussion of results.....	82
4.6	Conclusions	86
5	HM-coupled simulations	87
5.1	Introduction	87
5.2	Methodology	89
5.3	Modelling	90
5.4	Theoretical analysis.....	94
5.5	Results and discussions	103
5.6	Conclusions	127
6	Conclusions and outlook	129
6.1	Main conclusions.....	129
6.2	Implications for practical purposes	131
6.3	Outlook for future research	131
	Appendix	133
	A1: Wall update commands for FW approach in PFC ^{3D}	133
	A2: Cracks import and hydraulic property assignment in FLAC ^{3D}	134
	References	137

List of tables

Table 2.1 Coal samples, corresponding experiments and simulations	13
Table 2.2 Average parameters of coal samples	14
Table 2.3 Image properties used in reconstruction	19
Table 2.4 Mechanical parameters of coal samples	20
Table 2.5 Proximate analysis results of coal (Liu et al. 2017)	21
Table 2.6 Element mass fraction of coal samples (Liu et al. 2017)	21
Table 2.7 Mineral mass fraction of coal samples (Liu et al. 2017)	21
Table 2.8 Physical and mechanical parameters of coal samples (Zhao et al. 2010a)	21
Table 2.9 Particle based numerical models for UCS tests	28
Table 2.10 Mechanical parameters for numerical simulations	29
Table 2.11 Peak stress of sample models during UCS tests	32
Table 3.1 Basic physical and mechanical parameters of coal samples (average values)	37
Table 3.2 Measured values of permeability (coal samples)	41
Table 3.3 Fracture parameters of different coal samples after final destruction	53
Table 4.1 Physical and mechanical parameters of coal samples obtained from uniaxial compression tests	65
Table 4.2 Mechanical parameters of PFC ^{3D} model	73
Table 4.3 Physical and mechanical parameters of realistic coal sample (Zhao et al. 2010a)	74
Table 4.4 Micro-mechanical parameters of the numerical coal model	74
Table 4.5 Composition of coal samples	76
Table 4.6 Damage patterns in models C1 and C4	85
Table 5.1 Basic crack parameters exported from PFC ^{3D} model	93
Table 5.2 Mechanical and hydraulic parameters of numerical simulation	103
Table 5.3 Variables in Equation 5.19 for different confining pressures	126

List of figures

Figure 1.1 China's total annual coal output and mortality per million tons of mined coal over the past 11 years (2008~2018)	1
Figure 1.2 Concept of effective stress	6
Figure 1.3 Double-porous media	7
Figure 1.4 Generalized double porosity model	7
Figure 1.5 Flowchart illustrating the research strategy	9
Figure 2.1 Coal samples from underground mine Pingdingshan No. 8 (China)	13
Figure 2.2 Micro-xCT scanner associated with rock testing system. (a) Micro-xCT scanning device, (b) side view of schematic scanner layout, (c) Sample dimensions and scan slice spacing.	15
Figure 2.3 Input level curves at different phases: (a) raw image, (b) automatically adjusted image and (c) manually adjusted image	16
Figure 2.4 Representative slice image of sample C3 and gray value along profile line	17
Figure 2.5 Resolution reduction and gray scale value segmentation	18
Figure 2.6 3D model reconstruction based on 2D images: (a) stack of images, (b) cross-sections in horizontal and vertical directions and (c) final 3D reconstruction	19
Figure 2.7 Numerical models in (a) PFC2D, (b) PFC3D and (c) FLAC3D (green: matrix; red: inclusions; holes: pores)	20
Figure 2.8 3D representation of the mineral inclusions in virgin coal sample C3	22
Figure 2.9 3D distribution of pores and fractures in virgin coal sample C3	23
Figure 2.10 Fracture evolution in coal sample C3 during UCS test (vertical stress vs. vertical strain, see also Figure 2.11 and Figure 2.12)	24
Figure 2.11 Fractures in sample C3 shown by CT image at a selected cross-section	24
Figure 2.12 Evolution of fractures in coal sample C3 at different loading stages: (a) 1500 N (2.93 MPa), (b) 2000 N (3.9 MPa), (c) 4000 N (7.8 MPa) and (d) 4500 N (8.78 MPa)	25
Figure 2.13 PFC ^{2D} models for cross-sections along different angles (based on sample C3)	27
Figure 2.14 UCS tests in PFC ^{2D} (vertical stress vs. vertical strain) for different cross-sections at angles of 0°, 30°, 60°, 90°, 120° and 150° (based on sample C3)	27
Figure 2.15 Fracture pattern (PFC ^{2D} and PFC ^{3D})	30
Figure 2.16 UCS tests results for (a) PFC ^{2D} model (b) PFC ^{3D} model	31
Figure 3.1 DBT A50-80-180 triaxial cell for hydro-thermo-mechanical coupled testing	38
Figure 3.2 Schematic of the experimental setup	39
Figure 3.3 Complete stress-strain curves of samples under triaxial compression	42
Figure 3.4 Differential stress (axial stress minus circumferential stress) and permeability evolution versus axial strain for sample C1	43
Figure 3.5 Strain value ϵ_d versus confining pressure	44

Figure 3.6 Permeability evolution and complete stress-strain curve	48
Figure 3.7 Permeability evolution at different confining pressures	49
Figure 3.8 Lagging characteristic (strain at peak differential stress vs. strain at peak permeability) as function of confining pressures	50
Figure 3.9 Peak differential stresses and permeability versus confining pressure	51
Figure 3.10 Peak differential stress and peak permeability versus confining pressure	51
Figure 3.11 Digital reconstructed structures of deformed samples	52
Figure 3.12 Complete deformed sample C16 with core sleeve	53
Figure 3.13 Main fracture angle in the coal samples versus confining pressure	54
Figure 4.1 Triaxial model with membrane formed by balls	59
Figure 4.2 Reconstructed DEM sample with FW membrane as outer vertical boundary	60
Figure 4.3 Sketch to illustrate the wall element updating process (FW approach)	61
Figure 4.4 Simulated stress-strain curves and crack evolution for coal sample C1 with 2.5 MPa confining pressure using the FW approach	62
Figure 4.5 Average stress components in z-, x- and y-directions for each measure region (negative stress values represent compression)	63
Figure 4.6 Cross-section of samples before and after 3-axial compression simulation	64
Figure 4.7 Stress-strain curves of uniaxial compression simulations with different pb_emod	66
Figure 4.8 Relationship between compressive elastic modulus and parallel bond group elastic modulus	66
Figure 4.9 Relationship between Poisson's ratio and axial strain for different pb_kratio under uniaxial compression	67
Figure 4.10 Relationship between Poisson's ratio and normal to shear stiffness ratio under uniaxial compression	68
Figure 4.11 Stress-strain curves for different ratios between tensile strength and cohesion (uniaxial compression tests)	68
Figure 4.12 Damage patterns for uniaxial loaded models with different ratios of tensile strength to cohesion (tensile cracks: green disks; shear cracks: red disks)	69
Figure 4.13 Stress-strain curves for different friction angles (uniaxial compression tests)	70
Figure 4.14 Damage patterns for uniaxial loaded models with different friction angles (tensile cracks: green disks; shear cracks: red disks)	71
Figure 4.15 Stress-strain curves with different expansion coefficients (uniaxial compression tests)	72
Figure 4.16 Relationship between peak stress and strength expansion coefficient (uniaxial compression tests)	72
Figure 4.17 Stress-strain curves for lab tests and numerical model after calibration	73
Figure 4.18 Reconstructed numerical models of coal samples (green: coal matrix, red: inclusions)	76

Figure 4.19 Stress-strain curves of numerical simulations and laboratory tests with 2.5 MPa confining pressure	77
Figure 4.20 Contact force chains with cracks for numerical model C1 with 2.5 MPa confining pressure in cross-sectional perspective (shear cracks: red, tensile cracks: green)	78
Figure 4.21 Stress-strain curves of numerical simulations and laboratory tests with 5.0 MPa confining pressure	79
Figure 4.22 Contact force chains with cracks for numerical model C3 with 5.0 MPa confining pressure (shear cracks: red, tensile cracks: green)	80
Figure 4.23 Stress-strain curves of numerical simulations and laboratory tests with 7.5 MPa confining pressure	81
Figure 4.24 Contact force chains with cracks for numerical model C4 with 7.5 MPa confining pressure (shear cracks: red, tensile cracks: green)	82
Figure 4.25 Differential stress and amount of cracks for model C1 versus axial strain during deviatoric regime for different confining pressures	83
Figure 4.26 Simulated stress-strain curves of 5 samples with different confining pressures	84
Figure 5.1 Flow chart illustrating the coupling between PFC ^{3D} and FLAC ^{3D}	90
Figure 5.2 Illustration of meshing the FLAC ^{3D} model	91
Figure 5.3 Zones occupied by a crack (disk)	91
Figure 5.4 Examples of fractures represented by zones in FLAC ^{3D} (above: real fracture, below: representation inside FLAC ^{3D})	92
Figure 5.5 Fracture zone assignment (projection view)	92
Figure 5.6 Illustration of a FLAC ^{3D} model for a specific stress state (25 MPa axial stress and 2.5 MPa confining pressure) with micro fractures	94
Figure 5.7 Zone types before and after parameter assignment based on PFC ^{3D} simulations	94
Figure 5.8 Tetrahedron structure of particles in contact	98
Figure 5.9 Relation between crack width and direct contact aperture	99
Figure 5.10 Relation between crack width and shear displacement	99
Figure 5.11 Crack width evolution as function of shear displacement	100
Figure 5.12 Scheme for hydraulic parameter transformation procedure	102
Figure 5.13 Flow rate evolution as function of calculation steps for model C1 (at axial strain of 0.0132, nearly stationary phase after about 30.000 calculation steps)	104
Figure 5.14 Pore pressure along vertical model axis for model C1 (at axial strain of 0.0132, stationary phase)	104
Figure 5.15 Simulated permeability evolution compared with lab results for different samples and confinement	105
Figure 5.16 Stress-strain curves and permeability evolution for sample C1 under 2.5 MPa confining pressure (stationary phase)	106

Figure 5.17 Stress-strain curves and permeability evolution for sample C13 (model reconstruction based on C1) under 5.0 MPa confining pressure (stationary phase)	107
Figure 5.18 Stress-strain curves and permeability evolution for sample C4 under 7.5 MPa confining pressure (stationary phase)	108
Figure 5.19 Schematic diagram for evolution of permeability and volumetric strain versus time (model C1 as example)	109
Figure 5.20 Permeability and strain evolution of coal sample C1 versus differential stress	112
Figure 5.21 Permeability and strain evolution of coal sample C2 versus differential stress	115
Figure 5.22 Permeability and strain evolution of coal sample C3 versus differential stress	118
Figure 5.23 Permeability and strain evolution of coal sample C4 versus differential stress	121
Figure 5.24 Permeability and strain evolution of coal sample C5 versus differential stress	124
Figure 5.25 Permeability versus volumetric strain for different confining pressures (regression lines refer to values after the expansion point)	126

List of variables

A	Cross sectional area [m ²]
A_{all}	Accumulated area of all fracture surfaces [m ²]
A_f	Cross section area of fracture [m ²]
a	Area contribution coefficient [-]
C	Cohesion [Pa]
C_{res}	Residual cohesion [Pa]
\bar{c}	Cohesion assigned to bond in PFC ^{2D} and PFC ^{3D} [Pa]
cbl	Coefficient connecting theoretical and numerical volumetric strain [-]
CT_{number}	CT number used to describe the attenuation data [-]
D	Sample diameter [m]
D_{ap}	Tensile displacement (particle surface aperture) [m]
d	Diameter of crack [m]
d_{CC}	Distance from crack center to zone center [m]
E	Elastic modulus ($emod$, pb_emod) [GPa]
g_c	Contact gap interval [m]
h	Sample length/height [m]
K	Configured permeability coefficient [m/s]
K^*	Normal to shear stiffness ratio ($kratio$, pb_kratio) [-]
k_0, k	Initial and actual permeability [m ²]
k_a	Intrinsic permeability [m ²]
k_{cl}	Permeability of closed fracture zone [m ²]
k_f	Permeability of one fracture segment in one zone [m ²]
k_P	Peak permeability [m ²]

k_i, k_z	Initial and actual permeability of zone [m ²]
Δk	Permeability change [m ²]
L	Side length of zone [m]
l	Length of crack segment observed in one zone [m]
m	Mass [g]
N	Total number of elements (particle or zone) [-]
P_u, P_d	Upstream and downstream pressures [Pa]
P_0	Reference pressure [Pa]
$P_u(t), P_d(t)$	Upstream and downstream pressures at time t [Pa]
ΔP_i	Initial pressure difference [Pa]
Q	Flow rate [m ³ /s]
Q_0	Flow rate at reference pressure [m ³ /s]
q	Gas flow through one fracture [m ³ /s]
R	Radius of sample model [m]
R_1, R_2	Inner radius and Width of outer ring [m]
r_p	Radius of particle [m]
S_u	Water bearing capacity of upstream container [m ³ /Pa]
S_d	Water bearing capacity of downstream container [m ³ /Pa]
T_1	Gray scale value threshold between pores/fractures and coal matrix [-]
T_2	Gray scale value threshold between coal matrix and mineral inclusions [-]
t	Test time [s]
v	Velocity (loading) [m/s]
v_{max}	Maximum velocity used for confinement [m/s]
W	Crack width (final width) [m]
W_0	Initial total aperture at low effective stress [m]

W_{res}	Residual aperture at high effective stress [m]
W_T	Width of tensile crack [m]
W_{S1}, W_{S2}	Width of shear crack type 1 and 2 [m]
W_{as}	Width of newly generated fracture [m]
ΔW	Aperture change [m]
$\Delta\delta$	Shear displacement change [m]
$\Delta\delta_1, \Delta\delta_2$	Shear displacement type 1 and 2 [m]
ε_d	Axial strain corresponding to σ_d [-]
ε_V	Volumetric strain [-]
ε_{VT}	Theoretical volumetric strain [-]
ε_{VP}	Volumetric strain measured in PFC ^{3D} model [-]
θ	Friction angle (pb_fa) [°]
θ_{res}	Residual friction angle [°]
θ_f	Angle of main fracture [°]
μ_c	Friction coefficient assigned to bond in PFC ^{2D} and PFC ^{3D} [-]
μ	Viscosity [Pa·s]
μ_x	Calculated X-ray attenuation coefficient [-]
μ_w	Attenuation coefficient for water [-]
ν	Poisson's ratio [-]
ρ	Density [kg/m ³]
ρ_d, ρ_g	Dry density and grain density [kg/m ³]
ρ_p	Density of particle [kg/m ³]
ρ_z	Density of zone [kg/m ³]
σ_c	Uniaxial compressive strength (UCS) [Pa]
σ_t	Tensile strength [Pa]

$\bar{\sigma}_c$	Tensile strength assigned to bond in PFC ^{2D} and PFC ^{3D} [Pa]
σ_3	Confining pressure [Pa]
σ_m	Stress point corresponding to minimum permeability [Pa]
σ_d	Stress point corresponding to firstly detected flow rate [Pa]
σ_P	Peak differential stress [Pa]
σ'_n	Effective normal stress [Pa]
σ_{nref}	Reference effective normal stress at initial aperture [m ²]
σ^t	Tension limit assigned in FLAC ^{3D} [m ²]
φ	Porosity [%]
$\bar{\Phi}$	Friction angle assigned to bond in PFC ^{2D} and PFC ^{3D} [°]
ψ	Dilation angle [°]
ψ_{dil}^{eff}	Effective shear dilation angle [°]
ψ_{dil}	Shear dilation angle [°]
ψ_1, ψ_2	Shear dilation angle type 1 and 2 [°]

* Units in this work may be different from given list, e.g. [Pa] is replaced by [MPa] etc.

1 General introduction

1.1 Research background

Coal occupies the major portion in the energy resource structure of China (National Bureau of Statistics of China, 2018). More electricity is in demand for industrial development and coal-fired power plants are still the main power source for decades, according to Chinese National Development and Reform Commission (NDRC). Coal is also the basic material for many fertilizer and chemical products. China is the world's largest consumer and producer of coal. As shown in Figure 1.1, the annual coal output increased significantly before 2014. Despite minor decreases in 2015 and 2016, the total output starts increasing again since 2017. An average increase of 75.5 million tons of coal was added to the total output every year. Along with the growth of production, more potential safety hazards were taken into consideration.

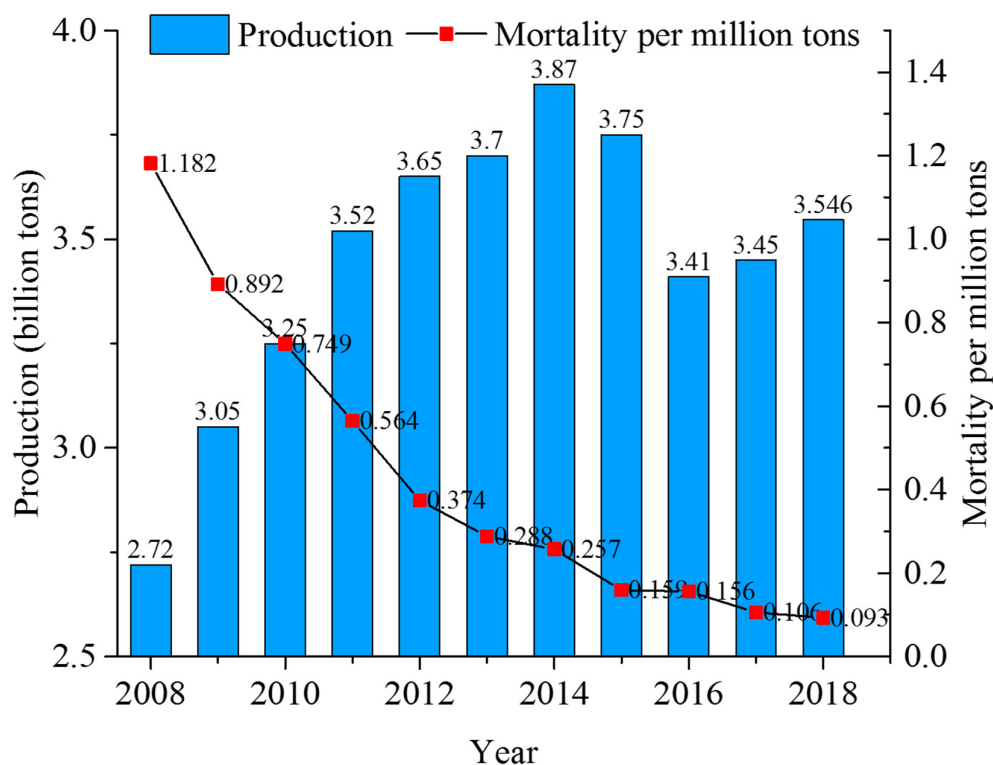


Figure 1.1 China's total annual coal output and mortality per million tons of mined coal over the past 11 years (2008~2018)

Environmental concerns and energy crisis are connected with each other. The exploitation and utilization of fossil resources is a double-edged sword. On the one hand, fossil resources contribute to the development of state economy and people's livelihood; on the other hand, large amount of pollution affect the sustainable development. The economic development is restricted by the environmental degradation. The dynamic balance between fossil resource utilization and environment deterioration is an important task for all developing countries.

Resource exhaustion is verified for the shallow coal seams, therefore exploitation is extended to greater depths. Man-made disasters are increasing at greater depths. Depth-dependent rock

mechanics became a pivotal research topic among scholars. Crustal stress, temperature and pore pressure become higher obviously with increasing depth. Mineral components, micro-structures and properties are also influenced by the depth, so mechanical behavior and engineering response are different to coal seams at shallow depth. Because of the extremely complex geological conditions, gas outbursts and water inrushes are happening more frequently. Especially the outburst of gas plays an important role during underground mining processes. These disasters are related to the fluid-solid coupling.

Natural gas is an effective and relatively clean energy resource. By generating 1 GJ heat, only 50.4 g CO₂ emission is created, compared to 890 g for coal and 70.6 g for petroleum. Natural gas has higher combustion efficiency and less emission. Increasing production and utilization of natural gas can relieve the energy crisis and the environmental pollution.

So not only coal itself is a valuable energy source, the coalbed methane (CBM) is also an important resource. As clean and less CO₂ intensive fossil fuel, vast quantities of CBM are stored in coal seams. Finding an optimum method to exploit CBM was and is the focus of many scholars. This topic is connected with the exploitation of coal and still a tough challenge. Exploitation of CBM is also an effective technique to prevent gas hazard. Working faces are protected by pre-extraction of gas. Extraction and storage of CBM and shale gas are important to solve the energy problems in China. However, the gas flow is complex in porous coal seams. The flow of CBM or shale gas doesn't follow the Darcy's law inside deep lying rock/coal. So the permeability evolution is always a core problem in natural gas exploitation and storage.

Petroleum is also an important energy source. Extraction and storage have been important research topics since the government's tenth national five-year plan. A complete oil reserve system will be formed. This system will be essential to meet domestic supply and balance the market. But until now, the construction is still falling behind the most developed countries in Europe or the US. Because of the huge petroleum consumption and the underdeveloped reserve technologies, a consistent supply capability is not yet guaranteed. So the study in oil reserving techniques is still one of the priority subjects.

There are still other challenges in exploitation and reserve of coal, natural gas and petroleum. Massive use of fossil energy has led to serious environmental hazards. Greenhouse gas emission, groundwater pollution and surface subsidence are typical cases. Among these problems, a proper design and construction of underground CO₂ storage can help relieving emission burdens. Groundwater pollution may be caused by different sources, such as nuclear waste leakage and oil spills. Together with CBM and shale gas extraction mentioned before, all these cases are related to permeation and diffusion of gas or liquid and demand the consideration of fluid-solid coupling. Mechanical and geometrical effects have to be considered, therefore a simple application of flow equations is not sufficient to reflect the real behavior. Without considering the coupling effects, huge errors occur in the evaluation of the flow field. Therefore, study of dynamic permeation laws in low permeable media is conducted to develop and optimize exploitation and storage. This study is also necessary to prevent and control groundwater pollution, fluid waste contamination and greenhouse gas emission.

The challenges mentioned before are mainly based on the imperfect coupled permeation theory, and the use of inaccurate fracture propagation laws. Micro-pores and fractures are the seepage paths of flow and diffusion, so the fracture propagation has top priority, and the permeation process has to be investigated based on structural changes.

1.2 Significance

Due to the stress redistribution in surrounding rocks and coal, the loading on goaf rocks and advanced coal bodies are changing permanently. An internal pore-fracture network develops with the deformation and breakage of coal. Meanwhile the permeability properties change because of the expansion or squeezing of seepage paths.

Along with the advance of working faces, coal went through different loading stages (Cai et al. 2013; Karacan et al. 2011). The stress variations during mining have been simulated and permeability tests under triaxial compression were conducted in the laboratory. A relationship between stress state, pore-fracture network and permeability evolution was established. In addition, numerical simulations were introduced to illustrate the full stress-strain process. The models showed accurate fracture structures inside the samples. Further prediction and evaluation of fracture propagation and flow process are also available via numerical simulations. This research is also significant for acquiring the hydraulic conditions of surrounding coal.

The study of pore-fracture characteristics is necessary to describe the internal geometrical structure under different stress states. The results achieved provide reference to predict the in-situ fracture evolution. Gas flow trends can be evaluated. At the end, gas outbursts and water inrush problems during practical exploitation can be investigated.

CBM is considered as an unconventional natural gas resource. It has some advantages, such as enhancing coal mining safety and increase of efficiency. It can help relieving the greenhouse effect. Some CBM is in a condensed liquid phase and absorbed on the pore surface, while the methane in fractures exist in form of free flowing gas. Both, liquid and gas phases exist because of the special adsorption ability of the coal matrix. If a pore diameter is smaller than $0.1\ \mu\text{m}$, it is considered to be a reserve cell. If the diameter is larger than $0.1\ \mu\text{m}$, the pore is assumed to act as a flow path for methane (Hou et al. 2015; Li et al. 2013; Yang et al. 2007; Yee et al. 1993). During the mining process, the hydraulic status of initial fractures and stress-induced fractures is continuously changing. Therefore, pore-fracture network characterization and propagating studies are particularly important.

The experiences in CBM exploitation can stimulate the research of other oil and gas reservoirs, such as shale gas and petroleum reservoirs. The fossil resources from low-permeable tight rock seams will become an attractive energy resource. So this research will contribute to the industrial application of energy storage, pollution control and waste disposal, and will also provide a vital theoretical basis for preventing gas outbursts and water inrushes.

1.3 Research status / State of the art

In recent years, pore-fracture networks have been monitored at different scales, and new techniques were invented and introduced, for example, low pressure nitrogen adsorption method (Hou et al. 2017; Nie et al. 2015), mercury intrusion porosimetry (MIP) (Zhao et al. 2016), nuclear magnetic resonance method (NMR) (Hou et al. 2017; Zhao et al. 2017), scanning electron microscope (SEM) (Ni et al. 2017; Nie et al. 2015) and X-ray micro-computed tomography (X-ray μ CT) (Jing et al. 2016; Mathews et al. 2017; Yao et al. 2009; Zhang et al. 2016). Due to laboratory limitations, seepage experiments were mostly coupled with loading or unloading conditions via conventional methods to evaluate pore and fracture features. Measurements at nanoscale, microscale and macroscale have been conducted with different techniques (Cai et al. 2014; Chen et al. 2015; Klobes et al. 1997; Liu et al. 2015; Yao et al. 2010; Yao and Liu 2012; Zhang et al. 2013). However, the geometrical character of pores and fractures were mostly investigated only at the less accurate macro- and microscopic scale. Some scholars studied at the nanoscale, but the measurements were restricted to the micrometer range. There are only a few cross-scale evaluations, because high accuracy and macroscopic measurements could not be managed simultaneously. This concerns especially the internal structure of coal and shale from the nano- to the macroscale. Also, the samples used for measurement and testing were different when monitoring the micro structures.

X-ray micro-computed tomography (X-ray μ CT) has become popular recently. This nondestructive method has the advantage to visualize and reconstruct the 3D structure. Therefore, it is the most widely used technique to characterize the pore-fracture network. The internal structure of coal samples at the laboratory scale has been reconstructed from CT scanning results (Mathews et al. 2017; Ramandi et al. 2016; Voorn et al. 2015; Zhao et al. 2016). The accuracy was in the order of several micrometers. Natural gases are stored in tiny pores, and they diffuse in the sample and flow through the seams. These micrometer scale pores and fractures were proved to be the main spaces and paths in every seepage related process (Cai et al. 2013). X-ray μ CT takes the real structures into consideration and provides a feasible basis for further modelling.

Seepage phenomena are related to many natural and man-made deformations, like considered for example in nuclear waste disposal, geothermal exploitation, petroleum and natural gas extraction, ground water utilization, slopes and dams, underground channels, or gas outburst and water inrush in coal mines (Tan 2013). Since 1960s, scholars started to investigate these phenomena.

The coal body is a typical porous medium, and most coals and rocks are low permeable media. Pores and fractures determine the permeability of coal. The gas and fluid flow patterns vary with different stress conditions. Permeability tests have been performed with different materials under different conditions. Zhang tested the permeability of sandstone with CO₂ (Zhang 2009). Jiang and his colleagues investigated soft and hard rock materials during the full stress-strain process, obtained a seepage rule and compared the different materials (Jiang and Ji 2001). Wang and Zhu investigated the seepage laws of several types of rock, including mudstone, sandy mudstone, sandy shale, fine sandstone and medium sandstone (Wang et al. 2011a; Zhu et al. 2002). Sun et al. (2006) used transient methods to determine the permeability, they also

derived a relation between inertial coefficient and acceleration coefficient for non-Darcy flow. The seepage flow in limestone didn't follow Darcy's law, and β became negative after reaching the peak strength, and flow showed turbulence features (Sun et al. 2006). Zhou et al. (2008) performed permeability tests on six artificial porous media and fluids with different kinematic viscosities. They used the fractal dimension method to analyze the seepage boundary appearance variation with time (Zhou et al. 2008).

So far laboratory tests concentrated mostly on three aspects: (1.) general permeability influenced by loading and pore pressure, (2.) general permeability influenced by fractures and (3.) permeability of one single fracture. These investigations focused on the permeability properties of different types of rock. Permeability rules for different fluids were also deduced. Most of the tests have considered the effect of different stress-strain conditions. So these studies are mainly based on macroscopic experimental phenomena. Few researchers have taken theoretical models, laboratory tests and numerical simulations into consideration simultaneously. And even less researchers have analyzed permeability from the point of view of microscopic generating mechanisms.

In recent decades, numerical simulations are gradually replacing analytical solutions and physical models in solving rock mechanical problems. Numerical simulations have many advantages, for example they can integrate special features like discontinuous, heterogeneous, anisotropic and inelastic features of the rock materials. The seepage process is very complex, therefore it is unlikely to get analytical solutions in most cases. Conventional methods are not able to figure out all the discontinuous deformation processes, such as pre-failure stage, post-failure stage, crushing and multi-phase coupling.

Numerical methods used in rock mechanics can be subdivided into 3 categories: (1) continuous methods including finite difference method (FDM), finite element method (FEM) and boundary element method (BEM), (2) discontinuous methods including discrete element method (DEM) and particle method (PM) and (3) mixed methods (Jing and Hudson 2002).

According to the task, each method has its own advantages and drawbacks. It is important to choose proper methods for specific cases. For instance, rock burst phenomena have been investigated quite early by simulating the dynamic failure process (Zubelewicz and Mroz 1983), continuum approaches were used to describe the deformation of weak layered rock and gas emission through porous rock (Guo et al. 2009), water-sand mixed flow was simulated with coupled simulations (Shan and Zhao 2014; Zhao and Shan 2013) as well as the ground water inrush process via pre-existing fractures under the condition of shallow coal seam mining (Zhong et al. 2017).

Some other scholars optimized the numerical simulations significantly by improving the modelling methods. For instance, CT techniques were introduced to reconstruct coal sample models (Zhao et al. 2010a), inhomogeneous granite samples were simulated by numerical models based on Weibull parameter distributions (Tan 2013).

Based on the material structure, seepage models are divided into two categories: porous media and fractured media. The relevant theoretical methods are continuum models, discrete models and double-porous models.

Rock samples are assumed to be fully saturated with water in classical continuum based models. The corresponding partial differential equations are based on Darcy's law, fluid mechanical continuity equations and the effective stress equations. Stress field and fluid flow field were solved by classical poro-elastic analysis. 1-dimensional consolidation theory was developed based on the concept of effective stress as shown in Figure 1.2 (Terzaghi 1943). The consolidation theory was extended to the 3-dimensional space by Rendulic (1936). Biot (1941) established the seepage control equation to present the relation between 3 - dimensional fluid flow and poro-elastic deformation. Then anisotropic theory, visco-elastic theory, finite deformation theory and non-linear theory were connected to poro-elasticity (Biot 1955, 1973; Biot and Temple 1972). Materials and geometries were assumed to be non-linear, the consolidation theory was extended to the generalized Biot theory (Zienkiewicz and Shiomi 1984). A permeability tensor was introduced to present anisotropy of fracture networks and fluid flow (Snow 1968).

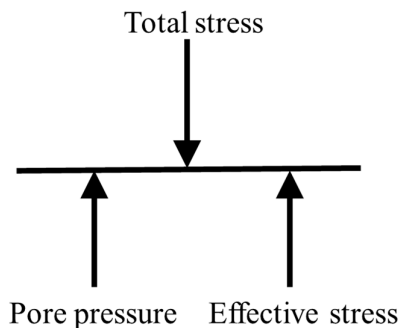


Figure 1.2 Concept of effective stress

In discrete fracture network (DFN) models, fluid flow is only available in discrete fractures or crack paths. Based on the stress-strain relationship for a single fracture, models at fracture intersections were built with fluid mass conservation principle applied to solve pressure and flow field problems. Macroscopic fluid-mechanical models were derived from microscopic theories of coarse fractures. For instance, Gangi (1978) established a classical needle bed model, Walsh (1981) established a Hertz contact model, aperture frequency and open space models were also developed (Neuzil and Tracy 1981; Tsang and Witherspoon 1981). Many other scholars described and explained fracture flow phenomena with empirical models (Kranz et al. 1979; Liu et al. 2001).

In double-porous models, fractured rock is assumed to be a combination of porous and fractured media. The fractures are assumed to be flow paths for fluid, and the pores storage the fluid. Stress and flow field problems are solved by coupled equations. These equations are derived by connecting pores and fracture flow equations. Many different double-porous models were established as shown in Figure 1.3 (Bai et al. 1994; Barenblatt et al. 1960; Boulton and Streltsova 1977; Valliappan and Khalili - Naghadeh 1990; Warren and Root 2007). Wu (2000) developed a generalized model as shown in Figure 1.4. In this model, large fractures are discrete

and tiny fractures are represented by a heterogeneous anisotropic continuum. The fluid exchange occurs only in large fractures.

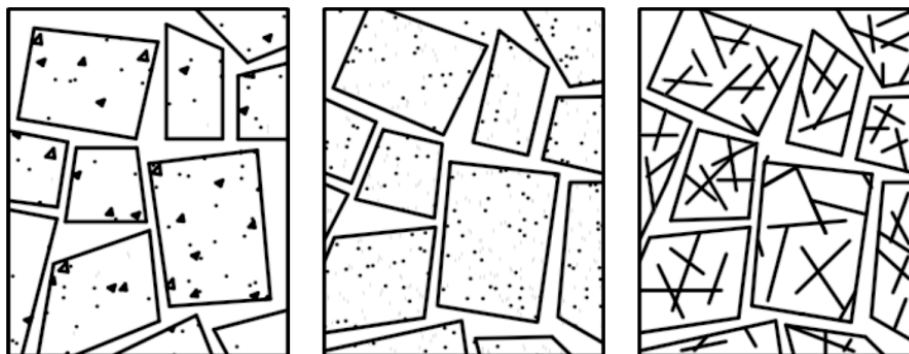


Figure 1.3 Double-porous media

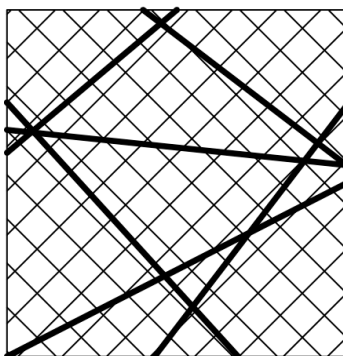


Figure 1.4 Generalized double porosity model

1.4 Research content

Two problems remain unsolved in previous studies. The first one is the contradiction between measurement accuracy and sample size, which means that the measurement accuracy is lower in case of large samples, or with other words, higher accuracy is accessible only when measuring small samples. The second one is the unique character of coal samples: it is not possible to investigate one particular sample under various stress conditions. The research in respect to the permeability evolution during the full stress-strain process focused mainly on loading tests. Different fluids and different rocks have been tested. Also different stress conditions were tested, including changes of both, confining and pore pressures.

During exploitation of deep coal, the coal experience different stages. The variety of stresses leads to continuous deformation and permeability changes with development of internal pore-fracture networks. The internal pore-fracture network governs the permeability and influences the methane exploitation and mining safety.

For the presented research, coal samples were collected from VI-15-14140 working face of Pingdingshan No. 8 Mine. The average depth of the coal seam is approximately 700 m. Pore-

fracture network and permeability evolution are studied within this work and the damage evolution is simulated and analyzed by numerical methods.

The key aspects of the study are as follows:

(1) The X-ray technique is incorporated into the research by scanning of coal samples in the thesis (Chapter 2). By setting proper threshold values to differentiate between different components of the sample, coal matrix, inclusions and fractures are identified by different gray values. 3D reconstruction techniques were applied to visualize the structure of coal samples at the laboratory scale. This method is the key to investigate the pore-fracture network and permeability evolution and is the basis for subsequent numerical simulations.

(2) The permeability evolution during triaxial compression lab tests is observed. In Chapter 3, laboratory tests under confined condition are described. A newly developed experimental system is employed to perform 3-dimensional loading and to measure the flow rate simultaneously. The coal sample goes through different stages in terms of permeability and deformation. The steady flow method with different confining pressures is adapted to monitor the permeability evolution. Permeability evolution, damage development and full stress-strain curves are combined in the final evaluation.

(3) The geometric models are transformed into numerical models. A self-developed triaxial compression model is presented on the basis of PFC^{3D}. This new approach is established in this work with significant improved handling of the confinement (Chapter 4). Triaxial tests are simulated in 3D with the particle-based DEM code PFC^{3D} using a new developed flexible membrane boundary. A series of triaxial compression tests with reconstructed numerical models are conducted.

(4) PFC^{3D} and FLAC^{3D} models are used in parallel to simulate the flow tests in Chapter 5. While the mechanical deformation and damage evolution is modeled in PFC^{3D}, the gas flow processes is reproduced in FLAC^{3D}. A theoretical approach for evaluating the permeability is proposed based on fracture distribution and single crack behavior. The permeability evolution observed during hydro-mechanical coupled triaxial compression tests is used for calibration and validation.

1.5 Research strategy

The research strategy is illustrated by the scheme shown in Figure 1.5.

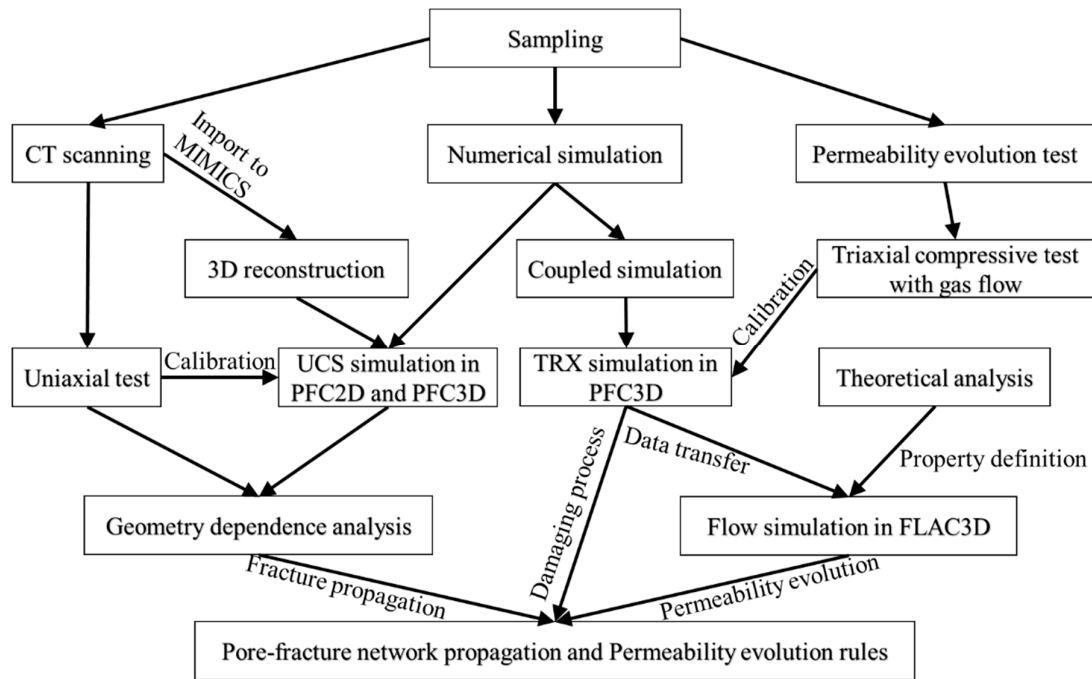


Figure 1.5 Flowchart illustrating the research strategy

Spatial distribution, dimension and hydraulic parameters of fractures are investigated on the basis of confined loading conditions. The evolution of the internal fracture network is investigated with DEM models. The development of microcracks is quantified by considering the loading, confinement and structural character of the rock samples. The simulation focus on the permeability evolution under triaxial compression. The spatial distributions of different components inside the samples produce a significant heterogeneity. Precise reconstruction of the coal samples in form of numerical models is essential for better quantification of the structural influence on damage pattern and permeability evolution.

2 CT reconstruction

2.1 Introduction

This chapter describes the use of X-ray micro-computed tomography (X-ray μ CT) to investigate the damage and fracture pattern in coal samples as well as the transformation of the fracture pattern into numerical particle-based models. Finally, uniaxial compressive (UCS) tests are simulated to quantify the fracture evolution.

The organic components of coal influence the methane adsorption capacity and diffusion (Karacan and Mitchell 2003; Yao and Liu 2007), while the main flow pathways incl. pores and fractures determine the permeability of coal and the production of CBM (Yao et al. 2008; Zuber 1998). Distribution and mechanical behavior of cleats also influence the failure pattern as well as the permeability. Anisotropy and strength characteristics of cleats are key parameters in studying the permeability evolution. Knowledge of the cleat properties is necessary as they influence the local and regional fluid flow (Close 1993; Laubach et al. 1998). Studies in-situ and in the laboratory suggest that fluid flow through natural fractures in coal and rock differ from the idealization of smooth parallel plates due to varying apertures (Cacas 1990; Nemoto et al. 2008; Watanabe et al. 2008, 2011a; b). Therefore, quantification of volume and spatial distribution of pores, fractures and minerals in coal are fundamental requirements for CBM reservoir evaluation and gas outburst prediction.

Fracture characteristics (e.g. density, connectivity and geometry) can be obtained by image analysis of core samples from the field (reservoirs, working faces, outcrops etc.) (Wolf et al. 2004). Techniques developed for the sub-meter scale are adopted to measure cleat densities and spatial distribution by using X-ray CT and image analysis (Mazumder et al. 2006; Wolf et al. 2008). In the 1980s, computer based tomography (CT) was already applied in petrology, petrophysics and petroleum reservoir engineering (e.g. Wellington and Vinegar 1987; Withjack 1988). The microfocus CT (μ CT) has been developed to characterize porous media such as clastic, carbonatic, volcanic and metamorphic rocks (e.g. Carlson and Denison 1992; Ketcham and Carlson 2001; Van Geet et al. 2001a; Ketcham and Iturrino 2005; Goldstein et al. 2007; Remeysen and Swennen 2008).

Recently, CT techniques were effectively used in coal petrological and petrophysical research. X-ray CT became an effective non-destructive method for analyzing internal structures in rock materials, especially fractures in coal (Ketcham and Carlson 2001; Polak et al. 2003; Zhu et al. 2007; Karacan 2009; Karpyn et al. 2009; Kumar et al. 2011; Cnudde and Boone 2013, Pyrak-Nolte et al. 1997; Karacan and Okandan 2000; Van Geet et al. 2001a; Mazumder et al. 2006; Wolf et al. 2008). Scholars developed porosity calculation and 3D reconstruction methods. The porosity variation in different loading stages were described by gray scale values in CT images (Wang et al. 2015). Mudstone models were reconstructed with visualization algorithms, and the relation between generalized porosity and pore size was studied by changing image resolution (Li et al. 2010). 9 different types of rock were scanned, binarization images were analyzed, and the relation between porosity after image segmentation and the fractal dimensions of porous structure were investigated (Peng et al. 2011).

Previous researches have demonstrated the ability to determine fracture aperture distributions using X-ray CT (e.g. Johns et al. 1993; Keller 1998; Montemagno and Pyrak-Nolte 1999; Bertels et al. 2001; Karpyn et al. 2009; Kumar et al. 2011; Watanabe et al. 2011a). The variations observed during analysis of the CT sequences and their distributions during destruction were analyzed (Yang et al. 1997). Based on the visualization of CT images, the internal damages and fracture propagations under uniaxial compression were monitored, a constitutive law related to CT sequence was established to describe rock deformation (Ren and Ge 2001). Fractures and matrix were distinguished by binarization of images, and trinization was then developed to separate matrix, inclusions and pores. 3D models of soil-rock mixture were reconstructed, and quantitative analysis was conducted under uniaxial compression (Sun et al. 2014).

Some studies (e.g. Verhelst et al. 1996; Simons et al. 1997; Van Geet et al. 2001b) documented the feasibility in differentiating pores, fractures and minerals in coal samples. By using the CT technique, also gas adsorption and transport characteristics were studied (e.g. Karacan and Okandan 2000; Karacan 2003, 2007; Karacan and Mitchell 2003). CT scanning, acoustic emission and supersonic techniques were applied to monitor the samples under triaxial compression, also the influence of geometrical characteristics, connectivity and stress states were analyzed (Cai et al. 2014).

However, previous studies are still insufficient in characterizing coal heterogeneity and spatial disposition of pores, fractures and minerals in coal during loading. In addition, detailed discussion about CT characteristics of coal samples along with fracture propagation and evolution has not yet been reported.

Numerical simulations have great potential in analyzing rock mechanical processes. Previous studies (e.g. Hoek and Bieniawski 1965; Vallejo 1988; Wong and Chau 1998; Tang et al. 2001; Sagong and Bobet 2002; Dyskin et al. 2003; Li et al. 2005; Wong and Einstein 2007; Park and Bobet 2009; Cao et al. 2015) investigated the fracture propagation by laboratory tests. With rapid development in computer science (hard- and software), numerical simulation techniques have become available to simulate crack initiation, propagation and coalescence.

Discontinuum methods such as the Discrete Element Method (DEM) (Cundall and Strack 1979) have been increasingly used for simulating the rock mechanical behavior. Particle based models which treat the rock as an assembly of bonded particles follow the law of motion and consider the formation and interaction of micro-cracks at the particle–particle contacts (e.g. Baumgarten and Konietzky 2012; Potyondy and Cundall 2004; Yan and Ji 2010).

CT techniques became popular in numerical modeling. Based on the reconstructed geometrical models, numerical models were generated to simulate the mechanical behavior (Yu et al. 2015). The reconstructed structures were imported to FLAC^{3D}, and the effects of loading speed on the compressive strength of coal samples were studied (Zhao et al. 2010a). To take the real structure of materials into consideration is important for modeling. Generation of more precise models is the trend in numerical simulation, and CT scanning technique is a very effective method to support this trend.

2.2 Sampling and Methodology

The tested coal samples are from the VI-15-14140 working face of Pingdingshan No. 8 Mine, China. Fresh bigger rock pieces of coal were obtained directly from the underground mine. According to the drilling data, the average thickness of coal seam located approximately 700 m below surface is 3.6 m. The average inclination angle of the seam is 22° . This working face is classified as outburst-hazardous with a gas pressure of 2.0 MPa and a gas content of $22.0 \text{ m}^3/\text{t}$. The density of coal rock is 1.31 t/m^3 . 13 coal samples (see Table 2.1) are collected and chosen to conduct different experiments. They are also used as basis for the numerical simulations.

Table 2.1 Coal samples, corresponding experiments and simulations

Sample	Laboratory experiments			Numerical simulation		
	CT scan	UCS	Seepage under TRX	UCS	TRX	HM-coupled
C1	√		√		√	√
C2	√		√		√	√
C3	√	√		√	√	√
C4	√		√		√	√
C5	√		√		√	√
C11			√			
C12			√			
C13			√			
C15			√			
C16			√			
C21		√				
C22		√				
C23		√				

Cylindrical samples as shown in Figure 2.1 were drilled out of bigger coal blocks with diameter of about 25 mm and length (height) of about 50 mm following the Suggested Methods of the International Society of Rock Mechanics (Ulusay and Hudson 2012).



Figure 2.1 Coal samples from underground mine Pingdingshan No. 8 (China)

These core samples were first dried and then exact dimensions, density and porosity were determined (see Table 2.2) before CT scans were conducted.

Table 2.2 Average parameters of coal samples

	Diameter D (mm)	Height H (mm)	Density ρ (g/cm ³)	Dry Density ρ_d (g/cm ³)	Grain Density ρ_g (g/cm ³)	Porosity ϕ (%)
Coal	25	50	1.30	1.30	1.39	6.5

The CT scans were performed on an ACTIS-225FFI micro-xCT scanner as shown in Figure 2.2(a). The installation of a 225 kV FeinFocus focal spot allows a minimum resolution of the scanner of 10 μm for a cubic sample size of 4.8 mm. A charge-coupled device (CCD) digital camera with a spatial resolution of 4.4 lp/mm (line pairs per mm) is used to capture and digitize the data of the Toshiba 3D image intensifier as detector system.

The tested cylindrical core sample was placed in the sample couch and positioned in the center of scanner's field of view. Under the applied conditions (180 kV, 200 μA at a raster of 750×750 pixels), the area of each pixel is approximately $50 \times 50 \mu\text{m}^2$. The scanning duration is 9 seconds per slice. Both, slice thickness and slice spacing were set to 50 μm . CT slice thickness and slice increments were kept as small as feasible to enhance both, resolution and contrast. Figure 2.2(b) and (c) show the layout of the micro focus xCT device and the scanned slices of the sample. To maximize the signal-to-noise ratio while minimizing or eliminating the artifacts, a series of standard calibrations were performed. Offset, gain and wedge calibrations were also included (Ketcham and Carlson 2001; Remeysen and Swennen 2006).

Each CT scan produces a series of CT images (1.010 slices for each scan). In total, 10.100 images were produced from one coal sample for 10 different stages of uniaxial stress. The obtained images were used to reconstruct the 3-dimensional structure of the samples using digital image processing software.

Some studies (e.g. Flannery et al. 1987; Montemagno and Pyrak-Nolte 1999; Ketcham and Carlson 2001; Cnudde et al. 2006; Yao et al. 2009; Mathews et al. 2011; Cnudde and Boone 2013) show that the basic principles of the μCT technique are similar to those of the conventional CT. The 2D images produced in CT scans are called "slices", because they correspond to the internal cross-sections if the sample is sliced along the scan plane. Each slice contains all X-ray attenuation coefficient data along the plane. These attenuation data are transformed to CT numbers that have a range determined by the computer system (Yao et al. 2009).

Theoretically, for a given X-ray energy, the CT number is a function of both, density and effective atomic number (Van Geet et al. 2001b). Because the structural coal components are characterized by distinct different densities, pores and fractures, mineral components and coal matrix can be identified by their respective CT numbers (Van Geet et al. 2001a; Simons et al. 1997; Verhelst et al. 1996).

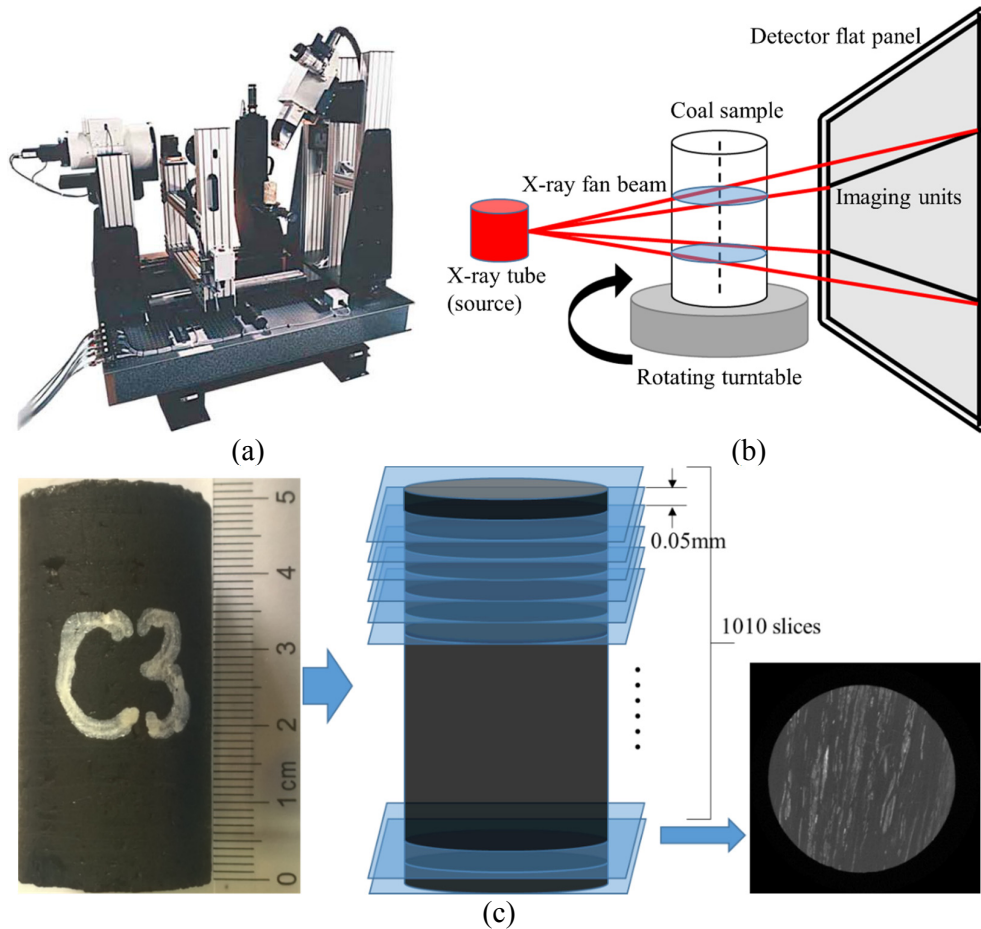


Figure 2.2 Micro-xCT scanner associated with rock testing system. (a) Micro-xCT scanning device, (b) side view of schematic scanner layout, (c) Sample dimensions and scan slice spacing.

As it is impractical to deal with the X-ray attenuation coefficients, as shown in Equation 2.1, CT numbers are defined:

$$CT_{number} = \left(\frac{\mu_x - \mu_w}{\mu_w} \right) \times 1000 \quad (\text{Equation 2.1})$$

in which, μ_x is the calculated X-ray attenuation coefficient and μ_w is the attenuation coefficient for water (Hunt et al. 1988; Karacan and Okandan 2001).

CT numbers given in Hounsfield unit (HU) were exported as a collection of coordinates and values. The original file was processed by a program developed in MATLAB software (Solomon and Breckon 2011). Using this program, the CT numbers were transformed into grey scale values, and the original files were transformed into 16 bit-gray-scale images.

The visibility of the original images (raw images transferred from data files) was poor. Therefore, some image adjustments were conducted in Photoshop (PS) software for better illustration (Wu et al. 2012). Since CT number increase with density (and atomic number), they were used to distinguish between coal matrix, mineral fills and open fractures. The gray scale

values were inferred from CT numbers in the original file. Afterwards the calculated gray scale values were distributed over a narrow range. The CT numbers of coal samples are commonly between 500 to 3000 HU (Yao et al. 2009), but the upper limit in the output file could reach 8000 HU. The span of grey values in the original data set is often restricted. By manipulating the output sliders the range of pixel values was stretched to cover values from 0 to 255. Several operations were performed to detect the pixel with the highest gray scale value. This pixel was defined as white pixel, and the corresponding level was set to 255. The remaining levels were redistributed between levels 0 and 255. This redistribution increased the contrast of the image. Level and exposure were adjusted automatically at first, but later also manually to achieve a better visual quality as shown in Figure 2.3. This step is very important for the gray scale value segmentation.

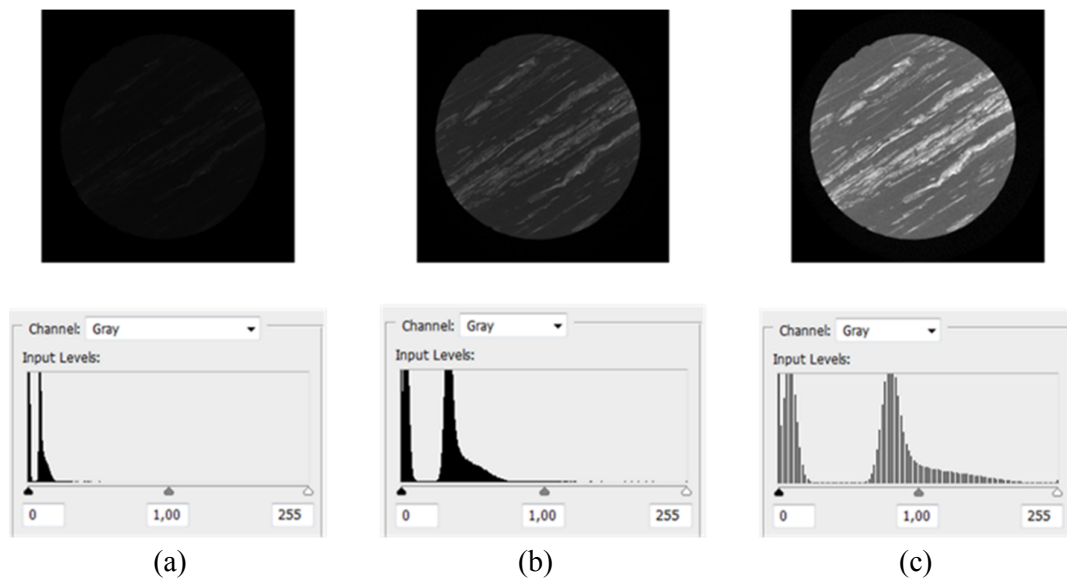


Figure 2.3 Input level curves at different phases: (a) raw image, (b) automatically adjusted image and (c) manually adjusted image

By examining the images, a variety of errors and image artifacts are detected. Beam hardening, scatter and unstable exposure during the scanning are common, which led to spuriously high CT numbers. After analyzing the images, the homogeneous core sample appeared to be denser around its periphery (Wellington and Vinegar 1987). Such noise appears in the form of isolated pixels with high gray scale values. It has been proven that errors caused by ray-beam hardening and scatter can be eliminated by using the image subtraction method. The author developed a program to detect these pixels. A nonlinear digital filtering technique (median filter technique) was used in MATLAB to remove the noise. Such noise reduction is a typical pre-processing step to improve the results of later processing stages. The filter ran through the gray scale value pixel by pixel, replacing each pixel with the median of neighboring pixels. So the gray scale values of isolated white pixels were replaced to eliminate noise.

Each pixel of the gray scale image has gray scale values between 0 and 255. Each of the three components (coal matrix, minerals and pores/fractures) cover a certain range of CT numbers, their gray scale values can be quantified by the threshold segmentation method (Auzerais 1996). This kind of segmentation is a ternary process. For the initial investigated coal samples, the CT

number for minerals is approximately 3000 HU; the CT number for pores/fractures is commonly less than 600 HU; and the CT number for the coal matrix is commonly between 1000 and 1600 HU (Yao et al. 2009). Taking sample C3 under loading as an example (Figure 2.4), fractures (dark black color) are identified by low CT number, minerals (light white color) are identified by high CT number, and the coal matrix is identified by medium CT number.

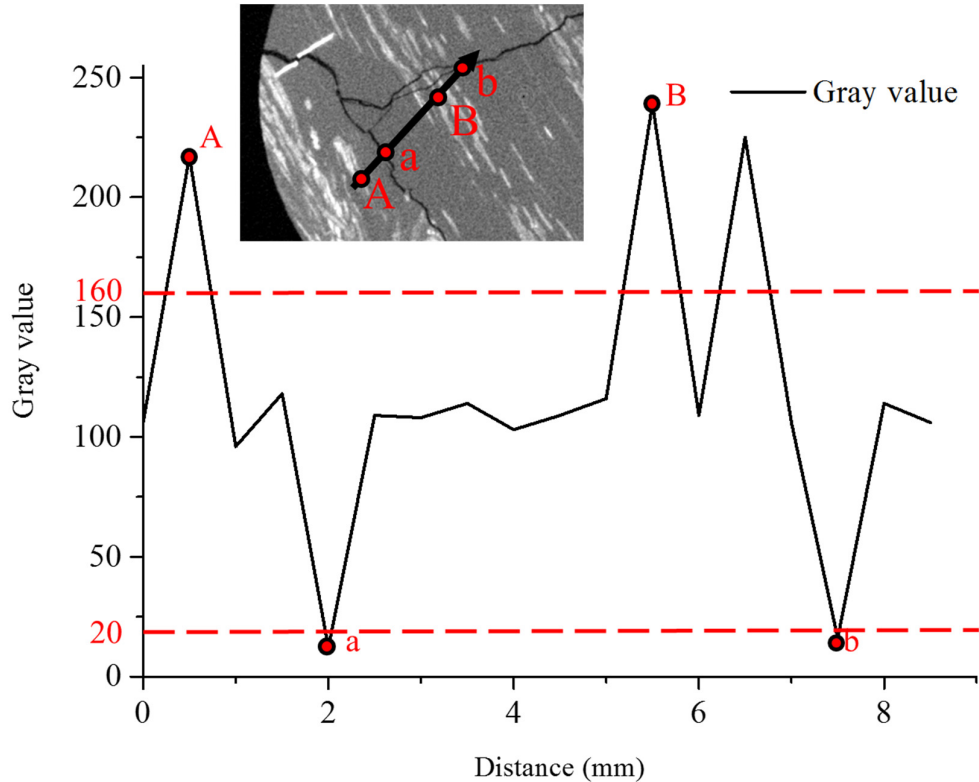


Figure 2.4 Representative slice image of sample C3 and gray value along profile line

As shown in Figure 2.4, a profile line shows the CT number distribution across coal matrix, mineral inclusions and fractures (features a and b indicate locations of fracture with dark color and low CT number/gray scale value, while the letters A and B indicate locations of minerals with white color and high CT number/gray scale value).

After transferring the original values into gray scale values, the segmentation technique defines an upper and a lower threshold of gray scale values for each component. Since CT values increase with density (and atomic number), they can be used to distinguish between mineral-filled and open fractures. According to the different characters of coal matrix and mineral inclusions, proper gray scale value thresholds have been chosen to segment the image. A gray scale value of 20 was set as threshold (T_1) switching from pores/fractures to coal matrix, and 160 was set as threshold (T_2) between coal matrix and mineral inclusions as shown in Equation 2.2. The ternary $f(x,y)$ process is defined as follows:

$$f(x, y) = \begin{cases} 0 & p(x, y) < T_1 \\ 100 & T_1 \leq p(x, y) < T_2 \\ 255 & p(x, y) \geq T_2 \end{cases} \quad (\text{Equation 2.2})$$

where, $p(x, y)$ is the raw gray scale value of a pixel at the location of (x, y) . The CT image is transformed into a black-white image with only three gray scale values, in which black ($f = 0$) stands for fractures/pores and background, gray ($f = 100$) stands for coal matrix and white ($f = 255$) for mineral inclusions. The boundaries of each component were recognizable, and various mineral inclusions were visualized more easily compared with the original image.

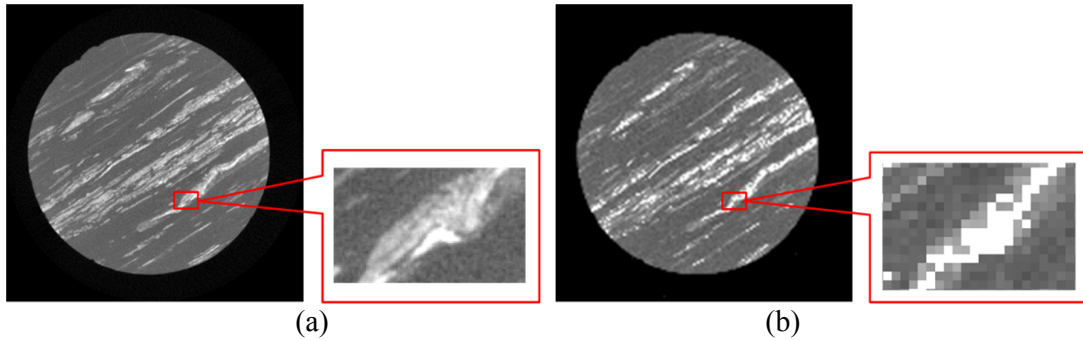


Figure 2.5 Resolution reduction and gray scale value segmentation

During the processing, careful and repetitious adjustments of T_1 and T_2 were performed to improve the accuracy and make sure that the upper and lower thresholds are universal for all slices of the sample. In order to define better thresholds, resolution was reduced to simplify the calculation before the segmentation. The image with less pixels could reduce the calculation effort of adjustment effectively, and presents the identical gray scale value characteristics corresponding to the original image as shown in Figure 2.5. After adjusting the thresholds to proper values, the threshold values were applied to the original images to achieve high definition images from the ternary process.

2.3 Sample reconstruction and numerical model set-up

The images achieved from CT scans illustrate only the 2D structure of the corresponding cross-section. To develop 3D models, it is necessary to convert the CT images into 3D models incl. fracture aperture distributions (e.g. Johns et al. 1993; Keller 1998; Bertels et al. 2001; Watanabe et al. 2011a). Within this process stage, images are stacked together mathematically to produce virtual core sections (multi-planar reconstruction) across the volume data set to reveal the inner heterogeneity of the sample. Materialise MimicsTM, a software tool which is commonly used in medical research, was used to conduct the coal sample visualizations on the basis of the X-ray images (Rédei 2008). The virtual core sections (multi-planar reconstruction) produced in Mimics show the inner heterogeneity of the cores. A total of 1010 scanned CT images (Figure 2.6(a)) of the coal sample were stacked. Every image was imported with its real dimensions as shown in Table 2.3. Clear views of the sample were obtained from horizontal and vertical cross-sections.

Table 2.3 Image properties used in reconstruction

Sample Nr.	Image size (mm)	Resolution	Pixel size (μm)	Slice interval (μm)
C3	35×35	750×750	46.67×46.67	50

In Mimics™, the boundaries of each component are traced. Closed polygons represent different components. The program also connects pixel with same grey values automatically between neighboring slices. All those polygons and lines form closed polyhedrons. Finally all individual parts were assembled and the internal structure of the sample is reproduced. Exemplary, Figure 2.6 illustrates the reconstruction process.

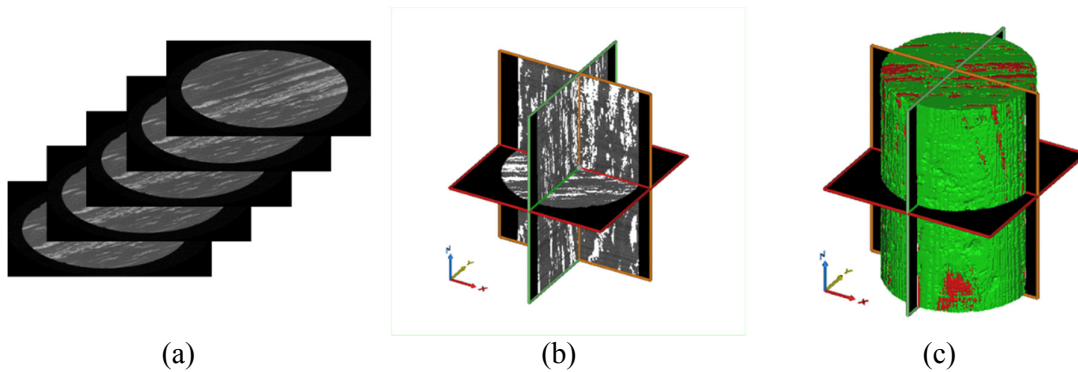


Figure 2.6 3D model reconstruction based on 2D images: (a) stack of images, (b) cross-sections in horizontal and vertical directions and (c) final 3D reconstruction

Next step is the transformation of the reconstructed 3D models into numerical models, either into PFC^{2D} and PFC^{3D} (both are particle based codes) or into FLAC^{3D} (classical mesh-based code). The geometries of the different components of the coal sample were exported from the Mimics™ software into a STL format (Rédei 2008). The geometries in STL format can be used to group particles (in PFC^{2D/3D}) or zones (in FLAC^{3D}) according to their spatial positions (Botsch et al. 2010; Ohbuchi et al. 2003). Reconstructed geometries can be transformed into wall elements. Different properties are assigned to the different groups. Finally, the numerical models of the coal samples are generated with real size and accurate component distribution (Zhao et al. 2010a). For 2D modeling, typical cross-sections of the reconstructed 3-dimensional model were selected, and exported as 2D geometries.

PFC^{2D} and PFC^{3D} numerical models were set-up to simulate the UCS test of coal samples. All the structural information provided by the reconstructed model based on the μCT analysis was used. The mineral inclusions are cleats of kaolinite, calcite and other minerals. The small grains of kaolinite are relatively loose in structure and produce lower strength at the macro-scale because they produce significant inhomogeneity. Two mechanical parameter sets are defined for particle groups representing the coal matrix and the mineral inclusions. The parameters were calibrated based on the RocLab™ software (Hoek et al. 2002). The parameters of the particle bonds govern the deformation.

Micro-mechanical bond parameters in DEM differ from macro-mechanical properties. Therefore, the micro-mechanical parameters have to be calibrated in such a way, that they

duplicate the macroscopic behavior. The linear parallel bond model was applied, which simulates a finite-sized cement-like connection between the two contacting particles. The parallel-bond component acts in parallel with the linear component and establishes an elastic interaction between contacting particles (Cundall 2004). The parallel-bond model considers rotations and displacements and can break to illustrate fracture evolution.

Exemplary, Figure 2.7 shows micro-mechanical models based on the above mentioned CT image processing for PFC^{2D}, PFC^{3D} and FLAC^{3D}. Those particles which occupy pore positions were deleted and corresponding zones in FLAC^{3D} got different parameters. The simulation of UCS tests in both, PFC^{2D} and PFC^{3D}, were launched by moving the top and bottom walls. In all PFC models, the matrix and the inclusions were represented by green and red particles/zones, respectively.

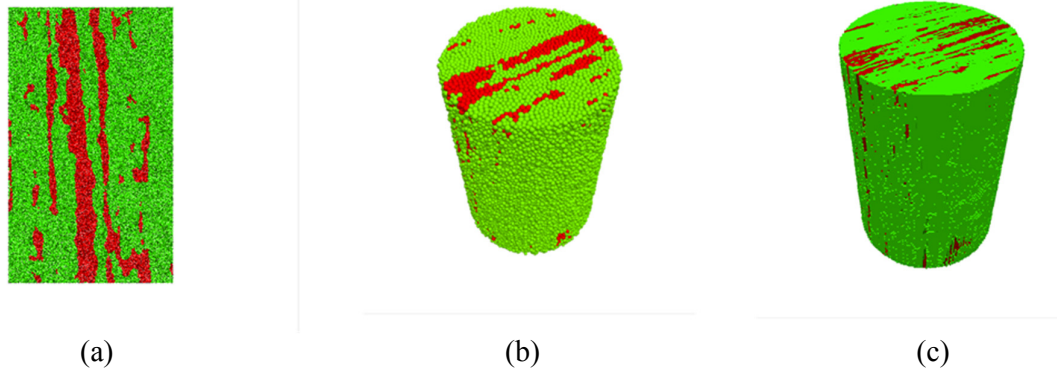


Figure 2.7 Numerical models in (a) PFC2D, (b) PFC3D and (c) FLAC3D (green: matrix; red: inclusions; holes: pores)

2.4 Application

2.4.1 Coal sample reconstruction

All coal samples were carefully packed at the mine face and were quickly transported to the laboratory for immediate processing. UCS tests of a large amount of samples were conducted to obtain the basic mechanical parameters of the coal samples. Average values are given in Table 2.4.

Table 2.4 Mechanical parameters of coal samples

UCS σ_c (MPa)	Elastic modulus E (GPa)	Poisson's ratio ν
10 ~ 16	2.1 ~ 5.5	0.3

According to Chinese national standard GB/T 212-2008 for testing methods, coal powder was prepared by sample grinding and sieving. Analysis results are shown in Table 2.5.

The depth of the Pingdingshan VI coal seam varies between 300 m to 1050 m. Control group samples are from a depth of 300 m. Moisture, ash and volatile contents in coal samples become less with increasing depth. On the other hand, the fixed-carbon content increases with depth.

After some basic calculations, the lower percentage of dry and ash free basis volatile content shows that the samples have a higher metamorphic degree, and the samples are classified as coking coal. Low porosity and high metamorphic degree of coking coal have significant influence on its mechanical properties and seepage features.

Table 2.5 Proximate analysis results of coal (Liu et al. 2017)

Depth (m)	Proximate analysis results (%)				Conversion result (%)	
	M _{ad}	A _{ad}	V _{ad}	FC _{ad}	V _{daf}	
Coal sample	700	0.82	6.70	22.36	70.12	24.18

Note: M_{ad}: air dry basis moisture content; A_{ad}: air dry basis ash content; V_{ad}: air dry basis volatile content; FC_{ad}: air dry basis fixed-carbon content; V_{daf}: dry and ash free basis volatile content.

X-ray fluorescence tests (XRF) and X-ray diffraction analysis (XRD) were performed in the laboratory. Both methods were used for composition and phase identification of sample powder. The selected coals exhibit similar mineralogy as shown in Table 2.6 and Table 2.7.

Table 2.6 Element mass fraction of coal samples (Liu et al. 2017)

Depth (m)	Element mass fraction (%)								
	C	O	Si	Al	Ca	S	Fe	Ti	
Samples	700	83.625	11.740	1.971	1.738	0.127	0.424	0.076	0.111
		Cl	Mg	P	Sr	Zr	K	Br	Ni
		0.091	0.020	0.007	0.004	0.006	0.033	0.004	0.003

The elements mainly exist in form of minerals. The amount of oxygen becomes smaller with increasing depth, so the samples have better coking properties than the control group (Nomura et al. 1999).

Table 2.7 Mineral mass fraction of coal samples (Liu et al. 2017)

Depth (m)	Carbon-containing organics	Kaolinite	Calcite	Others	
	(%)	(%)	(%)	(%)	
Samples	700	83.6	8.3	0.3	7.8

Kaolinite and calcite are detected as main mineral inclusions in the samples. The mechanical properties of coal matrix and inclusions were obtained by micro-hardness tests (Mahabadi et al. 2012; Randall et al. 2009; Zhao et al. 2010a). The mechanical properties of the samples can be presented based on their micro-hardness test results. Estimated properties as shown in Table 2.8 were obtained by analyzing lab test results (Zhao et al. 2010a). These properties obtained from literatures provide a basis for calibration. The differences are clearly noticed between components. Stress concentrations occur at the boundary to the hard materials where micro fractures initiate and propagate.

Table 2.8 Physical and mechanical parameters of coal samples (Zhao et al. 2010a)

	ρ (g/cm ³)	E (GPa)	ν	σ_t (MPa)	C (MPa)	θ (°)
Matrix	1.3	2.37	0.35	0.23	1.13	35
Inclusion	1.8	16	0.18	1.11	6.45	34.6

The presentation in Figure 2.8 focus only on the mineral inclusions represented by red polyhedrons, whereas the matrix is set transparent. The mineral inclusions are spread through the whole sample and show a laminated structure with good connectivity. The mineral layers are elongated along the sample axis. Both, coal matrix and stiff inclusions have significant influence on the strength.

Three main mineral layers were observed in the sample shown in Figure 2.8. According to the measurements in Mimics™, the length of the mineral inclusion L1 is 45 mm and goes through the whole sample, the length of L2 is 36.97 mm and the length of L3 is the shortest with 33.20 mm. The thicknesses of L1, L2 and L3 are 0.3 ~ 3.3 mm, 0.31 ~ 2.58 mm and 0.5 ~ 2.16 mm, respectively. The other parts are mainly smaller isolated mineral clusters.

Cleats/fractures are more easily to identify when mineral inclusions are present (Golab et al. 2013). Theoretically, the local distribution of the open micro-fractures is controlled by the boundaries between coal matrix and minerals. Due to the limitation of voxel size of the CT images only apertures larger than 50 μm can be resolved.

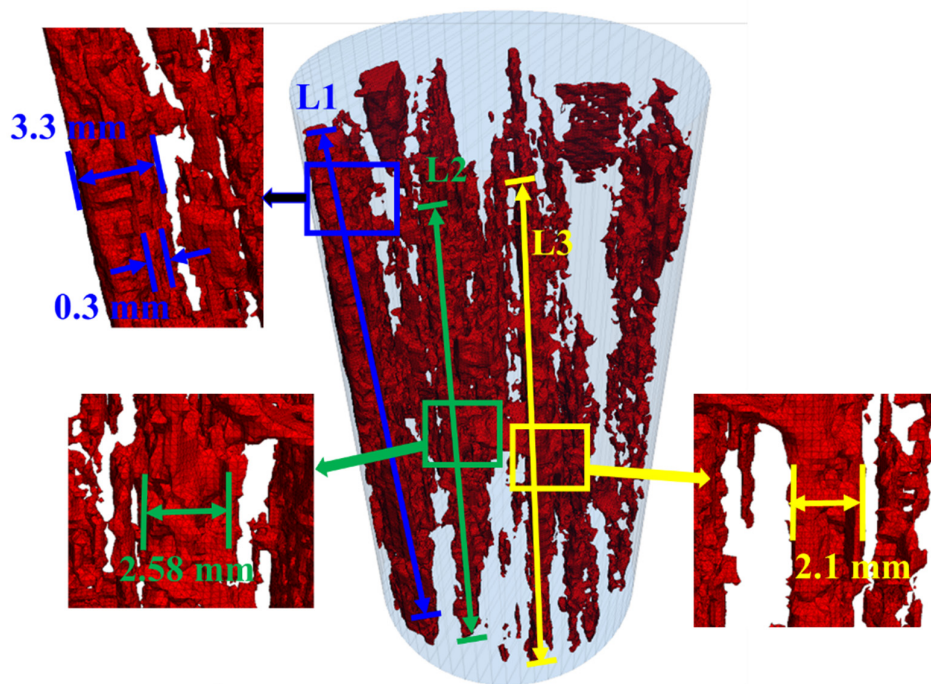


Figure 2.8 3D representation of the mineral inclusions in virgin coal sample C3

The natural fracture network of the virgin coal is illustrated by blue color in Figure 2.9. The fracture network is quite heterogeneous with bad connectivity in the virgin stage. Non-mineral occluded fractures are less developed (normally isolated pores or short fractures with poor connectivity). They are likely related to stress intensity under post diagenesis and hydrodynamic conditions (Cai et al. 2014).

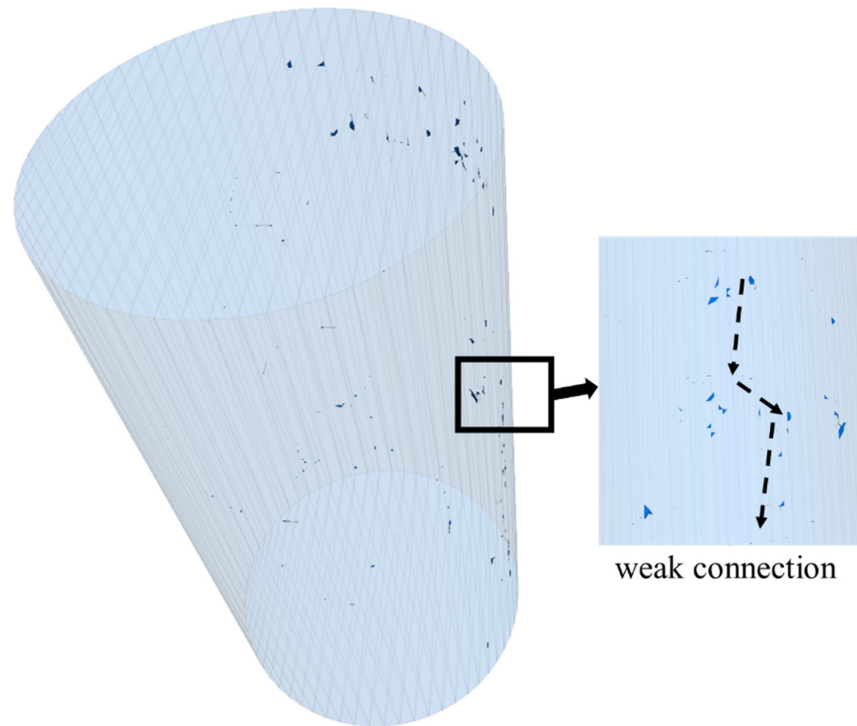


Figure 2.9 3D distribution of pores and fractures in virgin coal sample C3

At the initial (virgin) stage, most of the fractures are located near to the outer sample surface, and may be generated due to sampling and sample preparation.

In order to fully exploit the function of the CT device, an automated rock testing system was mounted to the scanner. The scanning process can be conducted while the UCS test is running (sample C3) at room temperature. The test was conducted in the State Key Laboratory of Coal Resources and Safe Mining at China University of Mining & Technology, Beijing. The intact coal sample was scanned before the test, and then the load was increased in steps of 500 N. At each load level the scanning operations were conducted. For each load level the corresponding 3D models were reconstructed and visualized together with the stress-strain curve to illustrate the damage evolution. During the loading process, fractures are detected as shown in Figure 2.10. Fractures appeared mostly in form of cleats within the core indicating that during axial compression more small fractures are created. Fracture F1 is aligned nearly parallel to the uniaxial compression (see Figure 2.11). Due to the abundant mineral inclusions, fracture F1 occurred at an early stage along the boundary of the mineral inclusion but inside the matrix. The fracture F2 occurred perpendicular to F1 through the coal matrix, and F3 was observed only before the test reached peak stress as shown in Figure 2.11.

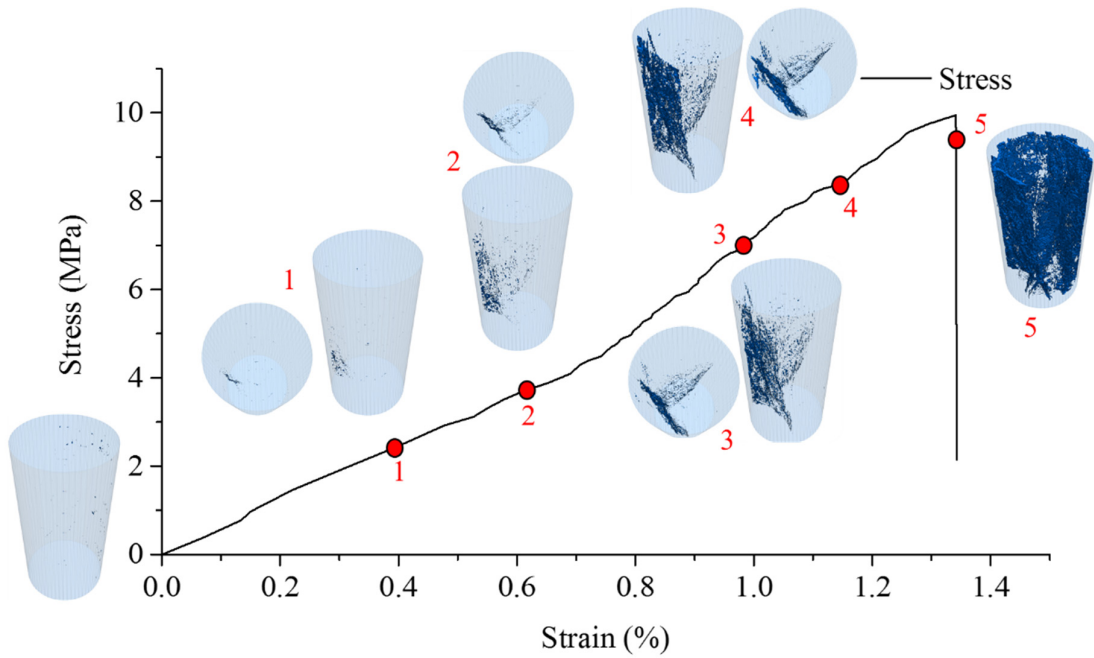


Figure 2.10 Fracture evolution in coal sample C3 during UCS test (vertical stress vs. vertical strain, see also Figure 2.11 and Figure 2.12)

To improve the visualization of the fracture pattern of the coal sample C3 at different loading stages, the fracture data have been transformed into a STL format (see Figure 2.11 and Figure 2.12(d)). The lengths of these three fractures F1, F2 and F3 are 41.86 mm, 32.35 mm and 16.64 mm at a load level of 4500 N (corresponding axial stress is 8.78 MPa).

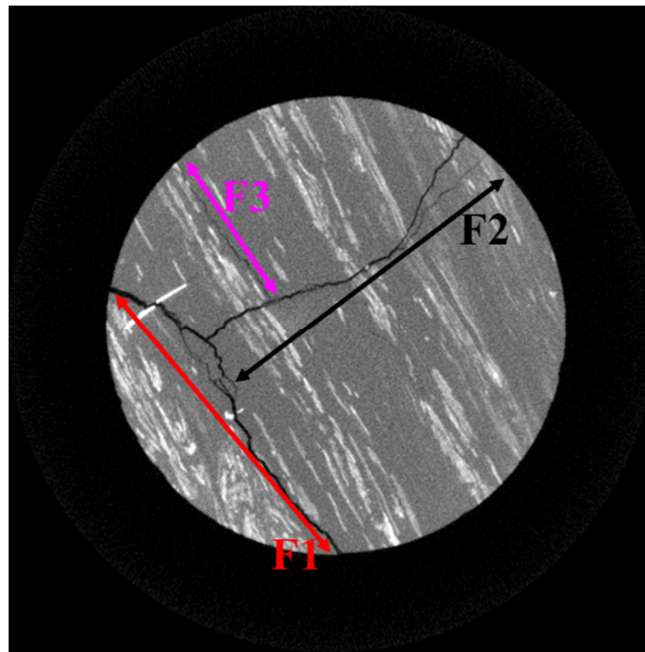


Figure 2.11 Fractures in sample C3 shown by CT image at a selected cross-section

Three sets of fractures are visible in Figure 2.12. Fracture F3 with largest width of 0.3 mm is the thinnest and shortest, which does not represent the main fracture in sample C3. Although fracture F2 has an opening of about 1 mm, it is only weakly connected. However, it is connected to the longest fracture F1, and thus contributes to a large extent to the sample deformation. As revealed in the figures, the fracture volume increased with increasing axial stress.

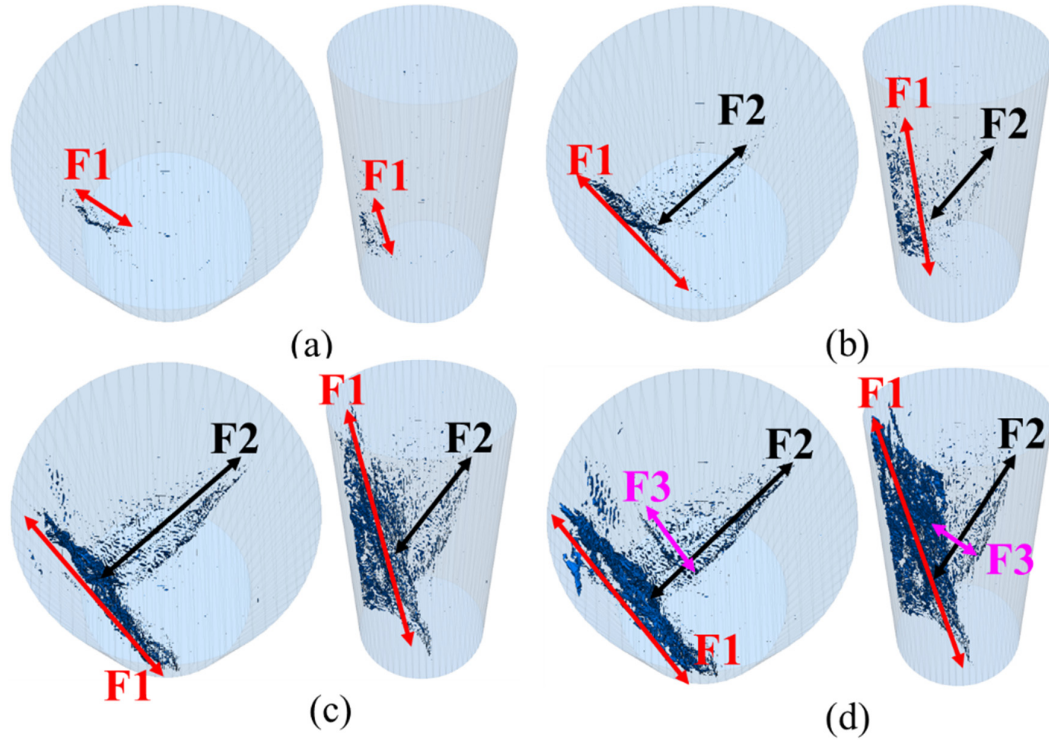


Figure 2.12 Evolution of fractures in coal sample C3 at different loading stages: (a) 1500 N (2.93 MPa), (b) 2000 N (3.9 MPa), (c) 4000 N (7.8 MPa) and (d) 4500 N (8.78 MPa)

2.4.2 Numerical simulation of coal samples under pure mechanical loading

Numerical UCS tests were performed with both, PFC^{2D} and PFC^{3D}. Downward and upward velocities were applied to the top and bottom walls with the same value to launch the simulation. Fracture and crack propagation as well as failure pattern were reproduced via numerical simulations. Control groups were set in certain sections to investigate the influence of the structures.

The linear parallel bond model is applied in the study. Matrix and inclusions are divided into different groups, and bonded with different mechanical parameters, because the hardness of matrix (carbon-containing organics) is different from the inclusions (kaolinite and others). Matrix and inclusions are represented by green and red particles. The connections of different components were realized by weaker bonds, the particles connected remain their original assignment. As shown in Figure 2.11 in previous section, fractures occurred mostly at the boundary, then propagated through the sample. The mechanical parameters used in the numerical simulations were calibrated by lab tests.

Elastic modulus, uniaxial compressive strength and Poisson's ratio are determined by lab tests. These properties are set to be calibration targets. The numerical simulations of UCS tests are performed to fit the stress-strain curve obtained from laboratory tests. In PFC, linear parallel bond group degrades to linear group after breakage, so the parallel bond affects both, compressive and tensile strength. The normal to shear stiffness ratio (*kratio*) has a linear relationship with the macroscopic Poisson's ratio in the elastic deformation stage. The bond effective modulus (*pb_emod*) controls the elastic modulus and also follows a linear relationship in PFC^{2D} and an exponential relationship in PFC^{3D}. The tensile to shear bond strength ratio influences the deformation pattern. If the tensile to shear bond strength ratio is fixed, the macroscopic strength changes linearly with increasing or decreasing tensile and shear strength. Friction angle (*pb_fa*) has no effect before simulation reaches peak stress. Also, the linear model is only activated after the failure of the linear parallel bond model. So, effective modulus and normal to shear stiffness ratio of linear group are always assigned with same values of the parallel bond group.

In PFC^{2D}, numerical models were generated based on different cross-sections of one sample. At different angles, the portion of the inclusion vary from 7.04% to 41.8%. Significant structural differences are clearly illustrated in the models. As shown in Figure 2.13, the 120° direction monitoring plane is mainly parallel to the inclusions, and only very few isolated inclusions are detected in that cross-section. The 120° model has a high uniaxial compressive strength of 15.74 MPa, due to the lowest content of inclusions. The UCS for different cross-sections is shown in Figure 2.14. The 0° and 150° models include a quite similar amount of inclusions (24.57% and 25.32%). The 30° model has distinct lower uniaxial compressive strength of 9.01 MPa, and the entire model is split by fracturing. A comparison of the 6 models illustrates the influence of the structural differences. The uniaxial strength of the sample decreased with increasing amount of inclusions. Also very important: the geometrical structures of inclusions (isolated or elongated) affect both, strength and deformation patterns of the sample.

The reconstructed 2D models are not a good option to represent the sample behavior in a realistic manner. But the influence of the internal structure is well documented by these simulations. Reconstructed 3D models are the better choice to duplicate the coal sample behavior considering all the mechanical and geometrical properties. In this study, traditional modelling method is used for the control group, so the influence of geometrical structures can be investigated.

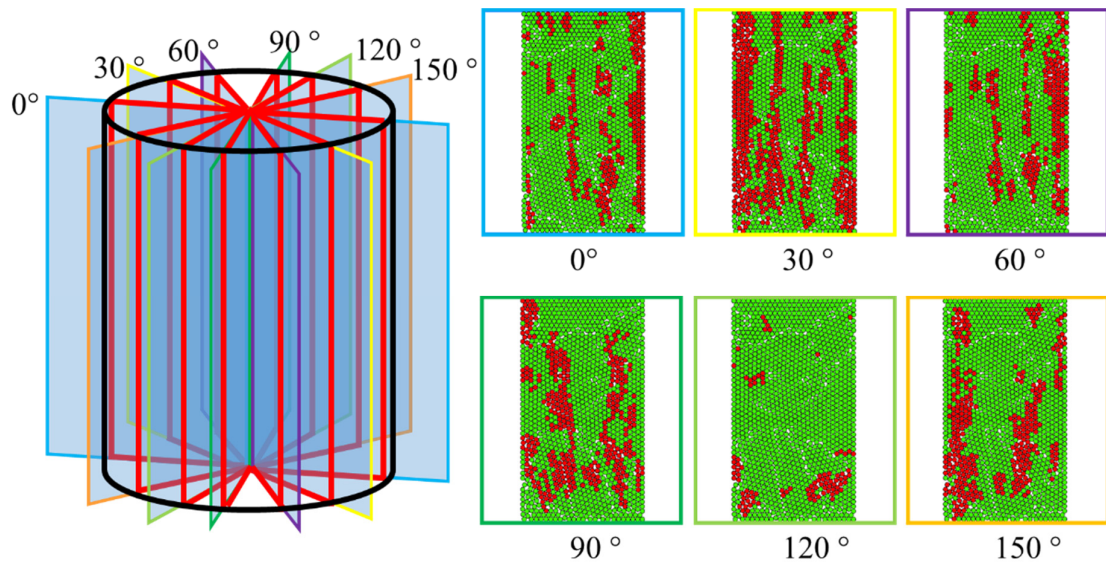


Figure 2.13 PFC^{2D} models for cross-sections along different angles (based on sample C3)

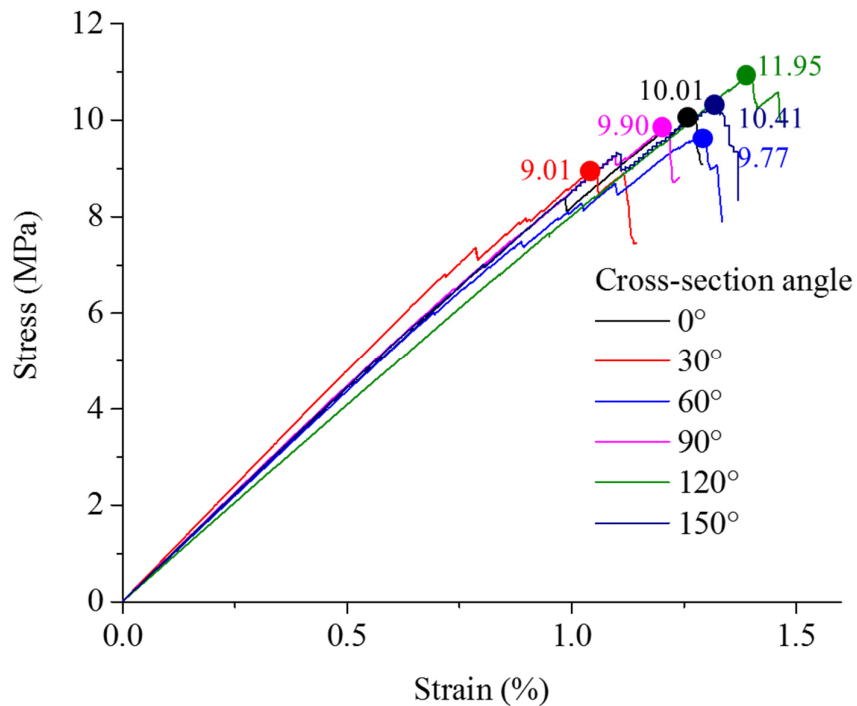


Figure 2.14 UCS tests in PFC^{2D} (vertical stress vs. vertical strain) for different cross-sections at angles of 0°, 30°, 60°, 90°, 120° and 150° (based on sample C3)

Control groups were generated based on the same dimensions as the virgin samples. The geometry files of pores and mineral inclusions were not imported to this model. As shown in Table 2.9, the particles representing mineral inclusions were distributed randomly based on the mineral content and sample porosities in Model 1-2 and 2-2. A sensitivity analysis was conducted to evaluate the influence of each parameter. The detailed calibration process is

described in Chapter 4. Same mechanical parameters were assigned to the reconstructed model and its counterpart in control groups, respectively (shown in Table 2.9).

Table 2.9 Particle based numerical models for UCS tests

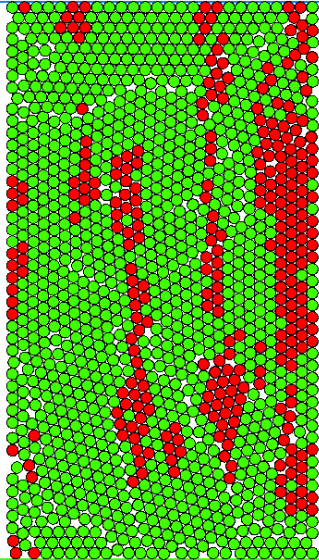
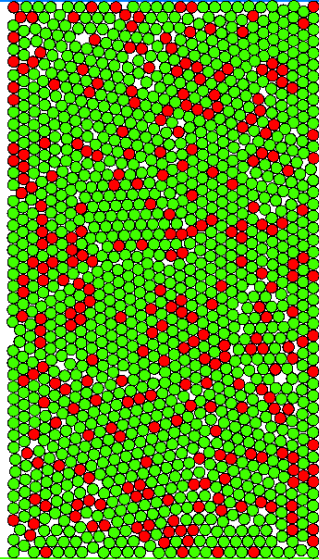
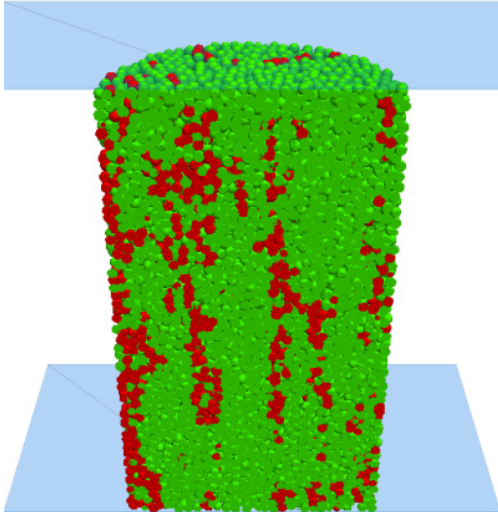
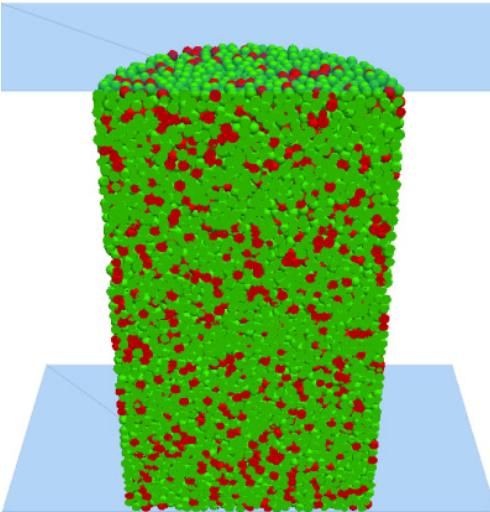
Sample	Reconstructed model	Control group model
2D		
	Model 1-1 (60° cross-section)	Model 1-2
3D		
	Model 2-1	Model 2-2

Table 2.10 Mechanical parameters for numerical simulations

Coal matrix					
Model Element	Parameter	Model 1-1	Model 1-2	Model 2-1	Model 2-2
	N	1036	1095	27390	27648
Particles	r_p (mm)	0.05		0.05	
	ρ_p (kg/m ³)	1390		1390	
	φ (%)	6.5		6.5	
Contacts	E (Pa)	4.0×10^8		6.34×10^8	
	K^*	6		14.65	
	$\bar{\sigma}_c$ (MPa)	8.40		6.08	
	\bar{c} (MPa)	2.10		1.52	
	$\underline{\mu}_c$	0.4		0.4	
	$\bar{\Phi}$ (°)	4		4	
	g_c (mm)	0.05		0.05	
	Mineral inclusion (kaolinite, calcite and others)				
Model Element	Parameter	Model 1-1	Model 1-2	Model 2-1	Model 2-2
	N	299	276	7218	6971
Particles	r_p (mm)	0.05		0.05	
	ρ_p (kg/m ³)	1810		1810	
	φ (%)	9		9	
Contacts	E (Pa)	5.6×10^8		8.66×10^8	
	K^*	2		2.44	
	$\bar{\sigma}_c$ (MPa)	10.0		11.40	
	\bar{c} (MPa)	5.0		4.56	
	$\underline{\mu}_c$	0.4		0.4	
	$\bar{\Phi}$ (°)	7		7	
	g_c (mm)	0.05		0.05	
	Boundary between matrix and inclusion				
Model Element	Parameter	Model 1-1	Model 1-2	Model 2-1	Model 2-2
Contacts	E (Pa)	3.5×10^8		5.77×10^8	
	K^*	1		1	
	$\bar{\sigma}_c$ (MPa)	3.2		3.99	
	\bar{c} (MPa)	1.7		1.99	
	$\underline{\mu}_c$	0.4		0.4	
	$\bar{\Phi}$ (°)	8		8	
Loading					
Model Element	Parameter	Model 1-1	Model 1-2	Model 2-1	Model 2-2
Walls	v (m/s)	0.005		0.01	

Stress-strain curves were achieved by processing the results from both, PFC^{2D} and PFC^{3D}. As shown in Figure 2.15, after calibrating the parameters, the numerical models were suitable to simulate the behavior of the original coal samples. By investigating the simulation results, the fractures generated during simulations were consistent with the deformation patterns observed in the lab.

As shown in Figure 2.16 and Table 2.11, the UCS of the models with real mineral structures are different from that of the control group. The comparison proves that, the internal structure

has significant influence on the strength. Therefore, traditional modelling methods cannot represent the real internal situation of a coal sample.

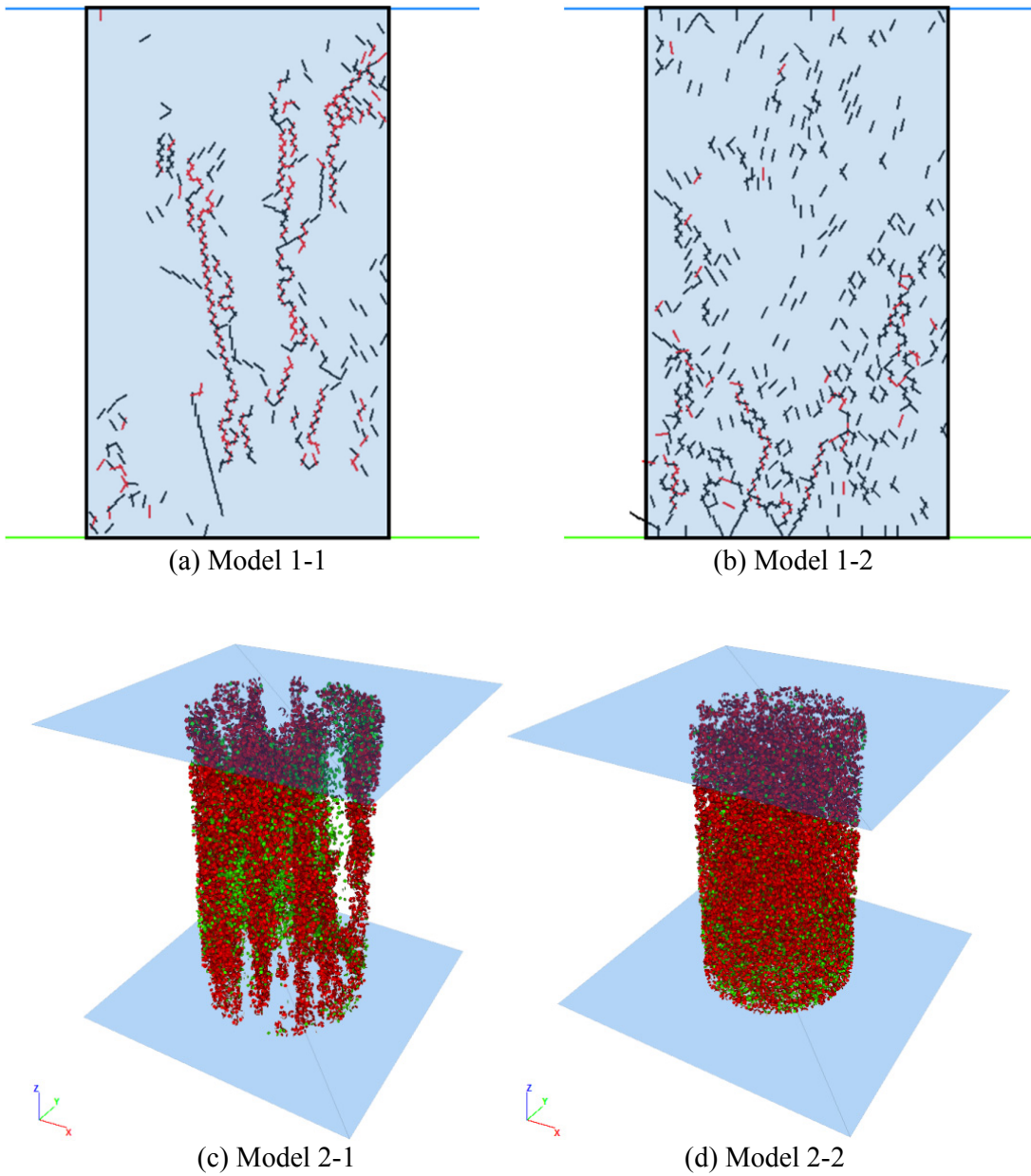


Figure 2.15 Fracture pattern (PFC^{2D} and PFC^{3D})

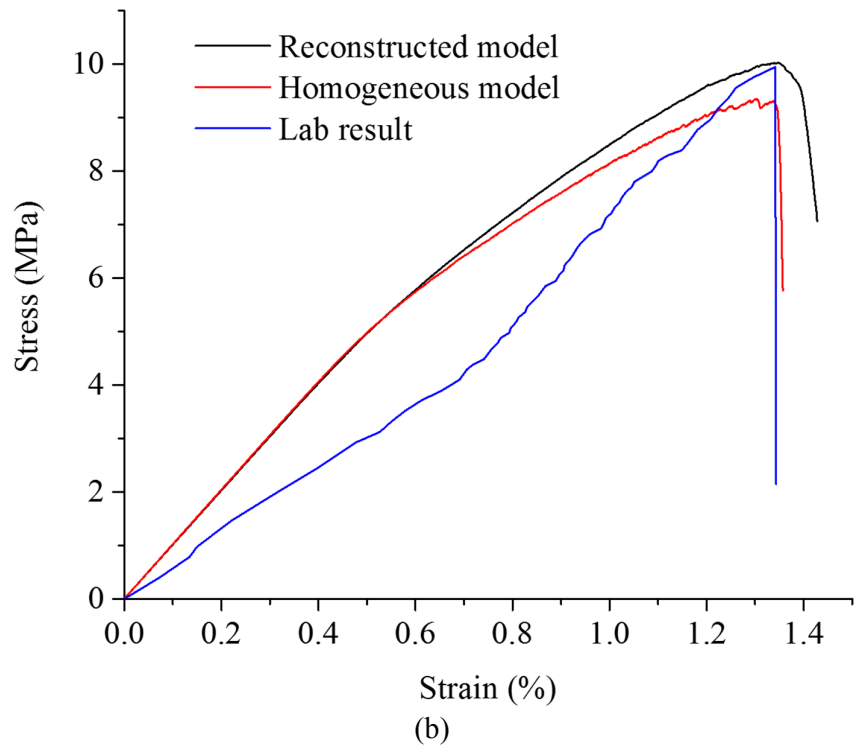
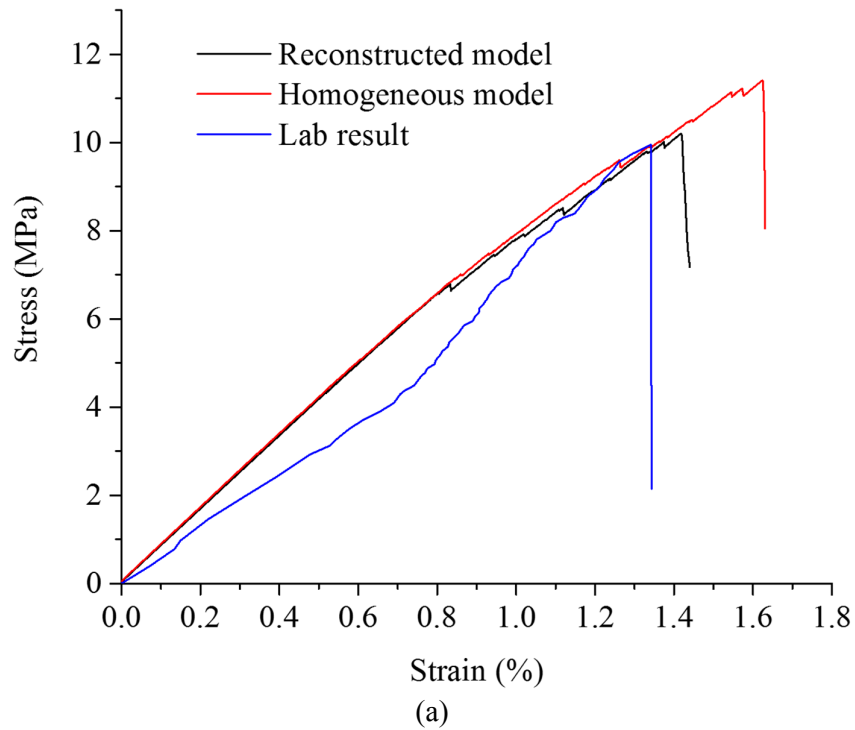


Figure 2.16 UCS tests results for (a) PFC^{2D} model (b) PFC^{3D} model

The reconstructed 3D model shows a higher strength than the control group model, which is opposite to the results of the 2D models. The reason is explained below.

Table 2.11 Peak stress of sample models during UCS tests

	Model 1-1	Model 1-2	Model 2-1	Model 2-2
σ_c (MPa)	9.77	11.41	10.01	9.35

Fractures are generated mostly on the boundaries in both, 2D and 3D models. In the reconstructed 2D model, fractures are generated along the boundaries and went through the model easily on one single trace. If one fracture cuts through the model, the sample can be treated as fully splitted. In model 1-2, the cracks are generated evenly, and it takes more efforts to form macro fracture. So model 1-1 has lower uniaxial compressive strength than model 1-2. On the contrary, particles were restrained by surrounding contacts in the 3D models, as well as the fractures, because all pre-existing boundaries are located inside model 2-1, and no one split the model. The spatial distribution of pure matrix and inclusions bodies provide enough support. So the flawless fragments impede the fracture propagation process. While tiny boundaries are distributed evenly in model 2-2, extension and connection of single fractures occur. Large fractures can form easier. As a consequence, the reconstructed model in 3D has a higher UCS in this particular case.

2.5 Conclusions

A series of tests were performed on coal samples, including conventional physical measurements, X-ray fluorescence tests and imaging by X-ray CT. CT scanning was conducted up to failure on sample C3 under uniaxial compression to determine the fracture evolution.

The following conclusions can be drawn:

X-ray CT techniques offer some remarkable advantages such as the non-destructive detection and 3D visualization of the inner heterogeneity of the samples. Three structural components were detected inside the coal sample: pores (including fractures), coal matrix, and minerals. A series of segmentation threshold values is derived for the five coal samples. The segmentation process is used for advanced evaluation of pore size and 3D spatial disposition of pores, fractures, and minerals.

Slicing analyses of the coal sample demonstrated that the distributions of both, pores and minerals, are highly inhomogeneous. Also, main fractures can be determined by 3D reconstruction of CT slices of sample under loading conditions. This made it possible to develop a technique for investigating the spatial flow of gas inside the coal, as outlined in the following chapters.

Numerical models of coal sample replicating the inner structure are generated to simulate the loading process and to calibrate the mechanical parameters. The detected inner spatial structure of the coal sample demands a complete 3D consideration. This is confirmed by the conducted comparative 2D and 3D simulations. 3D models based on the initial sample show more realistic macroscopic mechanical behavior and deformation patterns.

During the loading process, the deformations of the samples are directly related to the fracture connectivity. Fracture aperture, fracture plane evolution and fracture orientation are the main

factors to evaluate the degree of damage. The obtained stress-strain curve can be directly related to the accumulation of fractures.

3 Permeability evolution under triaxial compression

3.1 Introduction

Permeability is the most important physical property which affects seepage and migration of fluid in rocks at different scales. As previous studies indicate, coal rock disasters and gas outbursts are becoming more serious with increasing mining depth due to increasing stresses. Permeability is also affected by stress variations. Laboratory tests are conventional methods to investigate the permeability evolution.

Standard coal briquettes made up of powdered coal and adhesive were used for testing firstly (Zhou and Lin 1999). This method is useful for pure coal sample without remarkable damage or inhomogeneity. However, in engineering practices, permeability depends heavily on internal pore-fracture networks. With the increase of loading, initial fractures close at first, re-open later and expand dramatically finally. In addition, new fractures are generated during the tests, and they extend and coalesce. Finally, the overall permeability increases significantly. This permeability evolution is a dynamic process and is closely related to the microscopic damage. Generally speaking, fracture propagation in rocks with high porosity is caused by the collapse of pores: the volume decreases and the permeability decreases. Rocks with low permeability undergo another process. Emerging, extension and connection of tiny fractures are causing shear induced dilatancy, which results in increasing permeability.

Coal is a typical low permeable rock. Permeability tests on coal samples are performed to investigate the relation between damage and permeability evolution.

The physical properties of different coal samples were determined under different stress conditions. It is assumed, that the propagation of initial fractures in coal samples is heavily influenced by compaction. The opening width of fractures was proven to influence permeability directly, so closure and extension of fractures led to big differences in permeability for different coal samples (Yang et al. 2007). Gas flow rate variation during the complete loading process shows a flat U-shape. Strain is lagging, and higher confining pressure suppressed the gas flow rate (Yin et al. 2010). Relations between permeability and stress and strain were established by many scholars (e.g. Hu et al. 1996; Wang and Miao 2005). An equation with stress-dependent permeability coefficient was established to describe the coupled relations between gas flow rate and loading conditions, including confining pressure and axial pressure (Zhao et al. 2009a).

Permeability k is an inherent property, but the measurement of permeability is influenced not only by the sample itself but also by fluid properties, test conditions and systematic parameters (Li et al. 2008b; Tan 2013). Grain compositions, grain shapes and solid mineral components are important factors. Porosity, saturation level, pore connectivity and microstructure depend on the in-situ conditions and will be also affected by the sampling process. Choice of test fluid, fluid phases and testing temperature depend on the investigation aim. All these previous mentioned factors have influence on the measurement results (Bear 2006). If any pre-defined condition is changed, the permeability calculated may be different. Therefore, nearly identical

test conditions were chosen for all the samples. Please note, that permeability values documented in this thesis are only valid for the specific test conditions.

In the laboratory, two test methods are popular to determine permeability: steady-flow method and transient method. The later one is especially suitable for low permeable materials. According to the research background, different fluids are chosen: nitrogen, helium, methane and CO₂ are the most used gases. Purified water, kerosene and mercury are conventional liquids (Chen et al. 2008; Liu et al. 2003; Wang et al. 2011b). The test fluids migrate through the samples in a steady-state manner applying the constant head permeability test or constant flow test. On the contrary, fluids are flowing unsteadily applying transient methods like the transient pulse test, the constant flow pump test (Olsen et al. 1985) or the pressure oscillation test (Kranz et al. 1990).

The constant head permeability test is the most common steady-state test, and Darcy's law as shown in Equation 3.1 can directly be applied. A constant pressure difference is applied at both ends of a cylindrical sample and the flow velocity becomes stable after a period of time. The steady-state velocity is directly related to the pressure difference. Darcy's law is given in Equation 3.1:

$$k = \frac{\mu Q}{A} \frac{H}{P_u - P_d} = \frac{\mu Q}{A} \frac{dh}{dp} \quad (\text{Equation 3.1})$$

in which, k is permeability (m²), Q is total flow rate (m³/s), μ is viscosity (Pa·s), A is cross sectional area (m²), P_u and P_d are upstream and downstream pressures (Pa) applied to ends of the sample, H is sample length/height (m), dh and dp are differential expressions of length and pressure. This equation is suitable for incompressible fluids.

Gases are compressible, and measurements are affected by the fluid compression/expansion. The gas flow rate at a reference pressure was considered under certain flow conditions. Equation 3.2 (Somerton et al. 1975) gives a corresponding relation for gases:

$$k = \frac{\mu Q_0}{A} \frac{2P_0 H}{(P_u^2 - P_d^2)} \quad (\text{Equation 3.2})$$

where, Q_0 is volumetric flow rate (m³/s) at reference pressure P_0 (Pa), other terms are the same as mentioned before.

Relatively high hydraulic gradients (large pressure differences) are set to prevent the generation of non-Darcy flow. When the permeability of a sample is very low, it takes a long time to reach steady-state flow. Very precise flowmeters are necessary to measure the flow rate.

A transient method is useful for low permeable rocks (Sun et al. 2013; Zhang et al. 2000a; b). The transient pulse method is the most common transient method. In this method, a cylindrical sample is connected with sealed containers. The pressure increases immediately (from upstream fluid tank) and fluid starts flowing through the sample to the downstream container. During this process, upstream pressure decreases and downstream pressure increases. So the pressure

difference also decreases. An analog model was established to describe this system: the sample was assumed to act as an electrical resistance and the containers act as capacitors (Brace et al. 1968). The pressure difference shows an exponential decay with time. Based on pressure variation curves permeability can be calculated by Equation 3.3 (Li et al. 2008b):

$$\left\{ \begin{array}{l} \frac{P_u(t) - P_d(t)}{\Delta P_i} = \exp(-\alpha t) \\ \alpha = \frac{kA}{\mu H} \left(\frac{1}{S_u + S_d} \right) \end{array} \right. \quad (\text{Equation 3.3})$$

in which, $P_u(t)$ and $P_d(t)$ are upstream and downstream pressures (Pa) at time t , ΔP_i is initial pressure difference between both containers (Pa), t is test time (s), k is permeability (m^2), A is cross-sectional area (m^2), μ is viscosity (Pa·s), H is sample length (m), S_u and S_d are the water bearing capacity of upstream and downstream containers (m^3/Pa), which represent the volumetric change of fluid in the container caused by unit pressure.

The test time of the transient method is much shorter. There are some other advantages: small range pressure manometers with high precision are used, and readings from flowmeter are more accurate. A theoretical model for granite was established (Brace et al. 1968), assuming an incompressible model with zero porosity. But this model is not suitable for pore structures. More calculation methods have been developed, some new graphical methods were established and more precise analytical solutions were achieved. The influence of upstream and downstream containers were investigated (Dicker and Smits 2007). New test systems were manufactured with high accuracy for reservoir core samples, such as coal and shale samples (Jones 2007).

3.2 Experimental setup

The basic properties of the coal samples are described in Chapter 2. All the coal blocks were sealed in water- and shock-proof foam immediately after being collected from the field. The foam prevented damage and oxidation. Cylindrical samples were manufactured in the laboratory. Diameter and length of the samples are about 25 mm and 50 mm, respectively. Sampling, transportation, processing and operating procedures are based on ISRM Suggested Methods for Rock Characterization, Testing and Monitoring (ISRM 2015).

The average physical and mechanical parameters of coal samples were obtained by a series of laboratory tests (see Table 3.1).

Table 3.1 Basic physical and mechanical parameters of coal samples (average values)

	ρ (g/cm^3)	φ (%)	σ_c (MPa)	E (GPa)	ν	C (MPa)	θ ($^\circ$)
Coal	1.34	2.19	16.38	4.70	0.38	2.84	34.95

The permeability evolution was investigated via HM-coupled standard triaxial tests arranged for steady-state flow. The coal samples were not permitted to physically shrink or swell freely as a result of uniaxial strain, because they are under lateral confinement similar to in-situ

conditions. The used test system is advanced, because it allows testing at high temperature and high pressure under static or dynamic load conditions. Measurements of hydraulic and mechanical pressures as well as strain and time were automatically conducted with sensors of high accuracy.

As shown in Figure 3.1, a special triaxial chamber was used for independent loading in radial and axial directions. This experimental system is capable to investigate gas permeation under different stresses and pore pressures. The tests were conducted at room temperature of 20 ± 3 °C.



Figure 3.1 DBT A50-80-180 triaxial cell for hydro-thermo-mechanical coupled testing

The cylindrical sample has been sheathed in a polyvinyl chloride (PVC) rubber core sleeve. The core sleeve provided optimal pressure transmission and maximum tightness during the entire test from low to maximum confining pressure. The samples are sealed even after failure. A pair of special designed loading devices was attached to the jacketed sample. The loading platens are equipped with flow distributors. The sample material itself and the axial platens have been isolated from the confining fluid by the core sleeve. The test gas migrated through gas channels, and was gathered at the upstream end of the sample without leakage. The end-platens were connected to gas reservoirs through pipelines and isolating plug valves. The distributor gas tank is capable to provide a maximum gas pressure of 1.5 MPa. The gas used in this experimental research is pure nitrogen, so no chemical reaction took place with the coal samples. The viscosity of nitrogen at laboratory temperature is measured to be 1.78×10^{-5} Pa·s. The main function of the different valves is to adjust upstream and downstream pressures. Several pressure transmitters have been used to monitor the uniform distribution of gas pressure in the system during the tests.

A stiff servo-controlled loading device is used to apply the axial loads. The maximum compressive force is 3600 kN. The high accuracy triaxial load cell was operated in a range from 0 to 1000 kN (calibration error is less than 0.05 %; sensitivity is ± 0.5 kN). The axial strain was measured by a linear variable displacement transducer (LVDT).

The confining pressure is also servo-controlled. A maximum oil pressure of 80 MPa can be applied. The system was run by professional control software packages, such as Test-Star-II Control System and Test-Ware from MTS.

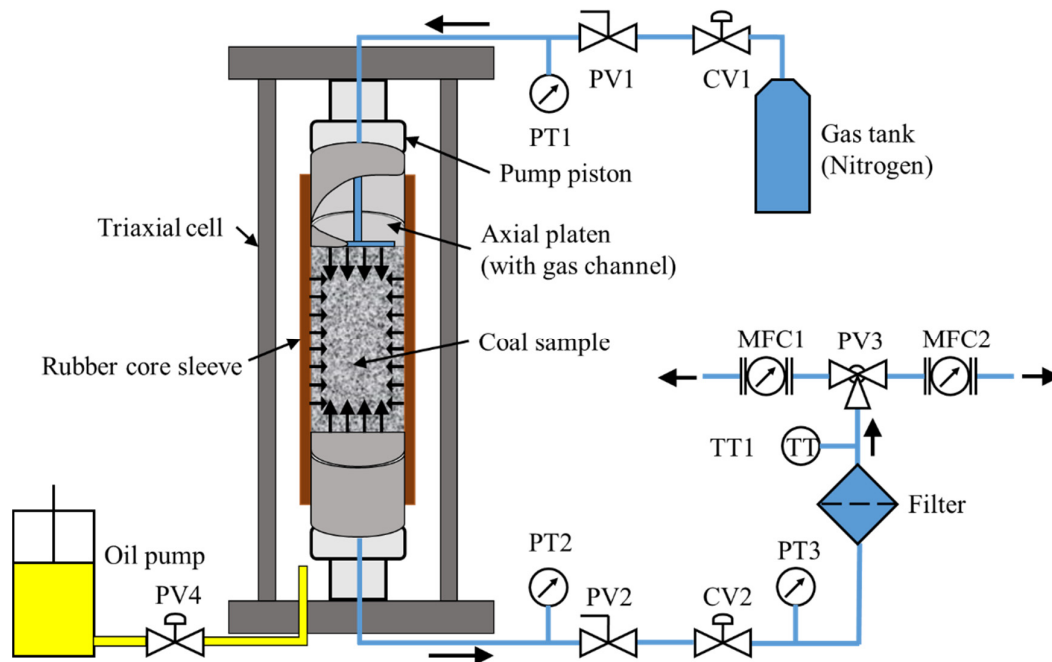


Figure 3.2 Schematic of the experimental setup

As shown in Figure 3.2, CV1 and CV2 are airflow control valves, PV1, PV2, PV3 and PV4 are plug/cock valves, PV3 is 3-way plug valve. PT1, PT2, PT3 are pressure transmitters, MFC1 and MFC2 are mass flow controllers to measure flow rate. TT1 is a temperature sensor.

During the testing process, highly compressed nitrogen flows out of the gas tank. The flow rate was controlled by outlet control valve CV1. The input upstream pressure was adjusted by changing the flow rate. This adjustment was precise enough to maintain constant upstream pressure values. A plug valve PV1 was directly connected to pressure transmitter PT1 and sample cell. PT1 was installed to monitor and record the upstream pressure. Multiple pressure transmitters were applied to control general pore pressure. Gas seepage and pressure control were intensively monitored.

Nitrogen gathered upstream was pushed into the sample cell and flowed through the coal sample. Pressure transmitter PT2 was located at the output side of the cell. PT2 was used to monitor and record the downstream pressure. A second plug valve PV2 was connected to PT2.

The plug valves PV1 and PV2 are very important to maintain the regular function of the entire system. When pressure data fluctuate dramatically, the strong airflow could damage the testing

devices and unexpected destructions of the sample may happen. The samples are isolated when both, PV1 and PV2 are closed. Closure of PV1 and PV2 immediately can protect the sample and triaxial cell from being heavily damaged.

Airflow control valve CV2 and a third pressure transmitter PT3 were attached behind PV2. CV2 was used to adjust the downstream pressure. Readings of pressure transmitters PT2 and PT3 were calibrated to work identically. Then the downstream pressure has been adjusted to a stable value, and the pressure difference was maintained constant. A filter unit was used behind PT2 to relieve the pressure and clean the gas, so that outlet gas flows into the devices steadily and smoothly.

TT1 is a temperature sensor. It was used to monitor and record the outlet temperature of the nitrogen gas. MFC1 and MFC2 are two mass flow controllers with different measurement ranges. The measurement range of MFC1 is 0 - 200 cm³/min with higher accuracy. The measurement range of MFC2 is 0 - 1000 cm³/min, with lower accuracy. At the early stage of the test, three-way plug valve PV3 was operated, and MFC1 was used to monitor the flow rate, while MFC2 act as backup (standby monitoring). When fractures are generated in the sample, enormous flow rates occur at the outlet. If the range of MFC1 is exceeded, MFC2 was activated.

In this system, the downstream outlet was not connected directly to the atmosphere, but the downstream pressure was set to 0.2 MPa. So the pressure difference was 0.8 MPa. In order to assure the tightness of the rubber core sleeve, the pore pressure has been set lower than the confining pressure.

Together with the test system, the oil syringe pump was connected to the triaxial cell with the plug valve PV4. The confining pressure was kept constant by the servo-controlled pump system.

3.3 Test procedure

Conventional triaxial loading experiments are still the most popular ones to measure permeability, deformability and strength of coal samples simultaneously under conditions similar to in-situ conditions.

The loading frame stiffness incl. the triaxial cell was first calibrated to obtain realistic deformations when samples were compressed. For gas permeability tests, leakage was checked prior to each conducted test. A standard metal specimen (dummy) is used to make sure that there is no leakage in the system.

Exemplary, sample C1 under 2.5 MPa confining pressure is used to describe the test procedure. After set-up and calibrating the test system, the servo-controlled program is activated to initialize the boundary conditions. Axial loading pressure and confining pressure are raised to 2.5 MPa to reach a hydrostatic stress state. Both pressures are held constant, and then the upstream gas pressure is applied gradually: its value is increased to 1 MPa as designed. At this early moment, no gas pressure can be detected at the downstream end. Gas seepage occurs inside the sample. After 6 - 8 hours, a downstream flow rate can be detected and tends to reach a stable state. By adjusting CV2, downstream pressure is set to 0.2 MPa, but minor pressure

occur at upstream and downstream after this operation. Therefore, CV1 and CV2 need to be further adjusted manually to maintain the desired gas pressure difference. After the system reaches steady flow state again, axial load is applied by further movement of the upper loading plate. The axial loading process is applied with a very small speed of about 8×10^{-5} mm/s. The axial loading process is discontinuously in steps: the loading process lasts 750 s followed by a pause, the stress condition is kept constant for a period of time during the pause and was then further increased. So the gas seepage reaches a stable state after several stress changes. This cycle of loading and holding was repeated through the whole testing process, and flow rates were monitored and recorded after each cycle synchronously. After the flow rate (permeability) reaches the peak value, the test process is monitored carefully and prepared for termination. The loading should be halted before the sample is fully damaged. So the damage pattern is still visible for investing internal crack propagation. Otherwise, all samples will break into tiny fragments with extremely developed crack network. The crack propagation and damage pattern are both valuable in displaying the flow paths. When axial stress and flow rate remain relatively constant, the permeability evolution process was evaluated incl. the corresponding stress-strain relations. Stress-strain curves of triaxial compression were measured, and permeability variations according to strains were calculated from corresponding recorded flow rates.

3.4 Results and discussion

Coal samples with standard size were tested in the laboratory. Permeability evolution tests were performed under triaxial compression, and CT techniques were applied to scan the samples before and after the tests. Permeability-strain curves and stress-strain curves were obtained. The images of the internal fracture networks were compared.

Nine coal samples have been tested with confining pressures of 2.5 MPa, 5.0 MPa and 7.5 MPa, respectively. Seven samples provide representative seepage characteristics. Due to some objective factors, it is not possible to evaluate the two other samples. Physical dimensions, confinement settings and final permeability (not the peak permeability) are obtained as shown in Table 3.2. With different confining pressures, the duration time varies from 20 to 40 hours. Peak permeability is reached after the peak axial differential stress. The permeability is not consistent after reaching the peak value. The relation of peak permeability corresponding to confining pressures is shown in later sections. The trend from peak permeability to final permeability is also analyzed.

Table 3.2 Measured values of permeability (coal samples)

Sample Nr.	Confinement	Dimensions		Final flow rate	Final permeability
	σ_3 (MPa)	D (mm)	H (mm)	Q (m^3/s)	k (m^2)
C1	2.5	25.50	50.60	4.20×10^{-6}	3.06×10^{-15}
C11	2.5	24.77	49.80	1.58×10^{-6}	1.14×10^{-15}
C13	5.0	24.99	50.02	1.23×10^{-6}	8.49×10^{-16}
C15	5.0	22.32	50.10	3.87×10^{-6}	3.84×10^{-15}
C4	7.5	25.47	50.85	1.20×10^{-6}	8.69×10^{-16}
C12	7.5	24.89	49.89	3.33×10^{-7}	2.67×10^{-16}
C16	7.5	24.54	50.28	4.20×10^{-7}	4.23×10^{-16}

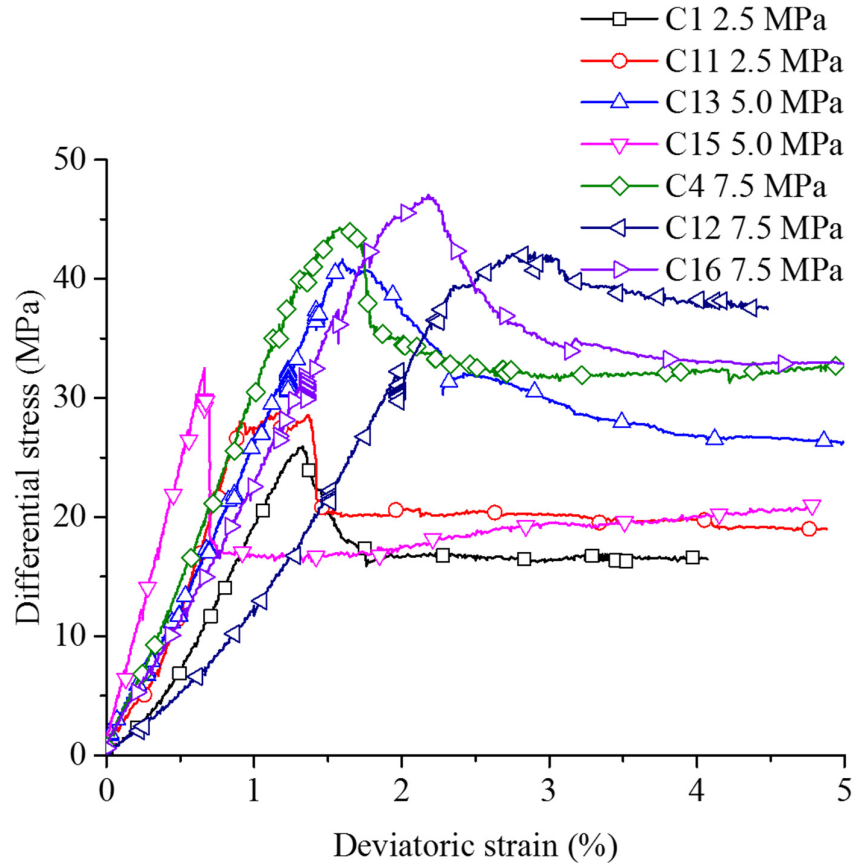


Figure 3.3 Complete stress-strain curves of samples under triaxial compression

As shown in Figure 3.3, peak differential stresses and corresponding strain values increase with increasing confining pressures. When confining stress and pore pressure are fixed, the seepage process shows a complicated pattern with axial stress variation. According to the stress-strain curve of sample C1 shown in Figure 3.4, the permeability-strain curve is lagging behind the stress-strain curve. The permeability in Figure 3.4 is shown in a logarithmic scale. The seepage process inside the coal sample undergoes the following five stages:

1. Initial compaction stage (I). Coal is a typical porous medium, where micro-cracks and pores are uniformly distributed. In the beginning, the permeability decreases linearly with increasing axial loading. The internal voids are closed due to the external compression, so the flow rate is decreasing due to the lack of seepage paths. The sample deforms evenly and initial pores are closing gradually. The general permeability decrease is small. The stress-strain curve with confining pressure of 2.5 MPa shows the typical behavior: the coal sample is compressed in this stage and behaves linear elastic. When the axial stress reaches 11.28 MPa (differential stress is 8.78 MPa) the permeability decreases towards the minimum value. When the permeability is at the minimum value, the corresponding stress point is defined as σ_m . It is difficult to observe the gas seepage behavior inside the sample.

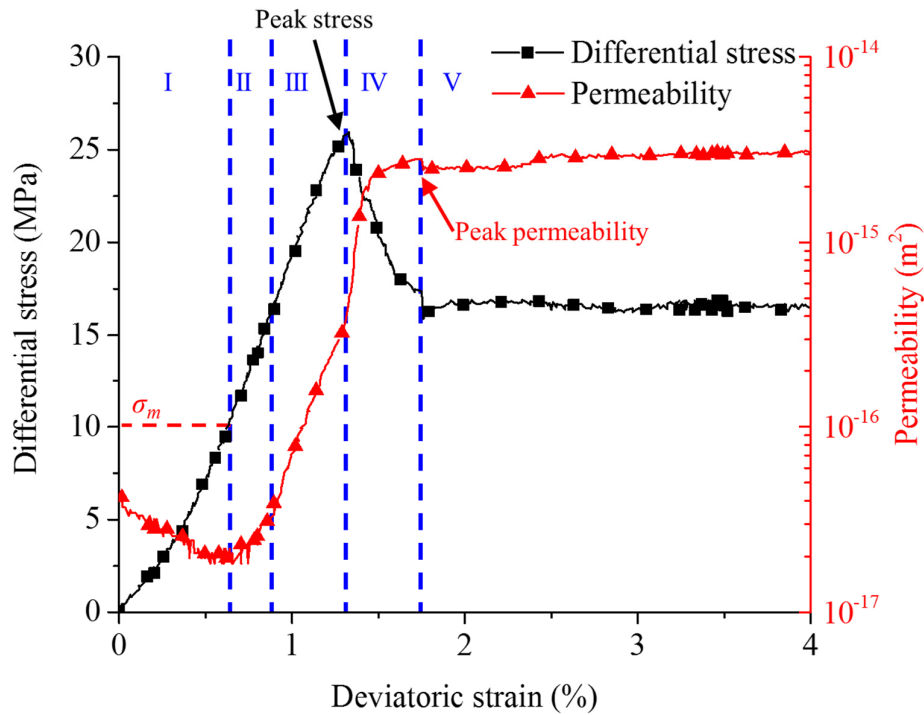


Figure 3.4 Differential stress (axial stress minus circumferential stress) and permeability evolution versus axial strain for sample C1

2. Linear elastic deformation stage (II). After axial stress reached the stress point σ_m , permeability, as well as gas flow rate increase moderately with axial stress. These rates raise significantly in the early phase. The trends follow the stress-strain curve in the linear elastic stage. In this stage, initial fractures propagate and new micro-cracks are generated under combined influence of axial pressure, confining pressure and pore pressure.

3. Nonlinear deformation and peak strength stage (III). With continuous increase of axial stress, fractures grow further and connect with each other. Macroscopic fractures begin to appear and permeability increases drastically.

4. Strain softening stage (IV). After the sample reaches the peak differential stress of 28 MPa, permeability is still increasing with increasing axial strain. Such scenario last until axial stress is decreased to 22.74 MPa. Then permeability and flow rate reach peak values and maintain constant. Shear displacements occur on macro fractures after the peak strength stage. Apertures and coalescence of fractures increase with extensive deformations, and the fracture system becomes fully developed. Based on the experimental results, the peak permeability occurs in this stage.

5. Residual stress stage (V). Ongoing deformations cause abrasion on fracture surfaces. With the decrease of surface roughness, the aperture decreases simultaneously. So - to a small extent - a compaction phenomenon appears and the permeability of the broken sample decreases with confining pressure. This decrease is more pronounced at higher confining pressures. Minor decline might occur afterward, which might be caused by macroscopic flow processes itself, further internal fracture propagation has less influences on seepage characteristics.

As mentioned already above, the stress point σ_m has some significance for the permeability evolution process. When the axial stress reaches σ_m , the gas seepage velocity reaches a minimum value, and the seepage phenomenon is restricted. Beyond σ_m , the gas seepage velocity changes qualitatively, it increases drastically with increasing axial stress. The pores inside the sample are poorly connected at the stress point σ_m , and the flow paths are in their narrowest states. Lowest permeability is the physical meaning of σ_m .

In engineering practice, horizontal and vertical in-situ stresses are monitored. Combined with laboratory works, permeability-stress curves of target coal samples are achieved, and the stress points σ_m are obtained. By avoiding such stress states, the extraction efficiency could be raised, and accidents may be avoided.

Because of the effect of confining pressure and the limitation of monitoring devices, initial flow rates under specific conditions are difficult to detect. The minimum detectable flow rate is 1.5 sccm (standard cubic centimeters per minute), which equals to $2.5 \times 10^{-8} \text{ m}^3/\text{s}$. Only for samples C1 and C15 it was possible to detect the σ_m values, so in this research the stress point σ_d is determined when flow rate was detected firstly. The value of σ_d is important to predict the change in permeability. With 7.5 MPa confining pressure, flow was detected firstly after the tests reached peak differential stresses. The corresponding strain at stress point σ_d is ε_d , which increases through the test. ε_d is also an important critical point to describe the permeability evolution trend as shown in Figure 3.5. The corresponding strain value at peak permeability is defined as ε_p .

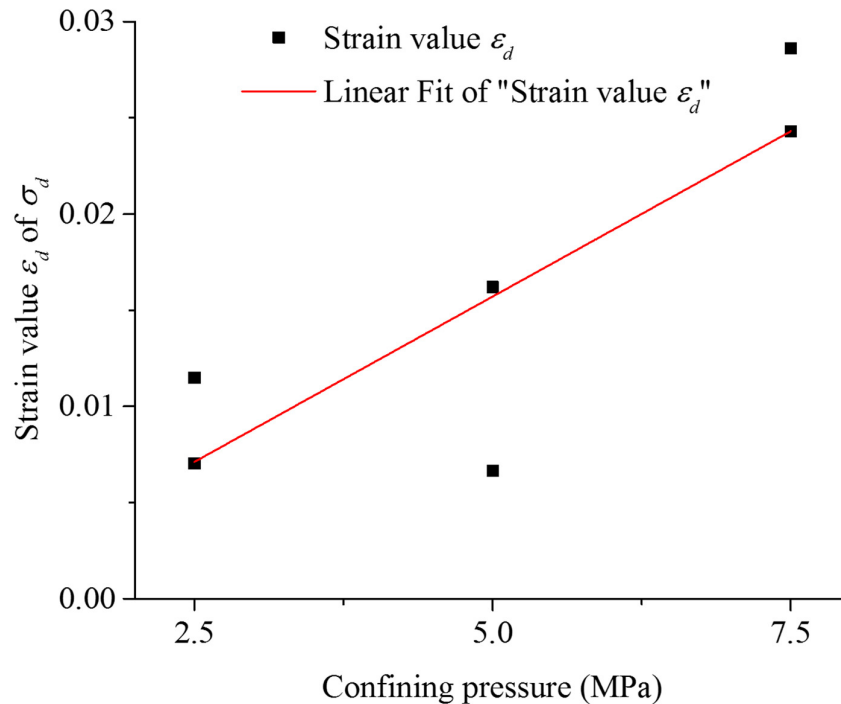
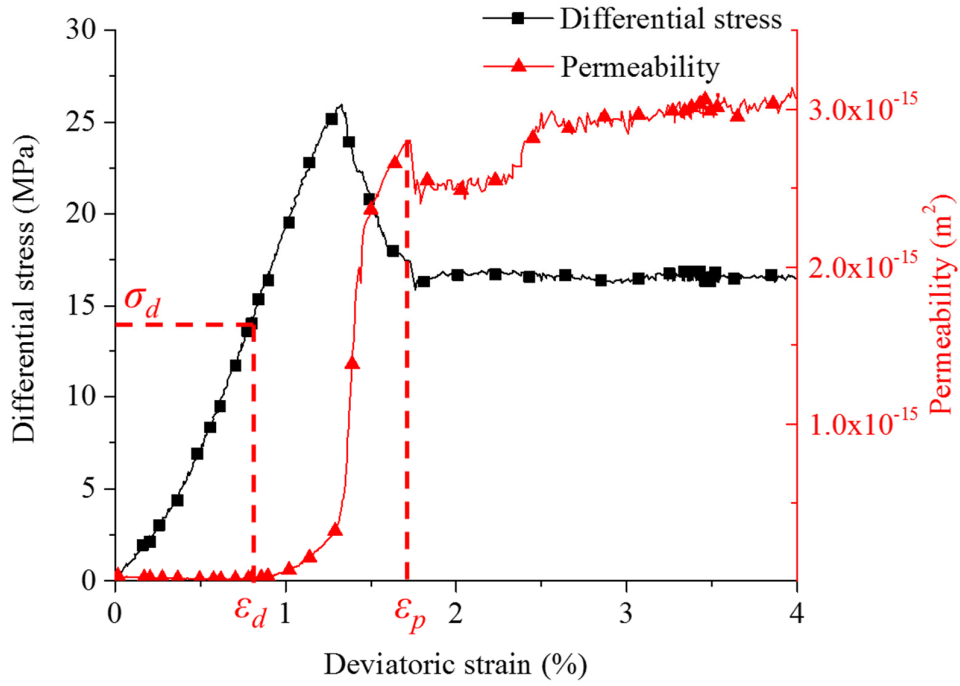


Figure 3.5 Strain value ε_d versus confining pressure

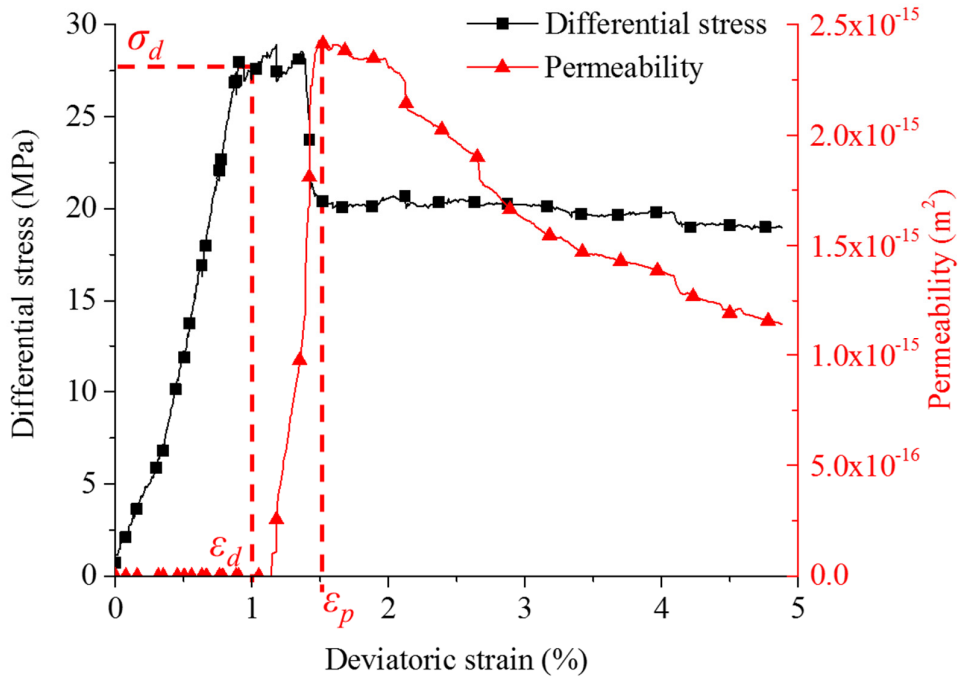
The linear fitting of ε_d versus confining pressure results in Equation 3.4 (see also Figure 3.5).

$$\varepsilon_d = -0.00147 + 0.00344 \cdot \sigma_3 \quad (R^2 = 0.63868) \quad (\text{Equation 3.4})$$

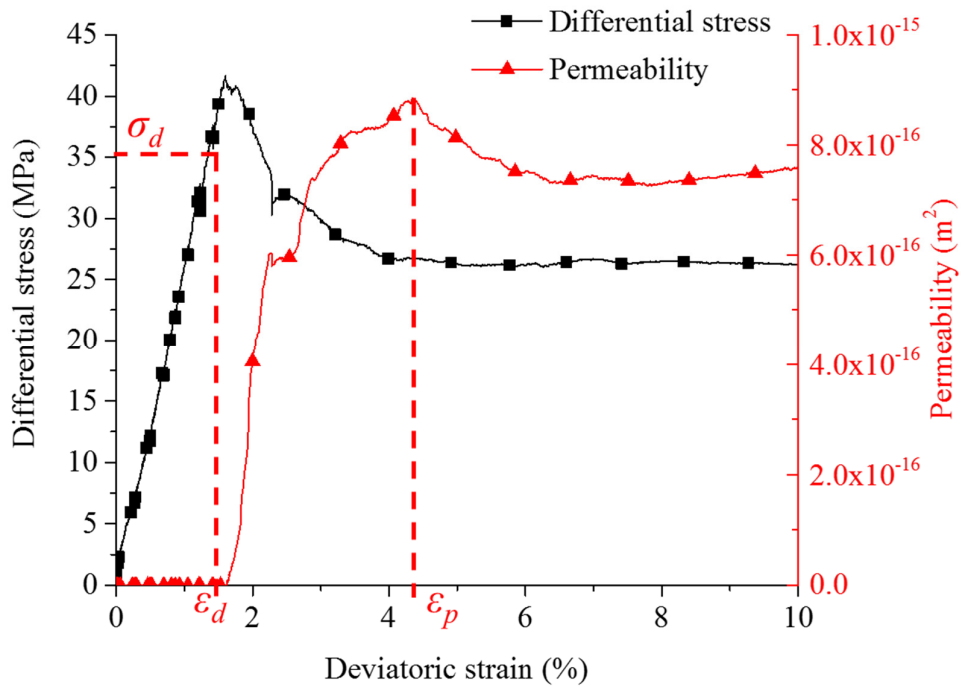
The permeability evolution (in linear scale) for different samples under various confining pressures is shown in Figure 3.6.



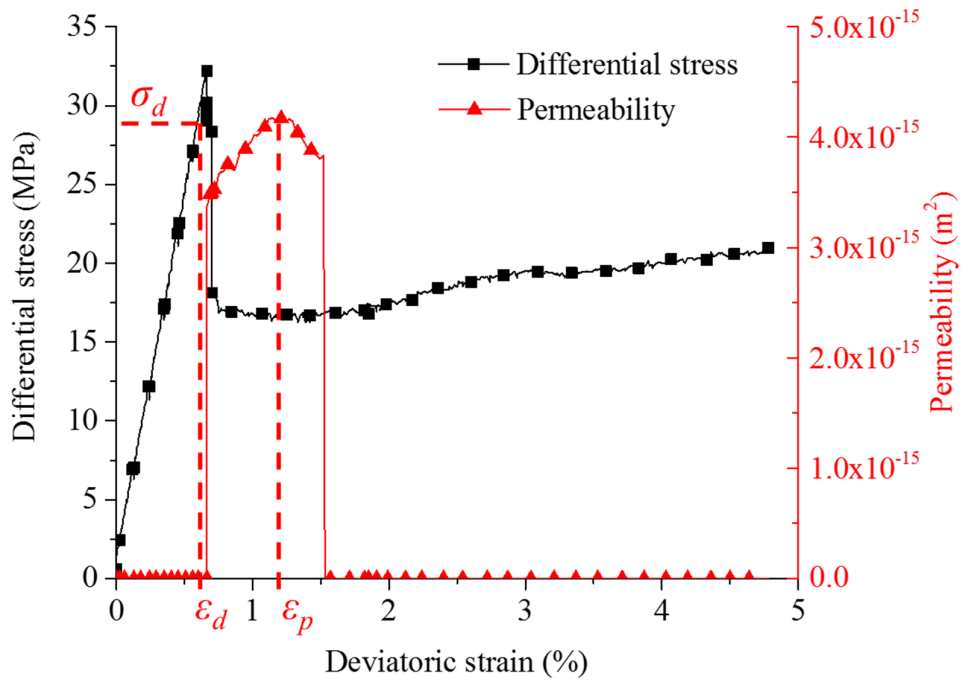
(a) C1



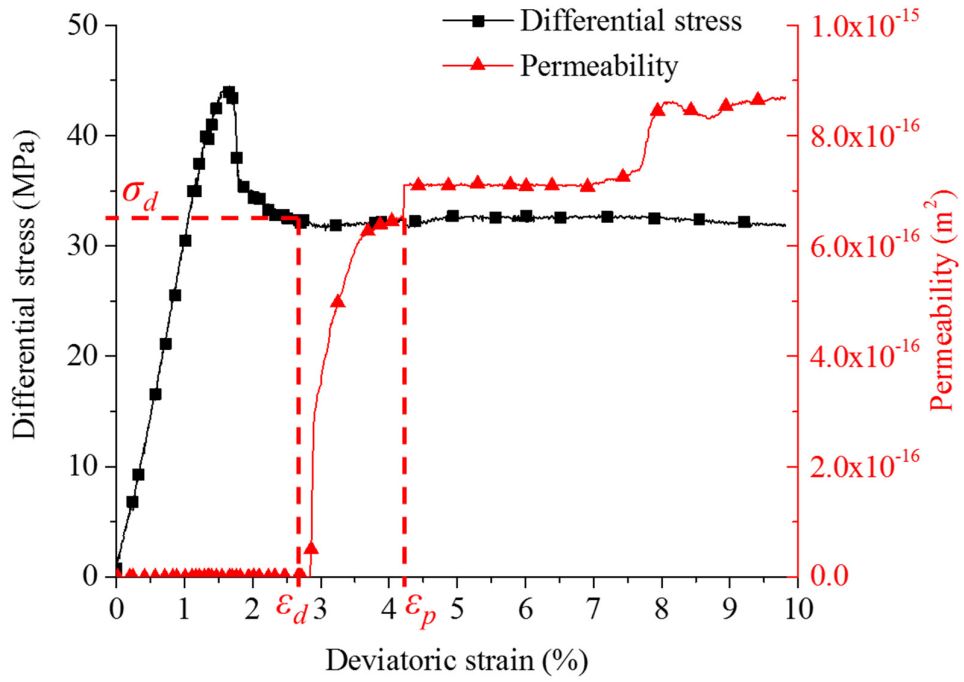
(b) C11



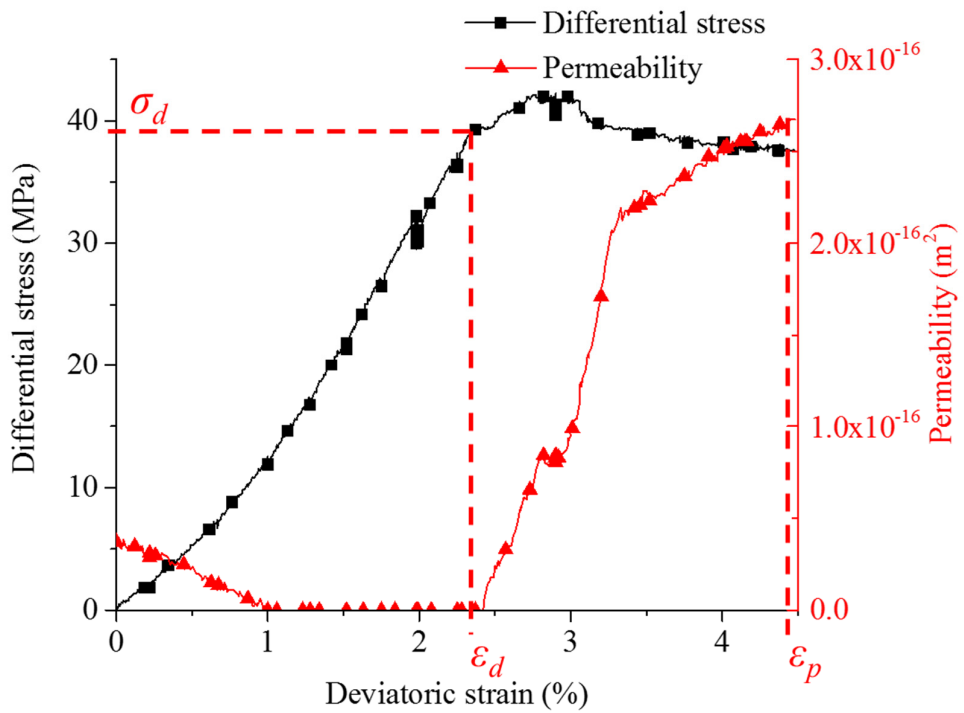
(c) C13



(d) C15



(e) C4



(f) C12

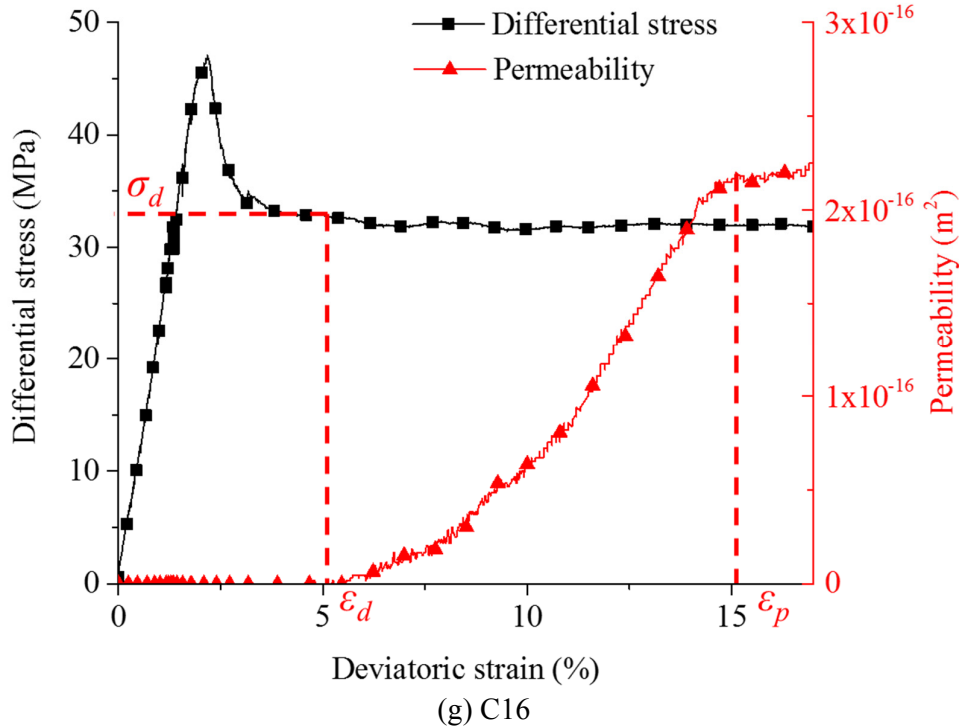


Figure 3.6 Permeability evolution and complete stress-strain curve

The permeability tends to decrease with low confining pressure, and the extreme low flow rates at high confining pressure cannot be detected in the early stage. The permeability evolution of sample C1 shows the typical trend (see Figure 3.6(a)). Stress points σ_d are monitored before peak strengths for confining pressures of 2.5 and 5.0 MPa, and σ_d values of samples at 7.5 MPa were observed after the peak strength. The permeability evolution of sample C15 shown in Figure 3.6(d) reveals an exactly different trend compared with other samples. The sudden increase of flow rate and cease of seepage behavior are possibly caused by its internal structure. It took very long time after peak strength to detect seepage in sample C16, which is also caused by its special structural character. So the permeability results of sample C15 and C16 are not considered when deducing a universal permeability evolution rule.

By analyzing the results, confinements are proven to restrict the permeability evolution. Confining pressures were applied perpendicular to the general flow direction, and fractures are generated predominantly parallel to the axis and were closed during the first phase. By comparing the models with different confining pressures, before the peak strength is reached, permeability is reduced by more than one order of magnitude when confining pressure changes from 2.5 to 7.5 MPa. In post peak stages, permeability varies in a much wider range with low confining pressure, sometimes permeability values maintain stable with minor increase such as sample C1 shown in Figure 3.6(a), or reduce to one third of peak value such as sample C11 shown in Figure 3.6(b). So the post-peak permeability is more sensitive at low confining pressure. Before peak strength is reached, axial stress restricts the seepage by a small extent. After the peak strength, applied axial stress is able to further increase the permeability at low confinement; on the other hand, axial stress causes more constraints on flow channels at high confining pressure.

It is believed that, the permeability decreases when stresses are compressive on the fracture. On the other hand, the permeability increases significantly when stresses induce tension/shear effects on the fractures. Compared with flow through macroscopic fractures, the permeability of coal for fluids (gas or liquid) is extremely small.

The permeability evolution curves shown in Figure 3.7 are obtained by investigating the laboratory test results. The results from sample C12, C15 and C16 have been neglected, because they are significantly affected by specific internal structures. The structural influences on sample permeability is documented in the following chapters. The internal structures affect the permeability by creating different fracture networks, especially in the post peak stage. The different performances of sample C1 and C11 under same confining pressure proved that, the fractures may behave divergently under same conditions which is discussed later in this chapter. The flow rate of sample C16 was detected much later with extreme low value due to the special structural features, so the permeability trend of C16 is also neglected when deducing the general rule. According to the trends of C11, C13, C4 and C12, the following is assumed: if the coal samples are fully destroyed under triaxial compression, all the fragments are still compressed by the confinement. The magnitudes of final permeability in different samples tend to converge to a stable value (which is about $8 \times 10^{-16} \text{ m}^2$ as shown in Figure 3.7).

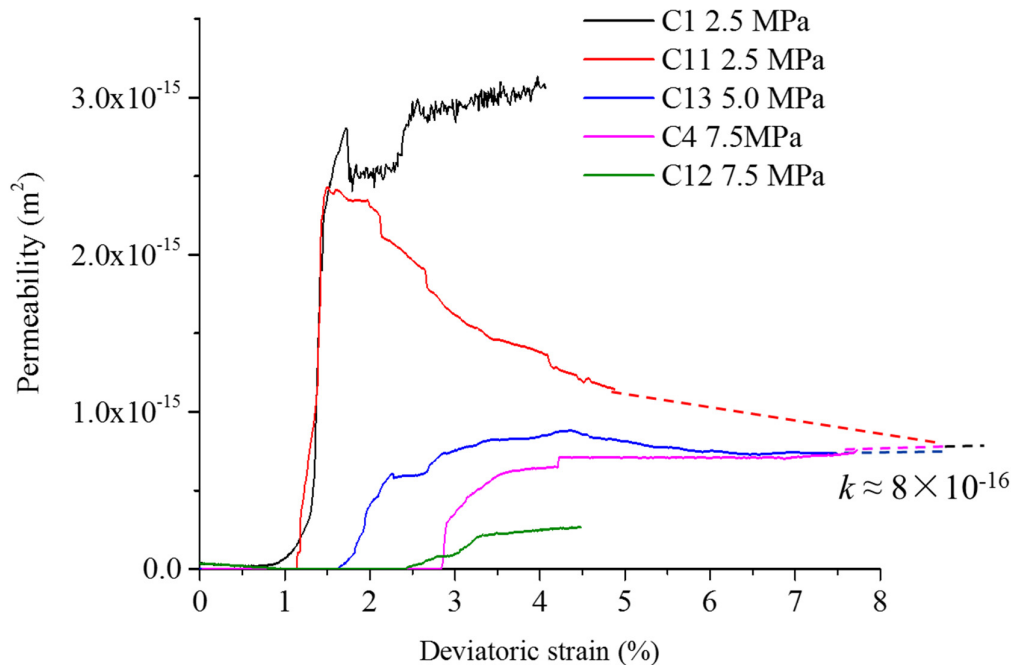


Figure 3.7 Permeability evolution at different confining pressures

Based on the results, the peak differential stress and peak permeability are in clear correlation with confining pressure. A lagging characteristic is observed between corresponding strain values at peak differential stress and peak permeability, which can also be noticed easily in Figure 3.6. Simple values of lagging axial strain differences are not clear to reflect the influence of confining pressure, but the ratio between strains at peak differential stress and peak permeability shows the lagging effects much better. A lower ratio value means larger difference

between these two strain values. So with higher confining pressure the lagging effect becomes stronger as shown in Figure 3.8.

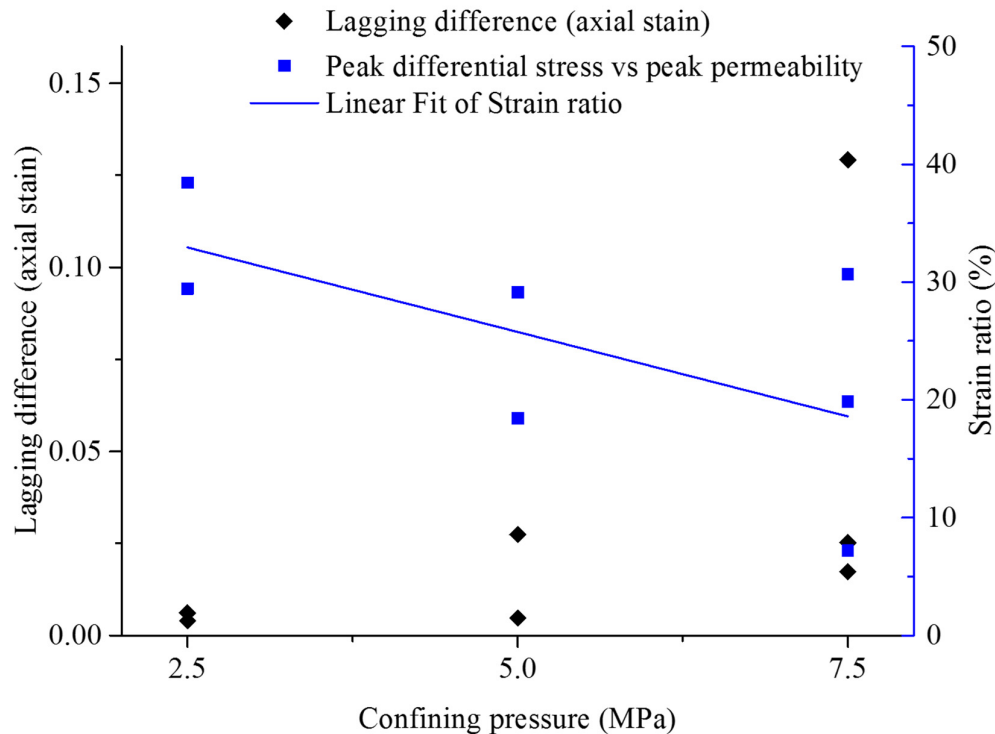


Figure 3.8 Lagging characteristic (strain at peak differential stress vs. strain at peak permeability) as function of confining pressures

Despite the lagging characteristic, for a better demonstration of permeability trends, the peak permeability of each sample is shown together with the peak axial differential stresses. Trends of peak differential stress and peak permeability for different confining pressures are shown in Figure 3.9. The permeability increased rapidly after axial stress reached the stress point σ_d . For developing a general permeability evolution trend, σ_d is an important criterion to predict the permeability. From the macroscopic view, the maximum permeability is assumed to appear immediately after stress point σ_d is reached. But for samples with 7.5 MPa confining pressure, the stress point σ_d occurred after the peak differential stress, which means the axial stress firstly increased to peak differential stress, and then reduces to σ_d . In order to avoid any misunderstanding, the peak differential stresses are used as the criterion. Peak permeability shows strong dependency on confining pressure. The final permeability is reached in a convergence process.

Line 1 and line 2 (see Figure 3.9) are reference lines of peak permeability and final permeability. This 3D figure is able to reveal the general trends of permeability evolution considering the combined effects of confining pressure and differential stress. By projecting the points into a plane, the relation between peak differential stresses and peak permeability versus confining pressure can be illustrated like shown in Figure 3.10. Peak differential stresses and peak permeability are predictable for specific confining pressures.

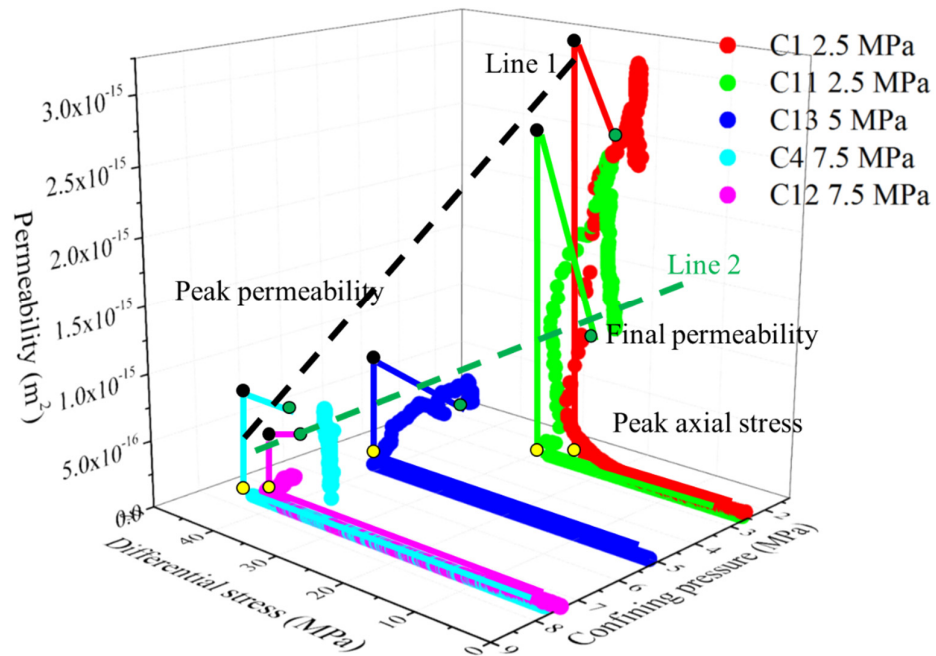


Figure 3.9 Peak differential stresses and permeability versus confining pressure

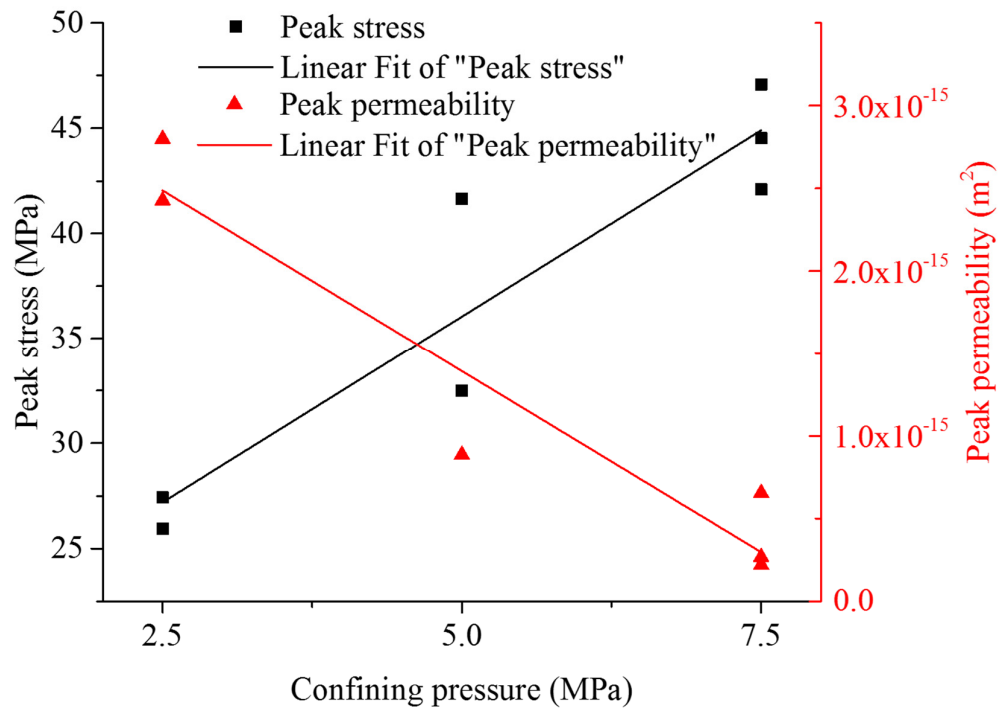


Figure 3.10 Peak differential stress and peak permeability versus confining pressure

A linear fitting for peak differential stress and peak permeability as function of confining pressure results in Equation 3.5 and Equation 3.6, respectively (see Figure 3.10).

$$\sigma_p = 18.3432 + 3.54153 \cdot \sigma_3 \quad (R^2 = 0.86713) \quad (\text{Equation 3.5})$$

$$k_p = 3.5833 \times 10^{-15} - 4.3829 \times 10^{-16} \cdot \sigma_3 \quad (R^2 = 0.9217) \quad (\text{Equation 3.6})$$

in which, σ_p is peak differential stress (MPa); k_p is peak permeability (m^2). The rubber core sleeves were removed after testing and pictures were taken to observe the fractures. The apertures appeared larger because of the unloading behavior. The fragment structures of 4 samples after destruction have been rebuilt with a digital processing method as shown in Figure 3.11. The samples C11, C12 and C16 recovered from tests were tightly packed with rubber core sleeve. The samples were broken into tiny fragments as shown in Figure 3.12, and the main structure of the fractures could not be obtained.

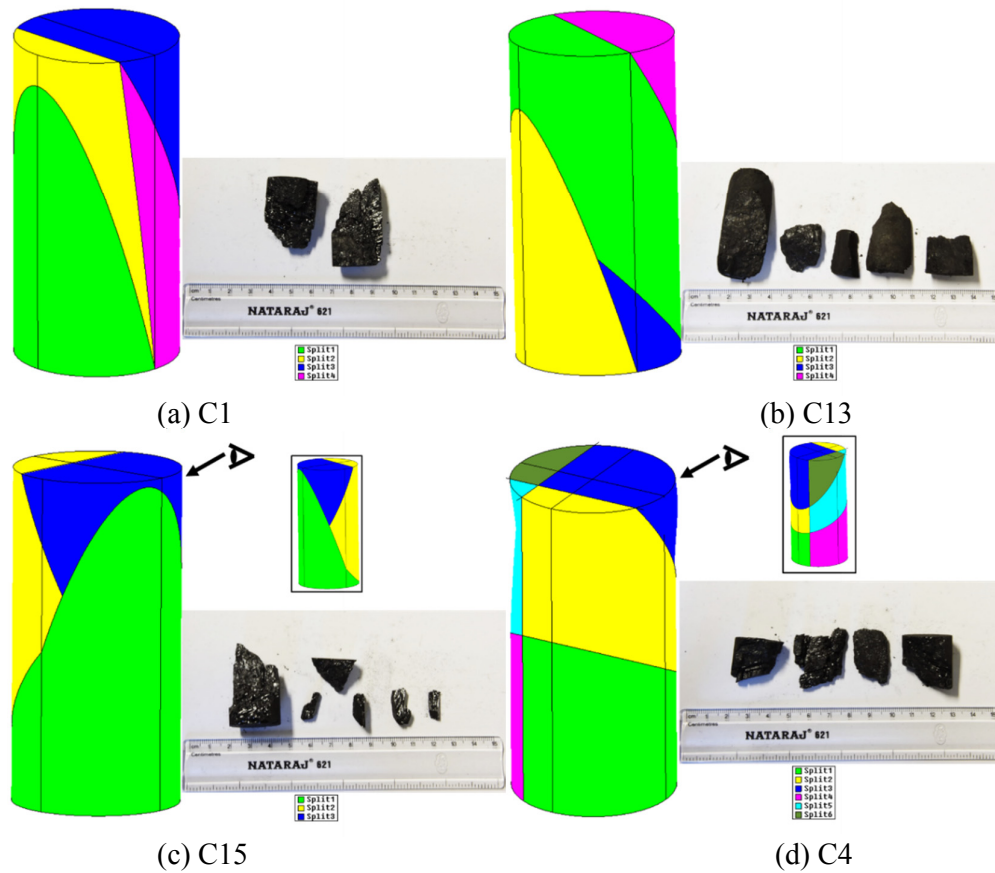


Figure 3.11 Digital reconstructed structures of deformed samples

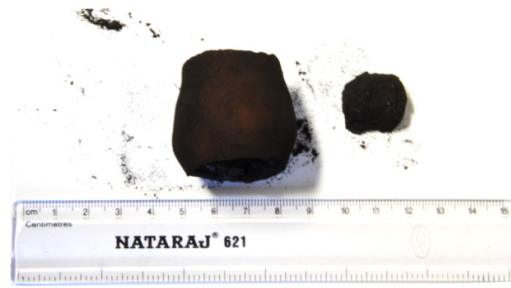


Figure 3.12 Complete deformed sample C16 with core sleeve

The fracture angle is the angle between fracture surface and the horizontal plane. According to the pictures, fracture angles for different confining pressures were achieved as shown in Table 3.3 (see also Figure 3.13). Under uniaxial compression, coal samples are damaged mostly by vertical splitting, and fracture angle was about 90° . The samples under triaxial compression are broken by shear fractures with angles from 50° to 80° . When the confining pressure was lower than 5 MPa, single shear fractures appeared. The fracture angles decrease with higher confining pressure, when multiple parallel fractures or intersected fractures appear. The observed reduction of fracture angle with increasing confinement supports the concept of a non-linear failure envelop (decreasing friction angle in terms of non-linear Mohr-Coulomb theory).

Table 3.3 Fracture parameters of different coal samples after final destruction

Sample Nr.	C1	C13	C15	C4	C11	C12	C16
σ_3 (MPa)	2.5	5.0	5.0	7.5	2.5	7.5	7.5
Main fracture angle θ_f ($^\circ$)	75	73	68	52			
Surface area A_{all} (mm^2)	917.00	904.30	1079.82	637.84	Not available		
Character descriptions	One main fracture with parallel fractures	Parallel fractures crossed by another fracture	V-shaped fractures	Multiple fractures with one vertical fracture			

The fractures connecting the top and bottom surfaces (final state of C1 and C15) are causing a tremendous increase in permeability. On the other hand, the fracture through the sample C4 also caused an increase in permeability, but not so significant. The fracture through sample C1 was generated in the early stage of compression, while the fracture in sample C4 occurred in a later stage. All the fragments of sample C4 were compacted and extremely tight.

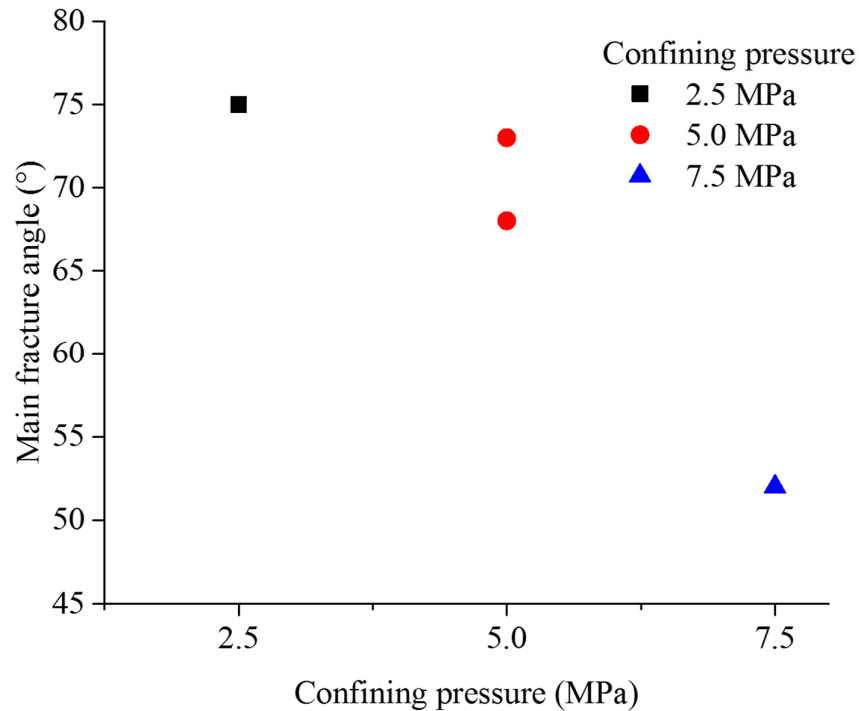


Figure 3.13 Main fracture angle in the coal samples versus confining pressure

3.5 Conclusions

The permeability evolution under different stress states has been investigated by HM-coupled conventional triaxial compression tests. An experimental test system is developed to measure flow rates under confined conditions. Laboratory tests are performed on several cylindrical coal samples from the Chinese Pingdingshan coal field.

At fixed confining pressures, the increase of axial stress generated complex strain and gas permeability evolution. The evolution process is described by five stages in terms of permeability and deformation. Each sample goes through the following five stages: initial compaction stage, linear elastic deformation stage, nonlinear deformation and peak strength stage, strain softening stage and residual stress stage.

Peak permeability appears after peak differential stress, and permeability remained at relatively high values during the subsequent plastic compaction stage. Peak differential stress and peak permeability of the samples depend heavily on confining pressure. In general, the permeability increased dramatically after the sample reached the stress point σ_d when flow rate was detected firstly or recovered from minimum states. According to the test results, the following is assumed: if the coal samples are fully destroyed under triaxial compression all the fragments are still compressed by the confinement. The magnitude of final permeability at different confining pressures tend to converge.

By further analyzing both - the image and lab test data - fractures propagate through the samples easily at low confining pressures, which leads to high permeability of the sample. On the

contrary, at high confining pressure, only a few main fractures are generated with orientation towards the side surfaces, and low permeability is maintained until failure of the sample.

4 Numerical simulation of triaxial tests

4.1 Introduction

Triaxial compression tests as described in previous chapters are the most common and effective method to investigate the rock behavior under different stress states. Progressive cracking of rock samples was investigated in the laboratory. Such tests document that different minerals produce distinct behavior during the failure process (Li et al. 2002). In addition to lab tests, numerical simulations of rock samples under triaxial loading are used to get deeper insight into the deformation and damage behavior.

The Distinct Element Method (DEM) has been used to simulate rock material, where the rock model is composed of cemented granular material of complex shaped grains. Both, grains and cement can be deformable and may break (Potyondy and Cundall 2004). The DEM has a great potential to simulate rock fracture problems (Kazerani and Zhao 2010; Lan et al. 2010). This method allows realistic simulations of crack initiation and propagation.

Some preliminary studies were performed to investigate sample deformation under different load configurations using PFC (Zhao et al. 2009b). This study considers simplified conventional triaxial compression and plane strain models to reproduce macroscopic measured stress-strain relations. The effect of boundary conditions on general elastic response, peak and critical state have been investigated. The properties and the implementation scheme of the boundary conditions influence the response of the granular system significantly. The simulation of triaxial compression tests on coal samples is used to illustrate details of the internal deformation and damage process. Heterogeneity of the sample can be taken into account, which means the microstructure in form of mineral inclusions (distribution, size and packing as well as contacts between the components).

A lot of numerical simulations of triaxial compression tests have been performed in two dimensions. Triaxial compression tests were simplified as biaxial tests with rigid or flexible membranes at outer boundaries where confining pressure is applied (e.g. Ciantia et al. 2016; Iwashita and Oda 2002; Wang and Leung 2008). A flexible membrane with bonded particles is commonly used in 2D biaxial simulations.

A 3D implementation of a flexible membrane generally requires a complex formulation or extensive computational power (Kuhn 1995; O'Sullivan and Cui 2009; Uthus et al. 2008). The increasing availability of DEM codes and advances in computational power enable researchers to model triaxial tests in 3D. Many researchers simulated true triaxial tests, in which cubic samples were fixed within flat rigid boundaries (Belheine et al. 2009; Salot et al. 2009; Sitharam et al. 2002). Rigid boundaries are the most common used boundary condition for triaxial simulations of cylindrical samples and parallelepiped specimens (Belheine et al. 2009; Hasan and Alshibli 2010; Lu and Frost 2010). The rigid boundary has its advantages in representing end platen in triaxial tests. Nonetheless, these works demonstrate how rigid boundaries inhibit localization, causing significant non-uniformities in the stresses along the boundary. This technique is not able to apply a uniform lateral stress, and the fixed shape hinders the onset and

growth of local strain as well as shear band in triaxial simulations (Cheung and O'Sullivan 2008).

Other researchers simulated the effect of confining pressure by applying forces directly to the sample and allowing it to deform freely (Cheung and O'Sullivan 2008; Cui et al. 2008; O'Sullivan and Cui 2009; Wang and Tonon 2009). A stress-controlled flexible boundary was used to model the membrane (sleeve). Some advanced researches have improved this technique remarkably. After boundary particles have been detected, their coordinates were projected to a rectangular plane using Voronoi cells, the corresponding area of each particle was monitored and the force applied was obtained. Then the forces are distributed to these particles to simulate a stress-controlled flexible boundary. However, change in virtual surface area of the sample was not considered accurately. Although this technique is quite effective, it assumes that the membrane remains cylindrical, which is not an optimal representation for a flexible sleeve boundary typically used for conventional triaxial tests. The forces are applied directly towards the axis of the sample rather than normal to the sample surface. A hydrostatic boundary has been proposed as an alternative strategy. Boundary conditions are reproduced by simulating the confining fluid pressure during triaxial tests. Additional boundary elements are not required, and computational time is decreased (Ng 2004). Another disadvantage of modeling confining pressure with forces solely is that, no actual membrane elements exist in the model, so there is no scope for observing the behavior of the membrane and the effects of its properties. Since no boundary elements are used in this approach, the membrane – sample interaction cannot be examined.

Periodic boundaries have been generated in some DEM simulations and the samples were assumed to be surrounded by identical elements in all directions (Lee et al. 2012; Ng 2002; Thornton 2000). Multiple cuboid elements were generated to cover the sample. A uniform strain field was created with this technique, and boundary effects were mostly eliminated. However, the triaxial application was difficult to reproduce due to the cylindrical shape of the sample.

To properly reproduce the flexible latex membrane, researchers have made some progress with the flexible bonding approach. Series of particles were generated to represent the membrane as shown in Figure 4.1. They were connected with flexible contact bonds (Iwashita and Oda 2002; Wang and Leung 2008). Bonded particles were assembled in the shape of a sleeve, and high pressure was applied to generate 3-dimensional conditions. The lateral stress conditions have been verified in detail by several researchers (de Bono et al. 2013; Cheung and O'Sullivan 2008). Adopting bonded particles as flexible membrane was a significant improvement in triaxial compression simulations. The modification of particle properties is easy, and detection of the boundary particles on the surface is unnecessary. Moreover, the investigation of membrane – sample interaction became possible, and this technique provides efficient numerical modeling. The accuracy of bonded particle membrane simulation was validated by visual comparison and macroscopic response analysis of numerical models in comparison to laboratory test results (Cleary 2000; O'Sullivan and Cui 2009). If the radius of membrane particles is much smaller than particle size and dimension of the sample, enormous amount of particles are necessary to simulate the membrane and the computational amount and simulation time increases significantly. However, the bonded particles are assigned with high stiffness,

and the bond also need to be strong to maintain their continuity. With the deformation of sample model, extreme stress concentration occurs between particles, large scale deformations are restrained.

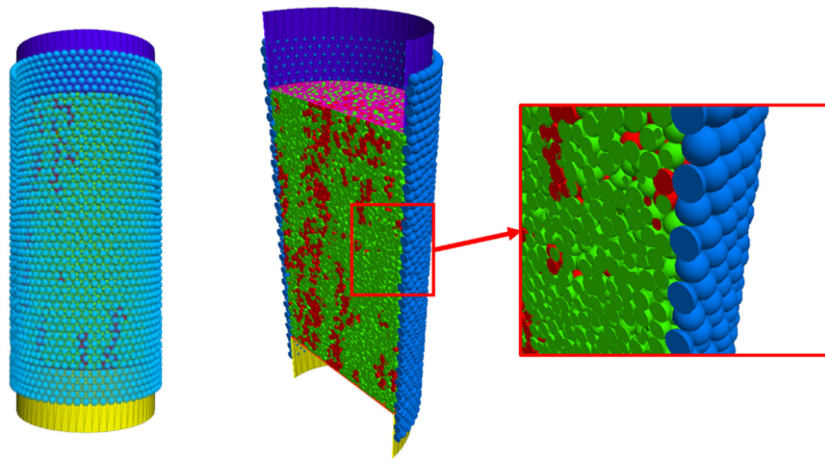


Figure 4.1 Triaxial model with membrane formed by balls

The main objective of this chapter is to develop a flexible membrane with independent wall elements for 3D conventional triaxial testing using DEM. Instead of connected membrane particles, independent wall elements are used. In contrast to a continuous rigid latex membrane, the new proposed membrane can stretch and shrink similar to a flexible membrane used during lab tests. The confining stress is uniformly applied on the surface, and a corresponding force to each wall element is calculated according to the target boundary condition. This approach involves an updating of the applied force on each membrane wall element based on the flexible nature of a rubber membrane.

4.2 Modelling

The new proposed modelling procedure of conventional triaxial loading (called ‘flexible wall approach’ = FW approach’) includes two steps:

(1) The first step comprises the sample generation. A 3-dimensional coal sample is generated and calibrated based on the process explained in previous chapters. The model is assigned with linear parallel bonds, and the geometric features of the real sample are included. At bottom and top of the sample horizontal walls are installed to apply vertical load. The numerical simulations were performed in a strain-controlled mode by specifying constant velocities at the top and bottom walls. For this purpose, only a small frictional coefficient of 0.1 was assigned to the interface between wall and top and bottom of the sample.

(2) The second step considers the confinement. Wall elements are distributed around the sample to provide the confining stress. The flexible rubber membrane is duplicated by a set of isolated wall elements, instead of one piece of cylindrical wall.

The spatial position of each wall element is determined by sets of Fish functions. In the parameter assignment file, the number of square wall units along the circumference is set to a

certain value (for instance 16 as shown in Figure 4.2). The number of wall elements along the circumference can be enlarged to increase the resolution. Coordinates of a series of points are firstly calculated, many circles of points can be assigned in space. A circle of basic triangular walls are formed by connecting two adjacent point circles. These triangular walls are generated in pairs. Each pair of wall element forms one square wall unit. By repeating this process, circular arranged wall elements are stacked together vertically to cover the entire sample as the membrane.

The cylindrical membrane should be longer than the sample to fully cover the model under any kind of deformation. Exemplary, sample model and wall elements are shown in Figure 4.2. To simulate the confinement, wall servo commands are applied to each wall element. The wall servo function is activated based on the parameter assignment.

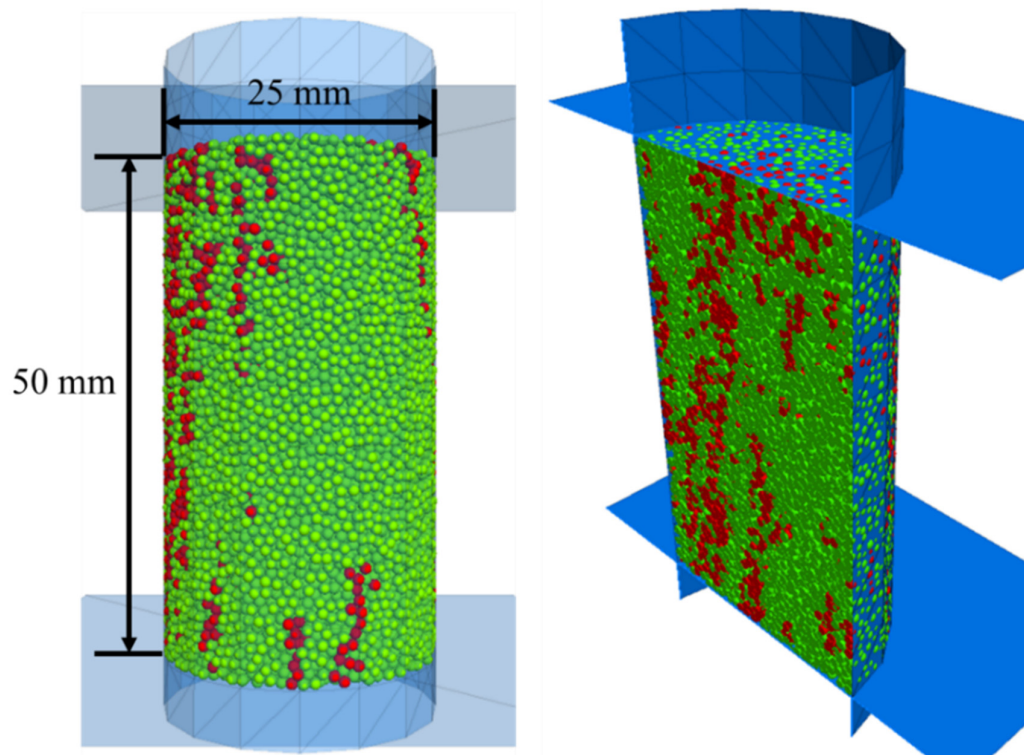


Figure 4.2 Reconstructed DEM sample with FW membrane as outer vertical boundary

Testing was performed with confining pressures of 2.5 MPa, 5 MPa and 7.5 MPa, respectively. For each wall element, the target force is calculated by the defined confining pressure multiplied by its actual area. The simulated hydraulic pressure acts on the normal direction of the wall elements. For instance, when there are 16 square units around the circumference, the confining pressure is 2.5 MPa and the edge length of the initial triangle wall is 4.8 mm, the target force on each wall is 30.21 N.

The wall elements representing the membrane are isolated from loading platens by assigning different groups. The coordinates of the vertices are permanently recorded during the simulation, which is essential for updating the confinement (position of wall corners and forces).

First, the model is run into equilibrium. Before triaxial loading, a new wall servo command is applied to the loading platens together with the confinement, and the model reaches a hydrostatic stress state first. Then loading process acts with given constant velocities of the vertical loading platens. Loading stops when residual stress value drops to 60% of the peak stress.

During the test, the model (sample) deforms continuously and the side surfaces become uneven due to the failure pattern. In this model, each wall element representing the membrane is isolated, and the dynamic state of a wall element is only determined by the wall-servo function. Deviations from the target force lead to a translational velocity on the wall elements to achieve the desired condition. Consequently, nearly constant target forces are maintained by the movement of the wall elements.

The Fish function (Fish is a code-internal program language) to update the contact force is activated every 1000 steps during the simulations, and the walls are either stretched or squeezed to maintain a closed membrane.

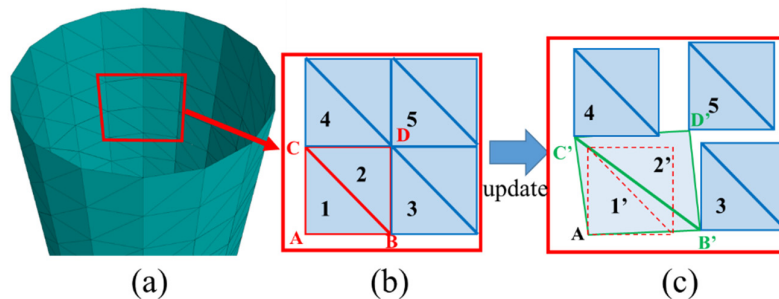


Figure 4.3 Sketch to illustrate the wall element updating process (FW approach)

Figure 4.3 illustrates the updating process for the wall elements representing the sleeve. Wall 1 and 2 consist of isosceles rectangular triangles as shown in Figure 4.3(b). Wall elements 3, 4 and 5 are the lower left triangles from the right unit (r), upper unit (u) and diagonal/opposite unit (o), respectively. Point B, C and D are the lower left vertices of wall elements 3, 4 and 5, respectively. After several steps, the wall elements move to new positions as shown in Figure 4.3(c) and the triangles 1 and 2 are stretched and become triangles 1' and 2' with the new vertices B', C' and D'. All the wall elements are adjusted according to the same rule, so that the confining structure is kept continuously updated to duplicate the deformed membrane.

When a wall is updated to a new shape, the wall area also changes because of the deformation. Constant target force is no longer correct for the new situation. According to the applied FISH function, the area of each wall unit is calculated again after stretching or squeezing, and a new target force (equivalent to the confining pressure) is applied. By running these functions, the overall confinement remains constant even if significant deformations occur.

The parameters of the wall-servo function affect the results, because the target forces on each wall element were updated automatically by Fish functions. Therefore, the maximum velocity of the wall units should be slightly larger than the loading velocity, and the gain factor should

also be adjusted to react to the deformation immediately. The codes of this function is shown in Appendix A1.

Exemplary, triaxial simulation results of sample C1 are shown in Figure 4.4 for confining pressures of 2.5 MPa. Formed fracture networks in each stage are also shown (shear and tensile cracks are represented by red and green disks, respectively). The final deformed membrane is plotted as a group of continuous smooth wall elements.

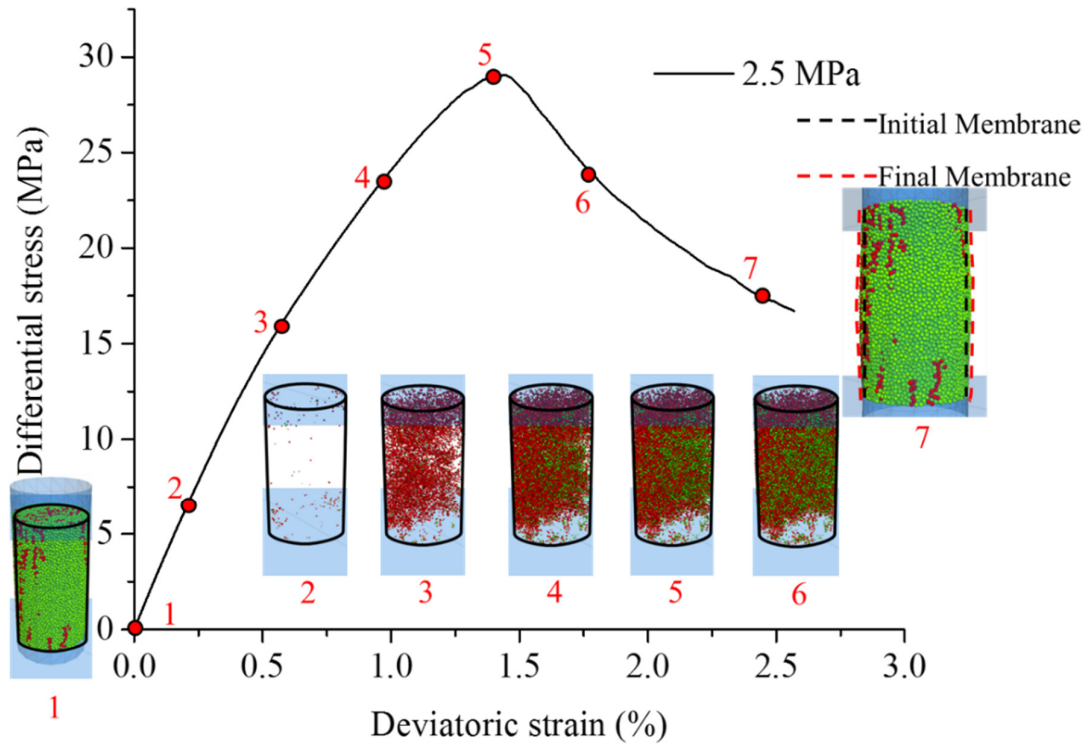


Figure 4.4 Simulated stress-strain curves and crack evolution for coal sample C1 with 2.5 MPa confining pressure using the FW approach

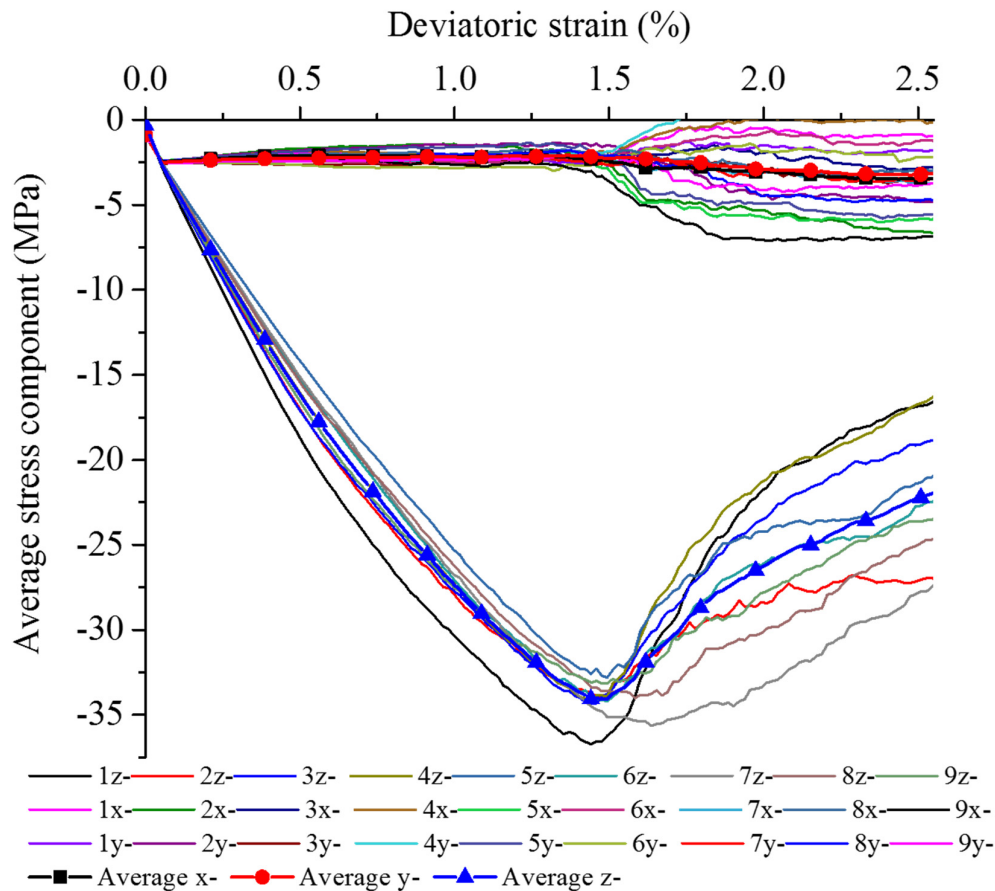


Figure 4.5 Average stress components in z-, x- and y-directions for each measure region (negative stress values represent compression)

Based on the given boundary conditions, the average (overall) state within the sample is assumed to be homogeneous to fulfill the force equilibrium. According to equilibrium, average vertical and horizontal stresses inside the sample should be consistent with applied boundary conditions. This criterion is used to validate the simulation results. Spherical measure regions have been created to check if boundary conditions and average horizontal stress - assuming constant confinement - remain constant, and that fluctuations which happen after reaching peak differential stress as shown in Figure 4.5 are small.

The final deformed state of the reconstructed samples C1 and C2 under 2.5 MPa confining pressure are shown in Figure 4.6. Extreme cases have been tested including models composed of different layers, where mechanical parameters in different layers have huge differences. The confining membranes remain closed even in case of large non-uniform deformations. The boundary conditions are well maintained.

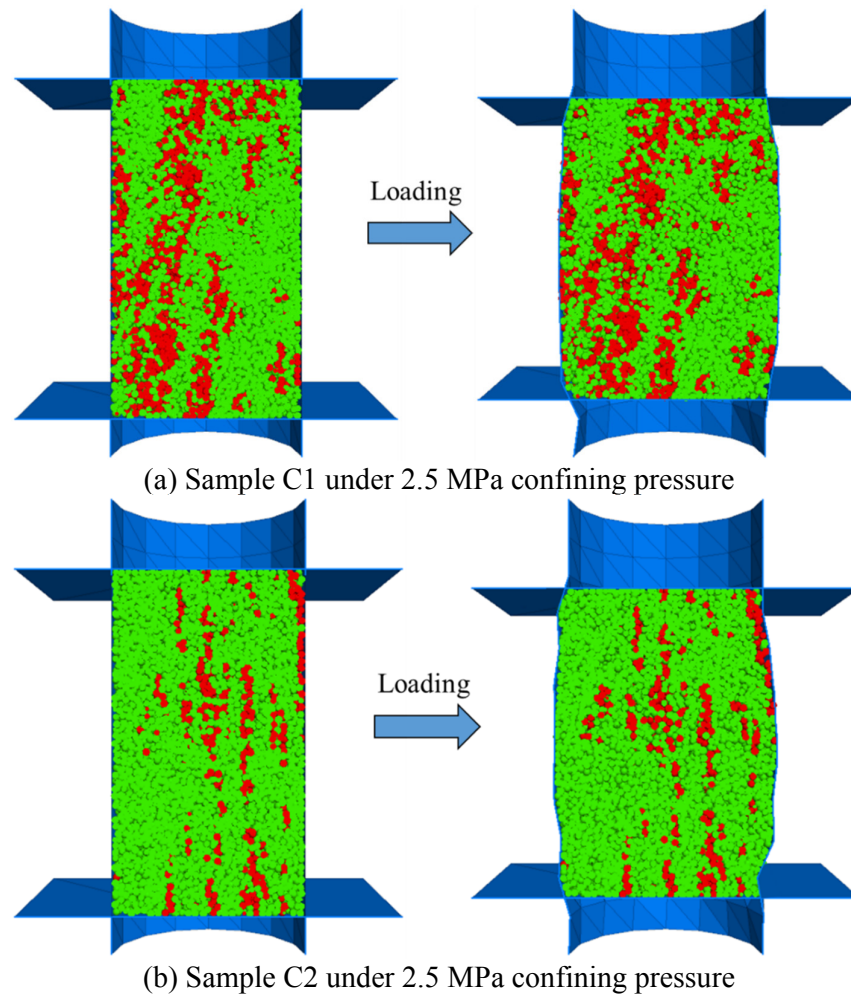


Figure 4.6 Cross-section of samples before and after 3-axial compression simulation

4.3 Calibration and verification

The mechanical parameters are calibrated primarily by uniaxial compression simulations. Later triaxial compressive conditions are used for further modifications of the parameters. Some basic relationships between the micro-mechanical parameters and macroscopic behavior are given by Kazerani and Zhao (2010) and Lan et al. (2010). This calibration process is based on previous researches, and modified to fit the laboratory results. Parallel bond contact is applied between particles in this work.

Realistic coal sample models consist of matrix and inclusions. Each component was calibrated with designed calibration routines. Due to the co-existence of both components more detailed calibrations have to be performed.

In order to perform the calibration, a series of microscopic mechanical parameters were considered in the numerical model, such as bond elastic modulus (pb_emod), normal to shear stiffness ratio ($kratio$), tensile and shear strength and friction angle (pb_fa). Some parameters have cross effects with each other on the macroscopic parameters, such as Poisson's ratio, peak

strength and failure patterns. Thus, a specific calibration methodology is proposed to overcome this cross dependency.

The hydraulic conditions were not considered during this process, only dry samples under uniaxial compression were considered in the calibration phase. Three cylindrical samples with diameter of 25 mm and length of 50 mm were selected from all samples and used as reference. Uniaxial compression tests in the laboratory have been performed and compressive elastic moduli, Poisson's ratios and UCS of each sample were obtained. The average UCS of the three samples is 14.97 MPa as shown in Table 4.1.

Table 4.1 Physical and mechanical parameters of coal samples obtained from uniaxial compression tests

Nr.	H (cm)	D (cm)	V (cm ³)	m (g)	ρ (g/cm ³)	σ_c (MPa)	E (GPa)	ν
C21	5.060	2.550	25.84	37.20	1.44	16.28	2.73	0.37
C22	5.080	2.553	26.00	37.28	1.43	13.08	2.21	0.34
C23	5.086	2.550	25.97	37.57	1.45	15.55	2.17	0.35
Average	5.075	2.551	25.94	37.35	1.44	14.97	2.37	0.35

According to experience, the parallel bond effective modulus (pb_emod) and the elastic modulus are proven to follow a linear relationship. The ratio of normal to shear stiffness ($kratio$) and the macroscopic Poisson's ratio show a logarithmic relationship in the elastic stage. The ratio of tensile to shear strength ($sratio$) influences the deformation pattern. When $sratio$ is fixed, the macroscopic strength changes linearly with the values of tensile and shear strength. Friction angle (pb_fa) has no significant effect before simulated samples reached peak strength, but it affects the ratio of tensile to shear cracks ($cratio$). These rules are adapted in this chapter to guide the calibration process. The following steps are performed to calibrate the mechanical parameters:

(1) In the first step, the linear group elastic modulus ($emod$) is analyzed. A default linear model has been assigned to all elements when generating the model. Then it has been replaced by parallel bond model between particles during the bonding phase. The linear group type is activated again only after the failure of the parallel bond group, so $emod$ has the same value as pb_emod . $kratio$ is also assigned the same value as pb_kratio in the parallel bond group.

(2) In the second step, the contribution of pb_emod to the macroscopic compression modulus is investigated. pb_emod and $emod$ have been assigned the same value. So the uniaxial compression is simulated to calibrate both, pb_emod and $emod$. Different pb_emod and $emod$ are introduced with predefined intervals, and all other parameters are set to relatively high values. The stress-strain curves and deformation patterns are shown in Figure 4.7. The relationship between elastic modulus and pb_emod is illustrated in Figure 4.8.

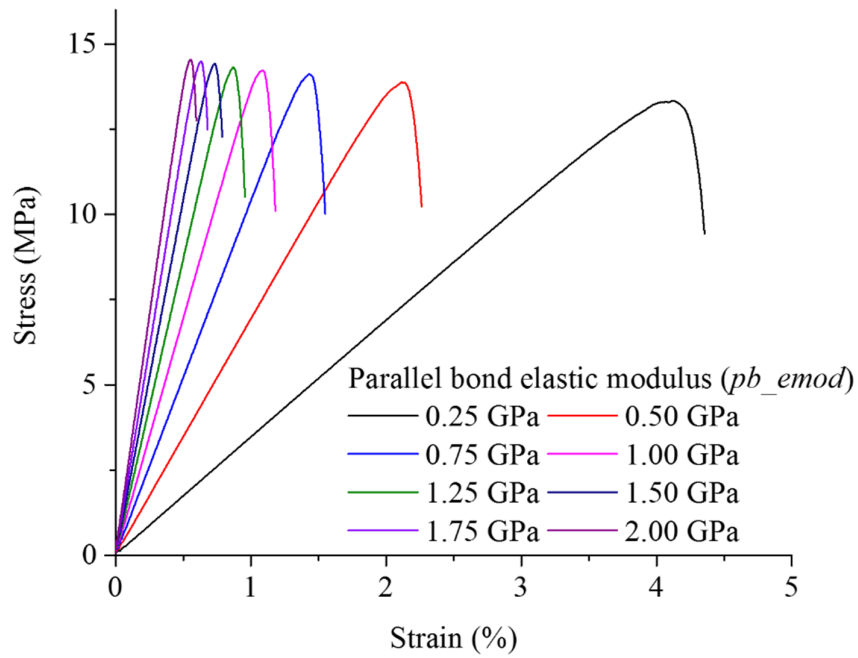


Figure 4.7 Stress-strain curves of uniaxial compression simulations with different pb_emod

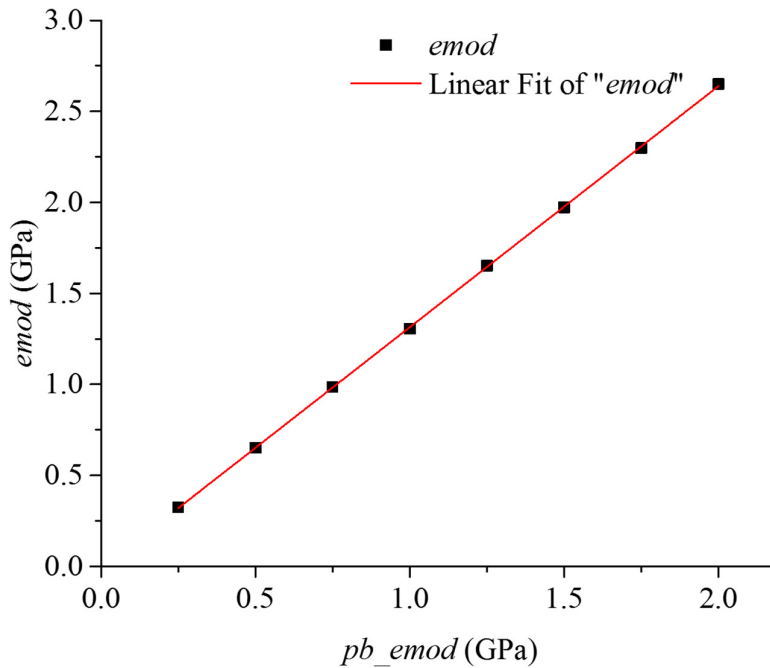


Figure 4.8 Relationship between compressive elastic modulus and parallel bond group elastic modulus

The fitting equation in Figure 4.8 is shown below:

$$E_c = 1.32524x - 0.01081 \quad (R^2 = 0.999) \quad (\text{Equation 4.1})$$

in which: E_c is compressive elastic modulus (GPa); x is the value of $emod$ (GPa). A typical tested elastic value of 2.2 GPa is substituted into Equation 4.1, then x is found to be 1.67. So $emod$ and pb_emod are assigned 1.67 GPa. The value of pb_emod is verified with direct tensile simulations. Other parameters are assigned with relative high value, the target elastic modulus of tension can be matched mostly. After this step, only uniaxial compression simulations are performed for calibration.

(3) In the third step, $kratio$ and macroscopic Poisson's ratio are established. $emod$ and pb_emod are fixed. $kratio$ and pb_kratio are assumed to be the same. Uniaxial compression simulations are performed with different pb_kratio , e.g. 3.0, 6.0, 9.0, 12.0, 15.0 and 18.0.

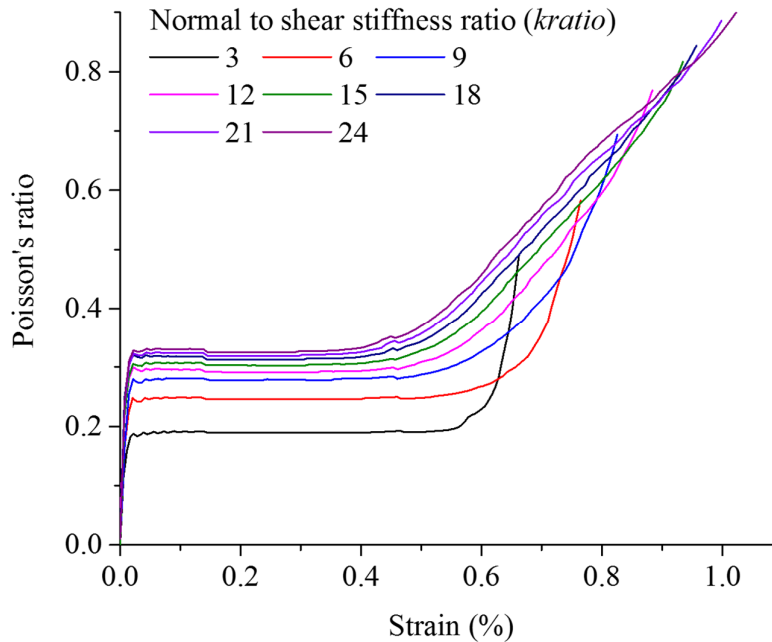


Figure 4.9 Relationship between Poisson's ratio and axial strain for different pb_kratio under uniaxial compression

The Poisson's ratios at different axial strains have been calculated for each model. The trend curves are shown in Figure 4.9. The fitting relationship can be seen in Figure 4.10, and the fitting equation is shown below:

$$\nu = 0.1810 + 0.0473 \ln(x - 1.7940) \quad (R^2 = 0.998) \quad (\text{Equation 4.2})$$

in which: ν is the macroscopic Poisson's ratio; x represents $kratio$. If the measured Poisson's ratio of 0.3 is inserted into Equation 4.2, $kratio$ and pb_kratio are obtained to be 14.65.

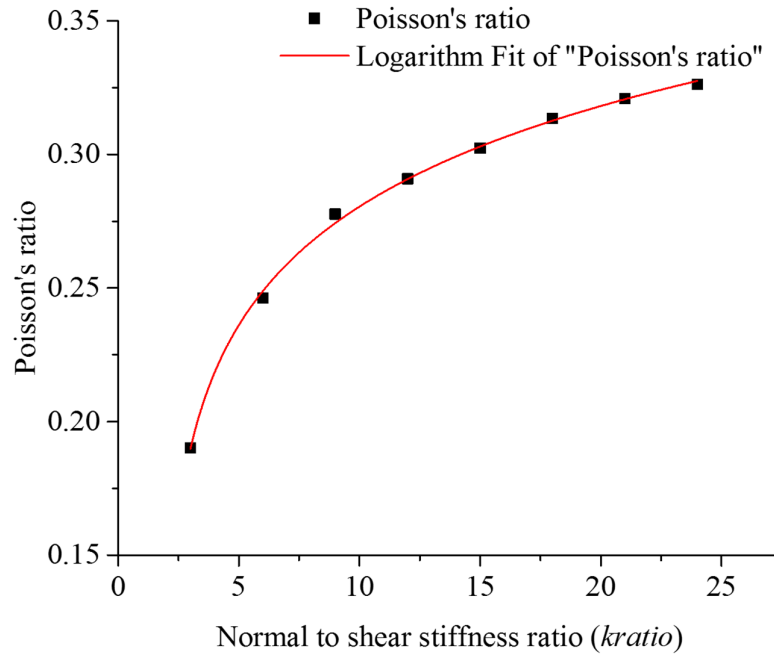


Figure 4.10 Relationship between Poisson's ratio and normal to shear stiffness ratio under uniaxial compression

(4) In the fourth step, s_{ratio} is investigated. With fixed e_{mod} , pb_{emod} , $kratio$ and pb_{kratio} , different normal to shear strength ratios have been proven to affect the deformation patterns. The particle bonds are assigned by pb_{emod} , pb_{kratio} , tensile strength (pb_{ten}), cohesion (pb_{coh}) and friction angle (pb_{fa}). The shear bond strength is not modifiable directly in the simulation, but is set via pb_{ten} and pb_{coh} .

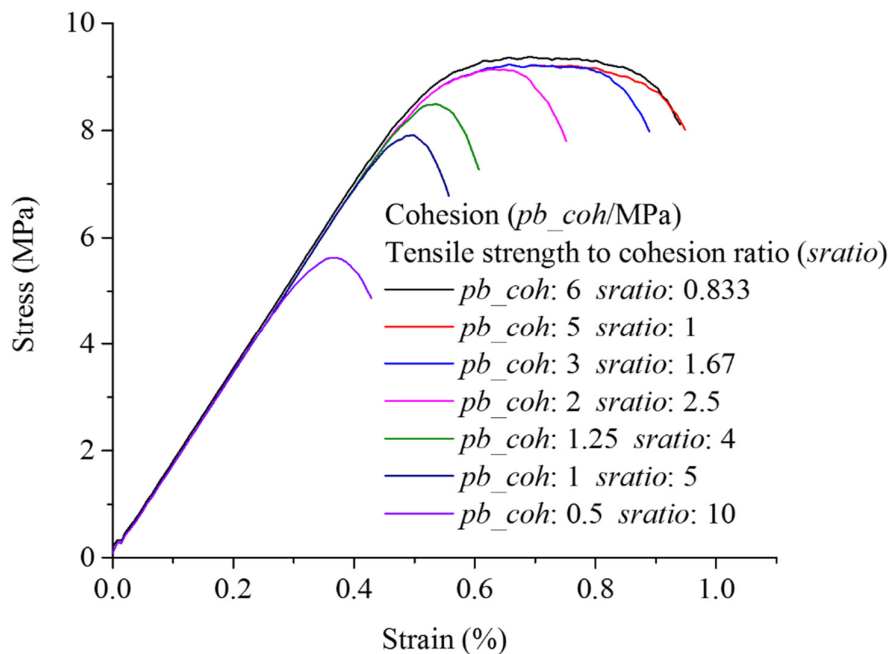


Figure 4.11 Stress-strain curves for different ratios between tensile strength and cohesion (uniaxial compression tests)

For all simulations shown in Figure 4.11, pb_ten is set to 5 MPa and cohesion ranges from 0.5 to 6 MPa. The models tend to fail with more shear cracks with high $sratio$, and more tensile cracks occur easily with low $sratio$. Based on a comparison with the lab test results, this $sratio$ is estimated to be between 1 and 5. $cratio$ and deformation patterns are shown in Figure 4.12. $sratio$ is constant for one specific material, so 4 and 5 are chosen for further calibration.

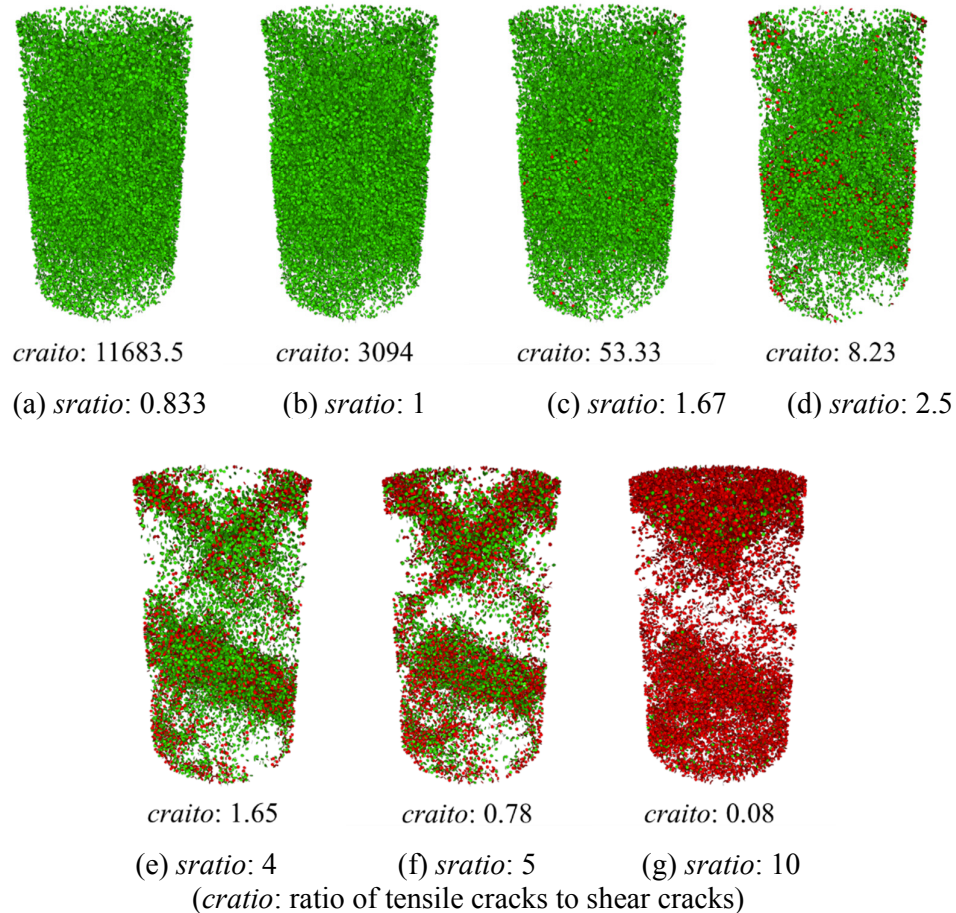


Figure 4.12 Damage patterns for uniaxial loaded models with different ratios of tensile strength to cohesion (tensile cracks: green disks; shear cracks: red disks)

When all the previous mentioned parameters are kept constant, the dilatancy behavior of the numerical model is controlled by the inter-particle friction angle. After choosing the proper friction angle, the relationship between strength values are also determined. According to the failure envelope, pb_fa follows the relation shown in Equation 4.3. pb_fa affects the failure types of the bonds before peak stress is reached. It has significant influence on damage and deformation pattern after peak stress.

$$0 \leq \tan \bar{\Phi} \leq \bar{c} / \bar{\sigma}_c \quad (\text{Equation 4.3})$$

in which: $\bar{\Phi}$ is the parallel-bond group friction angle, \bar{c} is cohesion and $\bar{\sigma}_c$ is uniaxial tensile strength. *sratio* is set to 4 and 5 one after another, and then friction angle is set between 0° and 21° .

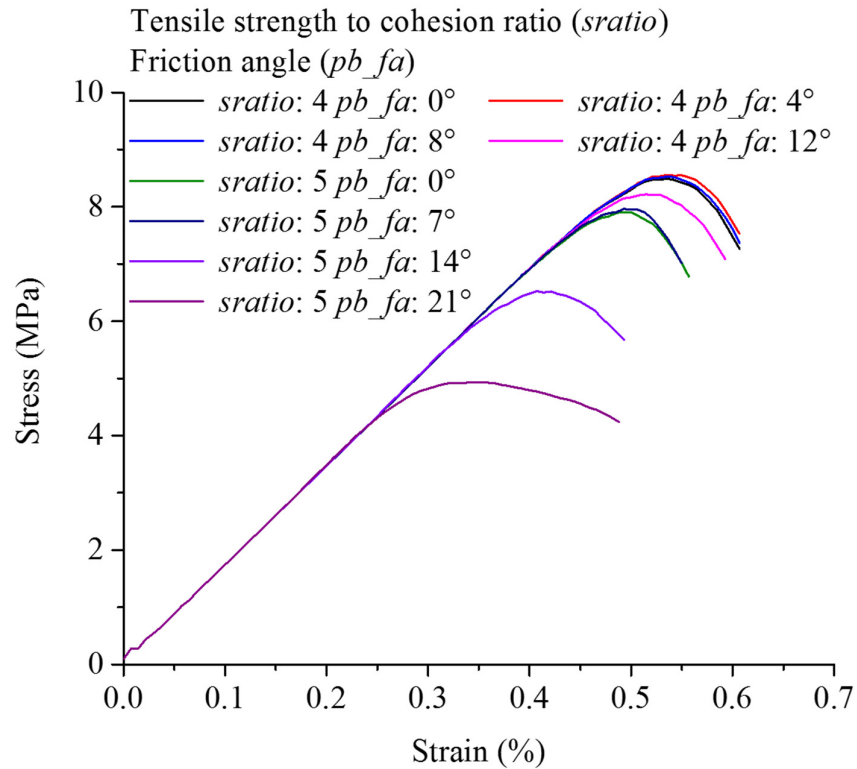


Figure 4.13 Stress-strain curves for different friction angles (uniaxial compression tests)

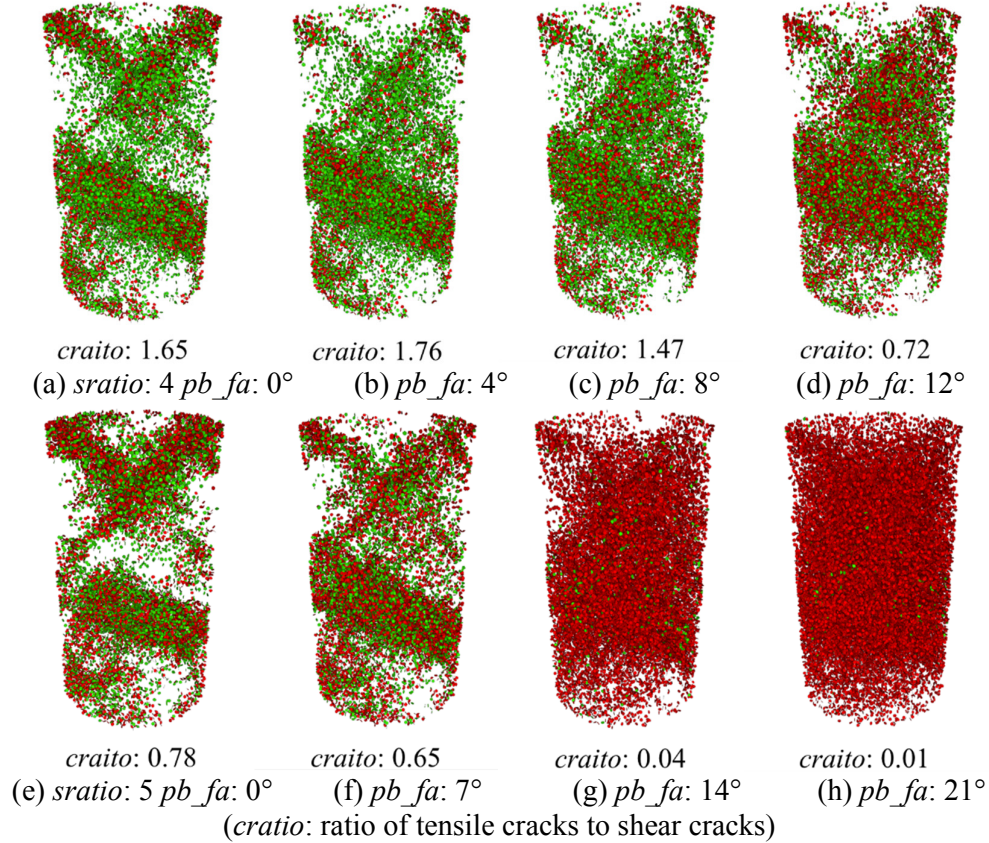


Figure 4.14 Damage patterns for uniaxial loaded models with different friction angles (tensile cracks: green disks; shear cracks: red disks)

A series of simulations are performed with fixed strength ratios, and *pb_fa* in each model is set to 0°, 4°, 7°, 8°, 12°, 14° and 21°, respectively (see Figure 4.13). As shown in Figure 4.14, when *sratio* is 4 and *pb_fa* is 4°, crack distribution and post-peak stage can be better represented.

(5) In the fifth step, a reference tensile strength of 2.5 MPa is defined. Then the reference cohesion is set to 0.625 MPa. In the simulations, an extra expansion coefficient is multiplied with the reference strength. With different expansion coefficients, a series of peak stresses are obtained for uniaxial compression simulations. The coefficient is set to 1, 2, 3, 4, 5 and 6, respectively. The complete stress-strain curves are shown in Figure 4.15, and the relationship between peak stresses and expansion coefficient is shown in Figure 4.16.

The fitting Equation 4.4 is shown below:

$$\sigma_c = 3.9478x + 0.6444 \quad (\text{Equation 4.4})$$

$$(R^2 = 0.999)$$

in which: σ_c is uniaxial compressive strength (MPa); x is the strength expansion coefficient. Based on the macro parameters $\sigma_c = 15$ MPa, x is 3.64. So the normal strength and shear strength were set to 9.09 MPa and 2.28 MPa respectively.

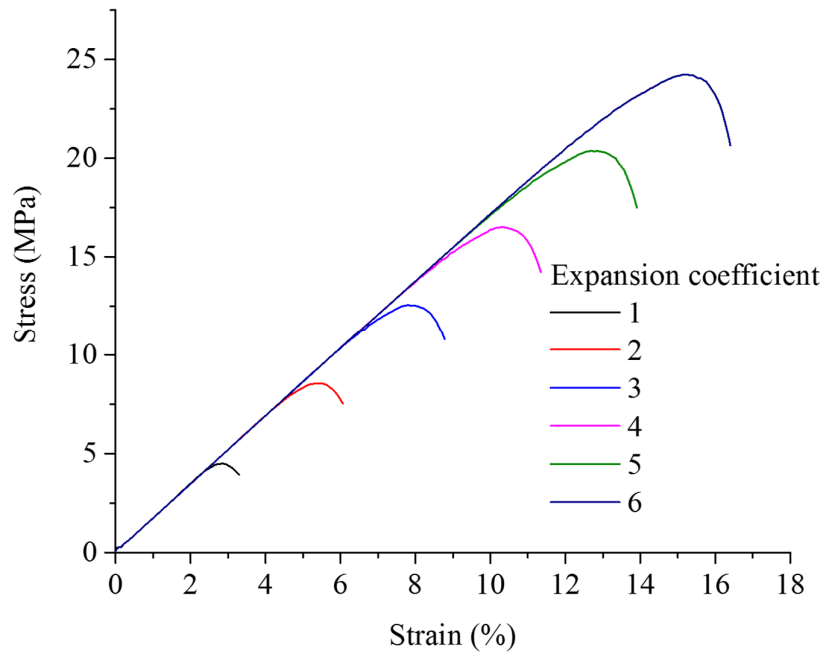


Figure 4.15 Stress-strain curves with different expansion coefficients (uniaxial compression tests)

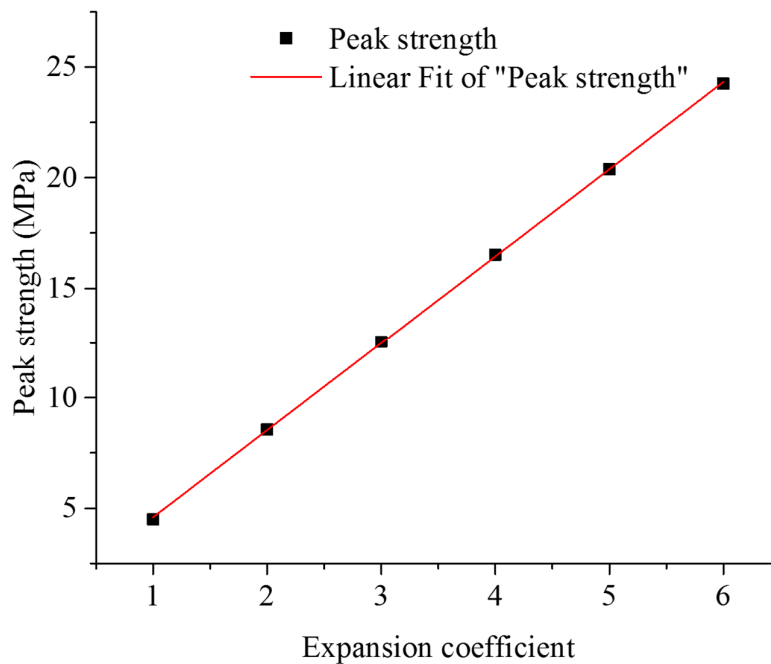


Figure 4.16 Relationship between peak stress and strength expansion coefficient (uniaxial compression tests)

(6) In the last step, the parameters are slightly modified according to the real simulation conditions. After previous steps, uniaxial compression tests and tensile tests are performed to

verify the mapping rule of the microscopic parameters. There are internal relations among all these parameters.

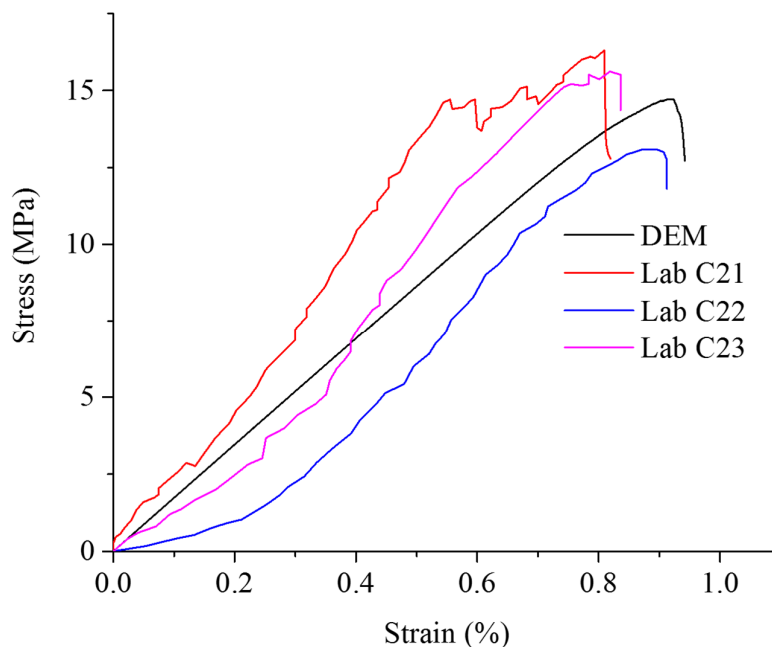


Figure 4.17 Stress-strain curves for lab tests and numerical model after calibration

Therefore, minor adjustments are essential, especially when parallel bond method is used. If the tensile strength is calibrated with uniaxial compression, the uniaxial tensile strength of the model is 20% to 30% of the compressive strength. This value is higher than the average compressive to tensile strength ratio of real rock and concrete materials, which is between 0.1 and 0.2. By reducing the gap interval (gap), fewer contacts are activated, so the general strength is reduced, and vice versa. The stress-strain curve of the calibrated model for uniaxial compression test is shown in Figure 4.17. The mechanical parameters assigned for the uniaxial compression model are shown in Table 4.2.

Table 4.2 Mechanical parameters of PFC^{3D} model

Model Element	Parameter	Coal matrix
Particles	N	34608
	r_p (mm)	0.5
	ρ_p (kg/m ³)	1390
Contacts	E (GPa)	1.67
	K^*	14.65
	$\bar{\sigma}_c$ (MPa)	9.09
	\bar{c} (MPa)	2.28
	$\bar{\mu}_c$	0.4
	$\bar{\Phi}$ (°)	4
	\bar{g}_c (mm)	0.05
	Loading velocity	
Walls	v (m/s)	0.01

The parameters of the inclusions (kaolinite) are also calibrated by the same method according to the mechanical properties given in literature (Mahabadi et al. 2012; Randall et al. 2009; Zhao et al. 2010a). The measured physical and mechanical parameters of the matrix (coal) and the inclusions (kaolinite) are shown in Table 4.3.

Table 4.3 Physical and mechanical parameters of realistic coal sample (Zhao et al. 2010a)

Groups	ρ (g/cm ³)	E (GPa)	ν	σ_t (MPa)	C (MPa)	Residual cohesion C_{res} (MPa)	Initial friction angle θ (°)	Residual friction angle θ_{res} (°)
Matrix	1.3	2.37	0.35	0.23	1.13	0.11	35.0	30.0
Inclusion	1.8	16.0	0.18	1.11	6.45	--	34.6	--

After some testing, it was found that the difference between assigned stiffness ratios (pb_kratio) of matrix and inclusion lead to poor synchronous expansion of the components. Splitting was observed inside the model and the Poisson's ratio of the sample model became significantly higher than that of both components. Therefore, the stiffness ratios (pb_kratio) of both material groups, especially the inclusion, were adjusted again to fit the lab test results.

The parameters calibrated under uniaxial compression may not suitable also under triaxial compression, because the behavior is heavily affected by the confinement. Under such a 3-dimensional stress field, the samples appear to have much higher macroscopic elasticity and peak compressive strength. The gas saturation may also reduce the overall strength of the sample model to a limited extent.

The mechanical parameters assigned in PFC^{3D} for 3-axial testing are shown in Table 4.4.

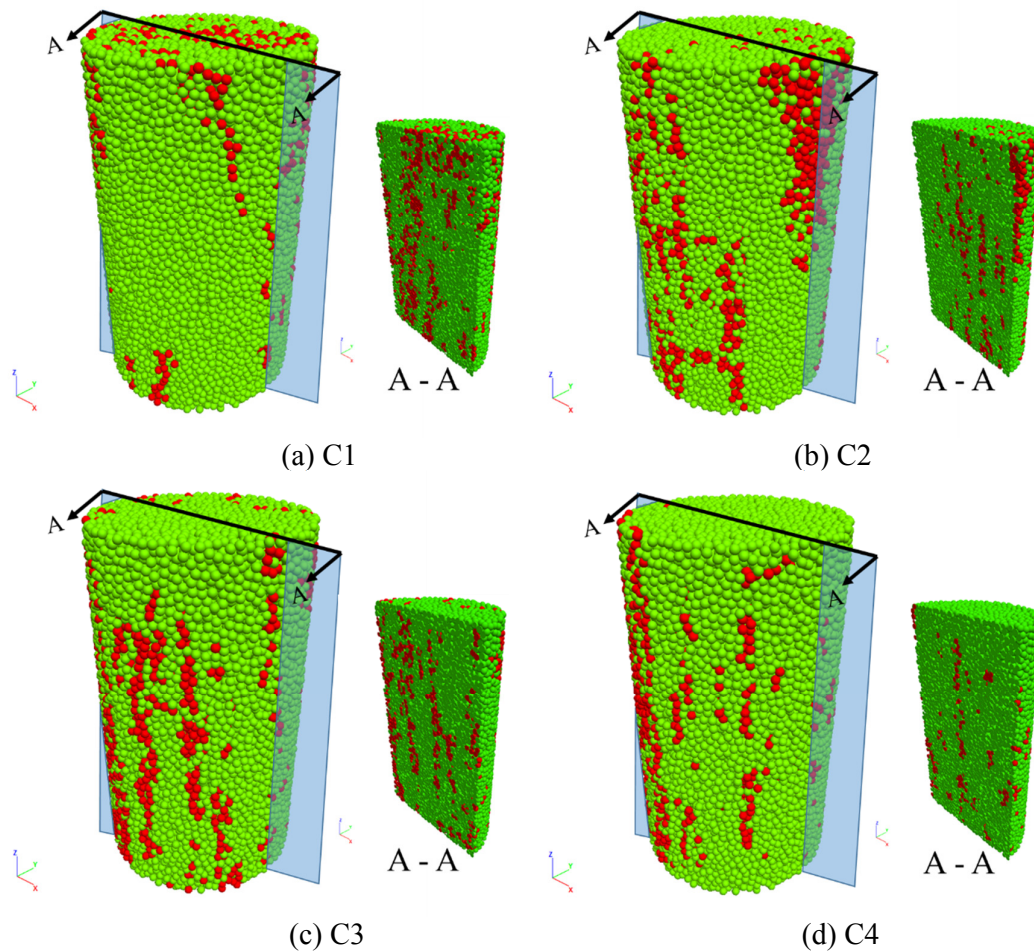
Table 4.4 Micro-mechanical parameters of the numerical coal model

Element	Parameter	Coal matrix	Mineral inclusion	Boundary between matrix and inclusion
Particles	N	27390	7218	--
	r_p (mm)	0.5	0.5	--
	ρ_p (kg/m ³)	1390	1810	--
Contacts	E (GPa)	2.09	2.84	1.90
	K^*	14.65	2.44	1
	$\bar{\sigma}_c$ (MPa)	17.40	30.50	11.60
	\bar{c} (MPa)	4.35	12.20	5.8
	μ_c	0.4	0.4	0.4
	Φ (°)	4	7	8
	g_c (mm)	0.05	0.05	0.05
Axial loading control				
Walls	ν (m/s)	0.005		
Confinement control				
Walls	Gain relaxation factor	0.1		
	Maximum velocity v_{max} (m/s)	0.01		

4.4 Sample reconstruction for modeling

As mentioned in previous chapters, coal samples have been reconstructed based on CT technique. Five samples are used to simulate triaxial tests. These five samples C1, C2, C3, C4 and C5, were generated according to the geometrical structure of real core samples.

The internal structures incl. the different components are shown in Figure 4.18 and Table 4.5. As the figures illustrate, there are significant differences in the internal structure of these five samples. The amount of inclusions in samples C1 and C3 are obviously higher than those in samples C2, C4 and C5. The inclusions, presented by red particles, have higher strength than the matrix as mentioned previously. The inclusions in C1 (shown in Figure 4.18(a)) are distributed parallel to the axis of the sample. On the contrary, the inclusions in C4 and C5 (shown in Figure 4.18(d) and (e)) are located isolated near the boundary surface in the central part and gathered at the top end, respectively. Especially in C4, both ends of the sample are composed of matrix particles, no large volume of inclusion has been monitored in this model.



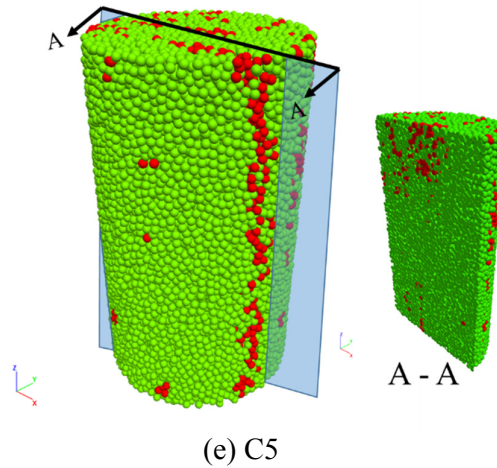


Figure 4.18 Reconstructed numerical models of coal samples (green: coal matrix, red: inclusions)

Table 4.5 Composition of coal samples

Samples	Composition proportion	
	Matrix	Inclusions
C1	80.12%	19.88%
C2	86.06%	13.94%
C3	79.06%	20.94%
C4	89.90%	10.10%
C5	90.20%	9.80%

The micro-mechanical parameters for the triaxial tests were calibrated using the experimental results of test with sample C1 and 2.5 MPa confining pressure. The calibrated parameters were also used to run the simulations of C3 with 5.0 MPa and C5 with 7.5 MPa for validation. Figure 4.19, 4.21 and 4.23 show the results of 3-dimensional triaxial numerical simulations using the FW approach in comparison with the corresponding laboratory tests. Minor fluctuations are shown in the numerical simulation results, because the movement of mono-sized spherical particles has caused relatively large overlaps between particles and loading walls occasionally. Good agreement has been achieved between numerical simulations and laboratory experiments. The differential stress reaches a nearly constant value in the post-failure region until the end of the simulation. The initial slope in the elastic stage and the trend of residual strength observed during laboratory tests are well reproduced by the numerical model using the FW approach.

Meanwhile, a model with traditional balls as membrane is also simulated for comparison (see Figure 4.1). The result is plotted in Figure 4.19. Same parameters are assigned to the numerical model, but the observed strength is significantly lower than using the FW approach. The force applied on each ball element is constant during the simulation. With this classical technique, the deformation of the sample cannot be transmitted to proper updated boundary conditions. Therefore, this method has some significant limitations. On the other side, the model with FW approach is able to follow realistic sample deformations.

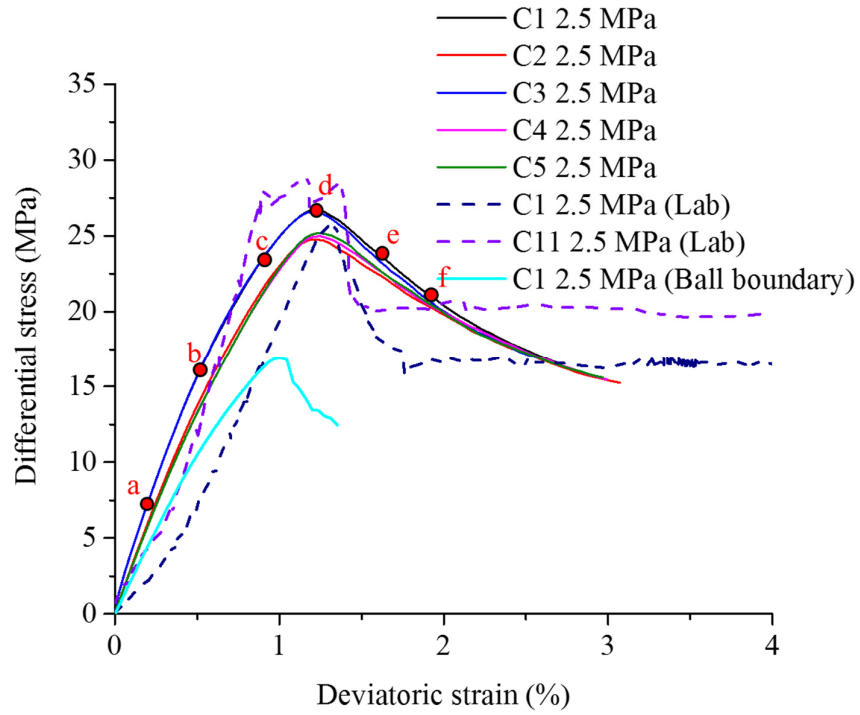
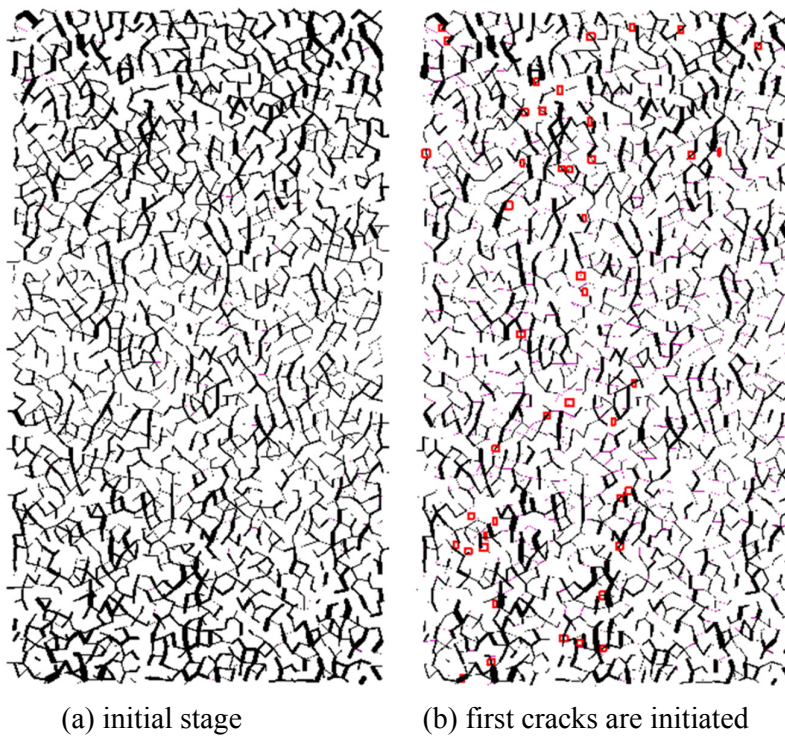


Figure 4.19 Stress-strain curves of numerical simulations and laboratory tests with 2.5 MPa confining pressure



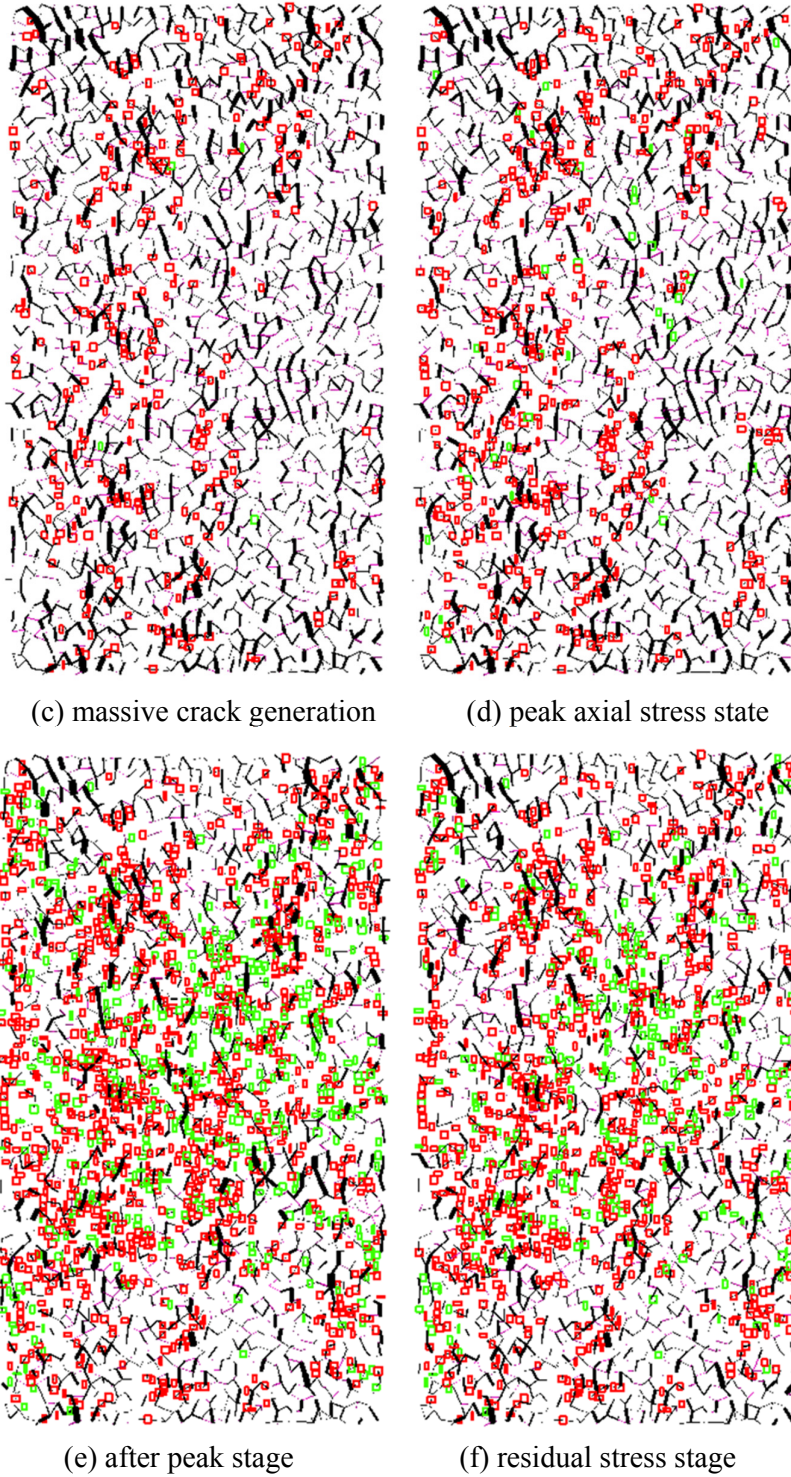


Figure 4.20 Contact force chains with cracks for numerical model C1 with 2.5 MPa confining pressure in cross-sectional perspective (shear cracks: red, tensile cracks: green)

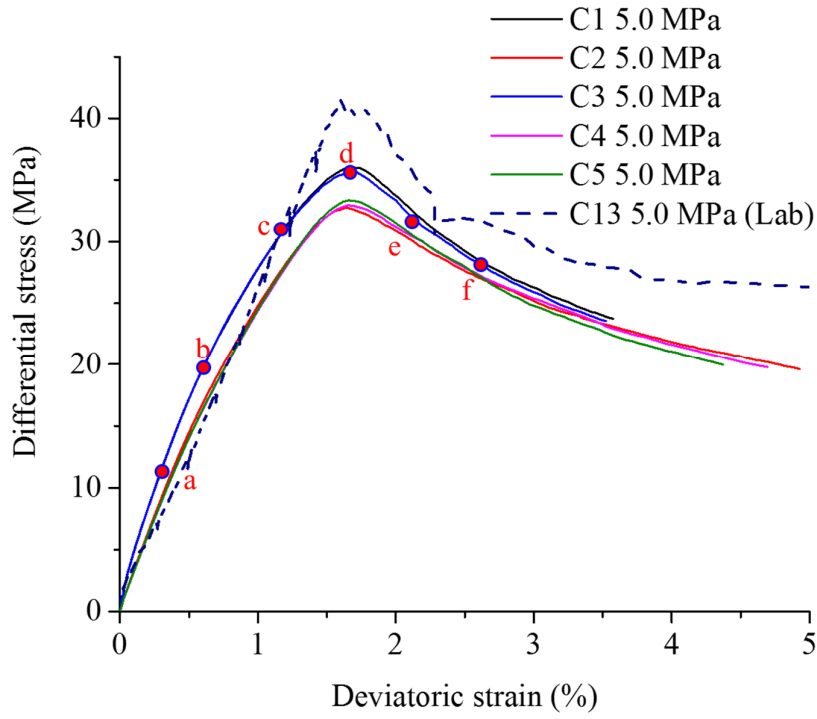
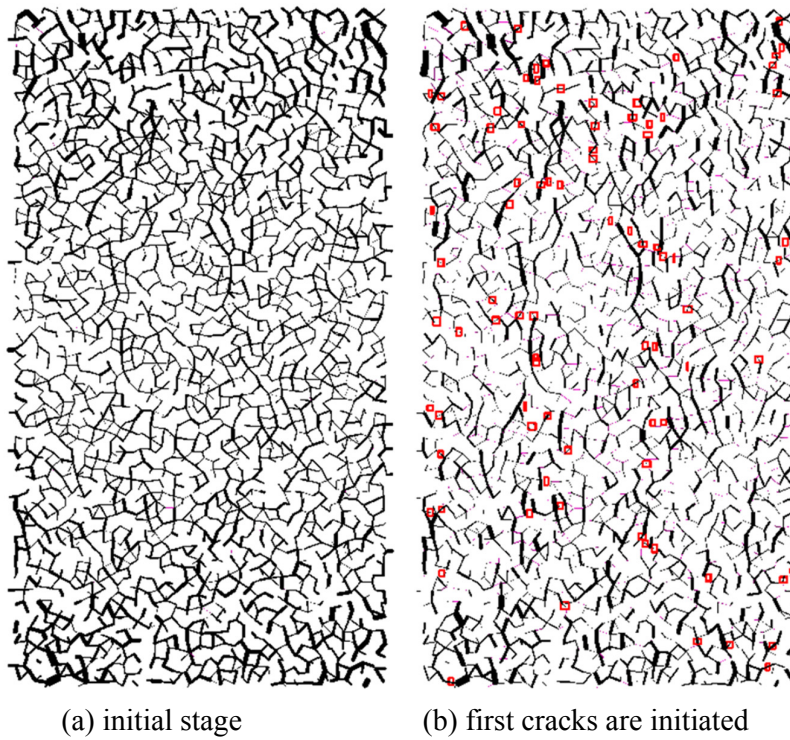


Figure 4.21 Stress-strain curves of numerical simulations and laboratory tests with 5.0 MPa confining pressure



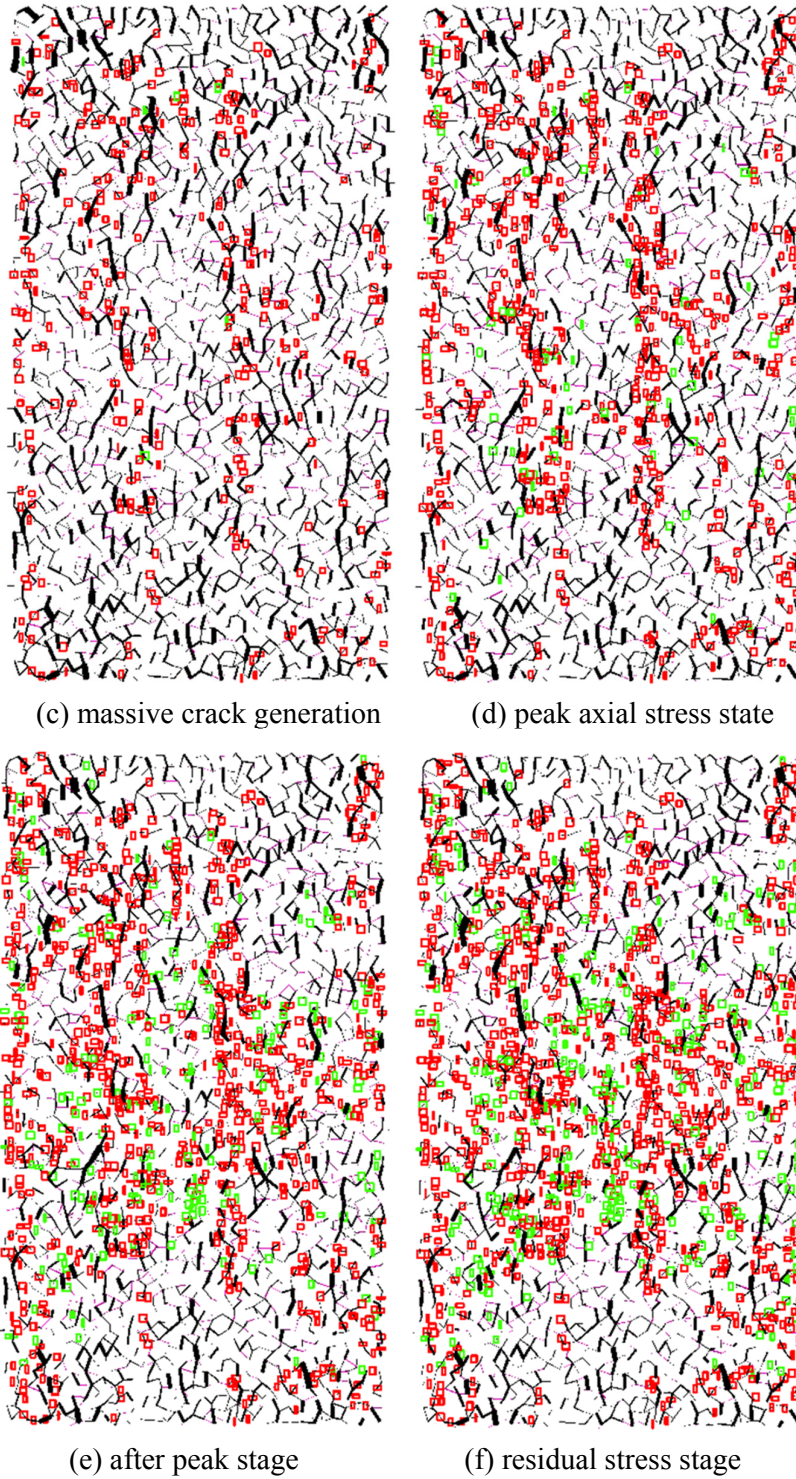


Figure 4.22 Contact force chains with cracks for numerical model C3 with 5.0 MPa confining pressure (shear cracks: red, tensile cracks: green)

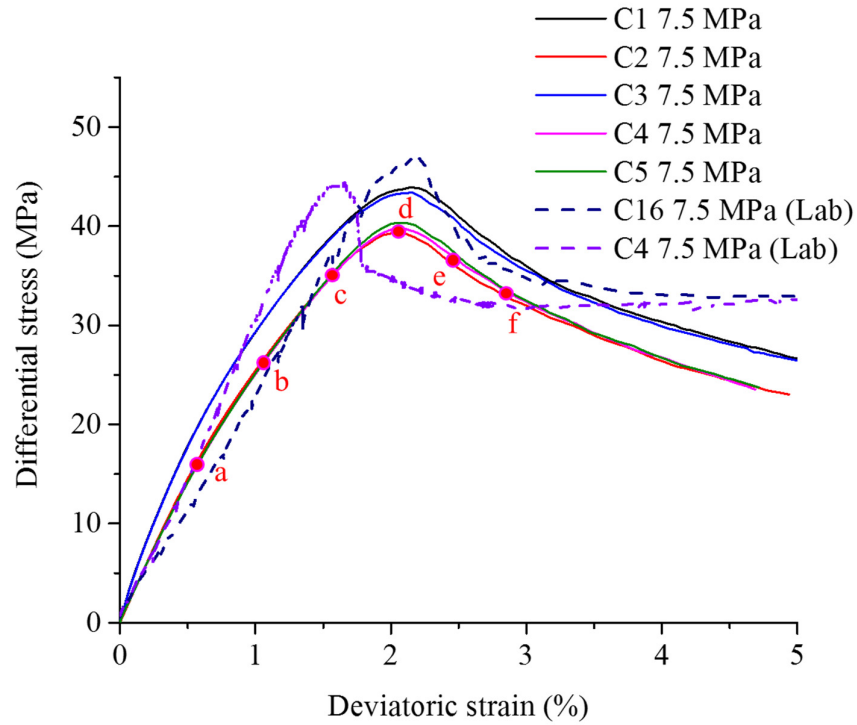
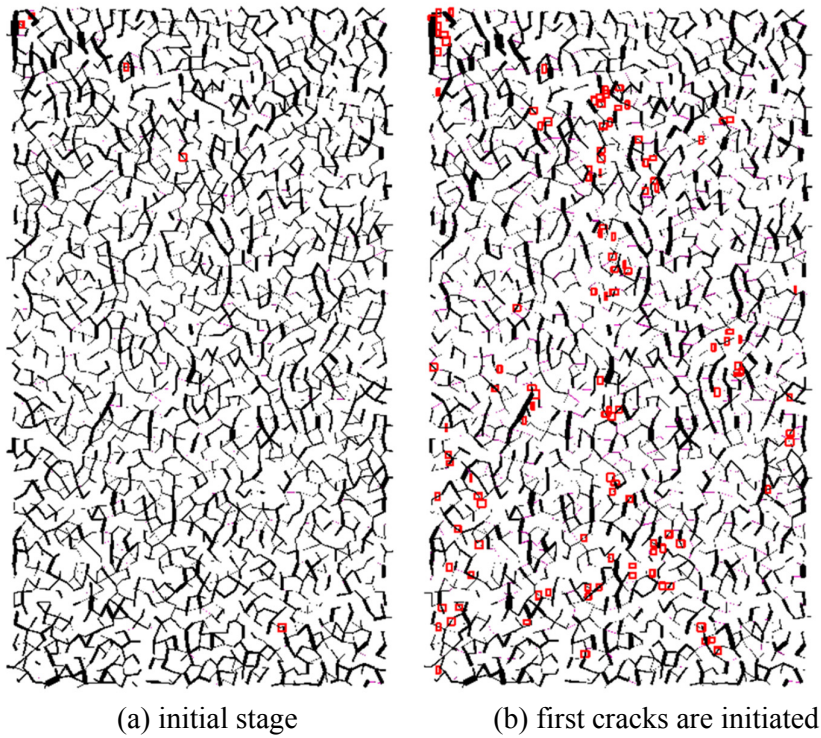


Figure 4.23 Stress-strain curves of numerical simulations and laboratory tests with 7.5 MPa confining pressure



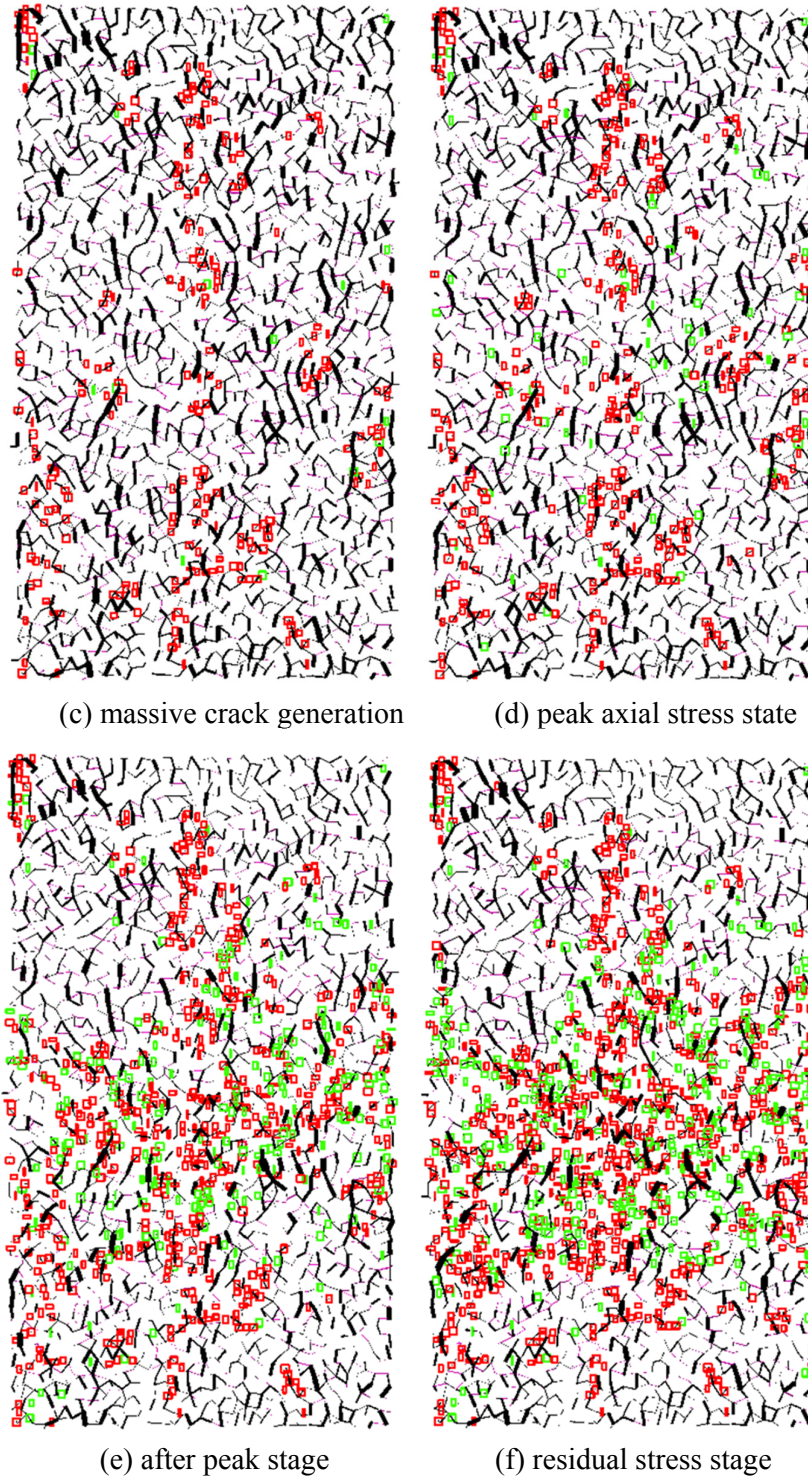


Figure 4.24 Contact force chains with cracks for numerical model C4 with 7.5 MPa confining pressure (shear cracks: red, tensile cracks: green)

4.5 Discussion of results

The numerical simulation of triaxial compression tests allows analyzing fracture propagation and failure pattern. Differential stress and number of triggered microcracks have been recorded

as well as the evolution of internal force chains. This provides insight from the microscopic perspective. Not only the heterogeneity in mineral composition, but also the distributions of inclusions and contacts between grains have influence on crack initiation and propagation.

With different magnitudes of confining pressure, the peak strength deviates significantly. The triaxial results for one specific bonded model C1 are shown in Figure 4.25 for confining pressures of 2.5, 5.0 and 7.5 MPa (the samples are loaded initially isotropic until desired confining pressure value is reached). In agreement with the experimental data, higher maximum differential stresses are strongly associated with higher confining pressures. The corresponding strain values at peak stress also increase with higher confining pressures.

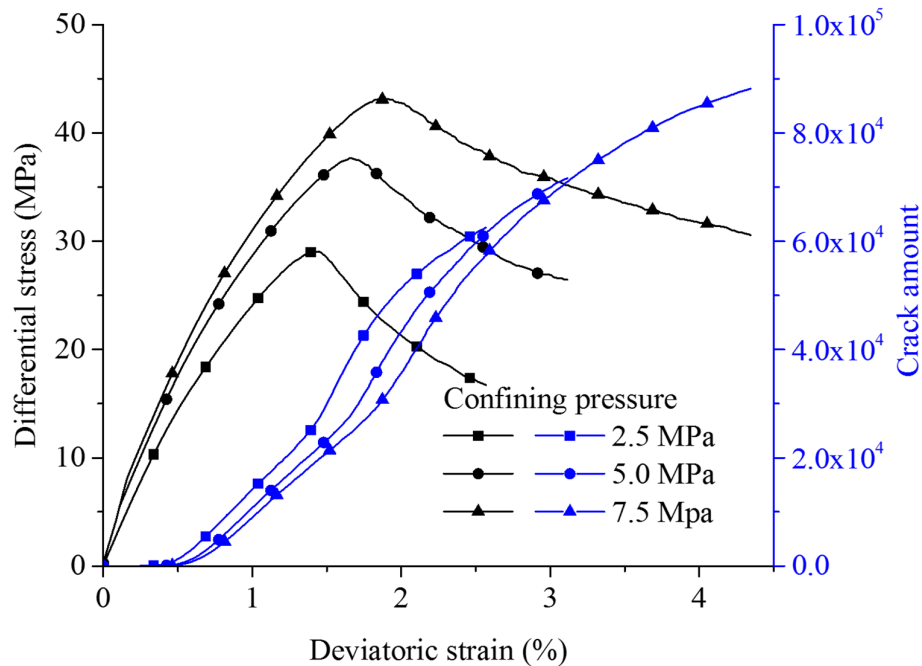


Figure 4.25 Differential stress and amount of cracks for model C1 versus axial strain during deviatoric regime for different confining pressures

Number of induced cracks increased drastically when axial stress reached about 30 to 40% of the peak value, and increases again slightly at peak stress. This means: large amount of micro cracks are generated long before peak stress is reached, but macroscopic fractures are formed later. In the final state of the simulation, more cracks are generated in models with higher confining pressures. Because the lateral deformation was restrained, instead of generating macroscopic fractures, more micro cracks developed inside the samples. Amount and spatial distribution of the inclusions have great impact on the peak strength. The orientation of the inclusions (inclusion bands) affected the angle the fracture propagation. Inclusions with nearly parallel orientation to the axial stress lead to dominant tensile splitting.

The coalescence of microcracks contributes to an increase of the macroscopic fluid conductivity, which intensifies the hydro-mechanical coupling and triggers further growth of microcracks. As a consequence and documented by a series of triaxial compression tests (see Chapter 3), the overall permeability of the samples increases very slowly in the first stage. The

increase in permeability becomes significant after reaching a specific stress state. According to the numerical simulations, the coalescence of enough number of microcracks leads to a step-wise increase in permeability. Opening and closure of microcracks influence the mechanical behavior of the damaged model directly.

In the model each microcrack is defined by its radius and normal direction. According to strength and stress components at the contact between particles, cracks may be triggered. The emerging of microcracks induce displacement jumps along crack surfaces (see also previous works of Kachanov (1982a, b)). Variation in mechanical behavior of fractures such as opening, closure, sliding and dilation are controlled by the relative motion of particles and the bonding method with predefined failure criteria.

Because of the distinct different amount and structure of the inclusions, the stress-strain behavior shows great differences. Also fracture patterns may be quite different. Samples C1 and C3 have similar amount of inclusions (about 20%), but samples C2, C4 and C5 have only 10% as mentioned in Table 4.5. Samples with larger amount of inclusions like C1 and C3 show higher peak strength compared with other samples under the same boundary conditions. This results proved that, compared with proportion of inclusions, the structural features have a decisive influence on the strength. Vertical aligned conclusions (see in Figure 4.18) provide more support to the model against uniaxial loading. At lower confining pressure, the differences become less pronounced (see Figure 4.26). With high confining pressure, splitting is restrained, the support of vertically distributed inclusions is more remarkable.

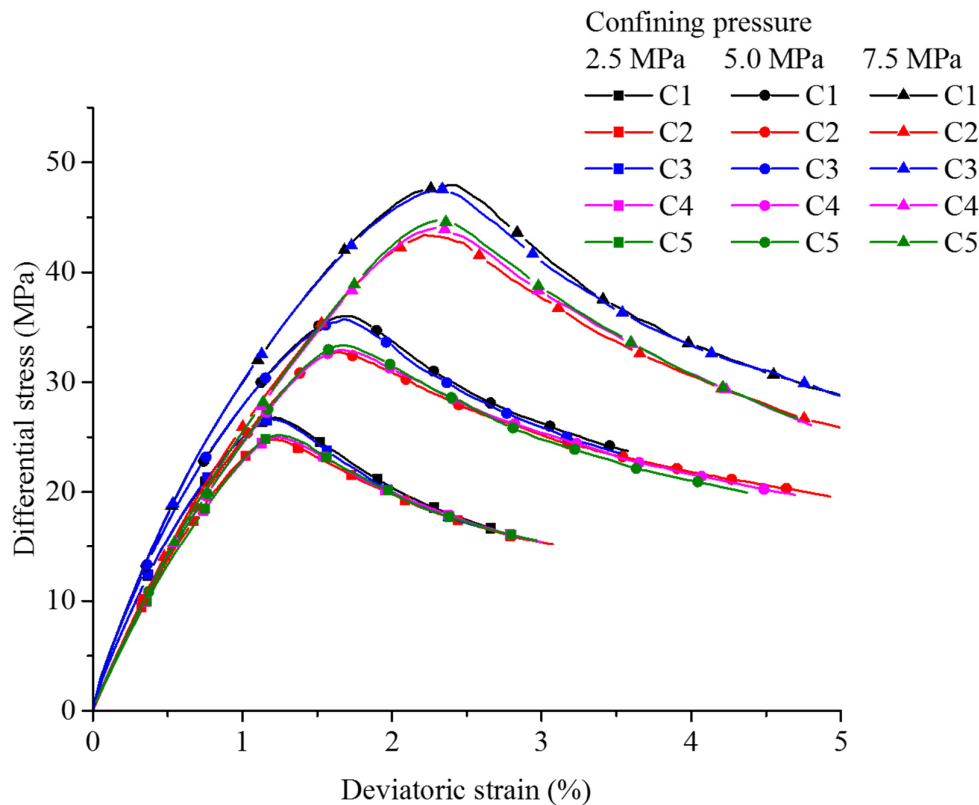
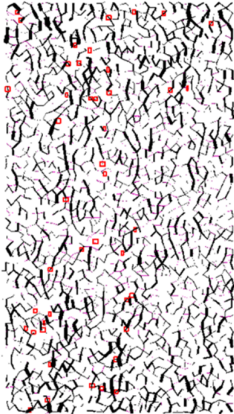
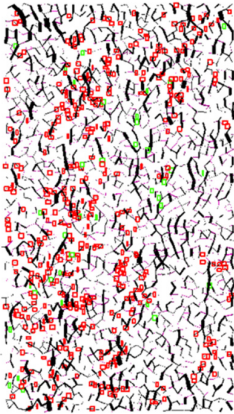
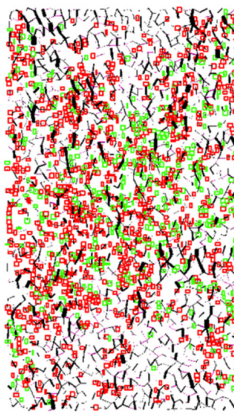
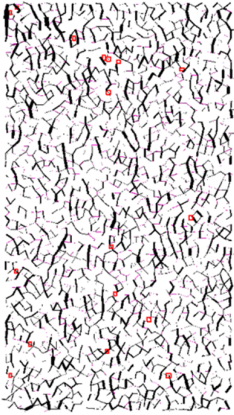
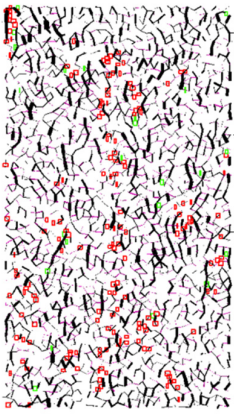
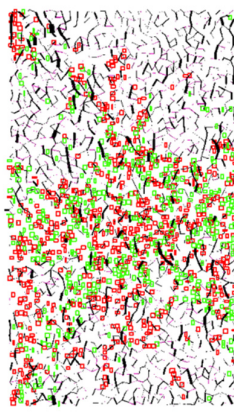


Figure 4.26 Simulated stress-strain curves of 5 samples with different confining pressures

The force chains and crack distributions inside the models C1, C3 and C4 at different confining pressures are shown in Figure 4.20, 4.22 and 4.24. Short straight lines represent the contact forces by connecting the centers of two attaching particles or touching particle and facet. The force networks are scaled visually by contact force magnitude. The line thickness is directly proportional to the magnitude. On the other hand, internal stress redistributions lead to initiation and propagation of cracks as also shown in Figure 4.20, 4.22 and 4.24. Crack elements are plotted as cubes in 3-dimensional plots and squares in 2-dimensional cross-sections to identify their positions and influence range. By investigating the evolution of cracks during the simulations, information about internal damage evolution can be obtained. Shear and tensile cracks are illustrated by different colors. The crack propagation during triaxial test simulations with FW membranes evolves with increasing axial compressive strain. The reconstructed samples produced uniquely oriented contact force networks.

The distribution of inclusions inside the coal matrix affecting the fracture propagating paths is shown in Table 4.6. The fractures were mostly initiated at the boundary between matrix and inclusions, and propagated along these boundaries. The plots indicate that denser crack networks are initiated in the central region vertically before failure. After failure, the crack network shows column-like distribution at lower confinement as shown in Figure 4.20(e); while the cracks tend to concentrate near the center of the sample at high confinement as shown in Figure 4.24(e).

Table 4.6 Damage patterns in models C1 and C4

Model	70% of peak stress	At Peak stress	Residual stage
C1 (σ_3 : 2.5 MPa)			
C4 (σ_3 : 2.5 MPa)			

The fractures extended along the direction of maximum principal stress. Up to the peak stress state, continuous shearing caused anisotropic extension of force chain network. The collapse of the main force chains led to the development of new force chains inside the model. Secondary contact force chains that carried smaller loads supported the major force chains that carried the majority of the applied deviatoric stress. This supports the statements of Cil & Alshibli (2014).

Compared with using a particle based membrane, the FW approach reveals a different crack propagation process in triaxial test simulations. Higher contact forces were able to form at the membrane-sample interface during the simulations. Because the forces are applied in direction normal to each wall element, better stress localizations along the membrane boundary is reached. The force network pattern demonstrated the significant effect of wall elements on the contact force distribution.

4.6 Conclusions

A new developed flexible membrane boundary has been developed to simulate triaxial tests in 3D with the particle-based DEM code PFC^{3D}. The flexible wall membrane is composed of triangular wall elements that form a cylindrical sleeve. In this approach, triaxial test simulations are validated by comparing the stress-strain response and fracture pattern of coal samples tested in the laboratory via triaxial compression tests. Force chains evolved at the contacts at the membrane – sample interface using this FW approach. The importance of realistic membrane boundary simulation is demonstrated by this study.

In this study, reconstructed models were simulated to match experimental measurements. The micromechanical behavior of the DEM simulations has been compared with micro-structures investigated by laboratory tests, and the capability of the DEM models in simulating particle-level interactions is verified.

A calibration theory has been established using uniaxial compression and direct tension simulations, in which effective modulus, normal to shear stiffness ratio, tensile to cohesion strength ratio, friction angle and expansion coefficient (tensile strength) are determined. After calibrating the parameters via uniaxial compression tests, the results showed that DEM models can capture the expected macroscopic response for triaxial compression simulations with varying void ratios, confining stresses and loading paths without additional complex model recalibration. Different failure modes have been reproduced with numerical simulations regarding varying confining pressures.

A series of triaxial compression tests with reconstructed numerical models were conducted. The composition of the samples (matrix and inclusions) influences the peak strength. Force chain development and crack distributions are also affected by the distribution of inclusions inside the sample. Increasing confinement leads to a change of damage pattern. The fractures tend to propagate towards side surfaces with higher confinement.

5 HM-coupled simulations

5.1 Introduction

Besides laboratory tests, numerical simulations play a vital role in investigating permeability evolution rules. Numerical simulations of permeability evolution during triaxial compression of lab samples are presented in this chapter.

Coal samples under external loads have been considered in different ways, especially under the aspect of microcrack nucleation and propagation inside the samples. Not only mechanical properties, but also hydraulic properties are affected by the damage patterns generated by fracture propagation (Zhang et al. 1996; Zhou et al. 2006). The permeability is considered as strongly coupled to plastic deformations. Furthermore, permeability evolution is directly dependent on the applied stress state. Coupled hydro-mechanical models are essential for representing the seepage behavior of porous coal samples under triaxial compression.

A specific coupled model was presented to simulate deformation, damage, failure and fluid flow in brittle rocks simultaneously (Tang et al. 2002). However, in this approach, the fluid flow is only guided by Biot's consolidation theory, and effects of microcracks on the permeability are not explicitly considered (only in a smeared manner by plastic deformations). The concept of flexibility tensor has been introduced to develop a coupled model by considering the influence of the hydraulic state on the mechanical parameters. More coupled formulations have been developed, and many non-linear elastic-plastic constitutive models were established based on fracture and damage mechanics considering the combined action of compressive shear or tensile shear failure. The effects of non-linear normal deformation and shear dilation were also considered (Sheng et al. 2000; Zhao et al. 2010b). All these theories provide a macroscopic qualitative analyses based on experimental observations and data. The relationship between the microstructural changes and macroscopic permeability evolution was not taken into account.

The quantification of the permeability properties of fractured coal relies on the knowledge of the geometrical parameters of the fracture network, such as orientations, extensions, apertures and densities of fractures (Lespinasse and Sausse 2000). Researcher verified that, permeability of brittle materials is closely related to microcrack evolution and macrofracture propagation. Based on previous works, the intrinsic permeability can increase by several orders of magnitude due to the occurrence of connected fractures (Bossart et al. 2002; Jiang et al. 2010; Oda et al. 2002; Souley et al. 2001; Suzuki et al. 1998; Wang and Park 2002).

Microcracks and pores are highly developed in coal samples. Due to the non-uniform distribution and size variation, it is not possible to apply explicit crack models in a comprehensive sense to simulate real pore-crack structures. Stress redistributions are responsible for micro damages inside the coal samples. On the one hand, initiation and connection of pores increase the seepage paths; on the other hand, changes of fracture apertures affect the local permeability. For instance, compression in a narrow region may cause closure of existing fractures, and shear stress causes dilatancy effects (Bai et al. 1999; Cao et al. 2009). Many researchers have investigated the damage of coal rock based on these two aspects.

Previous researches mostly described and explained fracture flow phenomena with empirical models. The initial and simple fracture flow model is the parallel plate model (cubic law) for viscous fluids (Boussinesq 1897).

Based on field investigations and fracture statistics, the Monte Carlo method was applied to generate flattened disk elements randomly to represent the internal fracture network. These three-dimensional disks were modeled to investigate the connection between microscopic failure and general permeability (Maleki and Pouya 2010). Artificial uniform fractures were designed to investigate this problem as reported in previous works (Ki-Bok et al. 2004; Min et al. 2004). A simple assumption was made: the rock matrix is impermeable and linear elastic, and the fluid flows only in the fracture network. A nonlinear algorithm was developed to predict the stress–displacement behavior of fractures and the correlation between fracture width and length is based on the Barton-Bandis model (Baghbanan and Jing 2008; Barton et al. 1985). However, in reality, relatively larger fractures with higher hydraulic conductivity increase the overall permeability significantly. Fracture systems simulated with uniform apertures are not appropriate to represent the real situation.

By studying the connecting rates and crack propagation rules, tensor evolution equations for the fracture propagating process under different stress conditions were established. The coupling between hydraulic gradient and mechanical failure were analyzed. A coupled hydro-mechanical model has been established and implemented into FLAC^{3D} (Zhao et al. 2010b). FLAC^{3D} has been widely used to simulate the permeability of damage zone based volumetric strain (Souley et al. 2001; Tan et al. 2015; Tan and Konietzky 2014).

Numerical fracture models have been generated to analyze fracture flow, and heterogeneous fracture distributions were considered (Nemoto et al. 2008, 2009; Watanabe et al. 2008). According to physical experiments, dilatancy has a significant impact on permeability of a single fracture. A small shear displacement can cause drastic increase in permeability (Lee et al. 2001). The coal samples are not available for repeated usage because damage cannot be cancelled. In order to get a maximum knowledge from the valuable samples, the development of a three-dimensional numerical model of flow within a particular fracture network is needed. Several theoretical methods for numerical simulations are available where fracture aperture is among the coupled parameters. The nondestructive aperture determination for coal samples should also be included.

Mechanical and hydraulic apertures were introduced separately. Mechanical aperture is the physical distance between fracture surfaces. The hydraulic aperture represents the equivalent distance for an assumed parallel plate model, in which a particular flow rate is considered. With the increase of mechanical aperture, the hydraulic aperture increases, but not in a linear relation (Barton et al. 1985; Esaki et al. 1991; McClure and Horne 2014; Park et al. 2013; Rutqvist and Stephansson 2003; Witherspoon et al. 1980; Xiong et al. 2014; Zimmerman et al. 1991). According to the results of laboratory tests on specimens with artificial fractures, the effective hydraulic aperture for a parallel plate model depends on the fracture roughness, fracture geometry and relative shear displacement (Cook 1992; Esaki et al. 1999; Hakami et al. 1995; Li et al. 2008a, 2014; Oron and Berkowitz 1998; Pyrak-Nolte and Morris 2000; Raven and Gale 1985; Renshaw 1995; Walsh 2003; Yeo et al. 1998).

The hydraulic conductivity of fractures was found to be large if shear displacements occurred according to laboratory tests. However, the increase in hydraulic conductivity become smaller with ongoing shear displacement (Chen et al. 2000; Durham and Bonner 1994; Lee and Cho 2002; Park et al. 2013).

For the simulation of flow through fractures different approaches have been developed (Koyama et al. 2006; Lespinasse and Sausse 2000; Matsuki et al. 2006; Pyrak-Nolte and Morris 2000; Sausse 2002; Unger and Mase 1993). These approaches were not finally validated, because of the difficulties to reproduce the required special conditions in the experiments. In previous works, these models failed to incorporate laboratory test results into numerical simulations. Fracture flow in numerical models mostly considers only stationary fractures. Influence of actual conditions like stress state were not synchronized to the fracture channels. The geometrical structure for particular coal fractures is related to tensile and shear displacements, and the structures have huge impact on fracture permeability. Therefore, the fluid flow under specific conditions should be determined by incorporation of stress induced aperture change directly.

However, the essential mechanism of stress-seepage coupling has not been completely discovered. In order to connect the mechanical properties and permeability characteristics, coupled numerical simulations with DEM and FDM are applied in this research. A series of triaxial compression tests have been performed with coal samples as shown in Chapter 3. Correspondingly, numerical simulations under same hydro-mechanical conditions are performed using a HM-coupled method. The models in this research are firstly coded for PFC^{3D} to simulate the fracture propagation as shown in Chapter 4. The DEM has been proven to be an efficient tool for simulating the failure process within brittle materials. In parallel equivalent models are also generated in FLAC^{3D} to simulate the hydraulics. Modeling in PFC^{3D} and FLAC^{3D} is performed in parallel with data exchange. As portrayed by the experimental and numerical data presented in Chapter 3 and 4, the permeability of brittle coal samples changes significantly due to the growth of internal fractures. In this chapter, relationships between fracture attributes and hydraulic properties are developed and explored on a theoretical basis, which allows linking them in a formal way.

5.2 Methodology

For samples which contain fractures, the majority of gas flows through internal fractures during the gas seepage process, while only very few gas flows through the rock matrix. According to the results of both, laboratory tests and numerical simulations, almost all the initial volume does not contribute to the gas flow. Therefore, the overall permeability, which may be calculated based on the total flow rate and entire cross-section area of the sample, is much lower than the real permeability of the fractured region.

The purpose of running parallel simulations is based on the advantages and shortcomings of both, PFC^{3D} and FLAC^{3D}. Figure 5.1 illustrates how the new developed coupling was realized.

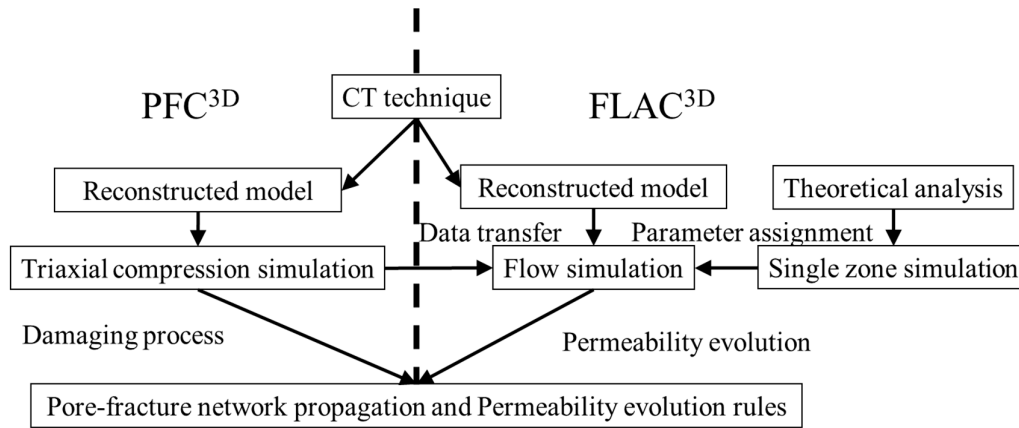


Figure 5.1 Flow chart illustrating the coupling between PFC^{3D} and FLAC^{3D}

According to the achievements described in Chapter 2, PFC^{3D} and FLAC^{3D} models have been reconstructed with same composition as virgin samples. PFC^{3D} is used to simulate triaxial compression tests as described in Chapter 4, especially to observe the microcrack evolution inside the model. Then, with a predefined step interval, data are exported from PFC^{3D} with actual crack information. Each data file is then imported into a corresponding FLAC^{3D} model to perform hydraulic simulations for the current state. All the zones in FLAC^{3D} are assigned with new hydraulic parameters according to the imported data file. Finally, flow-only numerical simulations are performed, which represent the current triaxial loading stage.

In this chapter the terms “crack” and “fracture” are used. “Crack” is a single disconnected unit, which refers particularly to one disk element generated between particles where the bond is broken in PFC^{3D} models. The combination of connected “cracks” is marked as “fracture” in both, PFC^{3D} and FLAC^{3D}. In FLAC^{3D}, “fracture” refers to connected “cracked” zones. The crack sizes is limited due to the size of particles and zones, respectively, which are constant in specific models. On the contrary, the size of fractures depends on the number of connected microcracks, which develop during the simulation. The length of one fracture may cover the length of the whole sample.

5.3 Modelling

The modelling process in FLAC^{3D} comprises several steps. Firstly, a model with uniform mesh is generated. Secondly, the zones in the model are grouped to represent the initial sample based on CT reconstruction. The third step is to import cracks obtained from a specific state of triaxial compression test. In the last step, the zones represent matrix, inclusion and different kinds of cracks are assigned with corresponding hydraulic parameters.

In general, the calculation in FLAC^{3D} tends to be more accurate when the zones have uniform size and a brick-like shape. Also, the data exported from the CT process are voxels, so for the purpose of model reconstruction in FLAC^{3D}, the zone elements should also be generated in a hexahedral pattern.

To obtain a satisfying mesh, the octagonal meshing method and extrusion into the third dimension is applied. First, an extrusion plane was defined to generate the grid layout in the x-

y plane. The mesh structure shown in Figure 5.2 has been created. The zones close to the axis (inside range A) are standard hexahedrons, and the zones further away from axis (inside range B) are created with curved edges to form an even side surface. The number of zones along inner radius R_1 and width R_2 of the outer ring are assigned manually. The ratio between R_1 and R_2 affect the uniform arrangement of zones. The basic layout is extruded along the z-direction to get the 3D model. By defining the model height h and the zone number along the z-direction, the entire sample model is generated with a relatively uniform mesh. The previous mentioned procedure has been translated into command strings, which are useful for further model generation with different parameters.

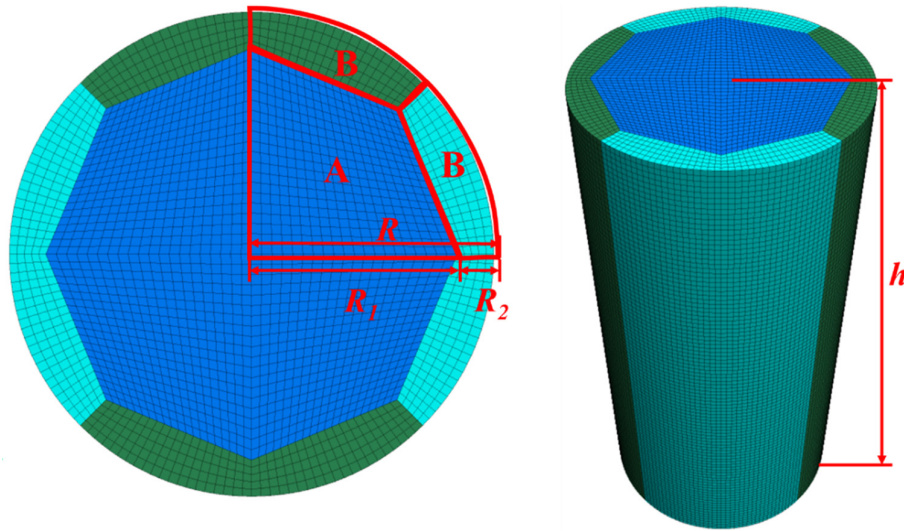


Figure 5.2 Illustration of meshing the FLAC^{3D} model

A volume checking function has been applied to examine the volumetric differences among zones, and the geometrical parameters for the extruding process are calibrated to reduce the differences. It was proven that the hexahedral zones are better suited to assign the properties from the reconstructed model.

Crack data, such as type, position, radius, normal direction and aperture, are exported from the PFC^{3D} model. These data are listed in ASCII data files.

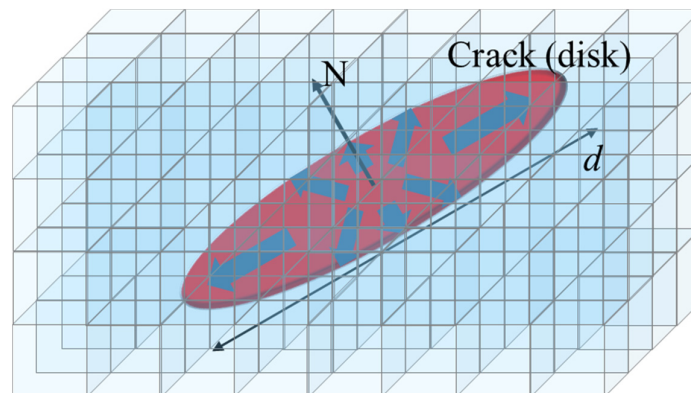


Figure 5.3 Zones occupied by a crack (disk)

In order to generate fractured models in $FLAC^{3D}$, the ASCII data are imported to create virtual disks inside the reconstructed model. Exemplary, the red disk shown in Figure 5.3 illustrates one single virtual fracture. The crack covers several zones, which are assigned with new (fracture) parameters.

Based on fine meshing, isotropic zones are generated to represent finally a non-uniform sample. The anisotropic character of the fractures is produced by spatial orientation of several connected zones representing one single crack or fracture. Figure 5.4 illustrates how connected cracked zones represent fractures with different orientation.

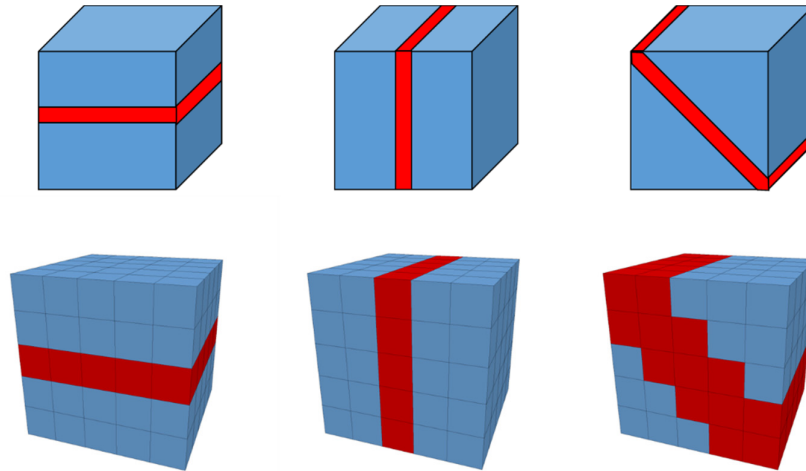


Figure 5.4 Examples of fractures represented by zones in $FLAC^{3D}$ (above: real fracture, below: representation inside $FLAC^{3D}$)

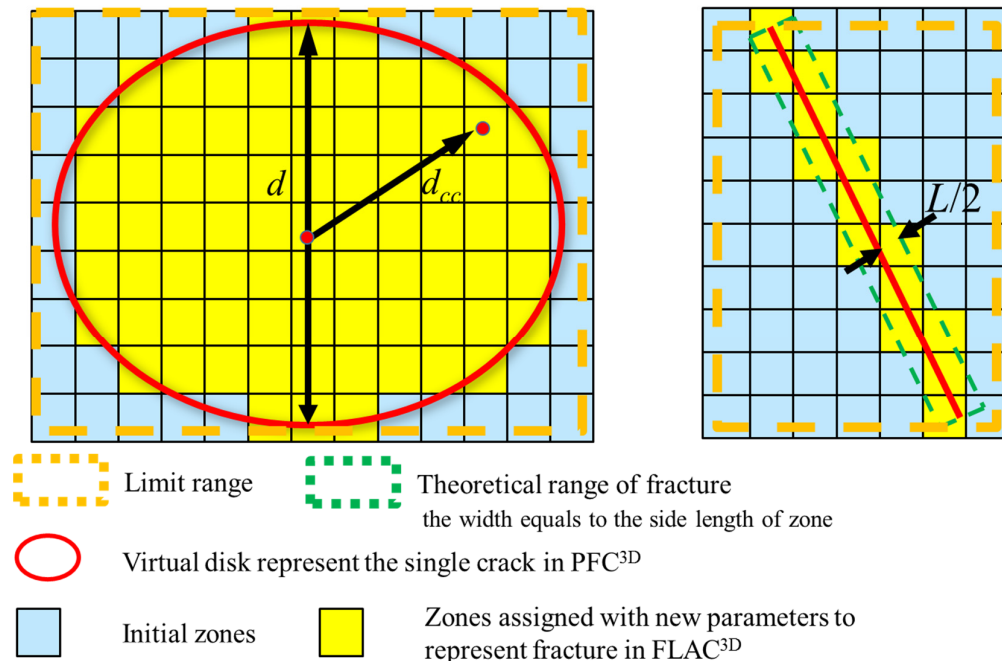


Figure 5.5 Fracture zone assignment (projection view)

The algorithm checks the zoning to meet the requirements for each imported crack. To improve computational efficiency, according to central position and size, the searching process is narrowed down to a limited range: only zones inside are checked for each crack (virtual disk shown in Figure 5.5). Then some zones are re-grouped if their centers are located within a block region covering the disk in the center, which means that distance between zone center and disk center (d_{cc}) is smaller than the disk radius (equal to $d/2$), and the perpendicular distance from zone center to disk plane is smaller than half of the region width. The width of the block region is set to be the zone's average side length. The new group with new parameters performs as fracture in FLAC^{3D}.

Sets of Fish functions are used to translate the properties from crack disks to zones. Parameters like location, porosity and permeability are important to characterize the hydraulics.

The geometrical parameters for characterizing and assigning the hydraulic properties of the zones are based on theoretical considerations. The basic information of the identified four sets of cracks is shown in Table 5.1. There are in total six zone groups in the models, including initial matrix and inclusion elements. These geometrical crack parameters serve only as data source for the generation of FLAC^{3D} models for flow-only hydraulic simulations. Mechanical interaction is not considered in the FLAC^{3D} simulations.

Table 5.1 Basic crack parameters exported from PFC^{3D} model

Category	Parameter
General parameters	Position (Cartesian coordinates)
	Group (Crack type)
Geometrical parameters	Diameter (Length)
	Normal direction (Unit vector)
	Aperture (Length)
	Shear displacement (Length)

Figure 5.6 shows exemplary the assignment of micro-fractures in terms of four crack types. Each model contains 240,000 small zones which are subdivided into six types of elements (two component types and four crack types) with different hydraulic parameters after importing the crack data. Zones, which represent coal matrix and inclusion, are plotted in light blue and red, respectively. The shear (fracsm) and tensile (fractm) fractures inside the matrix are plotted in magenta and dark blue, the shear (fracsi) and tensile (fracti) fractures inside the inclusion are plotted in green and yellow. The codes of this import and assignment function are shown in Appendix A2. The detailed rules to translate the crack data into hydraulic properties, included in codes, are described in the next section. In numerical models, this transfer is heavily geometry dependent.

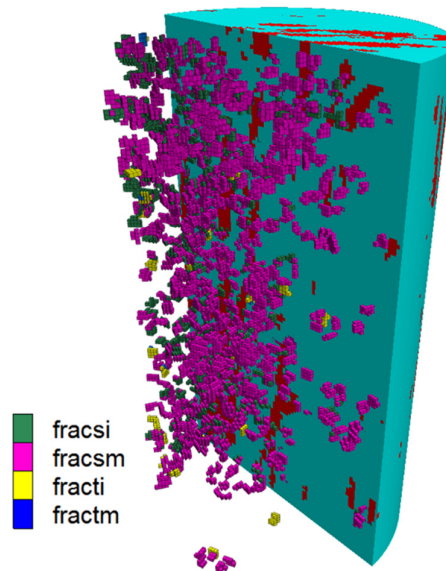


Figure 5.6 Illustration of a FLAC^{3D} model for a specific stress state (25 MPa axial stress and 2.5 MPa confining pressure) with micro fractures

Flow-only simulations are conducted for each model representing one specific state of stress during the triaxial compression tests. About 20 models have been set-up from one sample to represent different stress stages. In the initial state, there are only 2 types of zones, which represent matrix and inclusions. The four newly assigned types (micro fractures) contribute to the anisotropic flow features of the models as shown in Figure 5.7.

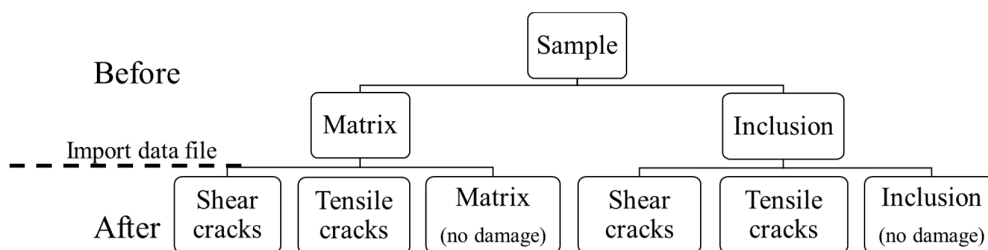


Figure 5.7 Zone types before and after parameter assignment based on PFC^{3D} simulations

Gas pressure is applied to both ends of the model and is kept constant. The simulated gas flow occurs – like in the lab – from one cylindrical end face to the other (upstream end to downstream end). The side surface is impermeable. The numerical model is designed to simulate steady state flow. Flow rates and pore pressure distribution have been recorded in each model. Based on Darcy’s law of gas, the permeability of the entire model is calculated. By simulating all the models, the permeability evolution is obtained and compared with laboratory test results (see Chapter 3).

5.4 Theoretical analysis

The micro-mechanical models used in this study account for the coupling between permeability variation and fracture propagation. Theoretical relationships have been developed for fracture properties (as categorized by crack type, size and aperture) and corresponding fracture attributes

(such as porosity and permeability). They are mentioned in previous works (Bonnet et al. 2001; Neuman 2008).

The determination of micromechanical model parameters is complicated. Ideally, the determination of parameters should be based on relevant data at the micro scale. Physical measurements are conducted at real samples, for instance: statistical survey of micro fracture distribution, monitoring of micro fracture growth in various orientations, experimental tests on samples with controlled deformation state. Equivalent aperture parameters have been defined from the experiments using travel time and flow rate or travel time and hydraulic head (Tsang 1992). However, it is still a serious challenge to perform such investigations on explicit internal fracture networks.

Under compressive stresses, the initial micro fractures are closed in various orientations during the first stage of triaxial compression tests. This leads to a reduction of permeability, as shown in the experimental data presented in the previous chapters. However, great diversities are noticed among different samples.

Note, that most existing micro mechanical and phenomenological models for anisotropic damage are generally developed in strain-based formulations. In-situ stress fields and hydraulic conditions are key factors in practical rock engineering. A damage evolution law is preferable expressed by stress and pore pressure. Therefore, stress-based numerical simulations are proposed for modeling anisotropic damage. Permeability changes are related to microfracture propagation.

Based on fracture aperture, diameter and orientation, the fracture permeability is estimated. As mentioned in Chapter 3, gas permeability of a coal sample can be defined by Darcy's equation as follows (Somerton et al. 1975):

$$k = \frac{\mu Q_0}{A} \frac{2P_0 H}{(P_u^2 - P_d^2)}$$

$$Q_0 = \frac{A(P_u^2 - P_d^2)k}{2\mu P_0 H} \quad (\text{Equation 5.1})$$

where, k is gas permeability of the sample (m^2); Q_0 is volumetric rate of flow at reference pressure (m^3/s); μ is gas viscosity ($\text{Pa}\cdot\text{s}$); H is length/height of core sample (m); P_0 is reference pressure (Pa); A is cross-sectional area of the core sample (m^2); P_u is upstream gas pressure (Pa); P_d is downstream gas pressure (Pa).

According to the principle of equivalent seepage resistance, the permeability k of the entire sample model at a given state is equal to the combination of the permeability of the initial sample (k_0) and the changes in permeability caused by fractures (Δk). The fracture induced permeability changes can be further expressed as the sum of contributions by the individual cracks.

In an explicit fracture system, length and width of fracture contribute to the micro- and macroscopic permeability of the core sample. The entire sample model can be subdivided into two sub regions: undisturbed body and cracked region.

The flow properties of the fracture network are in turn governed by the flow properties of the single fractures. The cracks generated during triaxial compression simulation in PFC^{3D} can be classified as follows: shear cracks and tensile cracks. Fractures generated from these two types of cracks have different effect on the hydraulic properties. Predefined constitutive relationships are applied to accomplish the normal displacement–normal stress behavior, and the elasto-perfectly plastic shear behavior.

Theoretically, the cubic law is assumed to be valid whether the fracture (crack) surfaces are open or closed under stress. The permeability of a tensile crack is defined by the aperture. At any given stress condition, aperture, pressure difference and flow rate are determined. For a given aperture, flow rate is observed to be proportional to pressure difference under experimental conditions (Witherspoon et al. 1980). A crack width (W) is introduced to represent the opening value of a crack without considering the cause.

For each fracture, fluid flow rates (under laminar flow condition) through narrow channels can be described with the following equation:

$$q = \frac{W^3 \Delta P l}{12 \mu L} \quad (\text{Equation 5.2})$$

where, W is the crack width (m); q is the gas flow through a specific crack (m³/s); ΔP is the pressure difference over the crack extended length (Pa); l is the length of the crack segment observed on one zone element surface (roughly equal to the length of side), (m); μ is gas viscosity (Pa s); L is side length of the zone in flow direction (m). Each zone is nearly a cube, and the fracture goes through the zone in perpendicular direction. So the value of l is literally equal to the value of L , and then all the l are replaced by L . Then the gas permeability of a specific zone is estimated. Darcy's law for incompressible fluid flow is given by:

$$q = \frac{k A \Delta P}{\mu L} \quad (\text{Equation 5.3})$$

From Equation 5.2 and 5.3, the permeability k_f of a fracture segment in a zone defined in SI units (m²), can be achieved with the following equation:

$$k_f = \frac{W^3}{12 A_f} L \quad (\text{Equation 5.4})$$

where, A_f is the cross section area of the fracture, excluding the initial region (m²).

The cross-section of fracture considering a rectangular shape is given by:

$$A_f = WL \quad (\text{Equation 5.5})$$

By substituting Equation 5.5 into Equation 5.4, k_f is obtained as follows:

$$k_f = \frac{W^2}{12} \quad (\text{Equation 5.6})$$

Not only direct opening of the fracture due to tensile failure, but also shear displacements with corresponding dilation are taken into consideration in the numerical model. The shear dilation is not accessible directly from the exported fracture properties, therefore the mechanical apertures are accessed on a theoretical basis.

When shearing a non-planar fracture (joint) in real coal samples, the asperities on opposite fracture surfaces slide over each other causing dilation in normal direction, which results in an increase in aperture. A given increment in shear displacement ($\Delta\delta$) leads to a positive change in mechanical aperture (ΔW) according to previous research (Barton 1976). The change in mechanical aperture is calculated based on the tangent of the dilation angle (ψ):

$$\Delta W = \Delta\delta \tan \psi \quad (\text{Equation 5.7})$$

The shear dilation angle (ψ) is determined by several physical properties, such as joint roughness coefficient (JRC), joint wall compression strength (JCS), and effective normal stress (σ'_n) applied on the fracture surfaces. Based on a large number of experiments (Barton and Choubey 1977), Equation 5.8 was obtained:

$$\psi = \frac{1}{2} JRC \log \left(\frac{JCS}{\sigma'_n} \right) \quad (\text{Equation 5.8})$$

Similar equations are used by researchers to describe fracture shear dilation behavior in numerical models. According to the reference (Willis-Richards and Wallroth 1995), for a shear fracture without abrasion effects between surfaces, the aperture can be presented as:

$$W = \frac{W_0}{1 + 9\sigma'_n / \sigma_{nref}} + \Delta W + W_{res} \quad (\text{Equation 5.9})$$

Where W is the calculated final aperture, ΔW represents the change in aperture due to any subsequent accumulated shear displacement, W_{res} is the “residual” aperture at high effective stress, W_0 is the initial total aperture of fracture at low effective stress, and σ_{nref} is the effective normal stress applied to cause a 90% reduction of the initial aperture. The change in aperture due to shear dilation, ΔW , can be obtained from an equation similar to Equation 5.7, except that the shear dilation angle is replaced by the effective shear dilation angle (ψ_{dil}^{eff}).

$$\Delta W = \Delta \delta \tan \psi_{dil}^{eff} \quad (\text{Equation 5.10})$$

The effective shear dilation angle (ψ_{dil}^{eff}), according to Willis-Richards and Wallroth (1995), is a function of both, fracture wall asperities and normal stress. Shear dilation angle (ψ_{dil}) at zero or low effective stresses can be measured in the laboratory, which is used to obtain the following relation:

$$\psi_{dil}^{eff} = \frac{\psi_{dil}}{1 + 9\sigma'_n / \sigma_{nref}} \quad (\text{Equation 5.11})$$

It should be noticed that the theoretical model described above neglects the discrepancy between mechanical and hydraulic apertures, so the permeability of a dilated fracture is overestimated.

In the particle based numerical model formed by a large amount of particles, direct tension and shear dilation act with different mechanisms. The particles are compressed tightly at the initial stage under in-situ stress conditions. The stress-induced breakage of bonds between particles leads to a change of the geometrical relationships between the particles. This causes tensile and shear dilation behavior normal and parallel to the cracks, as well as deformation of the entire sample. The aperture (crack width) is proven to be the most important parameter.

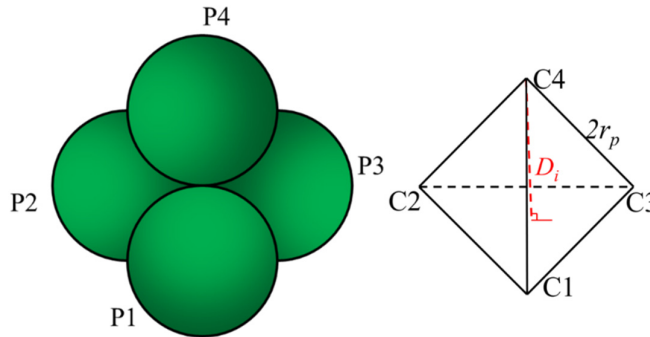


Figure 5.8 Tetrahedron structure of particles in contact

The mechanism of aperture calculation is illustrated separately for the two types. All the crack displacements are simplified to relative movements of particles. In all numerical models, the particles are generated with same radius, and compressed at the bonding stage to maintain contacted. The connections of initial centers of particles form a regular tetrahedron structure as shown in Figure 5.8. C1, C2, C3 and C4 are center points of corresponding particles P1, P2, P3 and P4, respectively. The tensile normal displacements of particles are transferred into direct apertures between particle layers following the relationship given by Equation 5.12 and shown in Figure 5.9.

$$D_i = \frac{2\sqrt{6}}{3} r_p$$

$$W_T = D_T - D_i = \sqrt{(2r_p + D_{ap})^2 - \frac{4}{3}r_p^2} - \frac{2\sqrt{6}}{3}r_p \quad (\text{Equation 5.12})$$

where, W_T is the tensile crack width (m); D_{ap} is the aperture caused by tensile cracking (m); r_p is the radius of the particles (m).

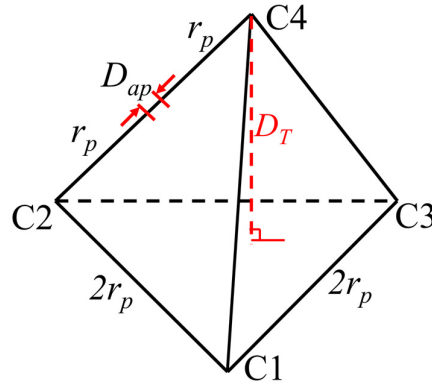


Figure 5.9 Relation between crack width and direct contact aperture (see also Figure 5.8)

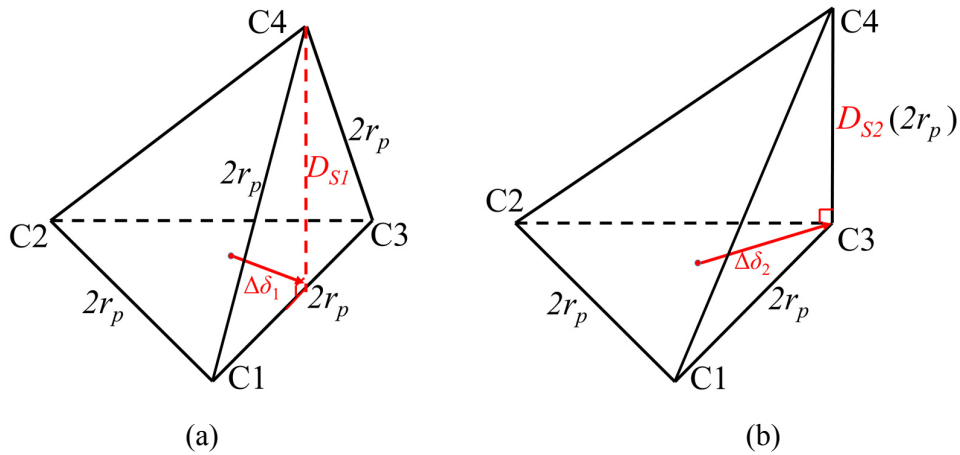


Figure 5.10 Relation between crack width and shear displacement (see also Figure 5.8 and 5.9)

As shown in Figure 5.10, shear displacement occurs along the surface between particle layers. The shear dilation is caused by the relative movement of particles. All the particles are defined as non-deformable rigid bodies, so for the relative position shown in Figure 5.10 dilation angles can be derived as described by Equations 5.13 and 5.14.

$$\Delta\delta_1 = \frac{\sqrt{3}}{3} r_p$$

$$\Delta\delta_2 = \frac{2\sqrt{3}}{3} r_p$$

$$W_{S1} = D_{S1} - D_i = \left(\sqrt{3} - \frac{2\sqrt{6}}{3} \right) r_p = \Delta\delta_1 \tan \psi_1 \quad (\text{Equation 5.13})$$

$$\tan \psi_1 = 3 - 2\sqrt{2}$$

$$W_{S2} = D_{S2} - D_i = \left(2 - \frac{2\sqrt{6}}{3} \right) r_p = \Delta\delta_2 \tan \psi_2 \quad (\text{Equation 5.14})$$

$$\tan \psi_2 = \sqrt{3} - \sqrt{2}$$

where, W_{S1} and W_{S2} are the shear crack induced widths (m). The shear displacements $\Delta\delta_1$ and $\Delta\delta_2$ are calculated based on the relative positions of the particles considering different shear orientations.

The relationships between crack width and shear displacement in two directions are shown in Figure 5.11. The shear dilation angle ψ_2 is chosen, and the crack widths caused by shear dilation are calculated by Equations 5.13 and 5.14.

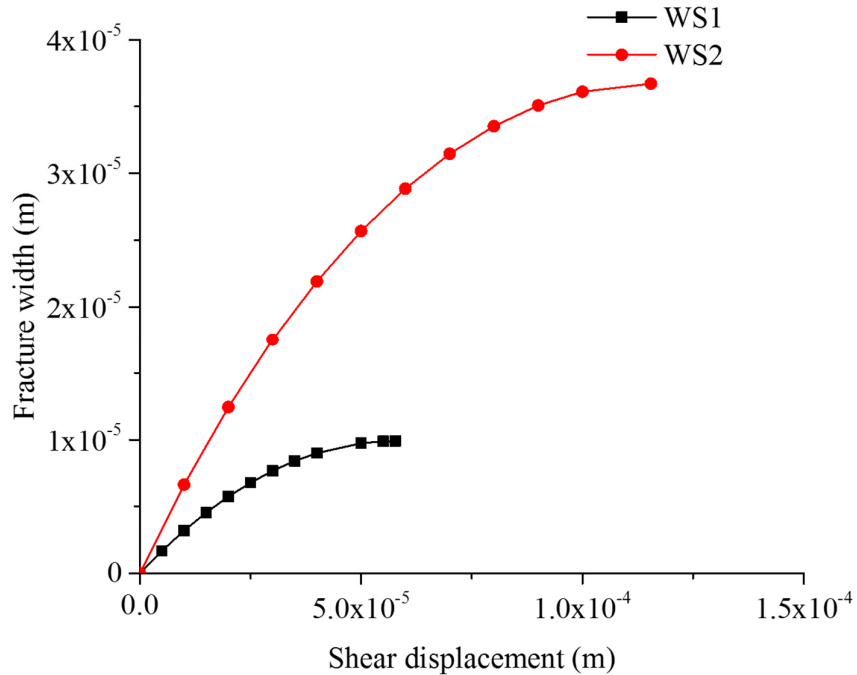


Figure 5.11 Crack width evolution as function of shear displacement

According to the crack data import rule, it is assumed that there is only one crack in each zone. Overall permeability (k_z) of one zone is the sum of two types of permeability, as given by the following equation:

$$k_z = ak_f + (1-a)k_i \quad (\text{Equation 5.15})$$

where: k_f is the permeability of the fracture (m^2); k_i is initial matrix permeability of the zone (m^2); a is area contribution coefficient. The area contribution coefficient (a) is calculated considering the ratio of cross-section area, A , and fracture area A_f as follows:

$$a = \frac{A_f}{A} = \frac{W}{L} \quad (\text{Equation 5.16})$$

where: A_f is the approximate rectangular area of the fracture cross-section (m^2). Equation 5.16 is then inserted into Equation 5.15, and k is obtained as follows:

$$k = \frac{W^3}{12L} + \left(1 - \frac{W}{L}\right)k_i \quad (\text{Equation 5.17})$$

Based on Equation 5.17, the permeability of one specific zone can be estimated from both, crack permeability and matrix permeability. In case both permeability values can be measured and monitored during laboratory tests and numerical simulations, the overall permeability evolution process of the coal samples can be reproduced. The coefficient (a) depends on the crack structure inside one zone. Even if the value of (a) appears to be small, the overall permeability can show a large increment, since fracture permeability is orders of magnitudes higher than matrix permeability.

According to the results of these thoughts, the crack size is limited to the particle dimension, the fracture length is an integral value with length of several zones. As a macroscopic parameter, fracture length is not further considered directly in the simulation. Instead, the coalescence of cracked zones creating fractures contributes to the local and overall gas permeability.

The value of fracture width has a major influence on permeability (see first component in Equation 5.17). The initial zone permeability (k_i) can barely influence the permeability of a fractured zone. Although the second term is much smaller than the first term, its value cannot be neglected when the corresponding fracture is tightly closed.

Equations 5.12 and 5.14 can be inserted into Equation 5.17 to achieve the permeability for tensile and shear fractures, respectively. Both, W_T and W_S are available in this equation to replace the variable W . The permeability is increasing with W^3 over the surface of a zone.

Friction angles for matrix and inclusion are 50° and 35° . Maximum dilation angle of fractures is defined as 17.63° calculated by Equation 5.14 according to the geometrical structure. Due to limitations of the particle-based modelling used in this research, the disk representing a crack

is generated only when the aperture between particles reaches a certain value. This means: the aperture value of a newly assigned fracture does not increase from the pre-defined value, but starts at zero. In the simulated models, tight cracks with width below 0.05 mm cannot be captured.

According to Equations 5.12, 5.13 and 5.14, particle radius is an important parameter for crack width monitoring.

According to the bond-deformability criterion, a small aperture value is given to those micro fractures. Width W_{as} of 0.05 mm was set to newly generated fractures. Based on the lab test results, this hypothetic value is not suitable for the ongoing compression process. Another important coefficient is introduced to balance the macro- and microscopic volumetric changes. With initially assigned aperture width, theoretical volumetric strain ε_{VT} of the sample can be calculated. In PFC^{3D}, the volumetric strain ε_{VP} of the whole model is monitored. A scaling coefficient is applied to individual fracture width, which can be derived from the relation of general lateral strain and volumetric deformation of the zone. The relationship between ε_{VT} and ε_{VP} is investigated to achieve a coefficient c_{bl} . As shown in Equation 5.18, the coefficient c_{bl} needs to be considered when assigning the permeability k_{cl} of closed fracture zones. This transformation relation depends on the resolution of both models.

$$k_{cl} = \frac{(c_{bl} \times W_{as})^3}{12L} + \left(1 - \frac{c_{bl} \times W_{as}}{L}\right) k_i \quad (\text{Equation 5.18})$$

Based on the previous analysis, the maximum derived aperture value caused by dilation is about 10 times the residual aperture value for each crack which has been proven by references (Ki-Bok et al. 2004).

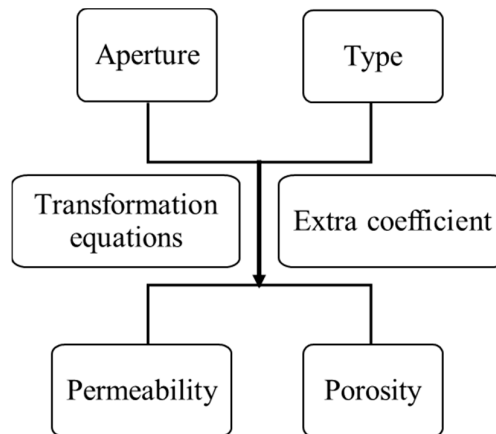


Figure 5.12 Scheme for hydraulic parameter transformation procedure

Based on the above given equations, hydraulic parameters have been assigned to the cracked zones as shown in Figure 5.12. The mechanical and hydraulic parameters can be seen in Table 5.2. Calibrations considering geometrical characteristics and permeability parameters were conducted.

Table 5.2 Mechanical and hydraulic parameters of numerical simulation

Parameters	Matrix	Inclusions
ρ (kg/m ³)	1500	2000
E (GPa)	1.5	3
σ' (Pa)	5×10^5	5×10^5
C (Pa)	2.7×10^6	7.8×10^6
ψ (°)	10	5
θ (°)	50	35
ν	0.35	0.35
k_a (m ²)	1×10^{-18}	5×10^{-16}
K (m/s)	8.75×10^{-14}	4.38×10^{-11}
φ (%)	6	9

5.5 Results and discussions

The hydraulic properties for zones in matrix and inclusion (both without fractures) are calibrated firstly according to references (Liu et al. 2017). Then the properties of fractured zones for both groups are calculated based on the previous given equations.

An iterative procedure for calibration was adopted. First estimations of parameters are obtained from one laboratory test. These parameters are then verified and fitted against other tests. Finally, these parameters are generalized and applied in numerical models to fit practical macroscopic data.

The seepage process is revealed by a series of independent simulations. A steady flow rate value was achieved in each of the simulations as exemplary shown in Figure 5.13. The final flow rate is used to calculate the permeability of the model. A negative permeability value is obtained to express the flow direction. The permeability evolution is characterized by permeability values for different compression stages.

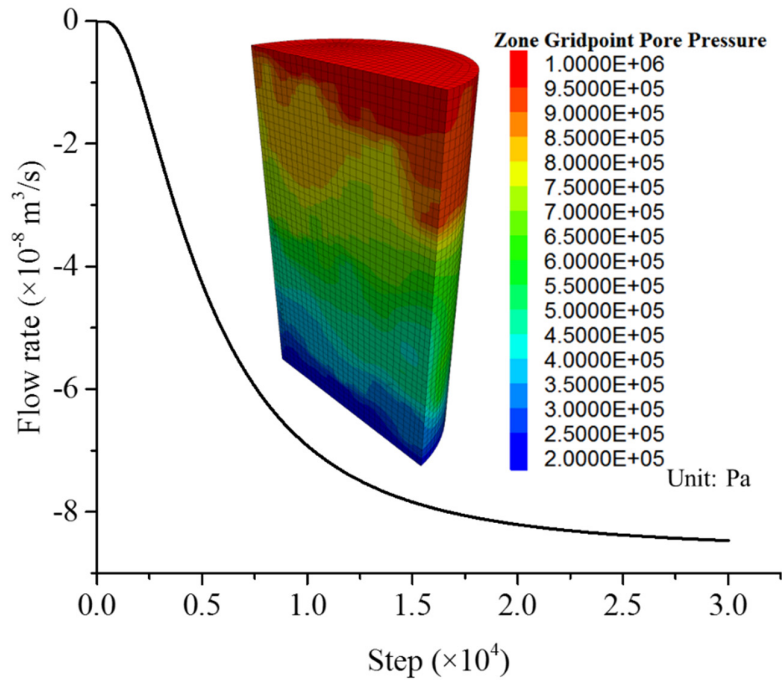


Figure 5.13 Flow rate evolution as function of calculation steps for model C1 (at axial strain of 0.0132, nearly stationary phase after about 30.000 calculation steps)

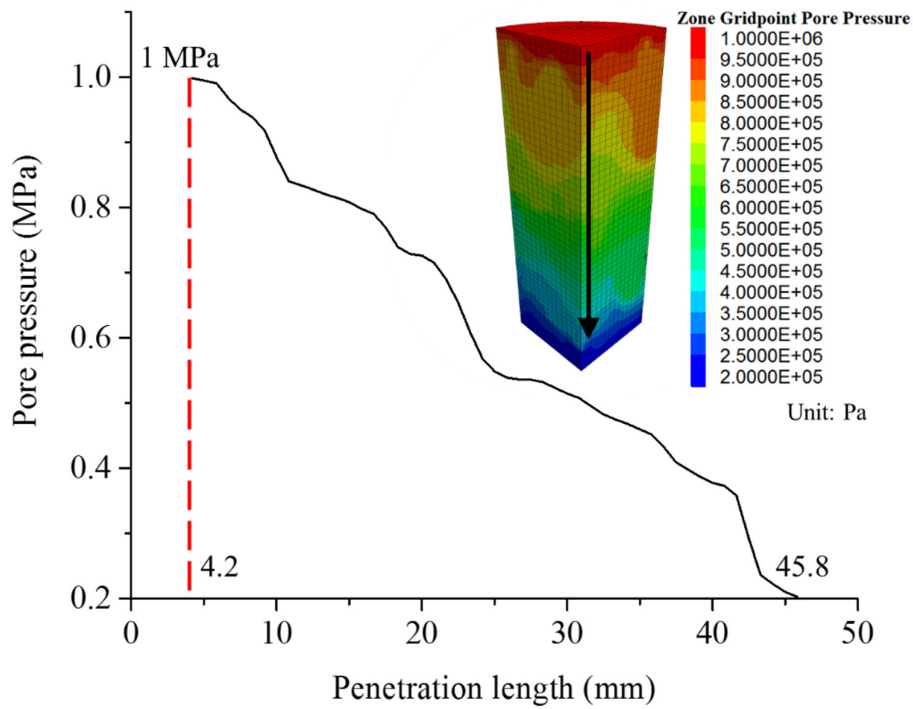


Figure 5.14 Pore pressure along vertical model axis for model C1 (at axial strain of 0.0132, stationary phase)

The pore pressure variation along the seepage direction shows a linear tendency, but also some local nonlinearities (see Figure 5.14). Significant pressure drop occurs when fractures are crossing zones. The flow shows local variations. The spatial distributions of crack (fracture) elements and their special hydraulic properties produce the heterogeneity of the entire model.

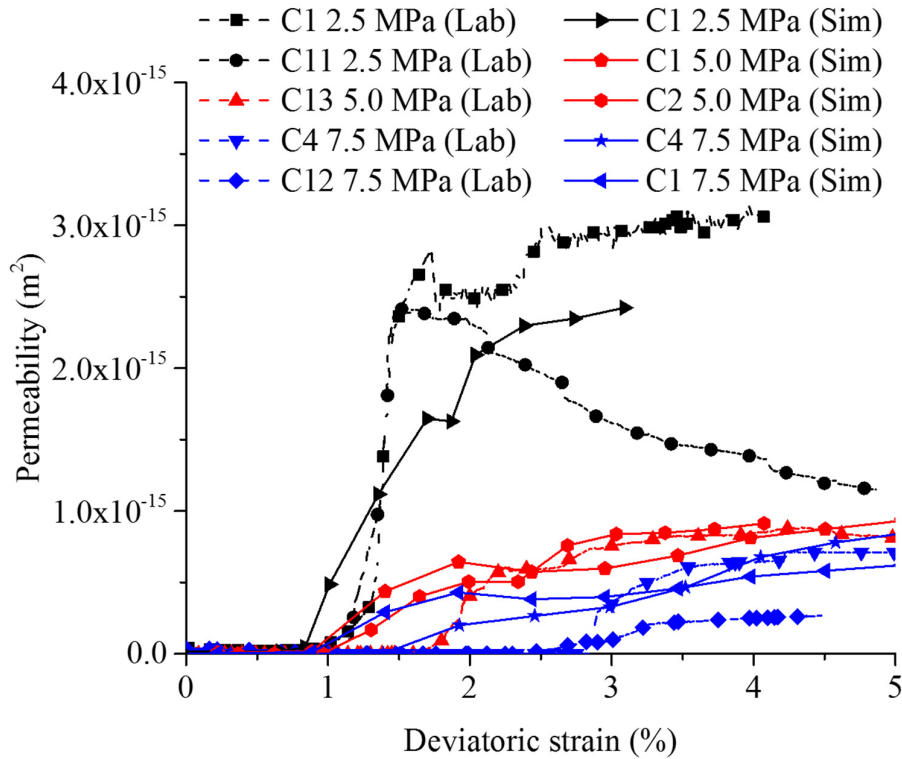


Figure 5.15 Simulated permeability evolution compared with lab results for different samples and confinement

Numerical permeability evolutions for different samples are shown in Figure 5.15. The simulations are performed with the reconstructed models under various confinements. The observed phenomena are discussed in detail using the numerical model C1 as example. Figure 5.16 shows the permeability evolution together with corresponding stresses and strains.

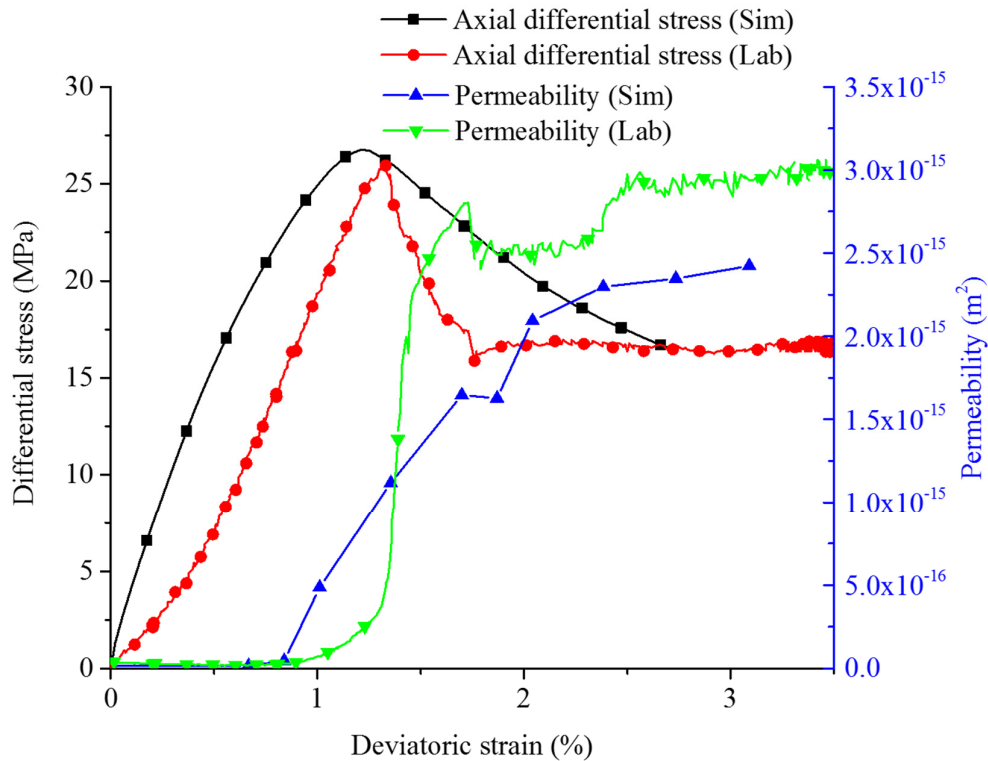


Figure 5.16 Stress-strain curves and permeability evolution for sample C1 under 2.5 MPa confining pressure (stationary phase)

In the early loading stage, the permeability increases barely, and remains at low values. This phenomenon can be explained by two reasons:

- (1) The total number of fractures increases slowly. Only 34 new cracks are observed before the axial strain reaches 0.01. These microcracks are distributed over the entire sample, and do not create significant flow paths.
- (2) The existing/initiated cracks cannot develop further, and remain tightly closed. The zones with closed cracks have approximately the same permeability as the virgin matrix. With higher confinement, the permeability is even lower than in the initial situation.

When approximately 30% to 40% of peak differential stress is reached, the number of cracks increases drastically. Also, after a specific strain value, the permeability shows a steady increase. Until the peak strength (axial strain of about 0.014), the total number of cracks increases to more than 600. Among them, 22 cracks are detected with noticeable apertures (their width is larger than 0.05 mm). In this stage, the frictional sliding-induced aperture ($\Delta\delta$) occurs only when the deviatoric stress exceeds the bond strength threshold. This threshold rises with higher confining pressure as mentioned previously in Chapter 4. By analyzing the crack state, significant rise of permeability occurs locally, when individual cracks become connected vertically (fracture formation). In this stage, more cracks emerge and propagate at the same time. When one complete end-to-end flow path is formed by connected cracks, the flow rate as well as corresponding permeability reach peak values. Zones show great pressure drop along the main flow path.

In the final stage, new fractures are generated continuously. More shear cracks are initiated in that stage. Because of the lateral confinement, the opening of pre-existing and newly generated cracks is limited. The permeability evolution in the post peak stage shows two different types: (1) the permeability increases to a peak value and then remains relatively constant until the end of the test; (2) the permeability increases to a peak value and then decrease to a residual value. As shown in Figure 5.16, the overall permeability of the sample C1 remains at a high level in its final stage.

The discrete and distinct structure of the samples causes distinct mechanical properties. Due to different internal structure, strength and permeability behavior do not fully follow the general trend as a function of confinement. This phenomenon is also proven by lab tests mentioned in Chapter 3 and Chapter 4.

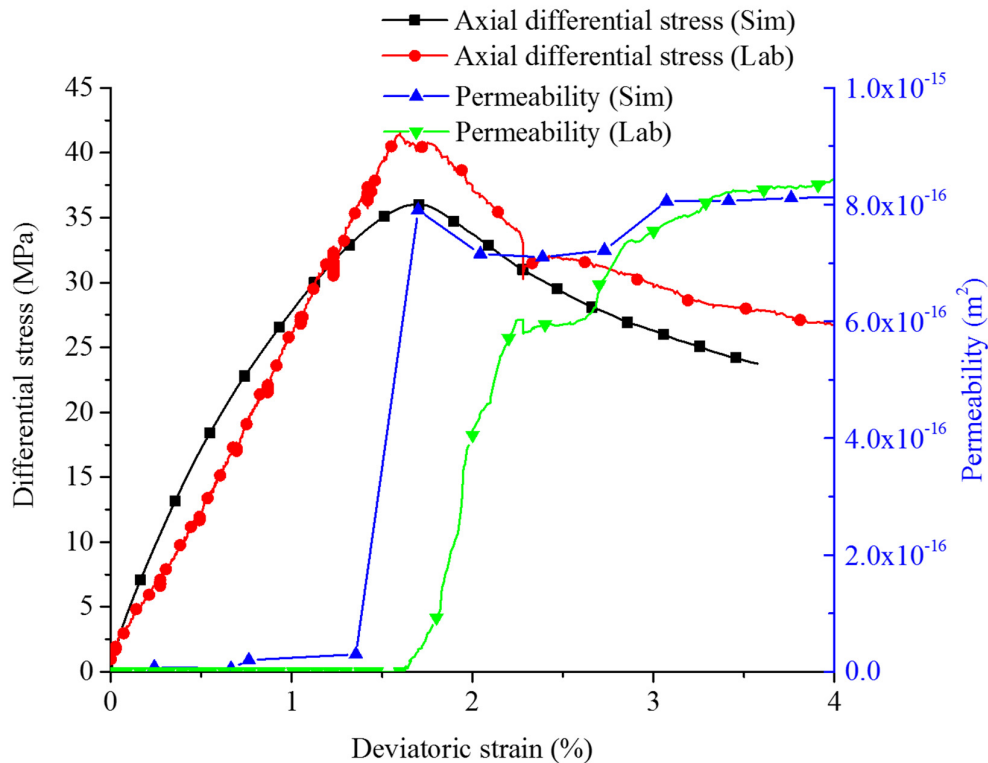


Figure 5.17 Stress-strain curves and permeability evolution for sample C13 (model reconstruction based on C1) under 5.0 MPa confining pressure (stationary phase)

Please note that, the numerical simulation results shown in Figure 5.17 are from reconstructed sample C1, because initial sample C13 was not reconstructed based on CT analysis. However, sample C1 and C13 are obtained from one coal block, and should have relatively similar components and structure.

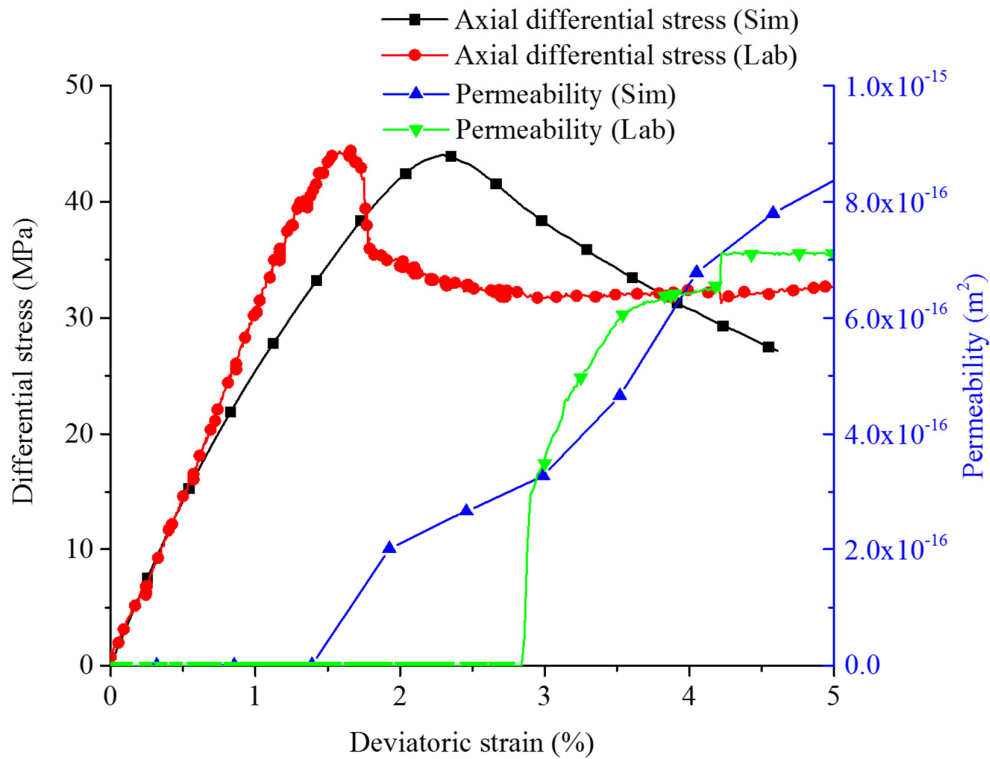


Figure 5.18 Stress-strain curves and permeability evolution for sample C4 under 7.5 MPa confining pressure (stationary phase)

As a result, the total number of cracks, number of opened cracks and accumulated total opening width are analyzed. Numbers of total and opened cracks are increasing continuously till the end of the simulation. These parameters cannot reflect the permeability evolution directly.

For some samples, a decrease of permeability occurs at the last stage where the sample model is fully damaged. By increasing axial stress and confinement, the main fractures and microcracks become closed. The effect of fracture closure dominates the process, and the residual permeability corresponds to the residual strength.

If the damage planes formed by fractures are parallel to the gas flow direction, the local permeability is quite high, as well as the overall permeability of the whole sample. On the contrary, if the damage paths cannot go through the entire height, the macroscopic permeability is much lower.

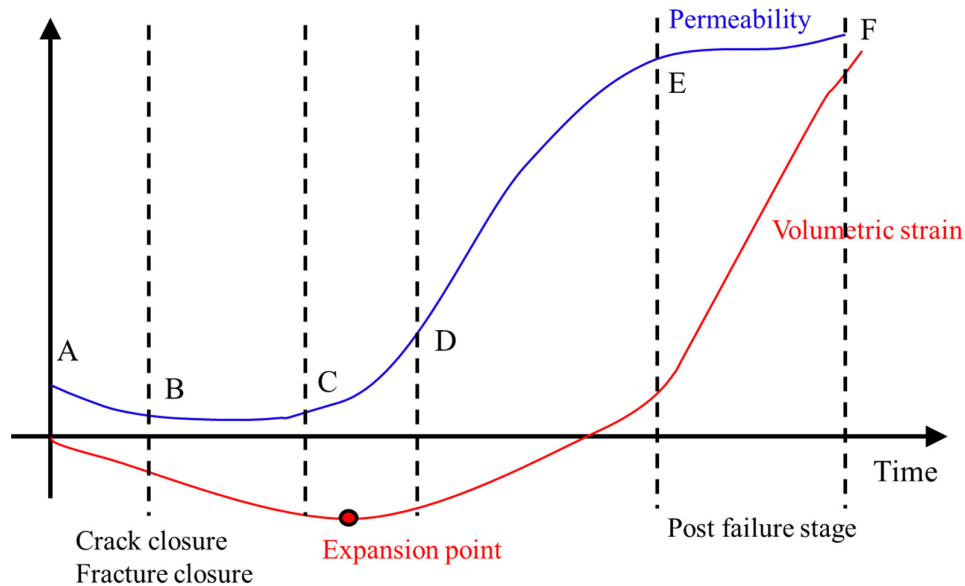
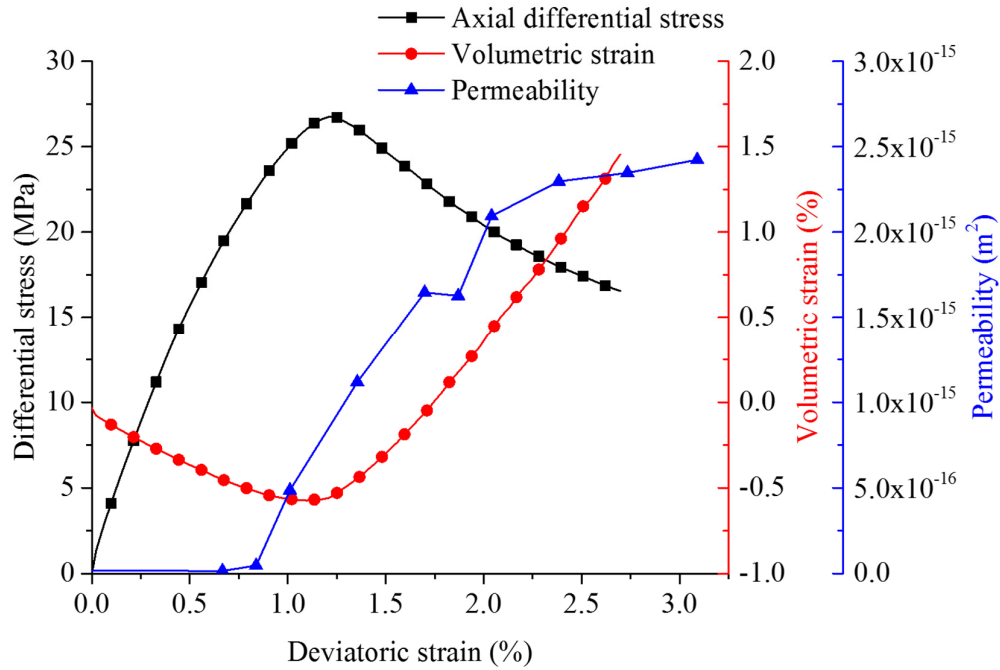


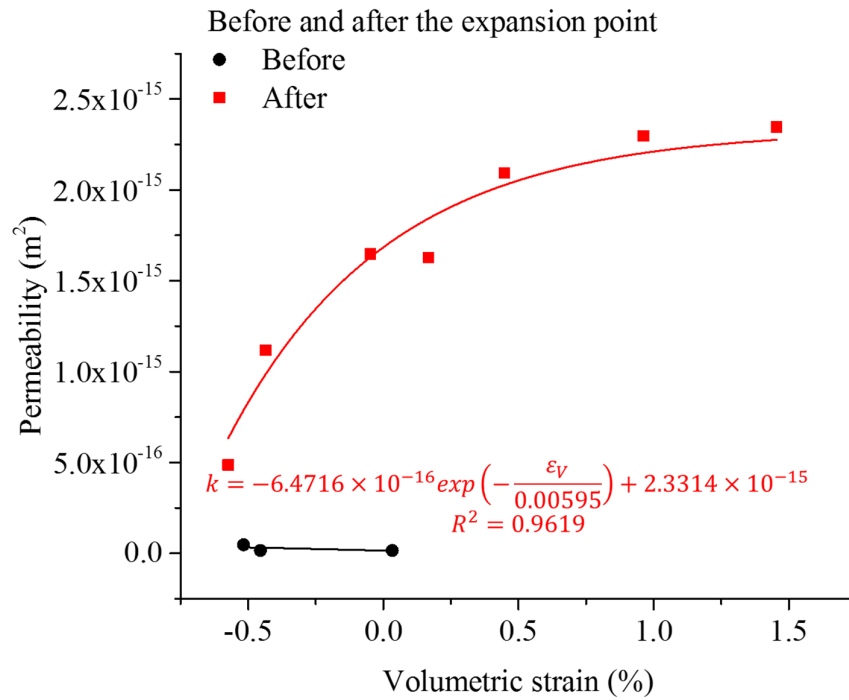
Figure 5.19 Schematic diagram for evolution of permeability and volumetric strain versus time (model C1 as example)

In general, permeability k is related to volumetric strain ε_V in brittle materials (e.g. Tan 2013). According to the permeability evolution trends as function of axial stress-strain relations, the permeability evolution can be divided into five stages as shown in Figure 5.19. In the first stage (A-B), both permeability and volumetric strain decrease with time. The initial cracks become closed at the beginning of this stage, followed by further closure of microscopic pores. In the second stage (B-C), the permeability tends to be stable at a very low level connected with closure of pre-existing pores and cracks, only a few new microcracks are generated. A dynamic balance is reached in this stage. In the third stage (C-D), volumetric strain turns from decreasing to increasing, the sample goes into the volumetric expansion phase (a corresponding expansion point can be noticed), and the cracks start to emerge, expand and connect with each other. Also in this stage, the permeability begins to increase, and the axial stress increases gradually up to the peak value. In the fourth stage (D-E), cracks are connected extensively, macroscopic fractures are formed, while the axial stress decreases drastically, the sample is in a failure state. The fifth stage (E-F) is the post failure stage, the volumetric strain increases continuously, but the increase rate slows down. The permeability evolution in this stage shows different types as mentioned before.

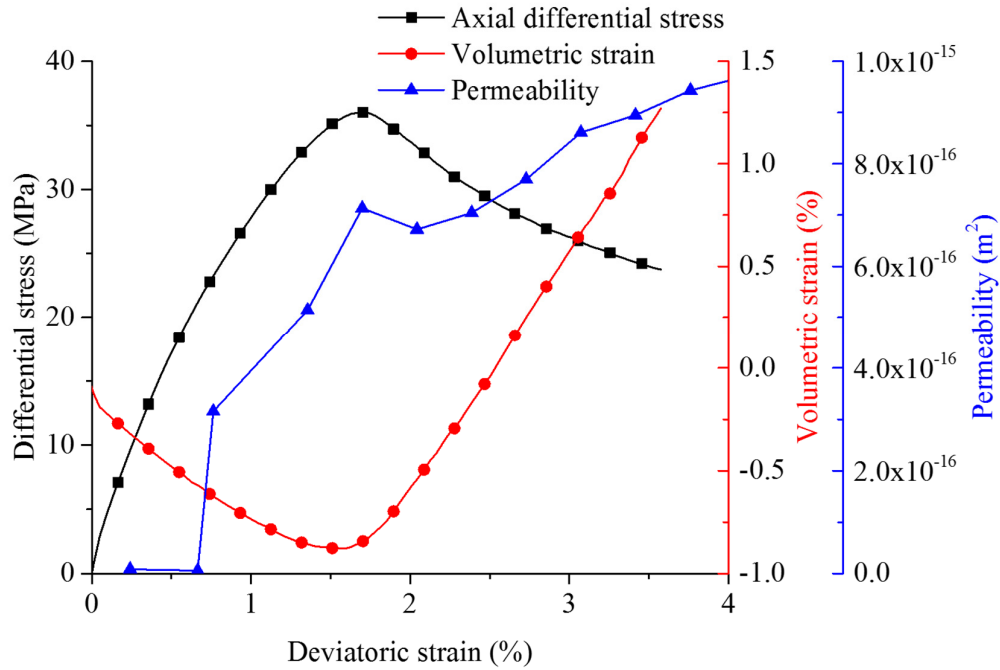
Axial differential stress, volumetric strain and permeability evolution as function of axial strain are shown in Figures 5.20, 5.21, 5.22, 5.23 and 5.24. As illustrated in these figures, volumetric expansion effects are observed in simulated models, and a fitting analysis is conducted to investigate the relation between permeability and volumetric strain.



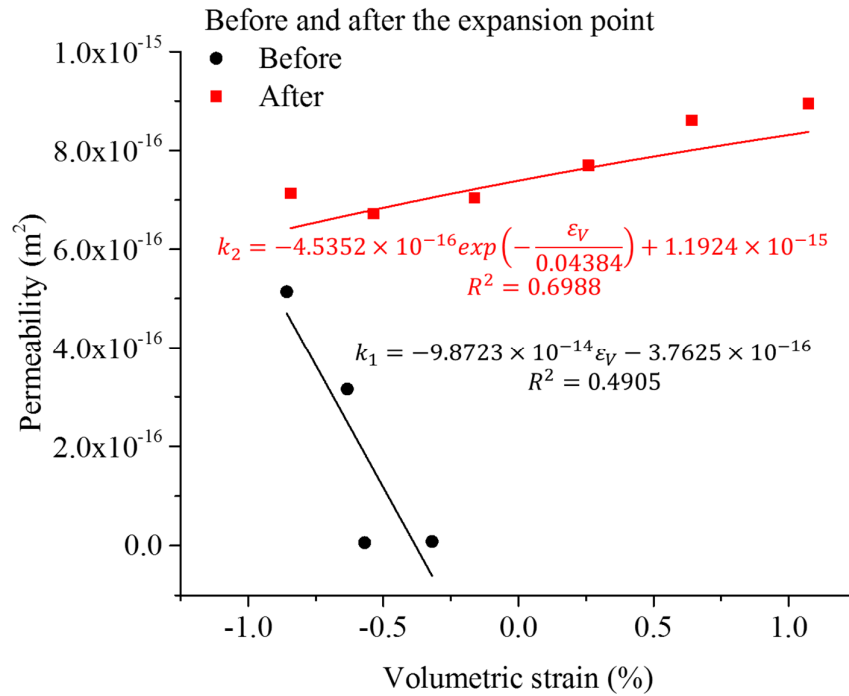
a-1: Differential stress, volumetric strain and permeability evolutions



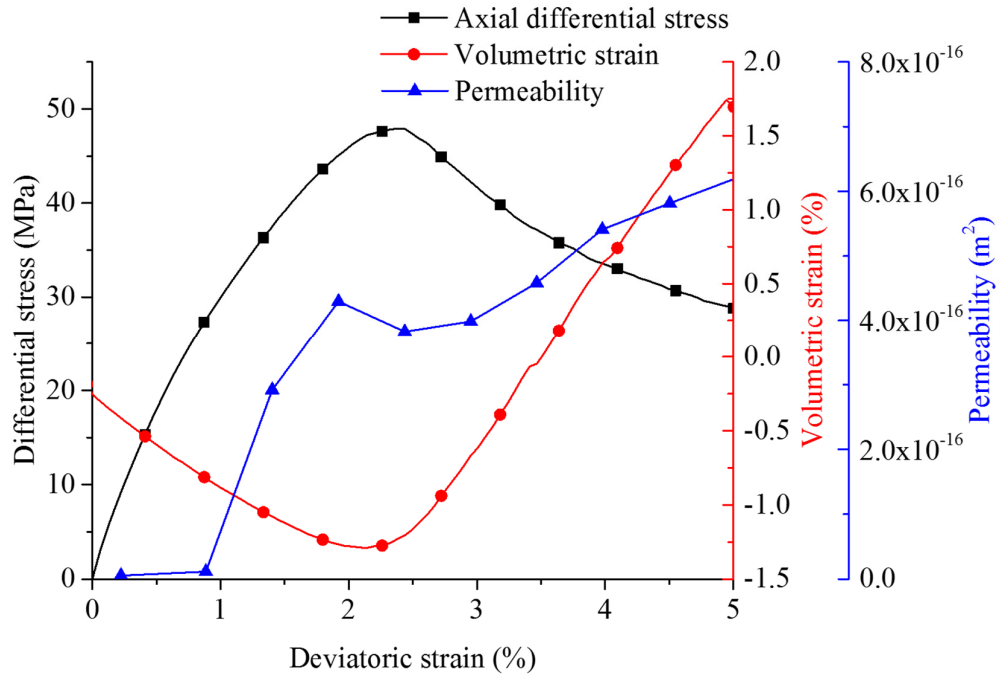
a-2: Fitting curve of permeability versus volumetric strain
 (a) 2.5 MPa confining pressure



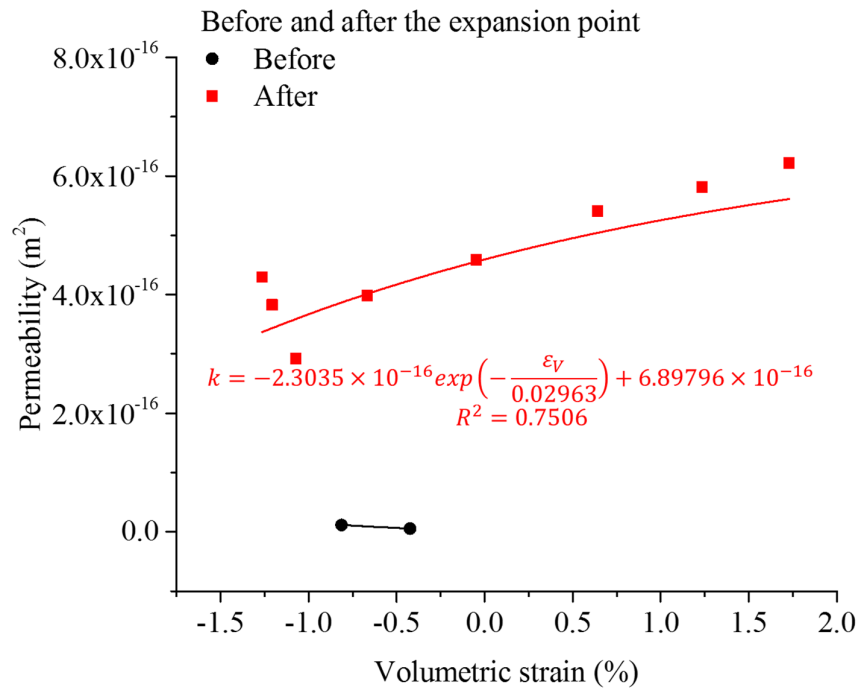
b-1: Differential stress, volumetric strain and permeability evolutions



b-2: Fitting curve of permeability versus volumetric strain
(b) 5.0 MPa confining pressure

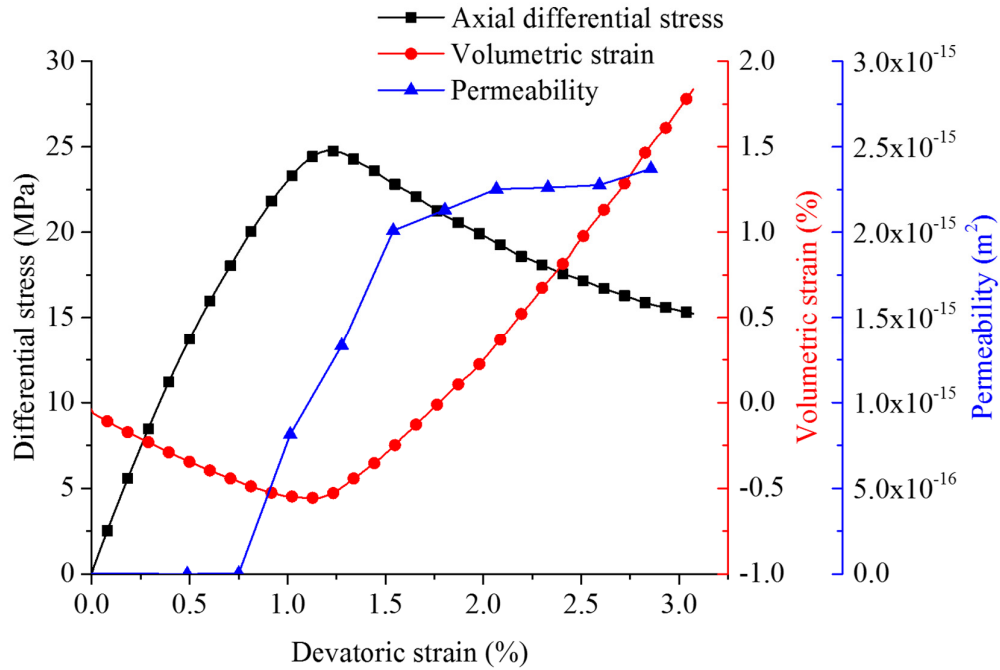


c-1: Differential stress, volumetric strain and permeability evolutions

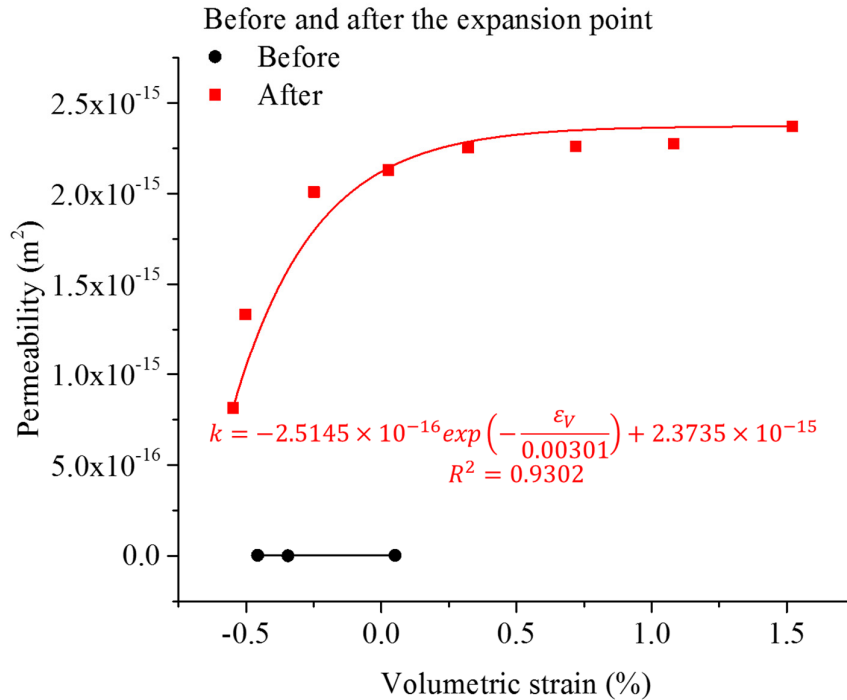


c-2: Fitting curve of permeability versus volumetric strain
(c) 7.5 MPa confining pressure

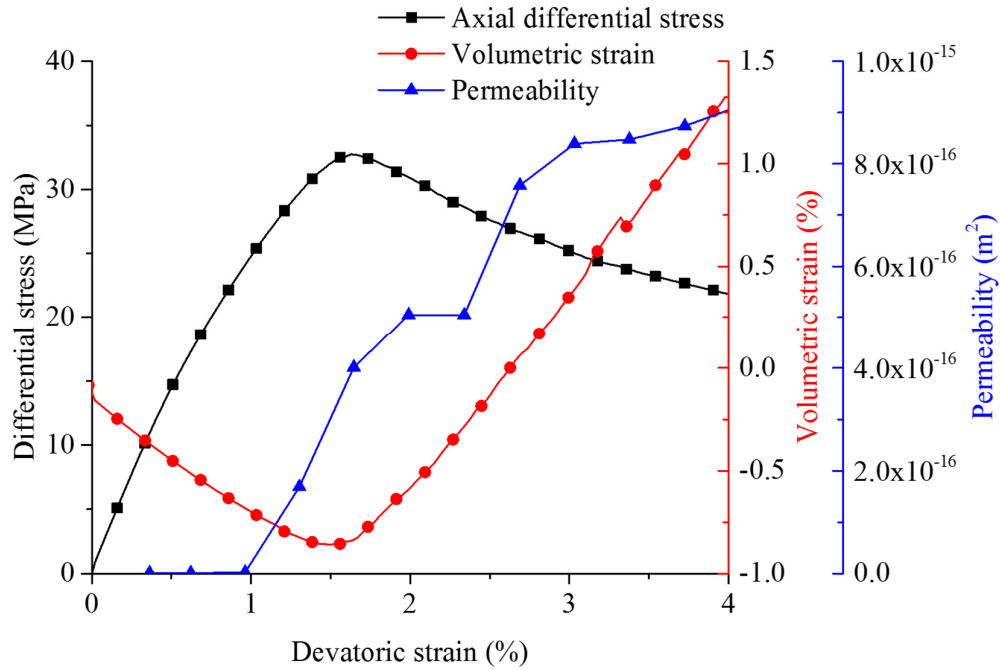
Figure 5.20 Permeability and strain evolution of coal sample C1 versus differential stress



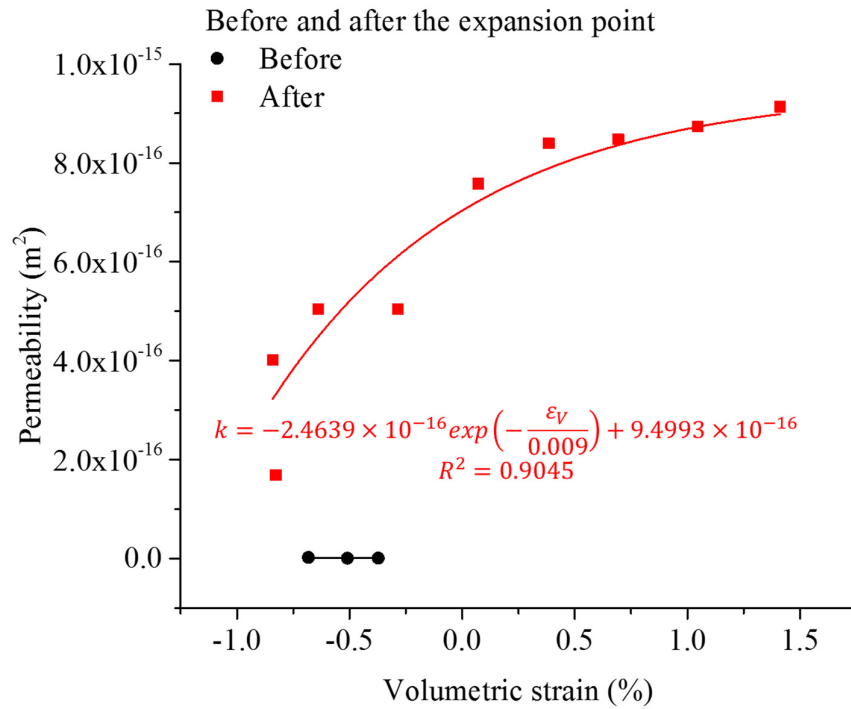
a-1: Differential stress, volumetric strain and permeability evolutions



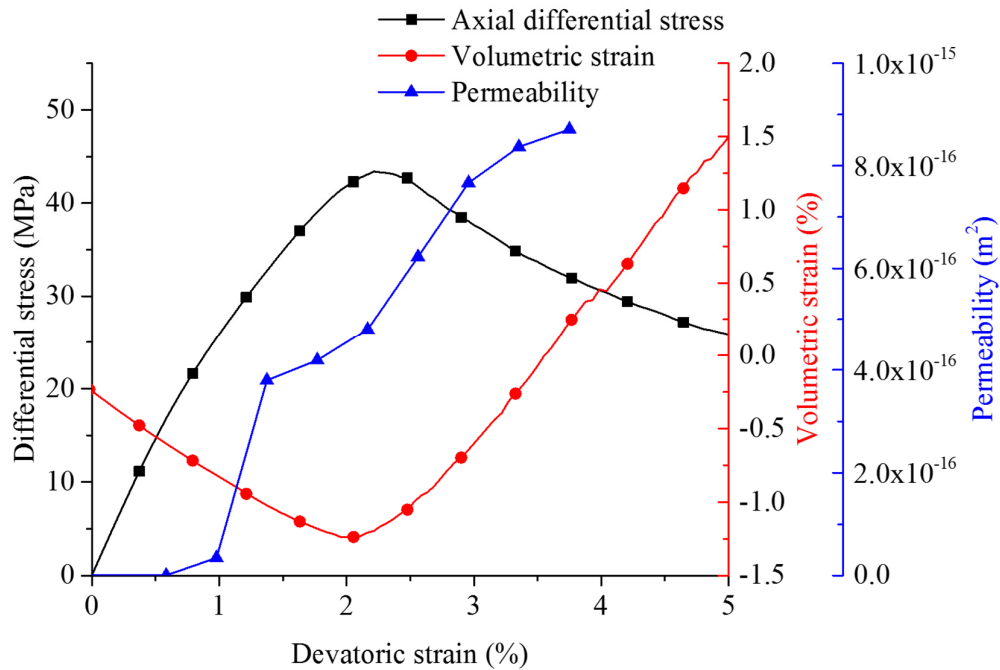
a-2: Fitting curve of permeability versus volumetric strain
(a) 2.5 MPa confining pressure



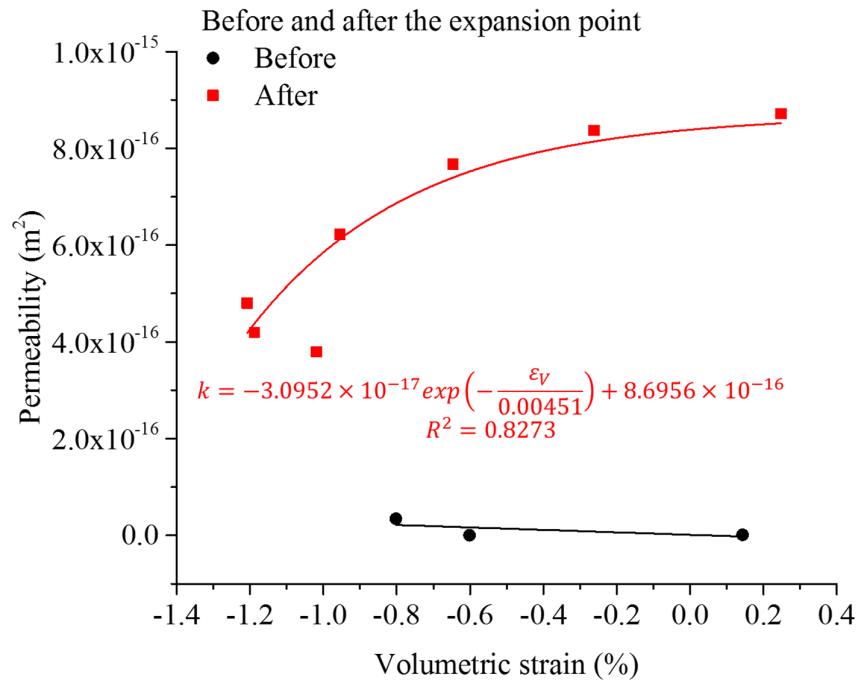
b-1: Differential stress, volumetric strain and permeability evolutions



b-2: Fitting curve of permeability versus volumetric strain
(b) 5.0 MPa confining pressure

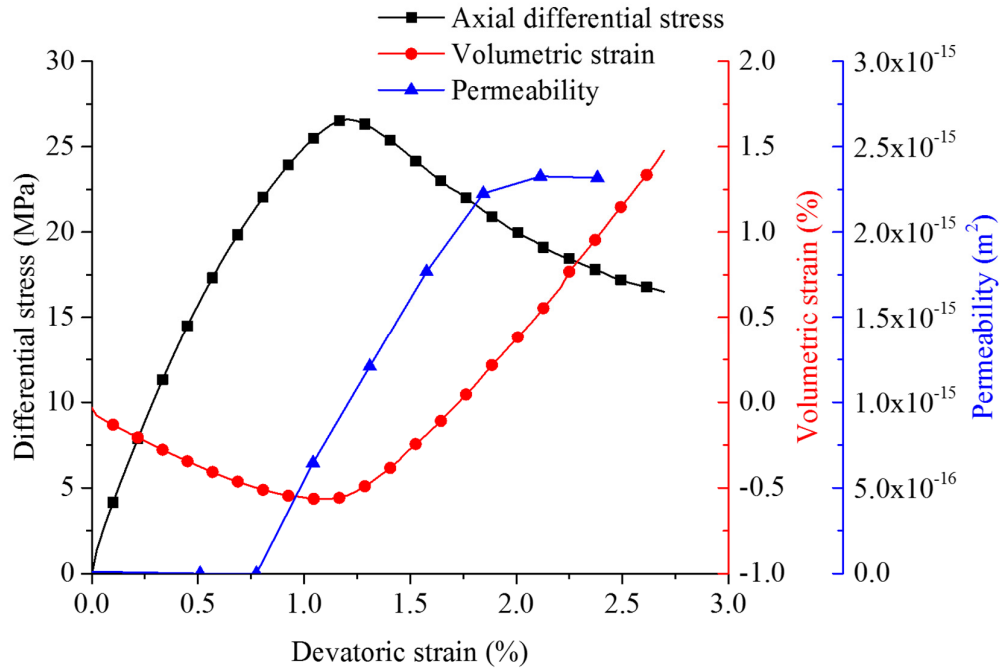


c-1: Differential stress, volumetric strain and permeability evolutions

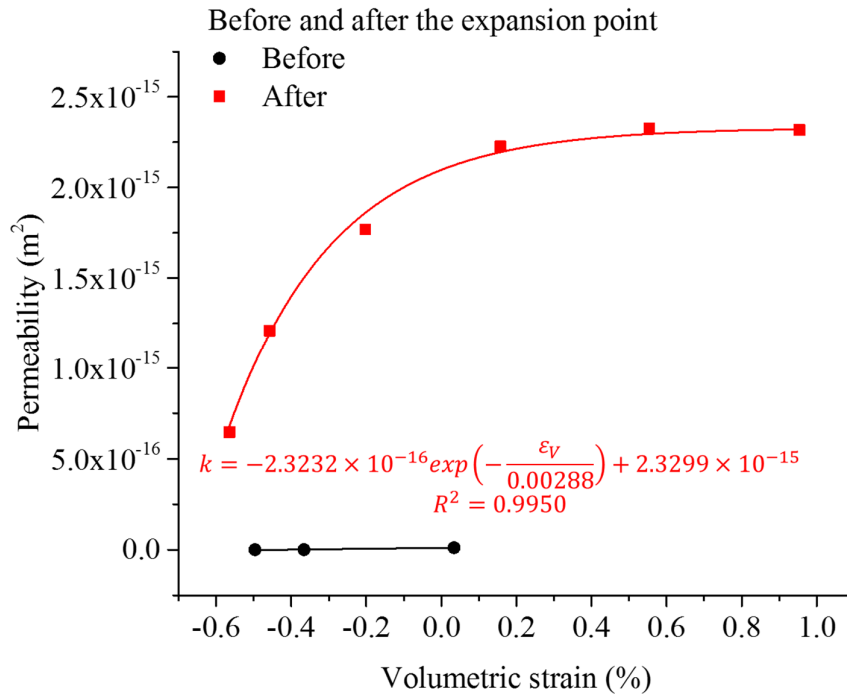


c-2: Fitting curve of permeability versus volumetric strain
(c) 7.5 MPa confining pressure

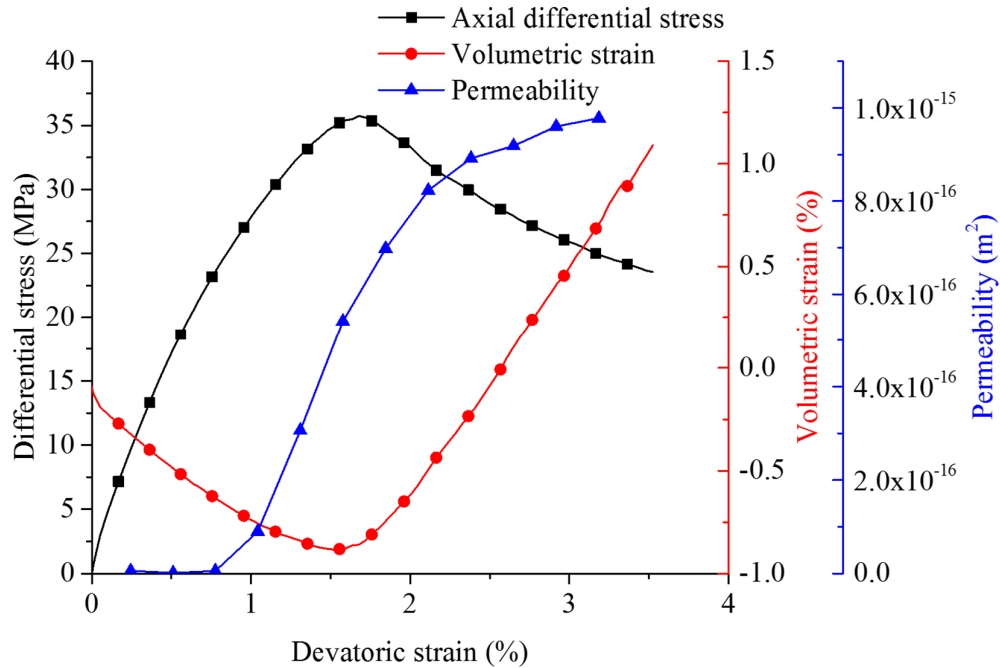
Figure 5.21 Permeability and strain evolution of coal sample C2 versus differential stress



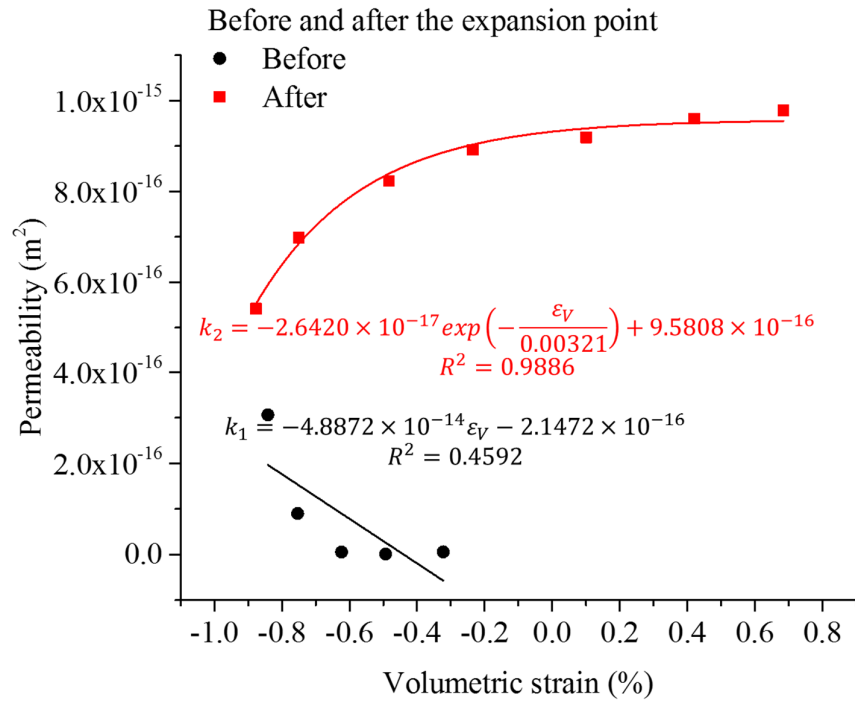
a-1: Differential stress, volumetric strain and permeability evolutions



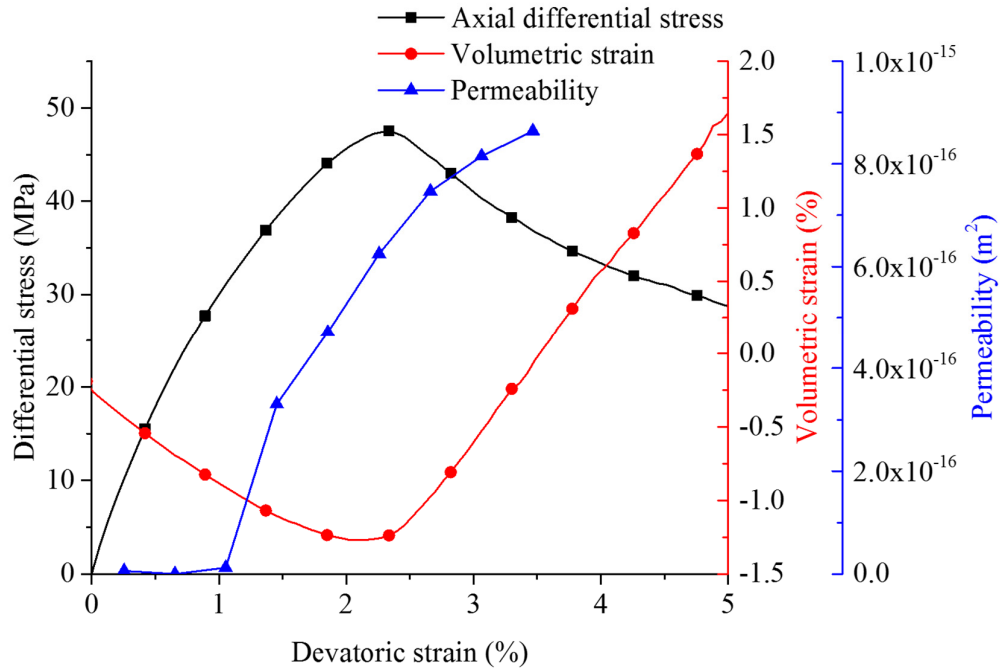
a-2: Fitting curve of permeability versus volumetric strain
(a) 2.5 MPa confining pressure



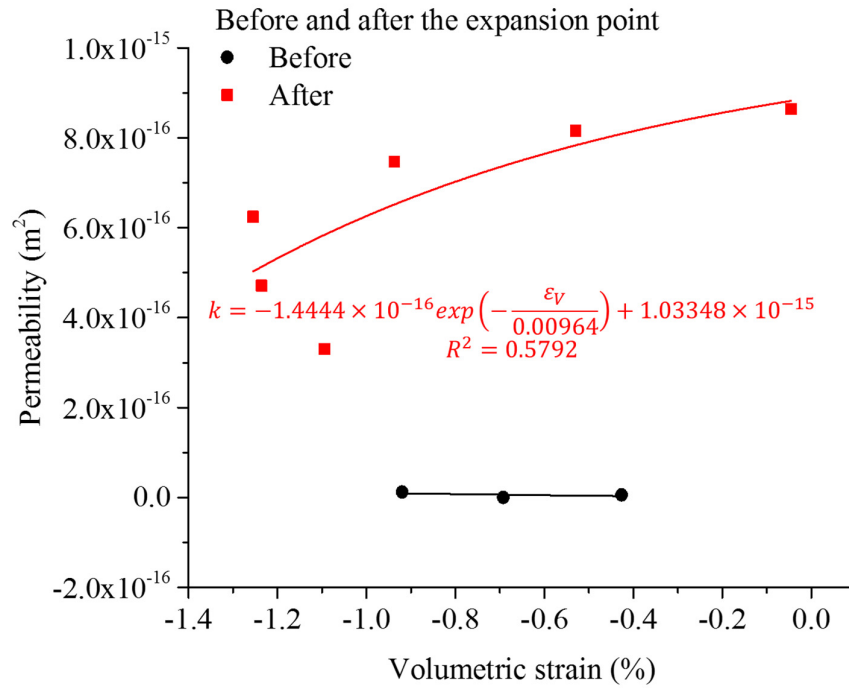
b-1: Differential stress, volumetric strain and permeability evolutions



b-2: Fitting curve of permeability versus volumetric strain
 (b) 5.0 MPa confining pressure

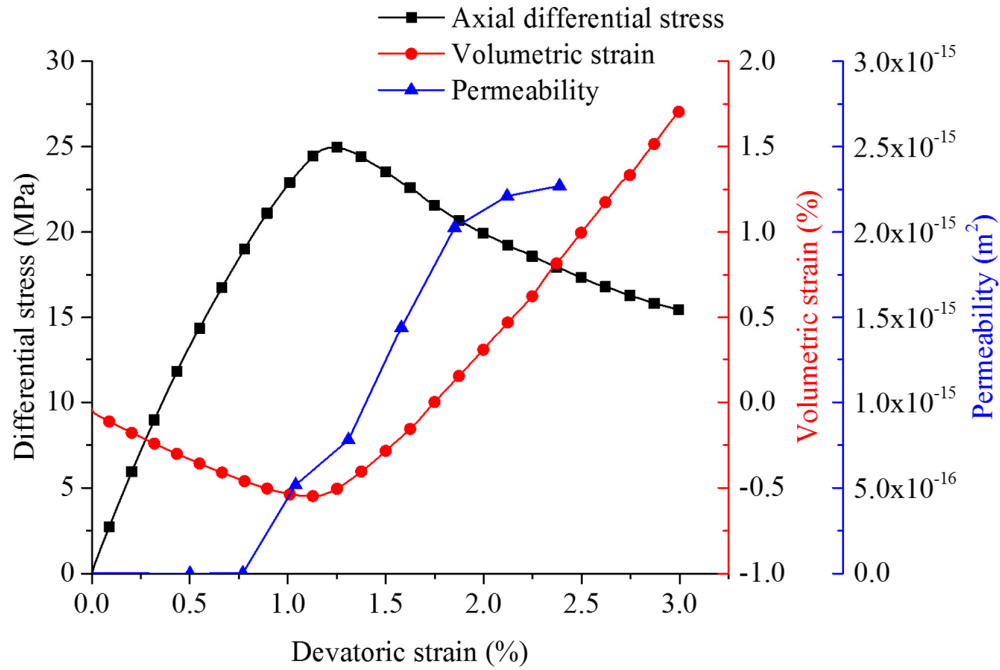


c-1: Differential stress, volumetric strain and permeability evolutions

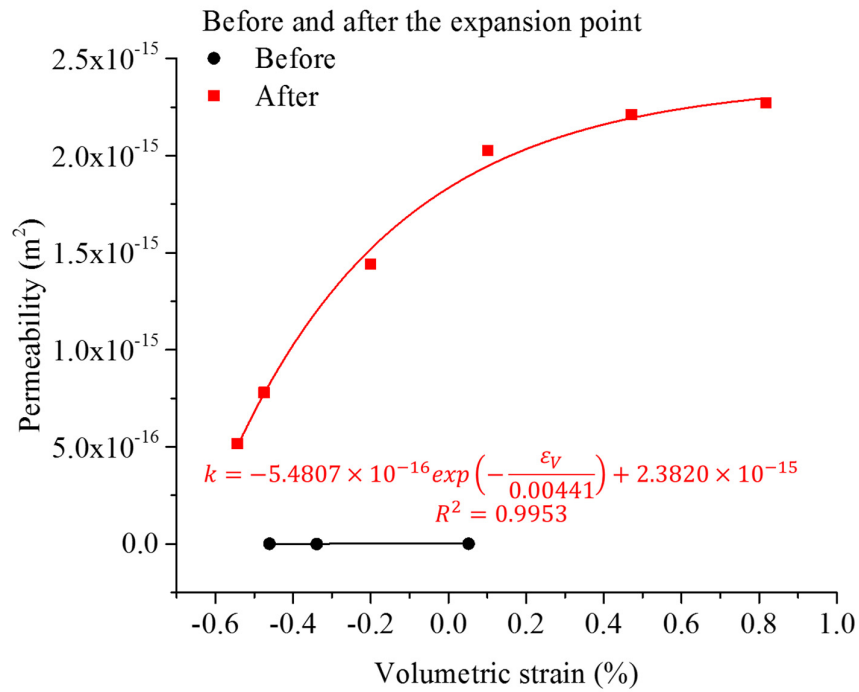


c-2: Fitting curve of permeability versus volumetric strain
(c) 7.5 MPa confining pressure

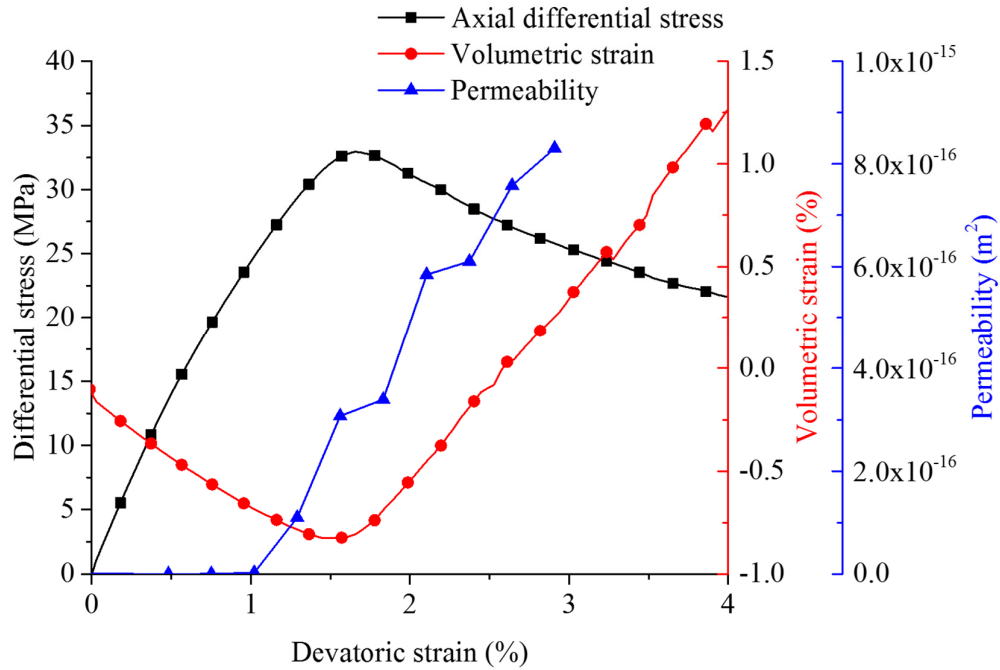
Figure 5.22 Permeability and strain evolution of coal sample C3 versus differential stress



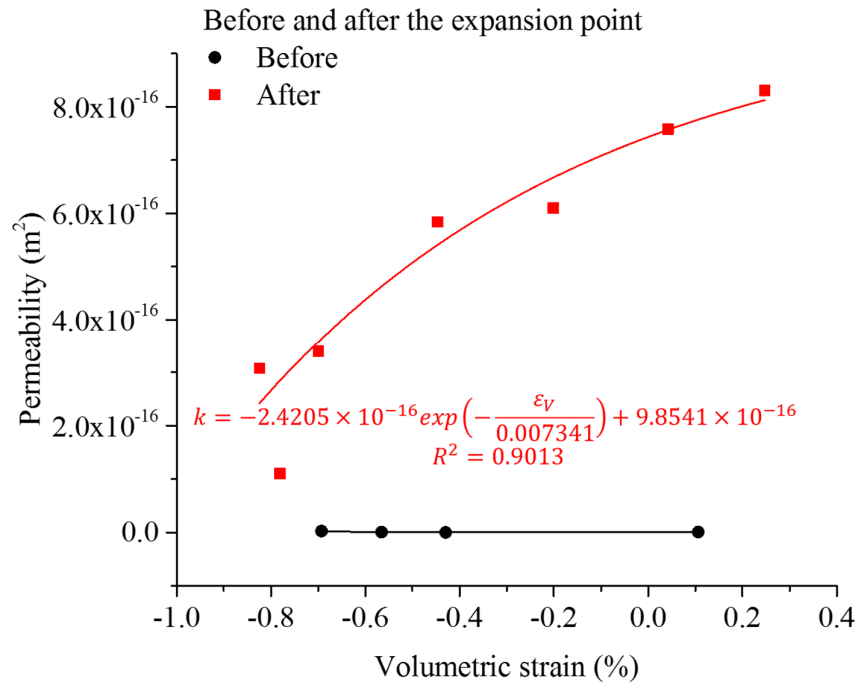
a-1: Differential stress, volumetric strain and permeability evolutions



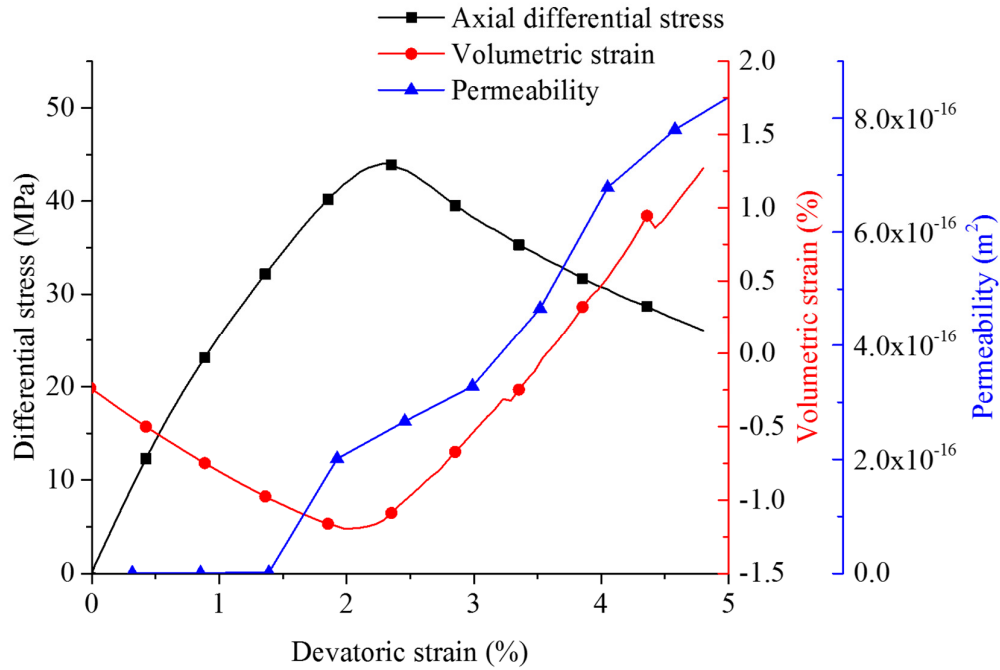
a-2: Fitting curve of permeability versus volumetric strain
(a) 2.5 MPa confining pressure



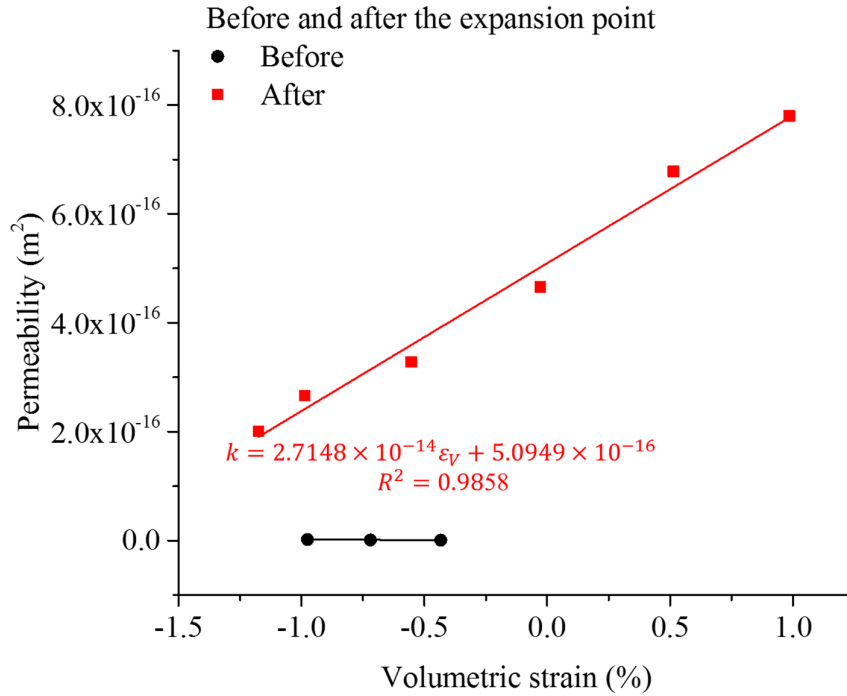
b-1: Differential stress, volumetric strain and permeability evolutions



b-2: Fitting curve of permeability versus volumetric strain
(b) 5.0 MPa confining pressure

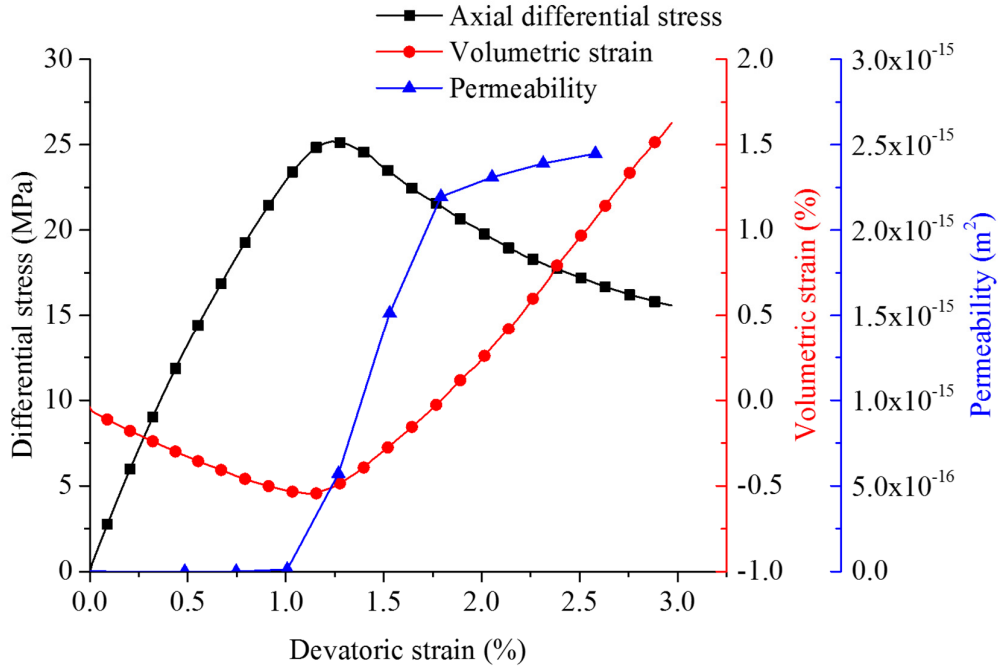


c-1: Differential stress, volumetric strain and permeability evolutions

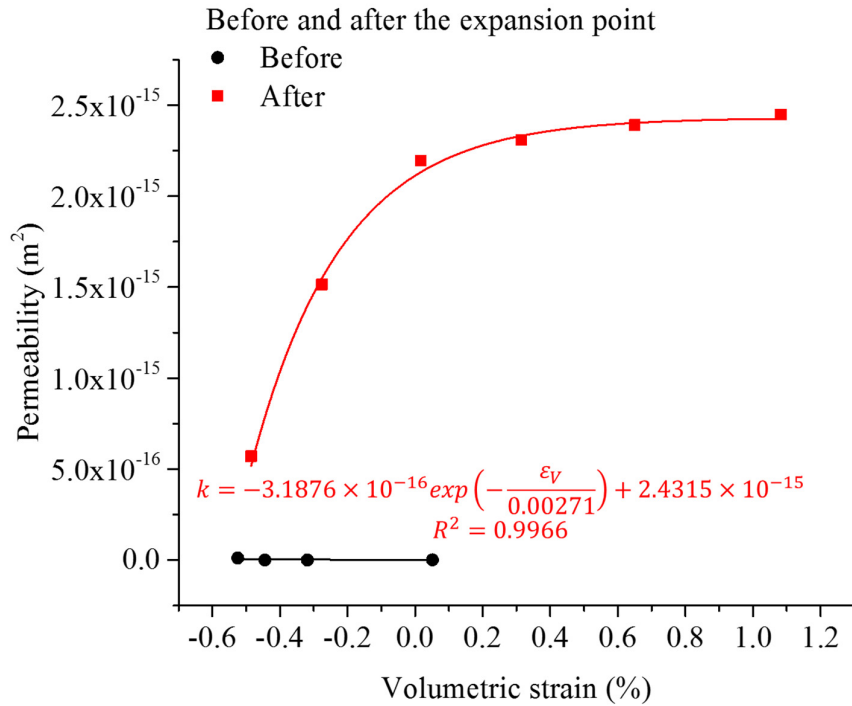


c-2: Fitting curve of permeability versus volumetric strain
(c) 7.5 MPa confining pressure

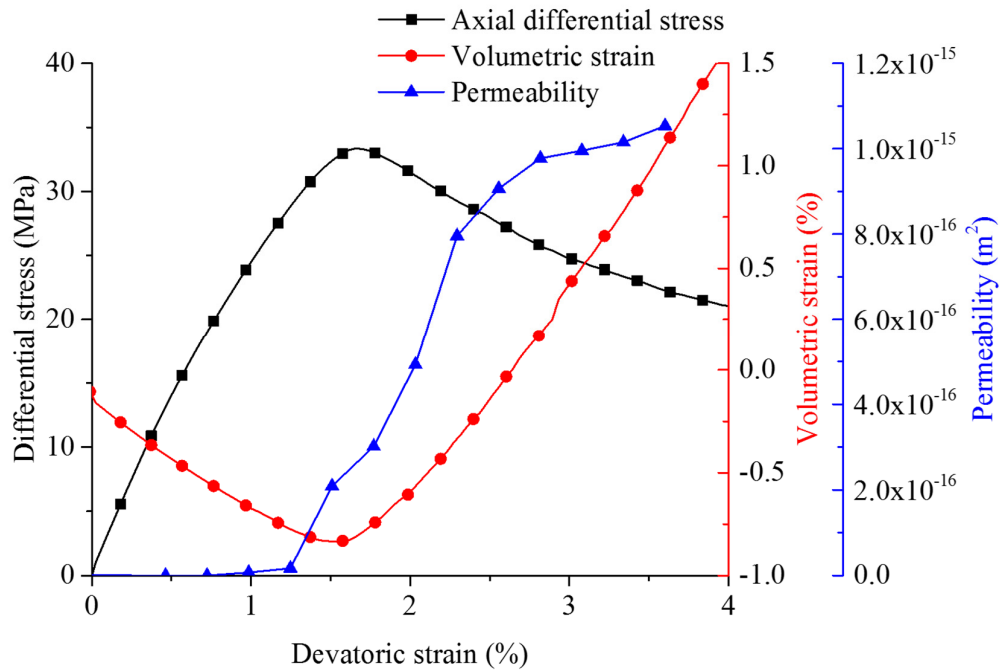
Figure 5.23 Permeability and strain evolution of coal sample C4 versus differential stress



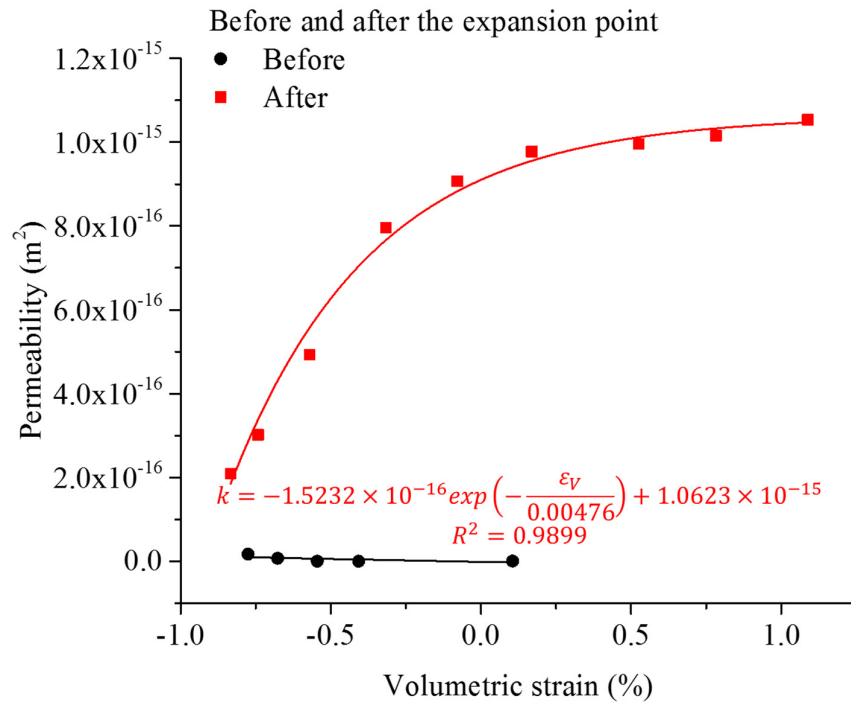
a-1: Differential stress, volumetric strain and permeability evolutions



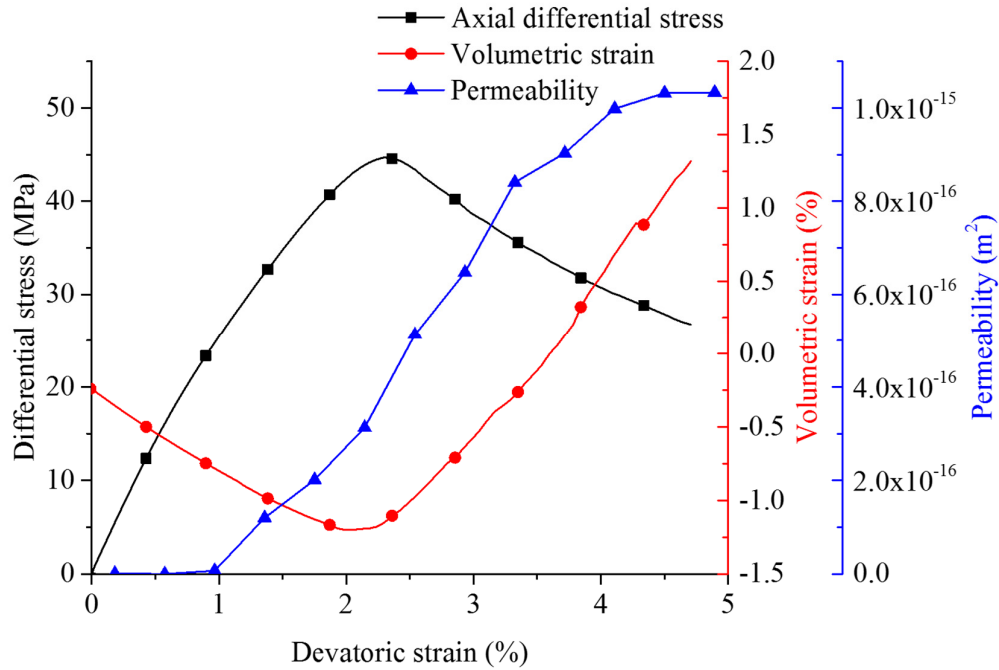
a-2: Fitting curve of permeability versus volumetric strain
(a) 2.5 MPa confining pressure



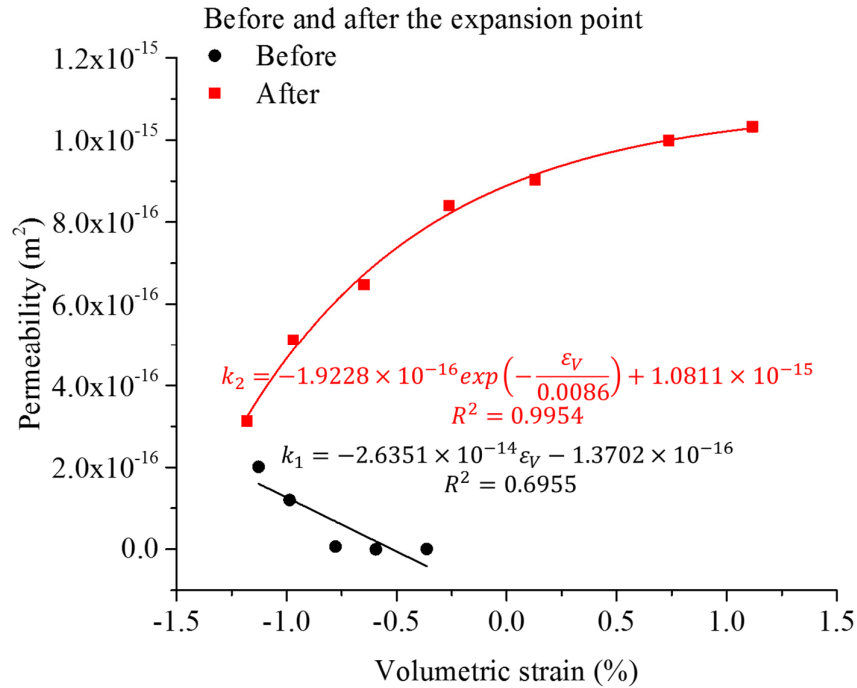
b-1: Differential stress, volumetric strain and permeability evolutions



b-2: Fitting curve of permeability versus volumetric strain
(b) 5.0 MPa confining pressure



c-1: Differential stress, volumetric strain and permeability evolutions



c-2: Fitting curve of permeability versus volumetric strain
(c) 7.5 MPa confining pressure

Figure 5.24 Permeability and strain evolution of coal sample C5 versus differential stress

As shown in the figures, permeability change and volumetric strain are relatively small prior to the expansion point, closures of pores and cracks lead to a volume decrease directly, but the permeability is only influenced by a very limited amount. After the expansion point,

permeability and volumetric strain show a nonlinear relation. The growing of macroscopic fractures can increase the volumetric strain and overall permeability simultaneously.

In one situation, the permeability at the expansion point is much higher than the initial permeability. A drastic increase in permeability occurs right before the expansion point. An average initial permeability can be used to represent the permeability prior to the expansion (see Figure 5.20(b,c), 5.21(c), 5.22(c) and 5.23(c)). The trends after the expansion point are fitted by exponential functions, but in special cases as shown in Figure 5.23(c), a linear relation provides better fitting.

In another situation, the permeability after reaching the expansion point is higher than before, but their values have the same order of magnitude. In this situation, permeability and volumetric strain are in good nonlinear exponential relation after the expansion point as shown in Figure 5.20(a), 5.21(a,b), 5.22(a), 5.23(a,b) and 5.24(a,b).

In a rare situation, the permeability begins to increase prior to the expansion point after only a very short decreasing and steady stage. This leads to another linear relation between permeability and volumetric strain before the expansion point. This special relation is determined by the specific structural character of the samples as shown in Figure 5.20(b), 5.22(b), and 5.24(c). Some weak planes failed and become connected with each other in the very early stage of compression.

As shown in Figure 5.20 and 5.22, all three situations mentioned above are observed during the simulations of sample C1 and C3. With a confinement of 2.5 MPa (see in Figure 5.20(a) and 5.22(a)), the permeability is constant in the contraction stage. Initial pores and cracks do not open in this stage. When the model expand, initial cracks open and new cracks are generated smoothly until failure of the models.

According to the structural characters of sample C1 and C3, obvious weak planes influence the results significantly. With a confinement of 5.0 MPa (see Figure 5.20(b) and 5.22(b)), the permeability decreases within a short period and then increases in the contraction stage. When new cracks are generated – especially shear cracks – and become connected along the weak planes – an increase is expected with compressed flow paths. In the expansion stage, the direct paths just expand to allow stronger gas flow through gradually.

This situation alters fundamentally with a confinement of 7.5 MPa as shown in Figure 5.20(c) and 5.22(c). As mentioned previously, a dynamic balance between closure of initial cracks and generation of new cracks is reached before the expansion point. Although shear cracks are created along the weak planes, the high confining pressure prevents crack opening. The permeability remains very low. As soon as the process reaches the expansion point, flow paths are formed and permeability becomes much higher than before.

For each numerical model, the exponential fitting curve shows high consistency. When analyzing the results of all the samples, the distinct structural features lead to obvious individual differences in permeability evolutions. As mentioned in Chapter 4, with high confining pressure, the structural differences are more pronounced in affecting the mechanical properties compared

to low confining pressure (see Figure 4.26). The permeability evolution, which is directly connected with damage pattern, shows similar behavior. The permeability evolution at a confining pressure of 7.5 MPa shows much higher scatter in a relatively small range. The obtained fitting curves may not allow to predict the behavior of individual samples, but deliver a reasonable overall trend.

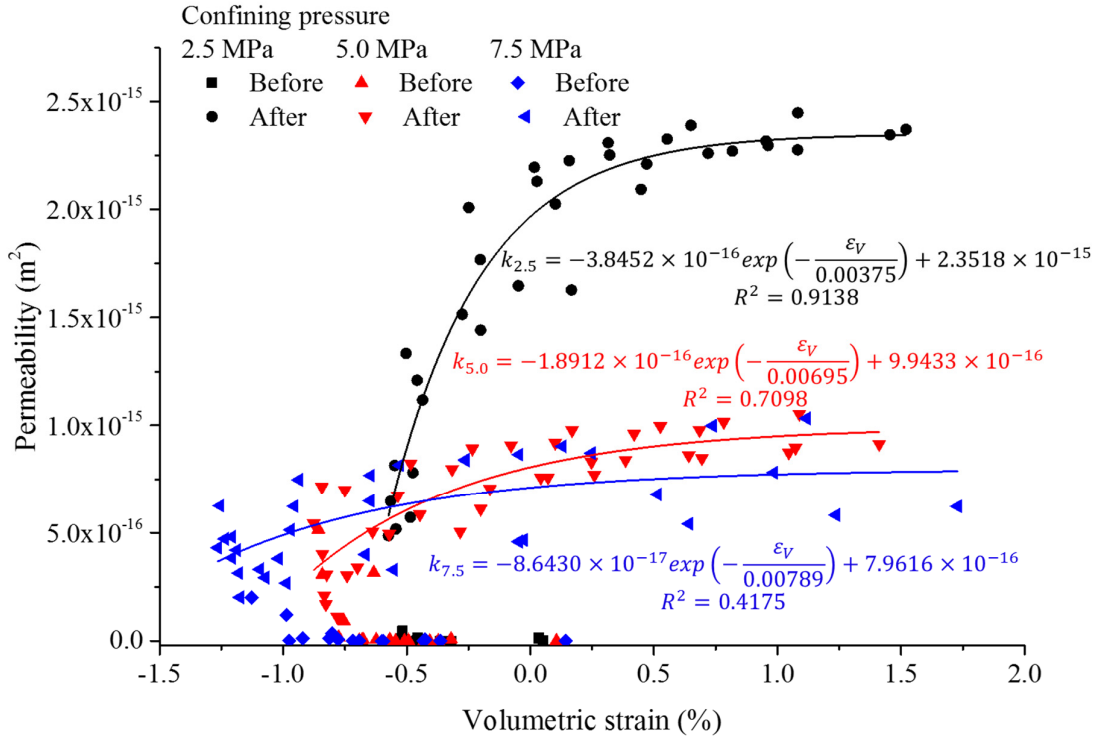


Figure 5.25 Permeability versus volumetric strain for different confining pressures (regression lines refer to values after the expansion point)

In Figure 5.25, relations between permeability and volumetric strain are shown for different confining pressures. Nonlinear exponential trends of permeability increase with volumetric strain are obtained for the expansion stage. The following Equation 5.19 is derived to express these trends. A “jump” in permeability values are clearly noticed around the expansion point. This phenomenon is more remarkable at high confining pressures.

$$k = A \cdot \exp\left(\frac{\varepsilon_V}{C}\right) + B \quad \text{(Equation 5.19)}$$

The values of variables A, B and C are listed in Table 5.3. Relations between overall permeability and volumetric strain under different confining pressures are obtained.

Table 5.3 Variables in Equation 5.19 for different confining pressures

σ_3 (MPa)	A ($\times 10^{-16}$)	B ($\times 10^{-16}$)	C	R^2
2.5	-3.8452	23.5180	-0.00375	0.9138
5.0	-1.8912	9.9433	-0.00695	0.7098

7.5	-0.8643	7.9616	-0.00789	0.4175
-----	---------	--------	----------	--------

Variables A and C decrease with the increase of confining pressure, while variable B increases in contrary. After considering the variations of A , B and C with σ_3 , Equation 5.20, 5.21 and 5.22 are obtained.

$$A = -5.1811 \times 10^{-16} + 5.9618 \times 10^{-17} \cdot \sigma_3 \quad (\text{Equation 5.20})$$

$$B = 1.0888 \times 10^{-14} \cdot \exp\left(\frac{\sigma_3}{1.2992}\right) + 7.6229 \times 10^{-16} \quad (\text{Equation 5.21})$$

$$C = 0.0154 \cdot \exp\left(\frac{\sigma_3}{2.0408}\right) - 0.0083 \quad (\text{Equation 5.22})$$

By substituting Equation 5.20, 5.21 and 5.22 into Equation 5.19, the permeability k can be calculated. These equations allow a rough prediction of permeability based on volumetric strain considering confinement at least for confining stresses between about 1.5 and 8.5 MPa.

The sample volume at the expansion point decreases with higher confining pressure. By analyzing all simulation results: the corresponding volumetric strain at the expansion point is about -0.49% under a confining pressure of 2.5 MPa. When the confining pressures are 5.0 and 7.5 MPa, the corresponding volumetric strains are -0.77% and -0.92% .

5.6 Conclusions

The coupling between permeability change and growth of microcracks is investigated. A special designed coupling between two different numerical models is effective in simulating the permeability of damaged coal samples. The coupling between PFC^{3D} and FLAC^{3D} uses the superiorities of both methods.

The permeability of damaged coal samples is closely associated with crack pattern in general and crack width in particular. Relations between hydraulic properties and fracture data are established. The properties of both, tensile and shear fractures are derived separately based on the mechanical interaction of particles. A specific region with tiny internal cracks exhibits significantly higher permeability than the intact state, furthermore a significant increase in permeability is detected with slight increase of the crack width.

A theoretical approach for predicting the permeability is proposed based on fracture distribution and single crack behavior. The coupled model simulates the seepage process (experimentally verified) as a function of opening and closure of microcracks.

Destruction of the coal sample is the final outcome of damage accumulation. The increasing permeability of up to 2 orders of magnitude is directly connected to the crack/fracture network evolution. Dilatancy (volumetric deformation) of shear fractures causes substantial increase of permeability.

Permeability and volumetric strain show good nonlinear exponential relation after the expansion point. Piecewise relations fit the whole process, the expansion point can be treated as critical point. The structural characteristics of the samples influence this relation before and after the expansion point significantly.

The model predictions are acceptably accurate on the conservative side. The numerical simulations provide guidance for practical gas control. Based on the experimental evidences, this micromechanical based modelling approach is applicable for the description of induced anisotropic damage and permeability evolution. The proposed model contains more parameters than classical macroscopic damage models. Therefore, adequate characterization of the internal structure as well as the hydro-mechanical properties and in-situ stress conditions (and its change due to engineering activities or tectonic causes) are key issues for a realistic understanding and quantification of permeability and its evolution.

6 Conclusions and outlook

This work presents results of an experimental and numerical study of the gas permeability evolution of coal samples under conditions relevant to mining disturbed coal seams. The study focuses primarily on quantifying and understanding the phenomena and processes associated with CT based sample reconstruction and gas flow under confined mechanical conditions using lab tests and numerical simulations. In particular, the study addresses the coupling between DEM and FDM for modeling gas-coal systems. This work is motivated by the need for an improved understanding of the micro-structural effects on the seepage processes in coal samples in the context of stress-induced situations, in order to help predicting the permeability properties of coal.

6.1 Main conclusions

The following main conclusions can be drawn:

(1) Five coal samples were scanned and reconstructed in this research. X-ray CT techniques offer some remarkable advantages such as the non-destructive detection and 3D visualization of the inner heterogeneity of the samples.

Slicing analyses of the coal samples demonstrated that the distributions of both, pores and minerals, are highly inhomogeneous. Also, main fractures can be determined by 3D reconstruction of CT slices. The detected spatial structure of the coal demands a complete 3D consideration. This is confirmed by the conducted comparative 2D and 3D simulations.

Deformations of the samples are directly related to the fracture connectivity. Fracture aperture, fracture plane evolution and fracture orientation are the main factors to evaluate the degree of damage. The obtained stress-strain curves can be related to the accumulation of fractures. Numerical models of coal sample replicating the inner structure are generated to simulate the loading process and to calibrate the mechanical parameters.

(2) The evolution of coal permeability under different stress states was investigated by HM-coupled conventional triaxial compression tests. The evolution process has been described by several distinct phases in terms of permeability and deformation. Peak permeability appears after peak stress, and permeability remains relatively constant at relatively high values during the subsequent plastic compaction stage.

Peak stress and peak permeability of the samples depend heavily on confining pressure. In general, the permeability increased dramatically after the sample has reached the stress point σ_d when flow rate was detected firstly or recovered from minimum states.

Fractures propagate through the samples easily at low confining pressures, which lead to high permeability of the sample. On the contrary, at high confining pressure, only a few main fractures are generated with orientation towards the side surfaces, and low permeability is maintained until the failure of the sample.

(3) Triaxial tests are simulated in 3D with the particle-based DEM code PFC^{3D} using a new developed flexible membrane boundary. In this thesis, triaxial test simulations are validated by comparing the stress-strain response and fracture pattern of coal samples obtained by lab testing. Force chains evolve at the contacts at the membrane – sample interface. The importance of realistic membrane boundary simulation is demonstrated and compared with other methods.

The results showed that DEM models can capture the expected macroscopic response considering varying void ratios, confining stresses and loading paths without additional complex model recalibration. Different failure modes have been reproduced with numerical simulations regarding varying confining pressures.

A series of triaxial compression tests with reconstructed numerical models were conducted. The composition of the samples (matrix and inclusions) influences the peak strength. Force chain development and crack distributions are also affected by the distribution of inclusions inside the sample. Increasing confinement leads to a change of damage pattern. The fractures tend to propagate towards side surfaces at higher confinement.

(4) A special designed coupling between two different numerical models is effective in simulating the permeability of damaged coal samples. This coupling between PFC^{3D} and FLAC^{3D} expands the superiorities of both methods.

Relations between hydraulic properties and fracture data are established. The properties of both, tensile and shear fractures are derived separately based on the mechanical interaction of particles. A specific region with tiny internal cracks exhibits significantly higher permeability than the intact state, furthermore a significant increase in permeability is detected with slight increase of the crack width.

A theoretical approach for predicting the permeability was proposed based on fracture distribution and single crack behavior. The coupled model simulates the seepage process (experimentally verified) as a function of opening and closure of microcracks.

Destruction of the coal sample is the final outcome of damage accumulation. An increasing permeability of up to 2 orders of magnitude is directly connected to the crack/fracture network evolution. Dilatancy (volumetric deformation) of shear fractures causes substantial increase of permeability.

Permeability and volumetric strain show nonlinear exponential relation after the expansion point. Piecewise relations fit the whole process. The expansion point can be treated as critical point. The structural characteristics of the samples influence this relation before and after the expansion point significantly.

The numerical simulations provide guidance for practical gas control. Based on the experimental evidences, this micromechanical based modelling approach is applicable for the description of induced anisotropic damage and permeability evolution. The proposed model contains more parameters than classical macroscopic damage models. Therefore, adequate characterization of the internal structure as well as the hydro-mechanical properties and in-situ

stress conditions (and its change due to engineering activities or tectonic causes) are key issues for a realistic understanding and quantification of permeability and its evolution.

6.2 Implications for practical purposes

The present study offers several new approaches for industrial use and numerical simulation development.

(1) The reconstruction process based on X-ray CT techniques offers non-destructive methods to investigate materials. This method is suitable for the research of sandstone, marble or other inhomogeneous rocks. If the components inside the materials show significant contrast, this method provides an accurate quantitative analysis for internal structures.

(2) The new designed 3-axial compression model showed that DEM models can capture the expected macroscopic response via simulations with varying void ratio, confining stress and loading path without the need for model recalibration. The results showed that the new developed FW approach can replicate the boundary conditions better than rigid membranes or particle based membranes. It has been proven that the simulations have the ability to accommodate various failure modes. Different failure modes have been reproduced with numerical simulations considering varying confining pressures. Furthermore, the modeling of salt rock with creep effects is suitable for this method too. A wall servo function with specified confining stress is accessible.

(3) The stress redistributions in surrounding coal rock in underground coal mines can be obtained by in-situ measurements and theoretical analysis. The coal samples from the field can be investigated following the methods mentioned in this work and relationships between permeability and volumetric strain can be achieved. After importing the relationship to in-situ conditions, the permeability evolution can be predicted at a specific position in the surrounding coal rocks.

Traditional lab tests, such as uniaxial and triaxial tests, are needed to provide basic mechanical parameters. Numerical simulations offer effective methods to reproduce the seepage process. New coupled modeling like generated in this work provide a quantitative analysis to connect crack propagation and hydraulic properties. Volumetric strain becomes an impotent indicator to evaluate the permeability of coal rock.

6.3 Outlook for future research

The results of the work described in this thesis have contributed to the understanding of structural effects on seepage processes in coal samples experiencing different boundary conditions. This works provides a basis for improved permeability evolution modelling and hence for improved risk assessment and behavior prediction for underground mining operations. Nonetheless, the coupled models employed include several assumptions, and there are shortcomings in the experimental method, the equipment and the computational capabilities. Moreover, new problems are also identified. Some issues and suggestions for future research are discussed below.

- (1) As all samples used are from one working face, they have similar structural characteristics and inclusive components. Investigations on more samples from different coal fields would be useful to get a more fundamental understanding for coupled effects.
- (2) All models in this study contain only one single type of inclusion. Sub-division of material is not included when analyzing the hydraulic properties. The influence of initial nano-pores and cracks is minor, their behavior cannot be completely captured with current laboratory apparatuses. Advanced measurement techniques are needed to research the sorption and diffusion processes at the μm -scale or even below.
- (3) The post-peak behavior related to strain and damage localization has not been considered in this paper, which may be one of the possible extensions of the present work. The validation against in situ measurements should also be crucial in view of engineering applications.
- (4) Future studies should therefore investigate the coupled effect of stress, swelling, sorption and diffusion on permeability of coal samples under in-situ boundary conditions. This can be approached by developing models linked to our property assignment at the microscopic level. These microscopic models should be validated by in-situ measurements or experiments. Also, how fracture permeability depends on gas pore pressure need to be investigated after considering these parameters.

Appendix

A1: Wall update commands for FW approach in PFC^{3D}

Wall elements are updated by pairs, initially a pair of triangle walls forms one square unit. The following command codes are used to stretch or squeeze a wall to remain connecting with its surrounding walls.

Code:

```

loop foreach fl_ fl1_ ;loop the first wall facet of target unit
v11_ = wall.facet.vertex(fl_,1)
v12_ = wall.facet.vertex(fl_,2)
v13_ = wall.facet.vertex(fl_,3)
c11_ = wall.vertex.pos(v11_)
c12_ = wall.vertex.pos(v12_)
c13_ = wall.vertex.pos(v13_)
;stretch or squeeze the wall element to the new shape by setting the new vertex positions
;setting of target wall
wall.vertex.pos(v11_) = c11_ ;set the vertex position of point Nr.1 (in vector)
wall.vertex.pos(v12_) = cu1_ ;set the vertex position to connect the unit upside
wall.vertex.pos(v13_) = cr1_ ;set the vertex position to connect the unit on right side
;the exact coordinate of 3 vertices of new wall 1
xc11_ = wall.vertex.pos.x(v11_)
yc11_ = wall.vertex.pos.y(v11_)
zc11_ = wall.vertex.pos.z(v11_)
xcu1_ = wall.vertex.pos.x(vu1_)
ycu1_ = wall.vertex.pos.y(vu1_)
zcu1_ = wall.vertex.pos.z(vu1_)
xcr1_ = wall.vertex.pos.x(vr1_)
ycr1_ = wall.vertex.pos.y(vr1_)
zcr1_ = wall.vertex.pos.z(vr1_)
; caculate the area of the new triangle wall
tf1_ = cons_ * ar1_ ; new target force, ar1_ is the new area of triangle wall
xv1_ = wall.facet.normal.x(fl_)
yv1_ = wall.facet.normal.y(fl_)
zv1_ = wall.facet.normal.z(fl_)
wall.servo.force.x(wp1) = xv1_ * tf1_

```

```

wall.servo.force.y(wp1) = yv1_ * tf1_
wall.servo.force.z(wp1) = zv1_ * tf1_
wall.servo.vmax(wp1) = _vmaxt      ;set the maximum velocity applied to reach target force
wall.servo.gainfactor(wp1) = _gainfactort
;setting of paired wall
wall.vertex.pos(vp1_) = cr1_
wall.vertex.pos(vp2_) = cu1_
wall.vertex.pos(vp3_) = co1_      ;set the vertex position to connect the diagonal unit
xco1_ = wall.vertex.pos.x(vo1_)
yco1_ = wall.vertex.pos.y(vo1_)
zco1_ = wall.vertex.pos.z(vo1_)
tfp_ = cons_ * arp_      ;arp_ is the new area of paired triangle wall
xvp_ = wall.facet.normal.x(fp_)
yvp_ = wall.facet.normal.y(fp_)
zvp_ = wall.facet.normal.z(fp_)
wall.servo.force.x(wpp) = xvp_ * tfp_
wall.servo.force.y(wpp) = yvp_ * tfp_
wall.servo.force.z(wpp) = zvp_ * tfp_
wall.servo.vmax(wpp) = _vmaxt
wall.servo.gainfactor(wpp) = _gainfactort
end_loop

```

A2: Cracks import and hydraulic property assignment in FLAC^{3D}

The following codes show the importing process from crack data to the FLAC^{3D} model. Each zone, which represents a crack, is assigned with specific hydraulic properties based on distinct crack conditions. The assigned permeability is calculated according to the theoretical analysis based on the geometrical relations.

Code:

```

loop local _i(1,n_)      ; n is the total fracture number, and also the first line of data file
l_ = file.read(line_,1)  ;load the line number
local cx_ = string.token(line_(1),1)  ;load the crack position x
local cy_ = string.token(line_(1),2)  ;load the crack position y
local cz_ = string.token(line_(1),3)  ;load the crack position z
local d_ = string.token(line_(1),4)   ;load the diameter of crack disk
local nx_ = string.token(line_(1),5)  ;load the normal direction vector x

```

```

local ny_ = string.token(line_(1),6) ;load the normal direction vector y
local nz_ = string.token(line_(1),7) ;load the normal direction vector z
local fap_ = string.token(line_(1),8) ;load the crack aperture
local fsd_ = string.token(line_(1),9) ;load the relative shear displacement
local fddir_ = string.token(line_(1),10) ;load the dip direction
local fdip_ = string.token(line_(1),11) ;load the dip
local g_ = string.token(line_(1),12) ;load the group name
local strain_ = string.token(line_(1),13) ;load the current strain value
loop foreach zp zone.list
id_ = id_ + 1
local x_ = zone.pos.x(zp)
local y_ = zone.pos.y(zp)
local z_ = zone.pos.z(zp)
local lam_ = math.abs((x_-cx_)*nx_ + (y_-cy_)*ny_ + (z_-cz_)*nz_)/1 ;the 1 below should
be math.mag2(nx_, ny_, nz_) ,but for a unit vector it is always equal to 1
local vd_ = math.mag(x_-cx_-(lam_*nx_) , y_-cy_-(lam_*ny_) , z_-cz_-(lam_*nz_)) ; the
distance from zone center to the disk
if z_ >= cz_ - 0.5*d_
if z_ <= cz_ + 0.5*d_
if y_ >= cy_ - 0.5*d_
if y_ <= cy_ + 0.5*d_
if x_ >= cx_ - 0.5*d_
if x_ <= cx_ + 0.5*d_ ; narrow the searching range
if lam_ < (0.5*lavg) ; ; value of half side length of zone
if vd_ <= (0.5* d_) then
if zone.group(zp) = 'matrix'
zone.fluid.model(zp) = 'isotropic'
zone.fluid.prop(zp,'porosity') = c_porosm ; equals to initial matrix property
zone.fluid.prop(zp,'permeability') = c_permm
if g_ = 'crack_tension'
zone.group(zp) = 'fractm'
zone.fluid.model(zp) = 'isotropic'
zone.fluid.prop(zp,'porosity') = (((1 - ((math.sqrt(((2*2e-3+(5e-5)+fap_)^2) ...
-((2e-3)^2)*4/3))-(math.sqrt(6)*2*2e-3/3))/lavg))*c_porosm) ...
+ (((math.sqrt(((2*2e-3+(5e-5)+fap_)^2)-((2e-3)^2)*4/3)) ...
- (math.sqrt(6)*2*2e-3/3))/lavg)

```

```

zone.fluid.prop(zp,'permeability') = ((math.sqrt(((2*2e-3+(5e-5)+fap_)^2) ...
- ((2e-3)^2)*4/3))-(math.sqrt(6)*2*2e-3/3))^3/(12*lavg) /(strain_*n_*0.05) ...
+ c_permm
else if g_ = 'crack_shear' then
zone.group(zp) = 'fracsm'
zone.fluid.model(zp) = 'isotropic'
zone.fluid.prop(zp,'porosity') = ((1 - (((fsd_+(math.sqrt((4e-3+5e-5)^2 ...
- (4e-3)^2))) * (math.sqrt(3)-math.sqrt(2)))/lavg))*c_porosm)...
+ ((fsd_+(math.sqrt((4e-3+5e-5)^2-(4e-3)^2))*(math.sqrt(3)-math.sqrt(2)))/lavg)
zone.fluid.prop(zp,'permeability') = ((fsd_+(math.sqrt((4e-3+(5e-5)^2 ...
- (4e-3)^2)))*(math.sqrt(3)-math.sqrt(2)))^3/(12*lavg) /(strain_*n_*0.05) ...
+c_permm
else
end_if
end_if
else
end_if
else
end_if
else
end_if
else
end_if
else
end_if
else
end_if
else
end_if
end_loop
end_loop

```

References

- Auzerais, F. M. (1996). "Transport in sandstone: a study based on three dimensional microtomography." *Geophysical Research Letters*, 23(7), 705–708.
- Baghbanan, A., and Jing, L. (2008). "Stress effects on permeability in a fractured rock mass with correlated fracture length and aperture." *International Journal of Rock Mechanics and Mining Sciences*, 45(8), 1320–1334.
- Bai, M., Ma, Q., and Roegiers, J.-C. (1994). "Dual-porosity behaviour of naturally fractured reservoirs." *International Journal for Numerical and Analytical Methods in Geomechanics*, 18(6), 359–376.
- Bai, M., Meng, F., Elsworth, D., and Roegiers, J. C. (1999). "Analysis of stress-dependent permeability in nonorthogonal flow and deformation fields." *Rock Mechanics and Rock Engineering*, 32(3), 195–219.
- Barenblatt, G. . I., Zheltov, I. . P., and Kochina, I. . N. (1960). "Basic concepts in the theory of seepage of homogeneous liquids in fissured rocks [strata]." *Journal of Applied Mathematics and Mechanics*, 24(5), 1286–1303.
- Barton, N. (1976). "The shear strength of rock and rock joints." *International Journal of Rock Mechanics and Mining Sciences and*, 13(9), 255–279.
- Barton, N., Bandis, S., and Bakhtar, K. (1985). "Strength, deformation and conductivity coupling of rock joints." *International Journal of Rock Mechanics and Mining Sciences and*, 22(3), 121–140.
- Barton, N., and Choubey, V. (1977). "The shear strength of rock joints in theory and practice." *Rock Mechanics Felsmechanik Mécanique des Roches*, 10(1–2), 1–54.
- Baumgarten, L., and Konietzky, H. (2012). "Stress-strain, strength and failure behavior of Postaer Sandstone in tension and compression tests–laboratory investigations and numerical modelling with PFC3D, Veröffentl." *Veröffentlichungen des Instituts für Geotechnik der TU Bergakademie Freiberg*, 1, 41–61.
- Bear, J. (2006). "Dynamics of Fluids in Porous Media." *Soil Science*, 120(2), 162–163.
- Belheine, N., Plassiard, J. P., Donzé, F. V., Darve, F., and Seridi, A. (2009). "Numerical simulation of drained triaxial test using 3D discrete element modeling." *Computers and Geotechnics*, 36(1–2), 320–331.
- Bertels, S. P., DiCarlo, D. A., and Blunt, M. J. (2001). "Measurement of aperture distribution, capillary pressure, relative permeability, and in situ saturation in a rock fracture using computed tomography scanning." *Water Resources Research*, 37(3), 649–662.
- Biot, M. A. (1955). "Theory of elasticity and consolidation for a porous anisotropic solid." *Journal of Applied Physics*, 26(2), 182–185.
- Biot, M. A. (1973). "Nonlinear and semilinear rheology of porous solids." *Journal of Geophysical Research*, 78(23), 4924–4937.
- Biot, M. A., and Temple, G. (1972). "Theory of Finite Deformations of Porous Solids." *Indiana University Mathematics Journal*, 21(7).

References

- Bonnet, E., Bour, O., Odling, N. E., Davy, P., Main, I., Cowie, P., and Berkowitz, B. (2001). "Scaling of fracture systems in geological media." *Reviews of geophysics*, 39(3), 347–383.
- de Bono, J., McDowell, G., and Wanatowski, D. (2013). "Discrete element modelling of a flexible membrane for triaxial testing of granular material at high pressures." *Géotechnique Letters*, 2(4), 199–203.
- Bossart, P., Meier, P. M., Moeri, A., Trick, T., and Mayor, J. C. (2002). "Geological and hydraulic characterisation of the excavation disturbed zone in the Opalinus Clay of the Mont Terri Rock Laboratory." *Engineering Geology*, 66(1–2), 19–38.
- Botsch, M., Kobbelt, L., Pauly, M., Alliez, P., and Levy, B. (2010). *Polygon Mesh Processing*. AK Peters/CRC Press.
- Boulton, N. S., and Streltsova, T. D. (1977). "Unsteady flow to a pumped well in a fissured water-bearing formation." *Journal of Hydrology*, 35(3–4), 257–270.
- Boussinesq, M. J. (1897). *Théorie de l'écoulement tourbillonnant et tumultueux des liquides*. (Gauthier-Villars, ed.).
- Brace, W. F., Walsh, J. B., and Frangos, W. T. (1968). "Permeability of granite under high pressure." *Journal of Geophysical Research*, 73(6), 2225–2236.
- Cacas, M. C. (1990). "Modeling fracture flow with a stochastic discrete fracture network: calibration and validation. 2. The transport model." *Water Resources Research*, 1(26), 491–500.
- Cai, Y., Liu, D., Mathews, J. P., Pan, Z., Elsworth, D., Yao, Y., Li, J., and Guo, X. (2014). "Permeability evolution in fractured coal - Combining triaxial confinement with X-ray computed tomography, acoustic emission and ultrasonic techniques." *International Journal of Coal Geology*, Elsevier B.V., 122, 91–104.
- Cai, Y., Liu, D., Pan, Z., Yao, Y., Li, J., and Qiu, Y. (2013). "Pore structure and its impact on CH₄ adsorption capacity and flow capability of bituminous and subbituminous coals from Northeast China." *Fuel*, 103, 258–268.
- Cao, L., Peng, X., Yang, C., and Ren, Z. (2009). "A meso-mechanical coupling constitutive model of damage and permeability in rock-like materials under triaxial compression." *Chinese Journal of Rock Mechanics and Engineering*, 28(11), 2309–2319.
- Cao, P., Liu, T., Pu, C., and Lin, H. (2015). "Crack propagation and coalescence of brittle rock-like specimens with pre-existing cracks in compression." *Engineering Geology*, 187, 113–121.
- Carlson, W. D., and Denison, C. (1992). "Mechanisms of porphyroblast crystallization: Results from high-resolution computed x-ray tomography." *Science*, 257(5074), 1236–1239.
- Chen, W., Yang, J., Wu, G., Tan, X., Jia, S., Dai, Y., and Yu, H. (2008). "Experimental study on permeability in low permeability media." *Chinese Journal of Rock Mechanics and Engineering*, 27(2), 236–243.
- Chen, Y., Tang, D., Xu, H., Tao, S., Li, S., Yang, G., and Yu, J. (2015). "Pore and fracture characteristics of different rank coals in the eastern margin of the Ordos Basin, China." *Journal of Natural Gas Science and Engineering*, 26, 1264–1277.
- Chen, Z., Narayan, S. P., Yang, Z., and Rahman, S. S. (2000). "An experimental investigation of

References

- hydraulic behaviour of fractures and joints in granitic rock.” *International Journal of Rock Mechanics and Mining Sciences*, 37, 1061–1071.
- Cheung, G., and O’Sullivan, C. (2008). “Effective simulation of flexible lateral boundaries in two- and three-dimensional DEM simulations.” *Particuology*, 6(6), 483–500.
- Ciantia, M. O., Arroyo, M., Calvetti, F., and Calvetti, F. (2016). “A numerical investigation of the incremental behavior of crushable granular soils.” *International Journal for Numerical and Analytical Methods in Geomechanics*, 40(13), 1773–1798.
- Cleary, P. W. (2000). “DEM simulation of industrial particle flows: Case studies of dragline excavators, mixing in tumblers and centrifugal mills.” *Powder Technology*, 109(1–3), 83–104.
- Close, J. (1993). “Natural Fractures in Coal.” *Hydrocarbons from Coal*, 38(1960), 119–132.
- Cnudde, V., and Boone, M. N. (2013). “High-resolution X-ray computed tomography in geosciences: A review of the current technology and applications.” *Earth-Science Reviews*, Elsevier B.V., 123, 1–17.
- Cnudde, V., Masschaele, B., Dierick, M., Vlassenbroeck, J., Hoorebeke, L. Van, and Jacobs, P. (2006). “Recent progress in X-ray CT as a geosciences tool.” *Applied Geochemistry*, 21(5), 826–832.
- Cook, N. G. W. (1992). “Natural joints in rock: Mechanical, hydraulic and seismic behaviour and properties under normal stress.” *International Journal of Rock Mechanics and Mining Sciences and*, 29(3), 198–223.
- Cui, L., O’Sullivan, C., and O’Neill, S. (2008). “An analysis of the triaxial apparatus using a mixed boundary three-dimensional discrete element model.” *Géotechnique*, 57(10), 831–844.
- Cundall, P. A. (2004). *PFC user manual*. (M. I. C. Group, ed.), Itasca Consulting Group Inc., Mineapolis.
- Cundall, P. A., and Strack, O. D. L. (1979). “A discrete numerical model for granular assemblies.” *Géotechnique*, 29(1), 47–65.
- Dicker, A. I., and Smits, R. M. (2007). “A Practical Approach for Determining Permeability From Laboratory Pressure-Pulse Decay Measurements.” *International meeting on petroleum engineering*, Society of Petroleum Engineers, 285–292.
- Durham, W. B., and Bonner, B. P. (1994). “Self-propping and fluid flow in slightly offset joints at high effective pressures.” *Journal of Geophysical Research*, 99(B5), 9391–9399.
- Dyskin, A. V., Sahouryeh, E., Jewell, R. J., Joer, H., and Ustinov, K. B. (2003). “Influence of shape and locations of initial 3-D cracks on their growth in uniaxial compression.” *Engineering Fracture Mechanics*, 70(15), 2115–2136.
- Esaki, T., Du, S., Mitani, Y., Ikusada, K., and Jing, L. (1999). “Development of a shear-flow test apparatus and determination of coupled properties for a single rock joint.” *International Journal of Rock Mechanics and Mining Sciences*, 36(5), 641–650.
- Esaki, T., Hojo, H., Kimura, T., and Kameda, N. (1991). “Shear-flow coupling test on rock joints.” *7th ISRM Congress.*, 389–392.
- Flannery, B. P., Deckman, H. W., Roberge, W. G., and D’amico, K. L. (1987). “Three-Dimensional X-

References

- Ray Microtomography.” *Science*, 237(4821), 1439–1444.
- Van Geet, M., Swennen, R., and David, P. (2001a). “Quantitative coal characterisation by means of microfocus X-ray computer tomography, colour image analysis and back-scattered scanning electron microscopy.” *International Journal of Coal Geology*, 46(1), 11–25.
- Van Geet, M., Swennen, R., and Wevers, M. (2001b). “Towards 3-D petrography: Application of microfocus computer tomography in geological science.” *Computers and Geosciences*, 27(9), 1091–1099.
- Golab, A., Ward, C. R., Permana, A., Lennox, P., and Botha, P. (2013). “High-resolution three-dimensional imaging of coal using microfocus X-ray computed tomography, with special reference to modes of mineral occurrence.” *International Journal of Coal Geology*, Elsevier B.V., 113(July), 97–108.
- Goldstein, L., Prasher, S. O., and Ghoshal, S. (2007). “Three-dimensional visualization and quantification of non-aqueous phase liquid volumes in natural porous media using a medical X-ray Computed Tomography scanner.” *Journal of Contaminant Hydrology*, 93(1–4), 96–110.
- Guo, H., Adhikary, D. P., and Craig, M. S. (2009). “Simulation of mine water inflow and gas emission during longwall mining.” *Rock Mechanics and Rock Engineering*, 42(1), 25–51.
- Hakami, E., Einstein, H. H., Gentier, S., and Iwano, M. (1995). “Characterisation of fracture apertures - Methods and parameters.” *8th ISRM Congress, 25-29 September, Tokyo, Japan, (1986)*, 751–754.
- Hasan, A., and Alshibli, K. A. (2010). “Discrete Element Modeling of Strength Properties of Johnson Space Center (JSC-1A) Lunar Regolith Simulant.” *Journal of Aerospace Engineering*, 23(3), 157–165.
- Hoek, E., and Bieniawski, Z. T. (1965). “Brittle Rock Fracture Propagation In Rock Under Compression.” *International Journal of Fracture Mechanics*, 1(3), 137–155.
- Hoek, E., Carranza, C., and Corkum, B. (2002). “Hoek-brown failure criterion – 2002 edition.” *Narms-Tac*, 267–273.
- Hou, Y., Wei, J., Zhang, S., Sun, C., Tang, S., and Zhang, T. (2017). “Nanopore Characteristics of Late Paleozoic Transitional Facies Coal-Bearing Shale in Ningwu Basin, China Investigated by Nuclear Magnetic Resonance and Low-Pressure Nitrogen Adsorption.” *Journal of Nanoscience and Nanotechnology*, 17(9), 6433–6444.
- Hou, Z., Xie, H., Zhou, H., Were, P., and Kolditz, O. (2015). “Unconventional gas resources in China.” *Environmental Earth Sciences*, 73(10), 5785–5789.
- Hu, Y., Zhao, Y., Wei, J., and Ren, Z. (1996). “Experimental study of permeating law of coal mass gas under action of 3-dimension stress.” *Journal of Xi’an Mining Institute*, 16(4), 308–311.
- Hunt, P. K., Engler, P., and Bajsarowicz, C. (1988). “Computed Tomography as a Core Analysis Tool: Applications, Instrument Evaluation, and Image Improvement Techniques.” *Journal of Petroleum Technology*, 40(09), 1203–1210.
- ISRM. (2015). *The ISRM Suggested Methods for Rock Characterization, Testing and Monitoring: 2007-2014. Environmental and Engineering Geoscience*.

References

- Iwashita, K., and Oda, M. (2002). "Rolling Resistance at Contacts in Simulation of Shear Band Development by DEM." *Journal of Engineering Mechanics*, 124(3), 285–292.
- Jiang, T., Shao, J. F., Xu, W. Y., and Zhou, C. B. (2010). "Experimental investigation and micromechanical analysis of damage and permeability variation in brittle rocks." *International Journal of Rock Mechanics and Mining Sciences*, 47(5), 703–713.
- Jiang, Z., and Ji, L. (2001). "The laboratory study on behavior of permeability of rock along the complete stress-strain path." *Chinese journal of Geotechnical Engineering*, 23(2), 153–156.
- Jing, L., and Hudson, J. A. (2002). "Numerical methods in rock mechanics." *International Journal of Rock Mechanics and Mining Sciences*, 39, 409–427.
- Jing, Y., Armstrong, R. T., Ramandi, H. L., and Mostaghimi, P. (2016). "Coal cleat reconstruction using micro-computed tomography imaging." *Fuel*, 181, 286–299.
- Johns, R. A., Steude, J. S., Castanier, L. M., and Roberts, P. V. (1993). "Nondestructive measurements of fracture aperture in crystalline rock cores using X ray computed tomography." *Journal of Geophysical Research*, 98(B2), 1889–1900.
- Jones, S. C. (2007). "A Technique for Faster Pulse-Decay Permeability Measurements in Tight Rocks." *SPE Formation Evaluation*, 12(01), 19–26.
- Kachanov, M. L. (1982a). "A microcrack model of rock inelasticity part I: Frictional sliding on microcracks." *Mechanics of Materials*, 1(1), 19–27.
- Kachanov, M. L. (1982b). "A microcrack model of rock inelasticity part II: Propagation of microcracks." *Mechanics of Materials*, 1(1), 29–41.
- Karacan, C. Ö. (2003). "Heterogeneous sorption and swelling in a confined and stressed coal during CO₂ injection." *Energy and Fuels*, 17(6), 1595–1608.
- Karacan, C. Ö. (2007). "Swelling-induced volumetric strains internal to a stressed coal associated with CO₂ sorption." *International Journal of Coal Geology*, 72(3–4), 209–220.
- Karacan, C. Ö. (2009). "Reservoir rock properties of coal measure strata of the Lower Monongahela Group, Greene County (Southwestern Pennsylvania), from methane control and production perspectives." *International Journal of Coal Geology*, Elsevier B.V., 78(1), 47–64.
- Karacan, C. Ö., and Mitchell, G. D. (2003). "Behavior and effect of different coal microlithotypes during gas transport for carbon dioxide sequestration into coal seams." *International Journal of Coal Geology*, 53(4), 201–217.
- Karacan, C. O., and Okandan, E. (2001). "Adsorption and gas transport in coal microstructure: Investigation and evaluation by quantitative X-ray CT imaging." *Fuel*, 80(4), 509–520.
- Karacan, C. Ö., and Okandan, E. (2000). "Fracture/cleat analysis of coals from Zonguldak Basin (northwestern Turkey) relative to the potential of coalbed methane production." *International Journal of Coal Geology*, 44(2), 109–125.
- Karacan, C. Ö., Ruiz, F. A., Cotè, M., and Phipps, S. (2011). "Coal mine methane: A review of capture and utilization practices with benefits to mining safety and to greenhouse gas reduction." *International Journal of Coal Geology*, Elsevier B.V., 86(2–3), 121–156.

References

- Karpyn, Z. T., Alajmi, A., Radaelli, F., Halleck, P. M., and Grader, A. S. (2009). "X-ray CT and hydraulic evidence for a relationship between fracture conductivity and adjacent matrix porosity." *Engineering Geology*, Elsevier B.V., 103(3–4), 139–145.
- Kazerani, T., and Zhao, J. (2010). "Micromechanical parameters in bonded particle method for modelling of brittle material failure." *International Journal for Numerical and Analytical Methods in Geomechanics*, 34(18), 1877–1895.
- Keller, A. (1998). "High resolution, non-destructive measurement and characterization of fracture apertures." *International Journal of Rock Mechanics and Mining Sciences*, 35(8), 1037–1050.
- Ketcham, R. A., and Carlson, W. D. (2001). "Acquisition, optimization and interpretation of x-ray computed tomographic imagery: Applications to the geosciences." *Computers and Geosciences*, 27(4), 381–400.
- Ketcham, R. A., and Iturrino, G. J. (2005). "Nondestructive high-resolution visualization and measurement of anisotropic effective porosity in complex lithologies using high-resolution X-ray computed tomography." *Journal of Hydrology*, 302(1–4), 92–106.
- Ki-Bok, M., Rutqvist, J., Tsang, C. F., and Jing, L. (2004). "Stress-dependent permeability of fractured rock masses: A numerical study." *International Journal of Rock Mechanics and Mining Sciences*, 41(7), 1191–1210.
- Klobes, P., Riesemeier, H., Meyer, K., Goebbels, J., and Hellmuth, K. H. (1997). "Rock porosity determination by combination of X-ray computerized tomography with mercury porosimetry." *Fresenius' Journal of Analytical Chemistry*, 357(5), 543–547.
- Koyama, T., Fardin, N., Jing, L., and Stephansson, O. (2006). "Numerical simulation of shear-induced flow anisotropy and scale-dependent aperture and transmissivity evolution of rock fracture replicas." *International Journal of Rock Mechanics and Mining Sciences*, 43(1), 89–106.
- Kranz, R. L., Saltzman, J. S., and Blacic, J. D. (1990). "Hydraulic diffusivity measurements on laboratory rock samples using an oscillating pore pressure method." *International Journal of Rock Mechanics and Mining Sciences and*, 27(5), 345–352.
- Kranz, R. L., Frankel, A. D., Engelder, T., and Scholz, C. H. (1979). "The permeability of whole and jointed Barre Granite." *International Journal of Rock Mechanics and Mining Sciences and*, 16(4), 225–234.
- Kuhn, M. (1995). "A flexible boundary for three-dimensional dem particle assemblies." *Engineering Computations*, 12(2), 175–183.
- Kumar, H., Lester, E., Kingman, S., Bourne, R., Avila, C., Jones, A., Robinson, J., Halleck, P. M., and Mathews, J. P. (2011). "Inducing fractures and increasing cleat apertures in a bituminous coal under isotropic stress via application of microwave energy." *International Journal of Coal Geology*, Elsevier B.V., 88(1), 75–82.
- Lan, H., Martin, C. D., and Hu, B. (2010). "Effect of heterogeneity of brittle rock on micromechanical extensile behavior during compression loading." *Journal of Geophysical Research*, 115(B01202).
- Laubach, S. E., Marrett, R. A., Olson, I. E., and Scott, A. R. (1998). "Characteristics and origins of coal cleat: a review." *International Journal of Coal Geology*, 35(1–4), 175–207.
- Lee, H. S., and Cho, T. F. (2002). "Hydraulic characteristics of rough fractures in linear flow under

References

- normal and shear load.” *Rock Mechanics and Rock Engineering*, 35(4), 299–318.
- Lee, H. S., Park, Y. J., Cho, T. F., and You, K. H. (2001). “Influence of asperity degradation on the mechanical behavior of rough rock joints under cyclic shear loading.” *International Journal of Rock Mechanics and Mining Sciences*, 38(7), 967–980.
- Lee, S. J., Hashash, Y. M. A., and Nezami, E. G. (2012). “Simulation of triaxial compression tests with polyhedral discrete elements.” *Computers and Geotechnics*, 43, 92–100.
- Lespinnasse, M., and Sausse, J. (2000). “Quantification of fluid flow: Hydro-mechanical behaviour of different natural rough fractures.” *Journal of Geochemical Exploration*, 69, 484–486.
- Li, B., Jiang, Y., Koyama, T., Jing, L., and Tanabashi, Y. (2008a). “Experimental study of the hydro-mechanical behavior of rock joints using a parallel-plate model containing contact areas and artificial fractures.” *International Journal of Rock Mechanics and Mining Sciences*.
- Li, J., Wang, D., and Kang, T. (2010). “Algorithmic study on rock pore structure based on micro-CT experiment.” *Chinese Journal of Geotechnical Engineering*, 32(11), 1703–1708.
- Li, L., Tsui, Y., Lee, P. K. K., Tham, L. G., Li, T., and Ge, X. (2002). “Progressive cracking of granite plate under uniaxial compression.” *Chinese Journal of Rock Mechanics and Engineering*, 21(7), 940–947.
- Li, S., Ding, Y., Zhang, T., Xu, G., and Wang, L. (2013). “Experiment on permeability properties of coal samples with low permeability in complete stress-strain process.” *Safety in coal mines*, 6(006), 5–8.
- Li, X., Wang, Y., and Wei, N. (2008b). “Research on measuring method of permeability by using storage-variable transient pulse method.” *Chinese Journal of Rock Mechanics and Engineering*, 27(12), 2482–2487.
- Li, Y., Chen, Y. F., and Zhou, C. B. (2014). “Hydraulic properties of partially saturated rock fractures subjected to mechanical loading.” *Engineering Geology*, 179, 24–31.
- Li, Y. P., Chen, L. Z., and Wang, Y. H. (2005). “Experimental research on pre-cracked marble under compression.” *International Journal of Solids and Structures*, 42(9–10), 2505–2516.
- Liu, J., Fokker, P. A., and Spiers, C. J. (2017). “Coupling of swelling, internal stress evolution, and diffusion in coal matrix material during exposure to methane.” *Journal of Geophysical Research: Solid Earth*, 122(2), 844–865.
- Liu, J., Liu, X., and Hu, Y. (2003). “Study on nonlinear seepage of rock of low permeability.” *Chinese Journal of Rock Mechanics and Engineering*, 22(4), 556–561.
- Liu, S. Q., Sang, S. X., Liu, H. H., and Zhu, Q. P. (2015). “Growth characteristics and genetic types of pores and fractures in a high-rank coal reservoir of the southern Qinshui basin.” *Ore Geology Reviews*.
- Liu, Y., Cai, Y., Liu, Q., and Wu, Y. (2001). “Thermal-hydraulic-mechanical coupling constitutive relation of rock mass fracture interconnectivity.” *Chinese Journal of Geotechnical Engineering*, 23(2), 196–200.
- Lu, Y., and Frost, D. (2010). “Three-dimensional DEM modeling of triaxial compression of sands.” *Soil behavior and geo-micromechanics*, LimitedDeep Foundation Institute, 220–226.

References

- Mahabadi, O. K., Randall, N. X., Zong, Z., and Grasselli, G. (2012). "A novel approach for micro-scale characterization and modeling of geomaterials incorporating actual material heterogeneity." *Geophysical Research Letters*, 39(1), L01303.
- Maleki, K., and Pouya, A. (2010). "Numerical simulation of damage-Permeability relationship in brittle geomaterials." *Computers and Geotechnics*, 37(5), 619–628.
- Mathews, J. P., Campbell, Q. P., Xu, H., and Halleck, P. (2017). "A review of the application of X-ray computed tomography to the study of coal." *Fuel*, 209, 10–24.
- Mathews, J. P., Pone, J. D. N., Mitchell, G. D., and Halleck, P. (2011). "High-resolution X-ray computed tomography observations of the thermal drying of lump-sized subbituminous coal." *Fuel Processing Technology*, 92(1), 58–64.
- Matsuki, K., Chida, Y., Sakaguchi, K., and Glover, P. W. J. (2006). "Size effect on aperture and permeability of a fracture as estimated in large synthetic fractures." *International Journal of Rock Mechanics and Mining Sciences*, 43(5), 726–755.
- Mazumder, S., Wolf, K. H. A. A., Elewaut, K., and Ephraim, R. (2006). "Application of X-ray computed tomography for analyzing cleat spacing and cleat aperture in coal samples." *International Journal of Coal Geology*, 68(3–4), 205–222.
- McClure, M., and Horne, R. (2014). "Characterizing Hydraulic Fracturing With a Tendency-for-Shear-Stimulation Test." *SPE Reservoir Evaluation & Engineering*, 17(2), 233–243.
- Min, K. B., Jing, L., and Stephansson, O. (2004). "Determining the equivalent permeability tensor for fractured rock masses using a stochastic REV approach: Method and application to the field data from Sellafield, UK." *Hydrogeology Journal*, 12(5), 497–510.
- Montemagno, C. D., and Pyrak-Nolte, L. J. (1999). "Fracture network versus single fractures: Measurement of fracture geometry with X-ray tomography." *Physics and Chemistry of the Earth, Part A: Solid Earth and Geodesy*, 24(7), 575–579.
- National Bureau of Statistics of China. (2017). *China statistical yearbook. China Statistics Press.*
- Nemoto, K., Watanabe, N., Hirano, N., and Tsuchiya, N. (2009). "Direct measurement of contact area and stress dependence of anisotropic flow through rock fracture with heterogeneous aperture distribution." *Earth and Planetary Science Letters*, 281(1–2), 81–87.
- Nemoto, K., Watanabe, N., and Tsuchiya, N. (2008). "Evaluation of fluid flow field in single rock fracture during frictional sliding." *AIP Conference Proceedings*, 123–128.
- Neuman, S. P. (2008). "Multiscale relationships between fracture length, aperture, density and permeability." *Geophysical Research Letters*, 35(22), 1–6.
- Neuzil, C. E., and Tracy, J. V. (1981). "Flow through fractures." *Water Resources Research*, 17(1), 191–199.
- Ng, T.-T. (2002). "Fabric Study of Granular Materials after Compaction." *Journal of Engineering Mechanics*, 125(12), 1390–1394.
- Ng, T.-T. (2004). "Triaxial Test Simulations with Discrete Element Method and Hydrostatic Boundaries." *Journal of Engineering Mechanics*, 130(10), 1188–1194.

References

- Ni, X., Chen, W., Li, Z., and Gao, X. (2017). "Reconstruction of different scales of pore-fractures network of coal reservoir and its permeability prediction with Monte Carlo method." *International Journal of Mining Science and Technology*, 27(4), 693–699.
- Nie, B., Liu, X., Yang, L., Meng, J., and Li, X. (2015). "Pore structure characterization of different rank coals using gas adsorption and scanning electron microscopy." *Fuel*, 158, 908–917.
- Nomura, S., Kato, K., Komaki, I., Fujioka, Y., Saito, K., and Yamaoka, I. (1999). "Viscoelastic properties of coal in the thermoplastic phase." *Fuel*, 78(13), 1583–1589.
- O'Sullivan, C., and Cui, L. (2009). "Micromechanics of granular material response during load reversals: Combined DEM and experimental study." *Powder Technology*, 193(3), 289–302.
- Oda, M., Takemura, T., and Aoki, T. (2002). "Damage growth and permeability change in triaxial compression tests of Inada granite." *Mechanics of Materials*, 34(6), 313–331.
- Ohbuchi, R., Nakazawa, M., and Takei, T. (2003). "Retrieving 3D shapes based on their appearance." *Proceedings of the 5th ACM SIGMM International Workshop on Multimedia Information Retrieval, MIR 2003*, 39–45.
- Olsen, H. W., Nichols, R. W., and Rice, T. L. (1985). "Low gradient permeability measurements in a triaxial system." *Geotechnique*, 32(2), 145–157.
- Oron, A. P., and Berkowitz, B. (1998). "Flow in rock fractures: The local cubic law assumption reexamined." *Water Resources Research*.
- Park, C. H., and Bobet, A. (2009). "Crack coalescence in specimens with open and closed flaws: A comparison." *International Journal of Rock Mechanics and Mining Sciences*, 46(5), 819–829.
- Park, H., Osada, M., Matsushita, T., Takahashi, M., and Ito, K. (2013). "Development of coupled shear-flow-visualization apparatus and data analysis." *International Journal of Rock Mechanics and Mining Sciences*, Elsevier, 63, 72–81.
- Peng, R. D., Yang, Y. C., Ju, Y., Mao, L. T., and Yang, Y. M. (2011). "Computation of fractal dimension of rock pores based on gray CT images." *Chinese Science Bulletin*, 56(31), 3346–3357.
- Polak, A., Elsworth, D., Yasuhara, H., Grader, A. S., and Halleck, P. M. (2003). "Permeability reduction of a natural fracture under net dissolution by hydrothermal fluids." *Geophysical Research Letters*, 30(20), 1–4.
- Potyondy, D. O., and Cundall, P. A. (2004). "A bonded-particle model for rock." *International Journal of Rock Mechanics and Mining Sciences*, 41(8), 1329–1364.
- Pyrak-Nolte, L. J., and Morris, J. P. (2000). "Single fractures under normal stress: The relation between fracture specific stiffness and fluid flow." *International Journal of Rock Mechanics and Mining Sciences*, 37(1–2), 245–262.
- Ramandi, H. L., Mostaghimi, P., Armstrong, R. T., Saadatfar, M., and Pinczewski, W. V. (2016). "Porosity and permeability characterization of coal: A micro-computed tomography study." *International Journal of Coal Geology*, 154, 57–68.
- Randall, N. X., Vandamme, M., and Ulm, F. J. (2009). "Nanoindentation analysis as a two-dimensional tool for mapping the mechanical properties of complex surfaces." *Journal of Materials Research*, 24(3), 679–690.

References

- Raven, K. G., and Gale, J. E. (1985). "Water flow in a natural rock fracture as a function of stress and sample size." *International Journal of Rock Mechanics and Mining Sciences and*, 22(4), 251–261.
- Rédei, G. P. (2008). "Mimics." *Encyclopedia of Genetics, Genomics, Proteomics and Informatics*, Springer Science & Business Media.
- Remeysen, K., and Swennen, R. (2006). "Beam hardening artifact reduction in microfocus computed tomography for improved quantitative coal characterization." *International Journal of Coal Geology*, 67(1–2), 101–111.
- Remeysen, K., and Swennen, R. (2008). "Application of microfocus computed tomography in carbonate reservoir characterization: Possibilities and limitations." *Marine and Petroleum Geology*, 25(6), 486–499.
- Ren, J., and Ge, X. (2001). "Study of rock meso-Damage evolution law and its constitutive model under uniaxial compression loading." *Chinese Journal of Rock Mechanics & Engineering*, 20(4), 425–431.
- Rendulic, L. (1936). "Porenziffer und porenwasserdruck in Tonen." *Der Bauingenieur*, 17, 559–564.
- Renshaw, C. E. (1995). "On the relationship between mechanical and hydraulic apertures in rough-walled fractures." *Journal of Geophysical Research: Solid Earth*, 100(B12), 24629–24636.
- Rutqvist, J., and Stephansson, O. (2003). "The role of hydrochemical coupling in fractured rock engineering." *Hydrogeology Journal*, 11(1), 7–40.
- Sagong, M., and Bobet, A. (2002). "Coalescence of multiple flaws in a rock-model material in uniaxial compression." *International Journal of Rock Mechanics and Mining Sciences*, 39(2), 229–241.
- Salot, C., Gotteland, P., and Villard, P. (2009). "Influence of relative density on granular materials behavior: DEM simulations of triaxial tests." *Granular Matter*, 11(4), 221–236.
- Sausse, J. (2002). "Hydromechanical properties and alteration of natural fracture surfaces in the Soultz Granite (Bas-Rhin, France)." *Tectonophysics*, 348(1–3), 169–185.
- Shan, T., and Zhao, J. (2014). "A coupled CFD-DEM analysis of granular flow impacting on a water reservoir." *Acta Mechanica*, 225(8), 2449–2470.
- Sheng, J., Su, B., Wang, Y., and Zhan, M. (2000). "Coupling analysis of elasto-plastic stress and fluid flow in jointed rock masses." *Chinese Journal of Rock Mechanics and Engineering*, 19(3), 304–309.
- Simons, F. J., Verhelst, F. F., and Swennen, R. (1997). *Quantitative characterization of coal by means of microfocal X-ray computed microtomography (CMT) and color image analysis. international Journal of Coal Geology*, 69–88.
- Sitharam, T. G., Dinesh, S. V., and Shimizu, N. (2002). "Micromechanical modelling of monotonic drained and undrained shear behaviour of granular media using three-dimensional DEM." *International Journal for Numerical and Analytical Methods in Geomechanics*, 26(12), 1167–1189.
- Snow, D. T. (1968). "Rock Fracture Spacings, Openings, and Porosities." *Journal of the Soil Mechanics and Foundations Division*, 94(1), 73–92.

References

- Solomon, C., and Breckon, T. (2011). *Fundamentals of Digital Image Processing: A Practical Approach with Examples in Matlab*. *Fundamentals of Digital Image Processing: A Practical Approach with Examples in Matlab*, John Wiley & Sons.
- Somerton, W. H., Soylemezoglu, I. M., and Dudley, R. C. (1975). "Effect of Stress on Permeability of Coal." *Int. J. Rock Mech. Min. Sci. & Geomech.*, 12(4), 129–145.
- Souley, M., Homand, F., Pepa, S., and Hoxha, D. (2001). "Damage-induced permeability changes in granite: A case example at the URL in Canada." *International Journal of Rock Mechanics and Mining Sciences*, 38(2), 297–310.
- Sun, H.-F., Ju, Y., Xing, M.-X., Wang, X.-F., and Yang, Y.-M. (2014). "3D identification and analysis of fracture and damage in soil-rock mixtures based on CT image processing." *Meitan Xuebao/Journal of the China Coal Society*, 39(3), 452–459.
- Sun, J., Yang, Z., Guo, H., Xiao, Q., Hao, M., and Xu, X. (2013). "Comparative study of tight reservoir permeability using steady-state and unsteady-state methods." *Rock and Soil Mechanics*, 34(4), 1009–1016.
- Sun, M., Huang, X., Li, T., Lei, G., and Mao, X. (2006). "Seepage properties of non-Darcy flow in complete failure process of limestone." *Chinese Journal of Rock Mechanics & Engineering*, 25(3), 484–491.
- Suzuki, K., Oda, M., Yamazaki, M., and Kuwahara, T. (1998). "Permeability changes in granite with crack growth during immersion in hot water." *International Journal of Rock Mechanics and Mining Sciences*.
- Tan, X. (2013). "Hydro-Mechanical Coupled Behavior of Brittle Rocks - Laboratory Experiments and Numerical Simulations." Technische Universität Bergakademie Freiberg.
- Tan, X., and Konietzky, H. (2014). "Numerical study of variation in Biot's coefficient with respect to microstructure of rocks." *Tectonophysics*, Elsevier B.V., 610, 159–171.
- Tan, X., Konietzky, H., and Frühwirt, T. (2015). "Numerical simulation of triaxial compression test for brittle rock sample using a modified constitutive law considering degradation and dilation behavior." *Journal of Central South University*, 22(8), 3097–3107.
- Tang, C. A., Lin, P., Wong, R. H. C. H. C., and Chau, K. T. T. (2001). "Analysis of crack coalescence in rock-like materials containing three flaws Part II: numerical approach." *International Journal of Rock Mechanics & Mining Sciences*, 38(7), 925–939.
- Tang, C. A., Tham, L. G., Lee, P. K. K., Yang, T. H., and Li, L. C. (2002). "Coupled analysis of flow, stress and damage (FSD) in rock failure." *International Journal of Rock Mechanics and Mining Sciences*, 39(4), 477–489.
- Terzaghi, K. (1943). *Theoretical Soil Mechanics*. JohnWiley & Sons.
- Thornton, C. (2000). "Numerical simulations of deviatoric shear deformation of granular media." *Géotechnique*, 50(1), 43–53.
- Tsang, Y. W. (1992). "Usage of 'Equivalent apertures' for rock fractures as derived from hydraulic and tracer tests." *Water Resources Research*, 28(5), 1451–1455.
- Tsang, Y. W., and Witherspoon, P. A. (1981). "Hydromechanical behavior of a formable rock fracture

References

- subject to normal stress.” *Journal of Geophysical Research*, 86(B10), 9287–9298.
- Ulusay, R., and Hudson, J. A. (2012). “Suggested methods for rock failure criteria: General introduction.” *Rock Mechanics and Rock Engineering*, 45(6), 971.
- Unger, A. J. A., and Mase, C. W. (1993). “Numerical study of the hydromechanical behavior of two rough fracture surfaces in contact.” *Water Resources Research*, 29(7), 2101–2114.
- Uthus, L., Hopkins, M. A., and Horvli, I. (2008). “Discrete element modelling of the resilient behaviour of unbound granular aggregates.” *International Journal of Pavement Engineering*, 9(6), 387–395.
- Vallejo, L. E. (1988). “The brittle and ductile behavior of clay samples containing a crack under mixed mode loading.” *Theoretical and Applied Fracture Mechanics*, 10(1), 73–78.
- Valliappan, S., and Khalili - Naghadeh, N. (1990). “Flow through fissured porous media with deformable matrix.” *International Journal for Numerical Methods in Engineering*, 29(5), 1079–1094.
- Verhelst, F., David, P., Fermont, W., Jegers, L., and Vervoort, A. (1996). “Correlation of 3D-computerized tomographic scans and 2D-colour image analysis of Westphalian coal by means of multivariate statistics.” *International Journal of Coal Geology*, 29(1–3), 1–21.
- Voorn, M., Exner, U., Barnhoorn, A., Baud, P., and Reuschlé, T. (2015). “Porosity, permeability and 3D fracture network characterisation of dolomite reservoir rock samples.” *Journal of Petroleum Science and Engineering*, Elsevier, 127, 270–285.
- Walsh, J. B. (2003). “A theoretical analysis of sliding of rough surfaces.” *Journal of Geophysical Research*, 108(B8).
- Wang, J. A., and Park, H. D. (2002). “Fluid permeability of sedimentary rocks in a complete stress-strain process.” *Engineering Geology*, 63(3–4), 291–300.
- Wang, J., Peng, S., and Meng, Z. (2011a). “Permeability rule in full strain-stress process of rock under triaxial compression.” *Journal of University of Science and Technology Beijing*, 23(6), 489–491.
- Wang, L., and Miao, X. (2005). “CUSP catastrophe model of relations among permeability, stress and strain of rocks.” *Chinese Journal of Rock Mechanics and Engineering*, 24(23), 4210–4214.
- Wang, W., Li, X., Li, Q., Shi, L., Wang, Y., and Bai, B. (2011b). “Small size in-situ transient pulse permeability measurement system and its experimental research.” *Rock and Soil Mechanics*, 32(10), 3185–3190.
- Wang, Y.-H., and Leung, S.-C. (2008). “A particulate-scale investigation of cemented sand behavior.” *Canadian Geotechnical Journal*, 45(1), 29–44.
- Wang, Y., Li, X., Que, J., and Li, S. (2015). “A porosity calculation method based on CT images and its application.” *Journal of Hydraulic Engineering*, 45(3), 357–365.
- Wang, Y., and Tonon, F. (2009). “Modeling Triaxial Test on Intact Rock Using Discrete Element Method with Membrane Boundary.” *Journal of Engineering Mechanics*, 135(9), 1029–1037.
- Warren, J. E., and Root, P. J. (2007). “The Behavior of Naturally Fractured Reservoirs.” *Society of Petroleum Engineers Journal*, 3(03), 245–255.

References

- Watanabe, N., Hirano, N., and Tsuchiya, N. (2008). "Determination of aperture structure and fluid flow in a rock fracture by high-resolution numerical modeling on the basis of a flow-through experiment under confining pressure." *Water Resources Research*, 44(6), 1–11.
- Watanabe, N., Ishibashi, T., Hirano, N., Ohsaki, Y., Tsuchiya, Y., Tamagawa, T., Okabe, H., and Tsuchiya, N. (2011a). "Precise 3D Numerical Modeling of Fracture Flow Coupled With X-Ray Computed Tomography for Reservoir Core Samples." *SPE Journal*, 16(03), 683–691.
- Watanabe, N., Ishibashi, T., Ohsaki, Y., Tsuchiya, Y., Tamagawa, T., Hirano, N., Okabe, H., and Tsuchiya, N. (2011b). "X-ray CT based numerical analysis of fracture flow for core samples under various confining pressures." *Engineering Geology*, Elsevier B.V., 123(4), 338–346.
- Wellington, S. L., and Vinegar, H. J. (1987). "X-ray computerized tomography." *Journal of petroleum technology*, 39(8), 885–898.
- Willis-Richards, J., and Wallroth, T. (1995). "Approaches to the modelling of HDR reservoirs: a review." *Science*, 24(3), 307–332.
- Witherspoon, P. A., Wang, J. S. Y., Iwai, K., and Gale, J. E. (1980). "Validity of cubic law for fluid flow in a deformable rock fracture." *Water Resources Research*, 16(6), 1016–1024.
- Withjack, E. M. (1988). "Computed Tomography for Rock-Property Determination and Fluid-Flow Visualization." *SPE Formation Evaluation*, 3(04), 696–704.
- Wolf, K. H. A. A., van Bergen, F., Ephraim, R., and Pagnier, H. (2008). "Determination of the cleat angle distribution of the RECOPOL coal seams, using CT-scans and image analysis on drilling cuttings and coal blocks." *International Journal of Coal Geology*, 73(3–4), 259–272.
- Wolf, K. H. A. A., Ephraim, R., Siemons, N., and Bossie Codreanu, D. (2004). "Analysing cleat angles in coal seams using image analysis techniques on artificial drilling cuttings and prepared coal blocks." *Geologica Belgica*, 7(3–4), 105–113.
- Wong, N. Y., and Einstein, H. H. (2007). "Coalescence behavior in Carrara marble and molded gypsum containing artificial flaw pairs under uniaxial compression." *Proceedings of the 1st Canada-US rock mechanics symposium*, 581–589.
- Wong, R. H. C., and Chau, K. T. (1998). "Crack coalescence in a rock-like material containing two cracks." *International Journal of Rock Mechanics and Mining Sciences*, 35(2), 147–164.
- Wu, J., Shen, X., and Liu, L. (2012). "Interactive two-scale color-to-gray." *Visual Computer*, 28(6–8), 723–731.
- Xiong, X., Li, B., Jiang, Y., Koyama, T., and Zhang, C. (2014). "Experimental and numerical study of the geometrical and hydraulic characteristics of a single rock fracture during shear." *Seismic Safety Evaluation of Concrete Dams*, 48, 513–538.
- Yan, Y., and Ji, S. (2010). "Discrete element modeling of direct shear tests for a granular material." *International Journal for Numerical and Analytical Methods in Geomechanics*, 34(9), 978–990.
- Yang, G., Sun, J., Xie, D., Zhang, C., and Pu, Y. (1997). "CT identification of the mechanic characteristics of damage propagation of rock." *Journal of Coal Science & Engineering*, 3(1), 21–25.
- Yang, Y., Song, Y., and Chen, S. (2007). "Test study on permeability properties of coal specimen in

References

- complete stress-strain process.” *Rock and Soil Mechanics*, 28(2), 381–385.
- Yao, Y.-B., and Liu, D.-M. (2007). “Adsorption characteristics of coal reservoirs in North China and its influencing factors.” *Zhongguo Kuangye Daxue Xuebao/Journal of China University of Mining and Technology*, 36(3), 308.
- Yao, Y. Bin, Liu, D. M., Cai, Y. D., and Li, J. Q. (2010). “Advanced characterization of pores and fractures in coals by nuclear magnetic resonance and X-ray computed tomography.” *Science China Earth Sciences*, 53(6), 854–862.
- Yao, Y., and Liu, D. (2012). “Comparison of low-field NMR and mercury intrusion porosimetry in characterizing pore size distributions of coals.” *Fuel*, 95, 152–158.
- Yao, Y., Liu, D., Che, Y., Tang, D., Tang, S., and Huang, W. (2009). “Non-destructive characterization of coal samples from China using microfocus X-ray computed tomography.” *International Journal of Coal Geology*, Elsevier B.V., 80(2), 113–123.
- Yao, Y., Liu, D., Tang, D., Tang, S., and Huang, W. (2008). “Fractal characterization of adsorption-pores of coals from North China: An investigation on CH₄adsorption capacity of coals.” *International Journal of Coal Geology*, 73(1), 27–42.
- Yee, D., Seidle, J. P., and Hanson, W. B. (1993). “Gas sorption on coal and measurement of gas content: Chapter 9.” *AAPG Studies in Geology Volume 38*, 203–218.
- Yeo, I. W., De Freitas, M. H., and Zimmerman, R. W. (1998). “Effect of shear displacement on the aperture and permeability of a rock fracture.” *International Journal of Rock Mechanics and Mining Sciences*, 35(8), 1051–1070.
- Yin, G., Li, G., Zhao, H., Li, X., Jing, X., and Jiang, C. (2010). “Experimental research on gas flow properties of coal specimens in complete stress-strain process.” *Chinese Journal of Rock Mechanics & Engineering*, 29(1), 170–175.
- Yu, Q., Yang, T., Tang, S., Liu, H., Liang, Z., Zheng, X., and Jia, P. (2015). “The 3d reconstruction method for quasi-brittle material structure and application.” *Engineering Mechanics*, 32(11), 51–62.
- Zhang, H. (2009). “Experimental on gaseous seepage properties of sandstone in complete stress-strain process.” *Journal of China Coal Society*, 34(8), 1063–1066.
- Zhang, M., Takahashi, M., Morin, R. H., and Esaki, T. (2000a). “Evaluation and Application of the Transient-Pulse Technique for Determining the Hydraulic Properties of Low-Permeability Rocks - Part 1: Theoretical Evaluation.” *Geotechnical Testing Journal*, 23(1), 83–90.
- Zhang, M., Takahashi, M., Morin, R. H., and Esaki, T. (2000b). “Evaluation and application of the transient-pulse technique for determining the hydraulic properties of low-permeability rocks—Part 2: experimental application.” *Geotechnical Testing Journal*, 23(1), 91–99.
- Zhang, R., Ai, T., Li, H., Zhang, Z., and Liu, J. (2013). “3D reconstruction method and connectivity rules of fracture networks generated under different mining layouts.” *International Journal of Mining Science and Technology*, 23(6), 863–871.
- Zhang, X., Sanderson, D. J., Harkness, R. M., and Last, N. C. (1996). “Evaluation of the 2-D permeability tensor for fractured rock masses.” *International Journal of Rock Mechanics and Mining Sciences and Geomechanics*, 33(1), 17–37.

References

- Zhang, Y., Xu, X., Lebedev, M., Sarmadivaleh, M., Barifcani, A., and Iglauer, S. (2016). "Multi-scale x-ray computed tomography analysis of coal microstructure and permeability changes as a function of effective stress." *International Journal of Coal Geology*, 165, 149–156.
- Zhao, H., Yin, G., and Li, X. (2009a). "Test study on coupling relationship between permeability characteristics and stress of outburst coal." *Chinese Journal of Rock Mechanics & Engineering*, 28(Supp. 2), 3357–3362.
- Zhao, J., and Shan, T. (2013). "Coupled CFD-DEM simulation of fluid-particle interaction in geomechanics." *Powder Technology*, Elsevier B.V., 239, 248–258.
- Zhao, J., Xu, H., Tang, D., Mathews, J. P., Li, S., and Tao, S. (2016). "Coal seam porosity and fracture heterogeneity of macrolithotypes in the Hancheng Block, eastern margin, Ordos Basin, China." *International Journal of Coal Geology*, Elsevier B.V., 159, 18–29.
- Zhao, X., Evans, T. M., and Asce, A. M. (2009b). "Discrete Simulations of Laboratory Loading Conditions." *International Journal of Geomechanics*, 9(4), 169–178.
- Zhao, Y., Liu, S., Zhao, G.-F., Elsworth, D., Jiang, Y., and Han, J. (2010a). "Failure mechanisms in coal: Dependence on strain rate and microstructure." *Journal of Geophysical Research: Solid Earth RESEARCH*, (6), 6924–6935.
- Zhao, Y., Sun, Y., Liu, S., Wang, K., and Jiang, Y. (2017). "Pore structure characterization of coal by NMR cryoporometry." *Fuel*, 190, 359–369.
- Zhao, Y., Wang, W., Huang, Y., Cao, P., and Wan, W. (2010b). "Coupling analysis of seepage-damage-fracture in fractured rock mass and engineering application." *Chinese Journal of Geotechnical Engineering*, 32(1), 24–32.
- Zhong, J., Zhou, H., Zhao, Y., Liu, Y., Yi, H., and Xue, D. (2017). "The two-phase flow of water-sand inrush under shallow coal seam mining: a coupled numerical study." *Engineering Mechanics*, 34(12), 229–238.
- Zhou, H., Zhang, Y., Li, A., and Qiu, D. (2008). "Laboratory research on flow seepage boundary evolution in porous media." *Chinese Science Bulletin*, 53(3), 351–358.
- Zhou, J. J., Shao, J. F., and Lydzba, D. (2006). "Micromechanical Study of Damage and Permeability Variation in Brittle Rocks." *Modern Trends in Geomechanics*, Springer, Berlin, 289 - 300.
- Zhou, S., and Lin, B. (1999). *Coal seam gas occurrence and flow theory*. China coal industry publishing house, Beijing.
- Zhu, W. C., Liu, J., Elsworth, D., Polak, A., Grader, A., Sheng, J. C., and Liu, J. X. (2007). "Tracer transport in a fractured chalk: X-ray CT characterization and digital-image-based (DIB) simulation." *Transport in Porous Media*, 70(1), 25–42.
- Zhu, Z., Zhang, A., and Xu, W. (2002). "Experimental research on complete stress-strain process seepage characteristics of brittle rock." *Rock and Soil Mechanics*, 23(5), 555–563.
- Zienkiewicz, O. C., and Shiomi, T. (1984). "Dynamic behaviour of saturated porous media; The generalized Biot formulation and its numerical solution." *International Journal for Numerical and Analytical Methods in Geomechanics*, 8(1), 71–96.
- Zimmerman, R. W., Kumar, S., and Bodvarsson, G. S. (1991). "Lubrication theory analysis of the

References

permeability of rough-walled fractures.” *International Journal of Rock Mechanics and Mining Sciences and*, 28(4), 325–331.

Zubelewicz, A., and Mroz, Z. (1983). “Numerical simulation of rock burst processes treated as problems of dynamic instability.” *Rock Mechanics and Rock Engineering*, 16(1), 253–274.

Zuber, M. D. (1998). “Production characteristics and reservoir analysis of coalbed methane reservoirs.” *International Journal of Coal Geology*, 38(1–2), 27–45.